Towards Controlled Crystallisation via Confinement and Epitaxy

ALAN BRASCHINSKY

Towards Controlled Crystallisation *via* Confinement and Epitaxy

A thesis submitted in partial fulfilment of the requirements for the degree of *Doctor of Philosophy*

Alan Braschinsky

Department of Chemistry

Durham University

2024

Abstract

Crystallisation is crucial across industries, including food and pharmaceutical, and consists of two steps – nucleation and crystal growth. However, the formation mechanisms of sub-critical nuclei remain elusive despite knowledge of the shape and size of critical nuclei for different materials. This thesis aims to gain understanding of the mechanisms of sub-critical nuclei formation by using single crystal X-Ray diffraction to visualise small molecular clusters confined in metal-organic frameworks (MOFs), termed Cluster Confining MOFs (CCMs). To achieve this, previously reported isostructural lanthanide-based frameworks, herein labelled CCM-1–4, exhibiting considerably large pores and high crystallinity were synthesised to be used as confining matrices. This works shows that while the intermolecular interactions of molecules inside the framework pores can mimic those in bulk, the shape of the confined clusters are significantly different to their bulk equivalents. For instance, 1,2,3-triazole crystallises in a 1:1 ratio of its *1H*- and *2H*-1,2,3-triazole tautomers in bulk and forms similar clusters inside the pores of CCM-1, maintaining hydrogen bonding and π–π interactions. This work also introduces a novel interpenetrated zinc(II)-based MOF CCM-5 with a complex topology and a larger void volume compared to those in CCM-1–4 MOFs, potentially accommodating larger molecular clusters. However, challenges in reproducing the synthesis of CCM-5 precluded these studies. Furthermore, this work explores controlling crystallisation outcomes in coordination complexes through crystal welding, targeting the synthesis of compounds with varied metal centres and halide ligands. While the epitaxial growth attempts were unsuccessful, this method has been reported to be sensitive to specific experimental parameters and thus would require further investigations. Overall, this work highlights the potential of high-crystallinity MOFs to provide novel findings regarding the formation of sub-critical nuclei and uncovering novel polymorphs.

Declaration

The work described in this thesis was undertaken in the Department of Chemistry at Durham University (UK) between October 2020 and September 2023, under the supervision of Professor Jonathan W. Steed of Durham University. This work has not been previously submitted for a degree at this or any other university.

All X-Ray structures were collected and processed by Dr. Dmitry S. Yufit and Dr. Toby J. Blundell. In Chapter 2, the crystallographic data for TAZ@CCM-3 was collected and processed by Dr. Toby J. Blundell using beamline I19 of the Diamond Light Source (DLS) synchrotron. In Chapter 3, the crystallographic data for compounds CCM-5 and CCM-8 were also collected and obtained by Dr. Toby J. Blundell using beamline I19 of the DLS synchrotron. In Chapter 4, the crystallographic data for compound **4.11** was also collected and obtained by Dr. Toby J. Blundell using beamline I19 of the DLS synchrotron. The topological analysis of metal-organic frameworks was performed with the help from Professor Davide Maria Proserpio. In Chapter 2, owing to kind help from Professor Robert Pal, the luminescence measurements of the europium(III)-based MOF CCM-2 were carried out by Dr. Dominic Black. The thermogravimetric experiments were run by Mr. Douglas W. Carswell. The elemental analysis experiments were run by Dr. Emily Unsworth. All other results are the product of independent work and investigations by the author.

Statement of Copyright

Funding

This work was funded by the Engineering and Physical Sciences Research Council (EPSRC).

Publications

A. Braschinsky, J. W. Steed, *Coord. Chem. Rev*, 2022, **473**, 214840.

Acknowledgments

First and foremost, I would like to express a great amount of gratitude towards Jon, whose guidance both inside and outside of the academic field was invaluable. From the better days of getting MOF single crystal structures and lab Christmas festivities to the worse days of lab floods and nothing seeming to work, I could not have asked for a more supportive and kinder supervisor. I would like to also thank my undergraduate supervisor Dr. Jason Keleher, along with my mentor Dr. Chuck Crowder, both of whom believed in me from the earlier days and always pushed me to do my best. I also had the pleasure of working with a plethora of other talented and amazing colleagues. I would like to thank Dr. Dmitry Yufit and Dr. Toby Blundell for their endless amount of patience towards analysing an otherworldly amount of crystal samples. Thank you to Douglas W. Carswell, Gary Oswald and Dr. Juan Aguilar Malavia for their guidance with TGA, PXRD and solution-state NMR spectroscopy, respectively. And finally, to all the experts and workers in the Department of Chemistry, thank you for making the place feel so welcoming.

On a personal note, I would like to thank Amy, Martin, Luke, James, Rafa, Jess and Edu from the Steed group for your positivity, encouragement and support both professionally and personally. From biscuit breaks in the office to discussing philosophy in the lab, you really made the hard work feel so much more fun. To my housemates at Old Elvet, thank you for making the past three years living together feel like another home. My dear friends Kev, James, Sean, Peter, Jen, Arnau, Carol and Karl, I cannot express how thankful I am to you for being who you are and letting me experience the world alongside you. To Chiara, who helped me keep my sanity during the final hectic months of finishing lab work and the following writing up period, thank you for your unwavering patience and support. Finally, I would like to thank my family for their support, help and trust in me to pursue the things that I am passionate about. I am eternally grateful that you have been there for me every time I needed you.

"How did I escape? With difficulty. How did I plan this moment? With pleasure."

– Alexandre Dumas

List of Abbreviations

3-AmPyz – 3-Aminopyrazole

2-PDN – 2-Pyrrolidinone

AA – Anthranilic Acid

AAO – Anodic Aluminium Oxide

AH – Abacavir Hemisulfate

API – Active Pharmaceutical Ingredient

ATR-FTIR - Attenuated Total Reflectance-Fourier Transform Infrared

BET – Brunauer-Emmett-Teller

bpydc - 2,2'-bipyridine-5,5'-dicarboxylic acid

CCM – Cluster Capturing Metal-Organic Framework

CPG – Controlled Pore Glass

CSD – Cambridge Structural Database

CSM – Crystalline Sponge Method

DBCC – Dichloromethane/dodecane/decane -1,10-bis(cyclohexyl carbamate)

DCM - Dichloromethane

DFM – Dark-Field Microscopy

DFT – Density Functional Theory

DHF – 2,3-Dihydrofuran

DMF – Dimethylformamide

DMSO - Dimethylsulfoxide

DSC – Differential Scanning Calorimetry

EtPyz – 1-Ethylpyrazole

GA – Glutaric Acid

FFA – Flufenamic acid

FT-IR – Fourier Transform Infrared

H_2BPDC – 4,4'-Biphenyldicarboxylic acid

H_2PZDC - 1-*H*-Pyrazole-3,5-dicarboxylate

H_3TATB - 4,4',4''-(1,3,5-triazine-2,4,6-triyl)Tribenzoic acid

HIV – Human Immunodeficiency Virus

HKUST – Hong Kong University of Science and Technology

HOMO – Highest Occupied Molecular Orbital

HRTEM – High-Resolution Transmission Electrom Microscopy

HUST – Huazhong university of Science and Technology

IMI – Imidacloprid

IRMOF – Isoreticular Metal-Organic Framework

IUPAC – International Union of Pure and Applied Chemistry

LUMO – Lowest Unoccupied Molecular Orbital

MIL – Matériaux Institut Lavoisier

MOF – Metal-Organic Framework

MUF – Massey University Framework

NDI – Naphthalenediimide

NP – Nanoparticle

NU – Northwestern University

microED – Microcrystal Electron Diffraction

NMR – Nuclear Magnetic Resonance

p-PCHE – poly(cyclohexylethylene)

PDP – 3-Pentadecylphenol

PMD – Pyrimidine

POM – Polyoxometalate

PSM – Postsynthetic Metalation

PVA – Poly(vinyl alcohol)

PXRD – Powder X-Ray Diffraction

PYZ - Pyridazine

SC-XRD – Single Crystal X-Ray Diffraction

SEM – Scanning Electron Microscopy

ssNMR - ^{13}C CP-MAS Solid State Nuclear Magnetic Resonance Spectroscopy

ROY – 5-methyl-2-[(2-nitrophenyl)amino]-3-thiophenecarbonitrile

SAXS – Small-Angle X-Ray Scattering

SBU – Secondary Building Unit

SWCNT – Single-Walled Carbon Nanotube

TAZ – 1,2,3-Triazole

TCNQ - 7,7,8,8-Tetracyanoquinododimethane

TEM – Transmission Electron Microscopy

TGA – Thermogravimetric Analysis

TPT – 2,4,6-Tris(4- pyridyl)-1,3,5-triazine

UiO – University of Oslo

UV – Ultraviolet

WAXD – Wide-Angle X-Ray Diffraction

XANES – X-Ray Absorption Near Edge Spectroscopy

ZIF – Zeolitic Imidazolate Framework

ZJU – Zhejiang University

1. Introduction

1.1 Crystallization

Crystallization is a process of self-assembly in which single molecules, generally in supersaturated solution, start forming ordered clusters by packing closely to each other. This small cluster of molecules is called a nucleus, which can then develop into a crystal according to classical nucleation theory by adding more single molecules to it, resulting in a long-range ordered structure. This is a non-equilibrium process governed by kinetic and thermodynamic conditions. The final structure of a crystal is thus dependent on the environment in which the molecules self-assemble and can result in the same molecules packing in different ways to form polymorphs. Crystals that are packed in a different way also exhibit different bulk properties, which has made the study of polymorphism immensely important in field such as the pharmaceutical, chemical, biochemical, and food industries.[1–4]

1.1.2 Crystallization Mechanisms

In evaluating crystal structures, it is important to understand the mechanism by which they were formed. Intermolecular interactions (hydrogen bonding, π–π interactions, dipole–dipole interactions *etc.*) play a key role in the crystal engineering landscape and in assessing crystal structures. These interactions generally provide a simplistic overview of how single components of a crystal structure cooperate to form the final structure, but it is crucial not to omit the mechanism by which crystallization takes place. Nucleation is the mechanism that determines the type of crystals that form.[5] However, nucleation is not very well understood due to its short timescale and small size scale that is difficult to observe optically.

Nucleation can be categorised as either primary or secondary. Secondary nucleation is the process of producing crystals by introducing their parent crystals into the solution, a process called seeding. This method is widely used in industrial settings, especially in the pharmaceutical industry, as it has proved to be a reliable and facile way of producing crystals of desired structure. Primary nucleation is a stochastic process involving a spontaneous transformation of the liquid phase to the solid phase. This can be categorised into homogeneous and heterogeneous primary nucleation. The latter is more common and undergoes in the presence of impurities, which act as catalysts. Impurities can be anything from a piece of glass to an uneven surface.

According to the classical nucleation theory (CNT), crystallization consists of two steps – nucleation and crystal growth. Nucleation involves the formation of ordered clusters called nuclei until a critical size is reached, which will then lead to crystal growth. The free energy change of the formation of a nucleus, ΔG_{crys}, is dependent on the sum between volume free energy and surface free energy. It is believed that the morphology, size, and shape of the nuclei affect the physical properties of the resulting solid. Thus, gaining control over the nucleation pathway could lead to significant improvements in obtaining the desired solid forms consistently. It is extremely difficult to measure nucleation due to its short timescale and small size scale that is too difficult to observe optically. The size of nuclei typically ranges from 100-1000 atoms.[6]

The thermodynamics of CNT was originally proposed in 1879 by J.W. Gibbs.[7] The theory posits that the overall change in Gibbs' free energy for a supersaturated solution is favourable as the solid state is more stable than the solution state. The free energy change associated with nucleation involves the solid/liquid interface created by the formation of clusters of molecules, which leads to an increase in the unfavourable surface free energy. As long as the size of the formed nuclei do not exceed the critical size, this term will dominate and the nuclei will dissolve. However, when a nucleus reaches the critical size, this will result in the volume free energy becoming the major term and decrease the overall free energy so that growth occurs spontaneously.

However, CNT has inherent approximations built into the theory.[6] For example, nuclei are treated as spheres with similar densities, which suggests uniform nucleus growth. This implies that separate sub-critical nuclei will not be able to come together to form one larger nucleus. Other assumptions include capillary approximation, molecule-by molecule growth, temperature-independence of the surface energy, and time-independence of the nucleation rate.[8,9] To address these shortcomings, multiple non-classical theories have been postulated. The two-step nucleation theory (TNT) aims to provide a more detailed description of the nucleation process. Unlike CNT, which mainly describes the change from the original supersaturated liquid to the final crystal solid, TNT argues that there exist intermediate phases prior to nucleation. The first evidence to support this theory was acquired computationally using biased Monte Carlo simulations of model globular proteins.[10] Large density fluctuations around the critical point lead to the formation of a dense droplet, inside which nucleation occurs.

In another computational study, the crystallization of acetic acid was monitored using molecular dynamics simulations.[11] More specifically, 50 acetic acid molecules were placed in a

box of 1659 solvent units and crystallization was induced by removing solvent units. By decreasing the droplet size and increasing the mole fraction of acetic acid, the formation of a microemulsion of liquid-like solute molecules was observed. Thus, the first step of nucleation is the formation of a microdroplet inside which nucleation, and subsequently crystallization, proceeds. Another key finding is that within these microdroplets no specific solute-solute ordering was observed, further supporting that crystallization proceeds from disordered precursors. Subsequently, TNT has been supported by further computational and experimental evidence.[5,6]

Other non-classical nucleation theories are shown in **Figure 1-1**. Barrier-free nucleation describes a process in which the critical nucleus size composes of a single atom or molecule.[12] In this case, the nucleation free energy is lower than the kinetic energy of atoms or molecules. Another theory (**Figure 1-1d**) suggests that the nuclei assume a structure similar to that of the parent crystal, but the nucleation barrier is not minimised.[13] This sort of nucleation was observed for a concentrated colloidal suspension.[14] Direct imaging of the crystallization of hard-sphere colloidal crystals revealed that the cores of the nuclei adopted disordered hexagonal close-packed layers. The crystal structure of the critical nuclei in the ordered layers were found to be that of the *rhcp* structure, which could only form from the bulk solid rather than a metastable phase. **Figure 1-1e** shows another non-classical nucleation in which the order parameter of the nuclei is not uniform, meaning that the nuclei do not adopt a strict tetragonal arrangement. This was reported by using atomic electron tomography to observe nucleation under atomic resolution.[15] In fact, only a few atoms in the centre of the nucleus exhibited maximum order parameter, which decreased as the distance from the core increased. The results also indicate that the shape of the nucleus changes as it grows larger while maintaining diffuse edges. Overall, better mechanistic understanding of nucleation and crystal growth could result in controllable outcomes in the crystallisation of a larger amount of target compounds. An extensive review article by Deepak and Li published in 2022 discussed the *in situ* kinetic observations reported during the crystallisation of metals and metal-based compounds, ice colloids and proteins, is recommended for the interested reader.[16]

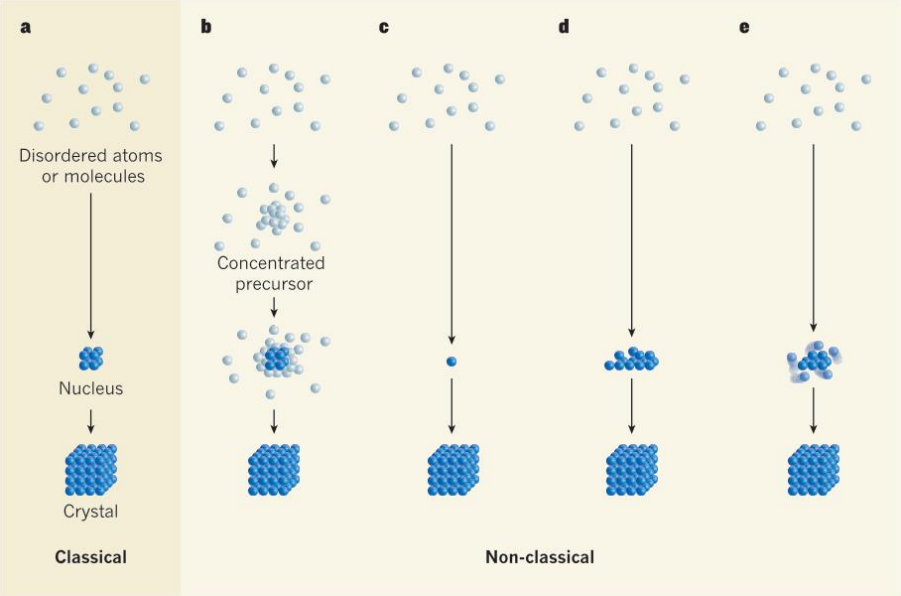

Figure 1-1. Classical and non-classical nucleation theories. a) Classical nucleation theory. b) Two-step nucleation theory showing the formation of a dense precursor. c) Barrier-free nucleation. d) Nucleation in which pre-critical nuclei adopt the structure that of the bulk material. e) Nuclei having diffuse edges and vary in shape. Reproduced with permission from ref. 13.

1.1.3 Polymorphism

Polymorphism can be defined as the ability of a molecule or compound to adopt different solid state arrangements. As a result, polymorphs exhibit different physicochemical properties such as bioavailability, solubility, stability, density, and packing.[17] In 1832, Liebig and Wöhler first reported the phenomenon of polymorphism of a small organic molecule benzamide.[18,19] Slow cooling of a boiling solution of benzamide resulted in the formation of a needle-shaped product. However, over time (from a few hours to days) this product changed shape to rhombic crystals. In 2007, the methods of the seminal study were reproduced using an automated lab reactor to for accurate control over crystallization conditions.[20] A second metastable form, form III, was characterised and was found to be more stable than the transient metastable form II. Although both forms have a needle-shape morphology, it was suggested that it is the form III that the seminal study described.

The study of polymorphism has grown significantly since the report of Liebig and Wöhler, which has been made possible due to immense advances in the field of structural determination. In fact, until the 1970s the determination of non-centrosymmetric crystal structures was extremely difficult.[21] In addition, structural disorder, structures with $Z' > 1$, and crystals that did not possess

"good" crystal quality were obstacles that were not overcome. Furthermore, the process was extremely time-consuming, generally requiring weeks. However, nowadays it is possible to determine a crystal structure within hours of collecting diffraction intensity data (which itself at times requires mere minutes), mainly thanks to advances in computing power, software automation, and data treatment. Consequently, this has allowed for much more facile and detailed studies of polymorphism, resulting in a significant increase in the interest toward polymorphism.

Many categories of polymorphism exist, which involve structural issues (conformational and packing polymorphism), sociological (disappearing polymorphism), and crystallization process phenomena (concomitant polymorphism).[22–24] Conformational polymorphs are polymorphs of a molecule in which one or more torsion angles vary above 95°.[24] This cut-off angle is used because above this, 99% of conformational pairs studied represent different gas-energy minima, meaning they exhibit true conformational changes rather than conformational adjustments. Packing polymorphism is when a molecule exhibits different packing arrangements in its solid state while maintaining the same conformation.[25] Disappearing polymorphs are generally described as polymorphs that have appeared upon crystallization but cannot be reliably reproduced. For example, recrystallization of the original polymorph of *N*-(4'-methylbenzylidene)-4-methylaniline was unsuccessful for years and the process resulted in the discovery of two new polymorphs.[22] It wasn't until this method was tried in a different laboratory where the crystals of other polymorphs were not obtained that the original polymorph was again successfully crystallized. Lastly, concomitant polymorphs are those that crystallize simultaneously. For instance, crystallization of m-class glutathione S-transferase from rat liver resulted in the simultaneous formation of three polymorphs (**Figure 1-2**).[26]

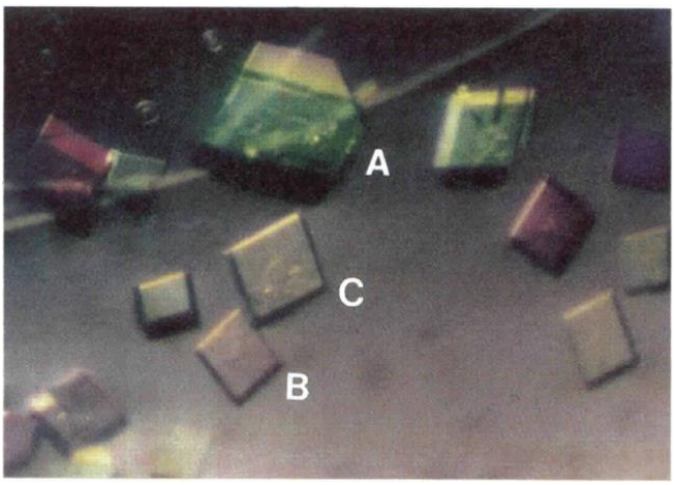

Figure 1-2. Simultaneous crystallization of three polymorphs (forms A, B, and C) of m-class glutathiose S-transferase. Reproduced with permission from ref. 26.

Ostwald's rule of stages states that the first phase to occur in crystallisation is that of the closest free energy to the mother phase.[27,28] Thus, during the crystallisation of any compound, all metastable forms in sequence should be observed before the formation of the most stable polymorph. In practical terms, this is illustrated in **Figure 1-3**, showing time-lapse micrographs of crystallization of potassium nitrate.[23] The appearance of rhombic crystals (β form) is observed at first, which then dissolve and recrystallise as the more stable needle-shaped α form. However, the Ostwald's rule of stages is not always true as it has been shown that the most stable form of some molecules can be directly crystallised, as evidenced in the case of *m*-hydroxybenzoic acid.[29] The metastable orthorhombic form is obtained by cooling a supersaturated solution of the solute in water, but the more stable monoclinic form is obtained *via* crystallisation from methanol.

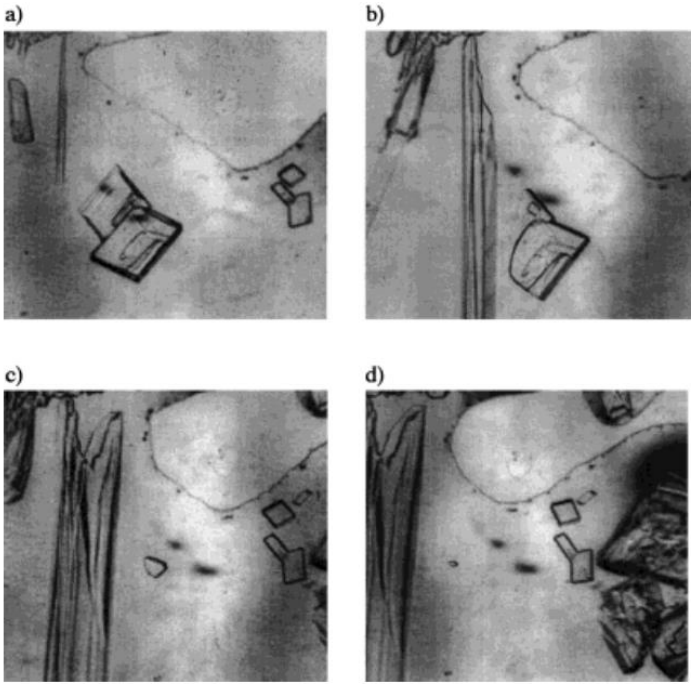

Figure 1-3. Time-lapse micrographs of potassium nitrate crystallization from an aqueous solution. Images taken after: a) 1 min. b) 5 min. c) 10 min. and d) 15 min. Reproduced with permission from ref. 23.

Polymorphism plays an especially important role in the development and application of pharmaceutical drugs. Due to the poor solubility of some pharmaceuticals, their bioavailability, efficiency and application are substantially limited.[30] Thorough polymorph screening can be of utmost importance as metastable polymorphs are known to be more soluble than the most stable ones. The superior solubility of metastable forms comes from increased and stronger intermolecular interactions within the crystal lattice of the most stable polymorphs, which are generally denser and exhibit more efficient packing, all of which lead to weaker interactions between the solvent and the solute.

It can be difficult to consistently crystallize the desired polymorph. Thermodynamic rules state that a system tends toward its most stable form. Based on this tendency, metastable polymorphs will tend to transform to their most stable packing arrangement. This has been observed for *m*-hydroxybenzoic acid – the metastable orthorhombic form obtained from methanol rapidly transforms to the more stable monoclinic form.[29] A notorious case of polymorph transition is that of ritonavir, a drug advertised for the treatment of HIV as a protease inhibitor. In the summer of 1998 (roughly 2 years after firstly being marketed), capsules started failing the dissolution requirement. It was identified that a polymorph had formed within the capsules. In fact, it was the

more stable polymorph, form II, which contains stronger hydrogen bonds within its crystal lattice and subsequently has lower solubility.[31] As a result, the new form started appearing throughout the bulk pharmaceutical and subsequently the production of ritonavir had to be stopped.

1.1.4 Solid-State Characterisation of Single Crystals

This section will mainly focus on the characterisation of crystal structures. Many general analytical techniques for characterisation of solid-state substances exist. Such techniques include spectroscopy, microscopy, crystallography, and thermal analysis.

X-ray crystallographic techniques include single crystal and powder X-ray diffraction (SC-XRD and PXRD, respectively). SC-XRD provides the most facile and precise route to determining the crystal structure of a compound.[32] In the absence of a significant amount of disorder, relative and absolute configuration of a substance can be determined. Other important properties, such as packing, bond lengths and angles, and unit cell parameters can be determined and compared to known polymorphs. However, the main drawback of this method is the need to prepare well-diffracting crystals of suitable shape and size. Often, fulfilling this requirement takes considerable time and effort. To overcome this threshold, PXRD analysis can be undertaken. The main advantage of this method is that is oversteps the requirement of growing single crystals and allows for the analysis of crystalline and amorphous materials.[33] Furthermore, this technique is rapid and does not require significant sample preparation.[34] PXRD can also be used to determine the presence of different polymorphs and to assess the crystallinity of a sample. It does not however provide as much information as SC-XRD and the unit cell determination of non-isometric crystal is complicated.[34]

Electron crystallography techniques are increasingly used for structural characterisation. Thanks to the charged nature of electrons, they can be used to obtain strong structural signals from highly localised areas of a material. In 1975, electron microscopy was first used to determine the structure of the purple membrane of *Halobacterium halobium* at a resolution of 7 Å.[35] A decade later, a density map of the purple membrane with a resolution of 3.5 Å was produced by applying beam tilt correction.[36] Further developments in instrumentation and data handling resulted in the 1.9 Å resolution diffraction patterns of aquaporin-0, a member of the aquaporin family that functions as a specific water pore.[37] Recently, electron cryo-microscopy (cryo-EM) was used for structure elucidation at a 1.25 Å resolution.[38] This was achieved by using an optimised electron source, a stable energy filter, and a camera operating at 248 Hz with the capability of estimating

event positions with sub-pixel accuracy. As remarkable as this is, it is likely that future technological developments will lead to even higher resolutions.

At times, crystals are too small to be studied *via* standard X-ray diffraction crystallography methods. Microcrystal electron diffraction (microED), first reported in 2013, is a method used to elucidate the crystal structures of microcrystals using cryo-EM.[39] One of the advantages of this method is that it can be used to analyse crystals thinner than 400 nm without causing any damage. To achieve this, the electron beam dose is reduced by a factor of 200 relative to standard low-dose cryoEM beams and data collection is performed during continuous rotation of the sample. By collecting 90 diffraction patterns using the reduced dose, Gonen and co-workers were able to elucidate the crystal structure of lysozyme at a resolution of 2.9 Å.[39] This method can thus be used to determine the crystal structures of radiation-sensitive materials which only yield nanocrystals. For example, in 2015 the first crystal structure of α-synuclein was determined at a resolution of 1.4 Å. **Figure 1-4** shows the wide selection of compounds whose crystal structure has been determined *via* microED.[40]

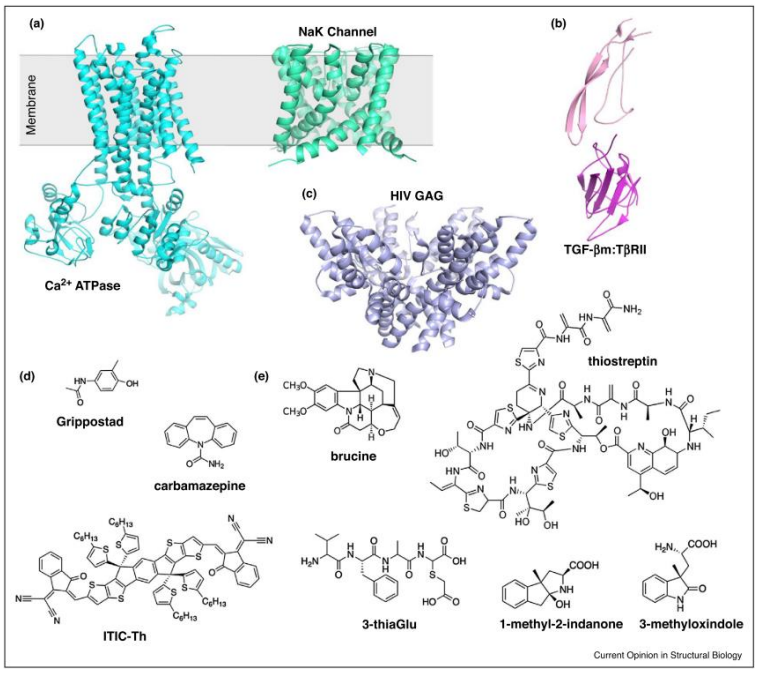

Figure 1-4. Compounds for which crystal structures have been determined using microED. a) Membrane proteins Ca^{2+} ATPase (light blue) and NaK channel (PDB 6CPV). b) TGF-βm:TβRII protein-protein complex (pink). c) HIV-GAG-bevirimat (PDB 6N3U) (purple). d) Grippostad and carbamazepine. e) Natural products thiostreptin, ITIC-Th, 3-thiaGlu, 1-methyl-2-indanone, and 3-methyloxindole. Reproduced with permission from ref. 40.

From the spectroscopic methods, solid-state nuclear magnetic resonance (ssNMR) spectroscopy can provide a complete assessment of polymorphism. NMR spectroscopy is highly sensitive to electronic environments and thus can differentiate between polymorphs. For example, ssNMR spectroscopy was recently used to successfully characterise three polymorphs of curcumin.[41] Due to the vast capabilities of NMR spectroscopy, this method has not only been used to study polymorphism, but also hydrogen bonding and disorder of solids.[32,42] This can be complimented with FTIR spectroscopy, which is a rapid and facile method and utilises the vibrational differences between polymorphs due to the influence of crystal environments on the energy of molecular vibrational and bending modes.[43] In the case of IR-inactive vibrations, Raman spectroscopy can be employed as it requires a change in polarizability and not dipole. Additionally, *in situ* Raman spectroscopy can be employed to study polymorph conversion during tableting.[44] Spectroscopic and crystallographic characterisation methods often go hand in hand as the former deals with short-range interactions and order while the latter is generally used for long-range order analysis.

Thermal analysis techniques for polymorph characterisation include thermogravimetric analysis (TGA) and differential scanning calorimetry (DSC). TGA and DSC analyse the weight changes and phase transitions that different polymorphs undergo, respectively. By obtaining DSC curves of solids, it is possible to discriminate between polymorphs by observing the peak positions – and in the case of overlapping peaks, changing experimental conditions and computational analysis can be undertaken to separate them.[45] TGA is a powerful tool for the characterisation of crystal solvates, also called pseudopolymorphs, by monitoring the weight loss at various temperatures.

1.1.5 Crystallization Methods

Many techniques have been developed to aid in the preparation of crystals of high quality. The most common techniques include solvent evaporation, vapour diffusion, seeding, and cooling the mother liquor.[46] The methods of solvent evaporation and vapour diffusion are quite similar. For the former, it is recommended that a saturated solution of the desired solute is prepared and left undisturbed. In order to decrease the rate of evaporation a beaker could be covered with a parafilm with small holes punched in. It is important to avoid fast evaporation, which results in the system reaching the supersaturated zone rapidly, leading to the precipitation of the solute. However, when

the solution is kept in the metastable zone as long as possible, it is more likely to yield crystals of sufficient size and quality for structure determination.

For vapour diffusion crystallization, an antisolvent is introduced into the environment which shares a common gas phase with the original solution. Generally, a small vial containing the mother liquor is placed into a larger vial containing the antisolvent, which is then sealed. Over time, the antisolvent diffuses into the mother liquor and reduces the concentration of the solute within it, resulting in crystallisation of the solute. It is important in this case that the solvent be more volatile than the antisolvent. Partially covering the inner vial to allow for slower diffusion can also be undertaken.[47] This could lead to the system staying in the metastable zone for a longer time period and result in high quality crystals. If the vapour diffusion method does not yield crystals of sufficient quality, it is recommended to try different solvent-antisolvent combinations.

Liquid diffusion is a similar method to vapour diffusion. A miscible antisolvent (and less dense relative to the solvent in which the solute is dissolved) is added carefully to a concentrated solution of the target solute. It is crucial to add the antisolvent carefully to ensure it forms a layer on top of the concentrated solution. This can be performed in two ways. Firstly, it could be slowly run down the side of the vial. The second method is displayed in **Figure 1-5**.[48] Briefly, the antisolvent is added to a vial, inside which a pipette containing a glass wool has been placed (**Figure 1-5a**). The concentrated solution of the target compound is added dropwise into the pipette which allows for an unmixed biphasic solution to emerge, after which the pipette is withdrawn (**Figure 1-5b**).

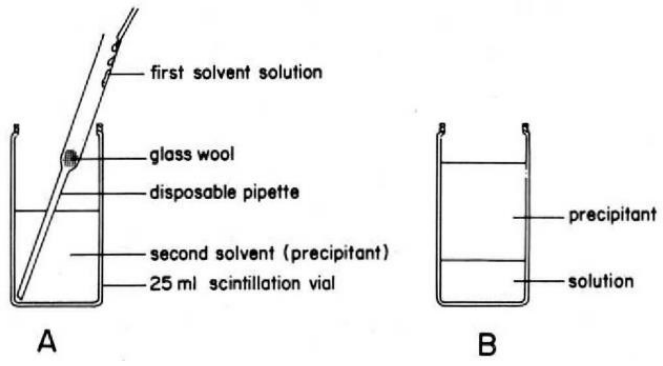

Figure 1-5. Illustration of the reactant diffusion crystallization setup. a) Preparing the mixture. b) Setup after the addition of the solvent containing the target compound. Reproduced with permission from ref. 48.

The sublimation method involves heating a solid material, which passes directly into the gas phase under vacuum. Subsequently, the gaseous bulk resolidifies onto a cold surface inside the apparatus. To successfully use this method, it is recommended that static vacuum be used instead of a dynamic vacuum. In addition, the solid should be dry as condensation can result in the resolidified material to wash off the cold surface. Convection utilises the heat gradient to carry the target compound from a heated part of the apparatus to a cold part, resulting in the recrystallization of the target compound. A Thiele tube can be used for this method. If recrystallization is unsuccessful, then varying temperatures can be used, and for low-melting compounds, the apparatus can be set into the refrigerator.[49]

Crystallization by cooling is a rather straightforward method. It is well known that the solubility of a solute usually increases with increasing temperature. This can be used to prepare an undersaturated solution at elevated temperatures, which is saturated or supersaturated at room temperature. The resulting solution can then be slowly cooled to reach the Ostwald's zone. The Ostwald's zone is roughly parallel to the solubility curve of a solute and inside the zone spontaneous nucleation is more likely to occur. It is referred to as a zone rather than a curve due to the stochastic nature of nucleation and is highly dependent on aspects such as the purity of the solvent and solute, cooling rate, and stirring rate and mode.[46]

Reactant diffusion crystallization is used to diffuse two reactants together to form crystals. If the diffusion of two solutions of reactants results in a product with low solubility in the solvent, then crystals of the product can form. To slow down the rate of diffusion, a silica gel can be used. A silica gel can be prepared inside a U-tube, into which the two reactant solutions will be added from separate sides. This method has been successfully used to prepare copper tartrate crystals from reactant solutions of copper sulfate and tartaric acid.[50]

Melt crystallization simply involves melting and cooling a solid material. To promote single crystal growth, slow cooling is highly recommended. Otherwise, heating a material between two glass slides and leaving the resulting melt to cool typically result in polycrystalline product. Melt crystallization has been used to obtain various polymorphs of ROY (5-methyl-2-[(2-nitrophenyl)amino]-3-thiophenecarbonitrile), a notoriously polymorphic compound with twelve known polymorphs.[51,52] Recently, a general melt microcrystallization method was shown to successfully used to prepare single crystals.[53] A partial melting of a small quantity of polycrystals of the target material should be undertaken until a single crystal remains. This single crystal is then

used as a seed to grow in an isolated microdroplet slightly below its melting point. The advantages of this method are that only small quantities of the target substance are required and secondary nucleation is inhibited by the minimal temperature decrease from the melting point.

The solvothermal method is used to synthesise crystalline materials at elevated temperature and pressure. This results in an increased solubility of the reagents and thus is widely used to prepare insoluble substances such as metal-organic cages, frameworks, and colloidal nanocrystals.[54–56] Generally, an autoclave is used to ensure the reaction vessel does not explode due to the temperature exceeding the boiling point of the solvent and results in increased pressure. In a standard synthesis, the precursors and solvent are loaded into an autoclave in stoichiometric ratios. The mixture is then heated and slowly cooled to facilitate crystal growth. This method is also referred to as hydrothermal synthesis when water is used as a solvent.[57]

Laser-induced crystallization proceeds through applying a laser onto a solution containing the target substance.[58] In one method, laser irradiation is applied for femtoseconds, which results in the formation of bubbles where the laser is focused. Crystallization then takes place on the surface of these laser-induced bubbles. Another method is that of laser trapping crystallization. Photon pressure of a laser beam induces the clustering of target molecules in a supersaturated solution. At the focal point, the local concentration of the target molecule is increased and crystallization is induced.

Seeding the mother liquor with the target compound is a widely used method, especially in the industrial setting. This method overcomes the rate determining step of spontaneous formation of nuclei, which then direct crystal growth, and is usually used for batch crystallisation.[59] This is an effective method for obtaining a desired polymorph, assuming that it has been previously procured and is available for seeding. Seeding also tends to give high yields of products. However, the possibility still remains that the polymorph, if not most stable, can undergo spontaneous post-crystallisation form transformations.

1.2 Crystallization Under Confinement

Section 1.2 in its entirety has been previously published as a part of a review article entitled "Molecular Clusters in Confined Spaces".[60] This section will provide a discussion of how confinement affects various aspects of crystallization such as nucleation and crystal growth processes, freezing and melting point depression and polymorphic and morphological control. In 1998, Luzzi and co-workers prepared ordered C_{60} inside carbon nanotubes.[61] The authors used

pulsed laser vaporization of graphite in the presence of metal catalysts, followed by HRTEM imaging of the as-prepared material. The images show an ordered array of C_{60} cages inside the nanotube with the fullerene centre-to-centre distances of 1.0 nm. While in this case C_{60} does not necessarily crystallize inside the nanotubes, it is an example of molecules forming an ordered structure under nanoconfinement. Ultimately gaining control of molecular ordering processes under nanoscale is a powerful tool toward crystallization of desired materials and their polymorphs. An extensive review article on crystallization under confinement by O'Shaugnessy and Meldrum published in 2020 is highly recommended for an interested reader.[62] The authors review the effect that various confining matrices with different shapes and sizes have on crystallization processes, freezing and melting points. As this section is not meant to be as exhaustive as the work by O'Shaugnessy and Meldrum, it discusses what are believed to be important findings in the field of confinement crystallization, followed by relevant work published since the 2020 review.

1.2.1 Crystallization in Nanopores

In 2000, Green and co-workers reported on the crystallographic analysis of one-dimensional single crystals of potassium iodide grown inside 1.6 nm single-walled carbon nanotubes (SWCNTs).[63] Crystals grown in the SWCNTs are merely two or three atoms wide but extend to tens of micrometres in length. Using HRTEM imaging, single atoms of potassium or iodide can be resolved and the crystal packing analysed. The packing arrangement of KI inside the nanotubes is different from that of bulk KI. In bulk, the lattice coordination is 6:6 while in the nanotube the face and edge atoms have 5:5 and 4:4 coordination, respectively. In addition, the crystals contract along the *c* axis as compared to the bulk, from K–I distances of 0.705 in bulk to 0.695 nm inside the nanotubes. Apart from the 1.6 nm nanotube, the KI was also crystallized inside nanotubes with different diameters. Crucially, the authors note that selective crystallization of desired strain states of KI crystals can be achieved by tuning the nanotube diameter.

In a 2005 review, Alcoutlabi and McKenna showed that the glass transition temperature of materials can change as a result of their confinement in nanopores.[64] Although a conclusive explanation to this phenomenon was not given, the authors hypothesised that this change in thermal properties of materials could be due to the intrinsic size effect, sample preparation, confinement effects, or a combination of thereof. Still, the results reviewed by Alcoutlabi and McKenna could be still interpreted as a result of confinement effect, which begs the question of whether

confinement could also affect the processes of nucleation and/or crystallization. In fact, substantial evidence exists to support the hypothesis that confinement affects these crystallization processes. For instance, confinement effects on crystallization are observed when form I of anthranilic acid (AA) is heated to 155°C and subsequently cooled down to room temperature inside the confined space of controlled pore glass (CPG) with diameters of 55, 23 and 7.5 nm.[65] The cooling step results in the formation of different polymorphs within CPGs of varying diameters. Inside CPG with a diameter of 55 nm, only form III is revealed by PXRD. The metastable form II of AA forms partially within the CPG of 23 nm in diameter while it is found in abundance inside the smaller CPG with 7.5 nm diameter. The formation of form II is attributed to the smaller critical nucleus size compared to those of form I and III.

Crystallization under confinement has also led to the discovery of size-dependent polymorphism, a phenomenon in which different polymorphs form depending on crystal size. Ward and co-workers performed nanoscale crystallization experiments on select α,ω-dicarboxylic acids and coumarin inside the pores of CPG and porous poly(cyclohexylethylene) (p-PCHE).[66] Recrystallization of bulk β-glutaric acid (β-GA) by cooling its melt produces the polymorph α-GA, which transforms to β-GA within 1 hour at room temperature. However, by cooling the melt inside 7.5, 23 and 55 nm CPG results in the crystallization of α-GA nanocrystals, which are stable at room temperature for months without transforming into β-GA. In the case of pimelic acid (PA), a new polymorph, δ-PA, was obtained *via* heating and cooling a methanolic solution of the solvate inside 7.5 nm CPG. Alas, δ-PA slowly transforms into α-PA over the course of a month. However, δ-PA crystallized from the PA melt inside 14 nm p-PCHE is stable for more than a year. A new polymorph of coumarin (C), β-C, was also obtained by crystallization from 23 nm CPG while crystallization from bulk forms the α-C polymorph. Both α-C and β-C forms are obtained inside 7.5 nm CPG and exclusively α-C forms inside 55 nm CPG. Overall, this work illustrates the polymorphic size-dependence upon crystallization where different polymorphs of a compound preferentially form depending on the limitations on the crystal size.

Following this work, Ward and co-workers reported on the preferred orientation of crystals of other α,ω-dicarboxylic acids under nanoscale confinement in p-PCHE pores of 14, 30 and 40 nm in size.[67] Crystals were grown by either imbibing a melt or a methanolic solution of the target compound in the pore walls. Malonic acid (C3) nanocrystals grown inside p-PCHE result in the formation of the α-C3 polymorph. More specifically, the nanocrystals align along the α(010) and

α(001) planes, perpendicular to the pore wall and pore direction, respectively. For glutaric acid (C5), when nanocrystals are grown using the methanol solution method, the 14 nm pores exclusively exhibit the α-C5 form while in pores of 30 and 40 nm the β-C5 form is found, showing the effect of confinement on polymiorphic outcome. On the other hand, the melt method produces α-C5 nanocrystals inside p-PCHE of 30 and 40 nm. Compared to the α-C5 grown in 14 nm pores, the α-C5 grown in 30 and 40 nm pores exhibit a 90° change in the nanocrystal orientation, ascribed to surface energy effects that become apparent at such length scales. Similarly to C5, pimelic acid (C7) also exhibits size-dependent polymorphism – α-C7 grows inside 14 nm pores while a mixture of α-C7 and δ-C7 (a novel polymorph) grows inside 30 nm and exclusively δ-C7 grows inside 40 nm pores of p-PCHE. Bulk crystals of α-C7 grown in benzene are needle-like with the α[$20\overline{1}$] long axis while the nanocrystals exhibit the α[010] long axis along with the α($10\overline{3}$) plane aligned perpendicular to the pore direction. The authors suggest that the preferred orientation of C7 stems from critical size effects not solvent effects due to the minimization of the ($10\overline{3}$) surface. Overall, the authors suggest that the preferred orientation of crystals under confinement is the result of critical size and surface energy of nuclei. The results indicate that precritical nuclei that are aligned with their fast growth axis along the pore direction are more likely to reach the critical size due to the minimization of the higher surface area planes. This can result in the formation of crystals in unique orientations and vastly different from those grown in bulk. Along with the reported size-dependent polymorphism, crystallization under confinement can result in unique material physical and chemical properties.

In 2013, the Ward group reported on crystallization of glycine inside anodic aluminium oxide (AAO) ranging from 20 to 2000 nm in pore diameter.[68] Inside the pores of AAO, β-form crystallizes initially and is stable indefinitely at ambient temperatures. However, when RH is increased to 90% for 24 hours, the crystals transform to the α-form as revealed by two-dimensional X-Ray microdiffraction. The addition of a droplet of water results in defects in the crystal structure of β-glycine, which triggers the solid-state transition to α-glycine. To further study the solid-state transition mechanism, the effect of chiral amino acids was examined. Interestingly, most racemic amino acids suppress the transition to the α form, potentially due to the amino acids binding to the {010} faces of the crystal structures and forcing the crystals to grow in the [001] rather than [010] direction. When enantiopure amino acids are added to the AAO pores prior to crystallization, β-glycine crystallizes in the [010] direction and transforms into α-glycine after the RH is increased.

Overall, the authors are able to demonstrate the suppression of a polymorph transition under nanoscale confinement by binding racemic amino acids to the polar {010} faces of β-glycine.

Apart from mechanistic insights into crystallization, physical properties such as pressure of a growing crystal can also be studied under confinement. Shahidzadeh and co-workers studied the force exerted by alkali halide, sodium chloride (NaCl) and potassium chloride (KCl), crystals during crystal growth between hydrophilic and hydrophobic glass walls at the nanoscale.[69] The authors use a custom setup in which they are able to control the distance between the glass slides and measure the force exerted on the plate during crystal growth. When crystallization occurs between hydrophilic glass slides, the measured pressure is 220 ± 50 MPa, which is strong enough to damage sandstone. Crystallization between hydrophobic glass slides results in the crystal growing between the slides without the formation of a thin film between the crystal face and the glass slide and thus no pressure is measured. The pressure arises from a repulsive force between the negatively charged crystal face and glass surface, which is separated by the thin film. The presence of the thin film between the crystal face and glass slide is crucial as it allows for more ions to be added to the crystal resulting in further growth and pressure exerted.

Linear chain alkanes can be used as model compounds to study the crystallization processes of polymers as the former are the building blocks of polymers. In addition, crystallization properties of *n*-alkanes are easier to study while polymers exhibit complicated crystallization processes.[70] Crystallization of 3-pentadecylphenol (PDP) as the model compound with the phenol end group was recently studied by Luo and co-workers to gain insight into the crystallization processes and thermal behaviour of polymers that have similar end groups.[71] PDP was confined within the 90, 180, 250 and 450 nm pores of AAO (AAO-PDP) *via* the melt infiltration method and crystallized by cooling from 60°C to 0°C. Wide-angle X-ray diffraction (WAXD) reveals that AAO-PDP exhibits two different crystallographic space groups *Pbcm* and *Fmmm* while bulk PDP crystallizes in the *Fmmm* space group. The diffraction peaks corresponding to the *Pbcm* space group become more distinct in the diffraction pattern with decreasing pore size of AAO (**Figure 1-6**). This solid-solid phase transition is thus more pronounced at smaller confined spaces. In addition, the crystallinity of AAO-PDP decreases with decreasing pore radii, which was also found to be true during crystallization of the linear analogue *n*-pentadecane (C_{15}). However, the decrease in crystallinity is more pronounced for AAO-PDP samples indicating that the presence of the phenol end groups disturbs crystallization under confinement more than linear alkyl chains. This

suggests that introducing different end groups to small organic molecules and polymers can result in different crystallization processes, which can be eventually used to adjust the confined crystallization behaviour of semicrystalline and polymer compounds.

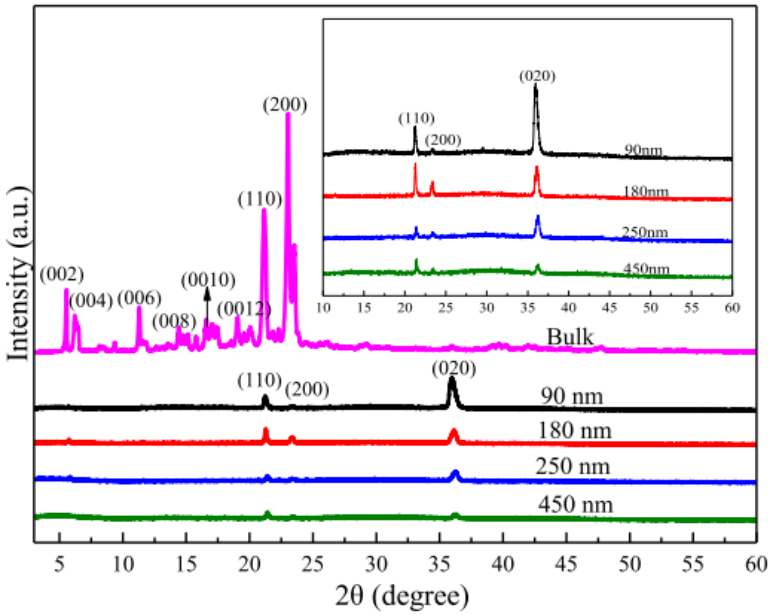

Figure 1-6. WAXD diffraction patterns of bulk and AAO-confined PDP. Reproduced from ref. 71.

Deep eutectic solvents (DESs) are a class of solvents that offer a "greener" alternative to common solvents due to their low vapour pressure which means they do not evaporate into the environment as readily.[72] In addition, DESs can be designed to biodegradable at low costs. The physical, chemical and thermal properties of DESs have been widely studied, but it was only recently when Lan *et al.* studied the thermal properties and cold crystallization of a DES, reline, under confinement for the first time inside CPG.[73] Reline exhibits melting point depression when confined inside the 50, 100 and 300 nm pores of CPG. In addition, the cold crystallization temperature increases under confinement compared to bulk reline. XRD patterns of bulk reline and confined reline crystals inside 100 and 300 nm CPG pores show similar reflections at 21.6°, 25°, 33.1° and 33.5°. However, an additional peak at 20.5° is present in the confined crystals. As no crystal structure of reline is known, the reflection could not be indexed and thus it is unknown what this peak represents. On the other hand, reline crystallized in 50 nm pores exhibits a different XRD pattern which does not correspond to neither reline nor to the individual components (choline chloride and urea). The authors conclude that this pattern most likely corresponds to a new crystal structure of reline.

Imidacloprid (IMI) is the most widely used insecticide to control the *Aedes* mosquito, and potentially the *Anopheles* and *Culex* mosquitoes.[74,75] However, the usage of IMI has resulted in soil, surface and underwater contamination, along with the decline of bee colonies. Thus, if the lethality of the insecticide could be increased, then the subsequent decrease in its required concentration would have a positive impact on the environment. Recently, seven new polymorphs (forms III–IX) of IMI, on top of the two previously known forms (forms I and II), were reported by Kahr and co-workers.[75] Of those seven forms, one (form VII) was obtained by nanoconfined crystallization. More specifically, form VII was obtained by crystallizing from a melt in CPG of pore sizes 35, 100 and 200 nm. This form was not characterised by SC-XRD analysis due to rapid cross-nucleation of form II when seeding larger crystals of form VII in bulk. Lethality studies showed that form IX ranks as the fastest acting insecticide towards female fruit flies and mosquitoes. The lethality ranking matched identically the metastability chart, *i.e.* the more thermodynamically stable the polymorph, the less lethal it is. Form VII ranks as the third least stable form, thus indicating it could be an effective insecticide. Overall, these results indicate the potential of confinement chemistry to increase the efficiency of materials by uncovering novel polymorphs.

Another highly polymorphic compound is flufenamic acid (FFA), an API used for the treatment of various inflammatory conditions. To date, nine polymorphs (forms I-IX) are known, with the first polymorph discovered as early as 1973.[76–78] Conventional bulk crystallization of FFA results in the formation of form I. Ward and co-workers used CPG with pores ranging from 4 to 200 nm to study polymorphic phase transformation under nanoscale confinement.[79] Under confinement of 4 and 8 nm CPG, amorphous FFA forms and remains stable for at least 6 months. However, under 30–200 nm confinement for VIII crystallizes first, confirmed by PXRD analysis. The results indicate that the polymorphic transitions can be dictated by varying the confinement imposed by CPG. For instance, form VIII forms first in CPG pores of 30–50 nm and transformation into forms II and I+II occurs over the course of 3 days and 6 months, respectively. However, in CPG pores of 100–200 nm, form VIII transforms into form IV and IV+III within 20 minutes and 3 days, respectively. Finally, in bulk, form VIII converts directly to form III upon heating. The authors conclude that nanoconfinement, on top of altering polymorph stability rankings, can also reshape polymorphic transformation pathways and unveil otherwise hidden pathways.

1.2.2 Crystallization in Droplets

Crystallization within microemulsions poses another method to confine the crystal growth of a compound and study the crystallization processes on a nanoscale.[80] Generally, a mixed solvent system containing a surfactant, solvent and the target compound is prepared, which is then either shaken or sonicated to obtain microemulsions that contain the target compound. The constituents can be mixed at elevated temperatures to obtain high saturation of the target compound, and the resulting mixture is then cooled to induce crystallization. In 2007, water crystallization from microemulsions was used to directly measure the critical nucleus size of ice molecules as water freezes.[81] For water pool with radii 1.2–1.8 nm, the critical nucleus contains between 90–350 molecules as determined by small-angle X-ray scattering (SAXS).

Microemulsion crystallization has also been used to obtain nanocrystals of mefenamic acid and 5-methyl-2-[(2-nitrophenyl) amino]-3-thiophenecarbonitrile (ROY).[80] For mefenamic acid, a concentration-dependent crystallization of the two known forms of the compound is observed. At lower supersaturations, predominantly the most stable form I is obtained while at higher supersaturations, the metastable form II becomes increasingly predominant. Glycine was also crystallized by adding methanol microemulsions to an aqueous glycine microemulsions to induce crystallization due to the lower solubility of glycine in methanol compared to water. Three polymorphs of glycine (α, β and γ forms) are known out of which γ-glycine is the most stable. The authors note that the most stable form is difficult to obtain from aqueous bulk solutions without the addition of additives or at very low supersaturation. Attenuated total reflectance-Fourier transform infrared (ATR-FTIR) was used to characterise the crystals that appeared after three weeks. At higher glycine concentrations, α-form is predominant and almost exclusively crystallized while at lower supersaturation concentrations, the γ-form becomes predominant. Bulk crystallization of neither glycine nor mefenamic acid do not yield the most stable form due to high nucleation barriers, which are overcome through three-dimensional nanoconfinement in microemulsions. Under confinement, thermodynamic control, *i.e.* crystallization of the most stable polymorph, is achieved by using low supersaturations which favour the crystallization of the most stable forms of glycine and mefenamic acid. Overall, the authors show that it is possible to attain thermodynamic control in nanoconfined systems. This is achieved by first finding the environment in which molecules are stabilized solely by nanoconfinement and subsequently increasing the

supersaturation inside the confined systems until thermodynamic control is reached, *i.e.* until the energy barrier to form stable nuclei of the most stable form is overcome.

In 2020, Hao and co-workers found that it is possible to control the morphological outcome of crystallization in microemulsions by varying the water-to-surfactant molar ratio.[82] Previous reports show that higher initial supersaturation upon crystallization from microemulsions leads to the formation of α-glycine while γ-glycine predominantly forms at lower supersaturation.[80,83] The Hao group used a nonionic surfactant in combination with different molar ratios of water to control the morphological and polymorphic outcome of glycine crystals. Antisolvent and cooling microemulsion crystallization were performed within microemulsions ranging from 1 to 5 nm as determined by SAXS. During antisolvent crystallization, polyhedral and needle-like crystals of glycine formed at high and low supersaturations, respectively. At high supersaturation, the microemulsion droplet can be imagined to be crowded by glycine molecules and rapid nucleation results in the glycine clusters agglomerating in different orientations, thus forming polyhedral crystals. In the case of lower supersaturation, the nucleation process is slowed down and oriented attachment of glycine clusters takes place resulting in needle-shaped crystals. Accordingly, both needle-shaped and polyhedral crystals of glycine are obtained under medium supersaturation. Interestingly, both needle-like and polyhedral crystals are those of α-glycine polymorph. This is due to the hydrophilic poly(oxyethylene) groups of the surfactant orienting in a winding shape when dissolved in water, which promotes the growth of α-glycine.

The pharmaceutical industry relies heavily on batch crystallization to consistently produce the desired polymorphs of small molecule active pharmaceutical ingredients (APIs). However, inconsistent particle size distribution (PSD) of crystals obtained *via* batch crystallization affects manufacturing processes and bioavailability of the APIs.[84] In 2020, Lakerveld and co-workers employed the emulsion crystallization method to control the crystal size distribution (CSD) of ibuprofen.[85] Ibuprofen was selected as it is a widely studied drug and it belongs in class II of the Biopharmaceutical Classification System, where many newly developed drugs also belong.[86] The authors prepared ibuprofen–water–heptane emulsions with various surfactants and crystallized ibuprofen by cooling. The most stable emulsions are formed with the nonionic surfactant Tween 20 while anionic and cationic surfactants are less stable. Using a homogenizer, small droplets form within the emulsion inside which crystallization is expected to occur. However, crystallization from these small droplets results in the formation of large crystals due to the droplets attaching

together as illustrated in **Figure 1-7** (Path I). Thus, crystallization in larger droplets obtained by stirring was undertaken. Larger droplets are able to confine the crystal growth of ibuprofen due to shorter induction time in a macroemulsion, leading to a smaller crystal mean size (Path II). Overall, different emulsification methods which result in varying droplet sizes could be a method to obtain consistently small crystals of APIs.

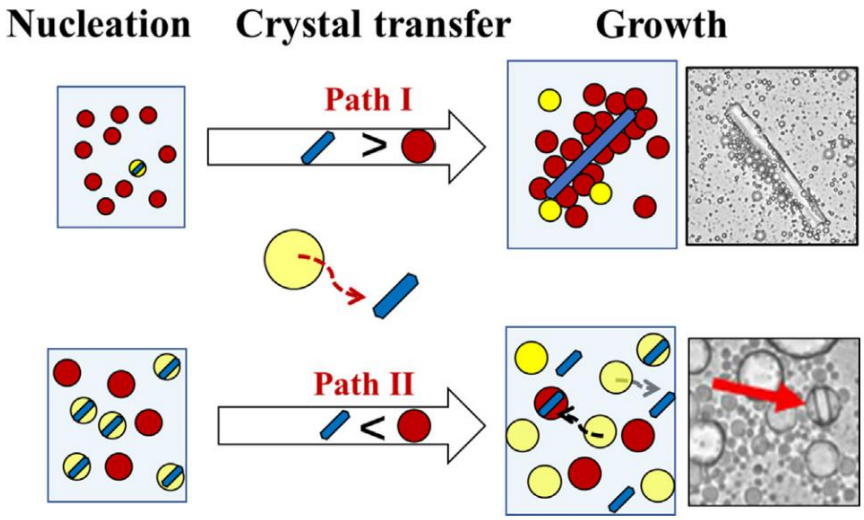

Figure 1-7. Illustration of the crystallization pathway in emulsions containing smaller and larger crystals. Reproduced with permission from ref. 85.

Also in 2020, Lai and co-workers demonstrated two methods of seeded microfluidic crystallization in water-oil emulsions to control the polymorphism and PSD of a small molecule API, abacavir hemisulfate (AH).[87] The first method is that of solvent extraction in a mixed solvent emulsion system, in which a mixture of surfactant in pentyl acetate and API in water solutions are ran through a droplet generator into a petri dish, resulting in a solution in which droplets containing the API are formed in a solution of pentyl acetate. The crystallization of AH is induced by cooling this mixture, which results in spherical agglomerates of the API crystallizing in the droplets. The second method involves combining a seed suspension and dissolved solution of AH, which is then emulsified. The resulting droplets are cooled below the saturation limit to induce crystallization. This method results in successful crystallization of single crystals of AH. In addition, decreasing the concentration of seeds in the input stream results in larger single crystals with an overall decrease in PSD. The authors also demonstrate a novel temperature cycling method to decrease the number of seeds in droplets with the goal to obtain a single seed in every droplet. The cycling

process reduces the number of seed crystals from 9 to 3 inside a single droplet. Overall, this seeded droplet microfluidic system grants good control of the PSD of single crystals of an API and can also be scaled up and optimised for manufacturing operations and bioavailability.

Microcapsules are used in various industries such as pharmaceutical, cosmetics and agriculture for storage and delivery applications. Their most common form is that of a solid sphere encapsulating a fluid in which the target compound is dissolved. Recently, Bon and co-workers reported on the fabrication of microcapsules from emulsion droplets.[88] The microcapsules are interlocked by needle-like crystals which crystallize during the evaporation of the solvent. Droplets are formed by injecting a solution containing dichloromethane/dodecane/decane-1,10-bis(cyclohexyl) carbamate (DBCC) into a poly(vinyl alcohol) (PVA) phase. Evaporation of dichloromethane triggers the crystallization process and within 10 minutes, spiky microcapsules form. The adhesive properties of spiky microcapsules are superior to the smooth equivalents and their shape can be controlled when recrystallized in different geometric confinements.

Overall, crystallization under confinement can be effectively used for polymorphic and crystal size control and to unveil novel polymorphic phase transitions. However, while obtaining novel polymorphs for pharmaceutical applications is highly sought after, it is difficult to predict and obtain the desired polymorphs from bulk solutions which would have advantageous physicochemical properties compared to previously known polymorphs. In this light, using confinement on the scale of tens of angstroms to design matrices to obtain nuclei with a specific shape and size can result in gaining control over the molecular packing of the resulting crystal. Cooper and co-workers showed that controlling the supersaturation under nanoconfinement in microemulsion leads to thermodynamic control over crystallization.[80] In addition, Green and co-workers have reported that confinement of KI in SWCNTs leads to a closer packing of KI, which indicates that crystal size and shape can be controlled as well.[63] These findings suggest that control over crystal form, size and shape could be attained *via* careful design of crystallization matrices and conditions. In addition, further insights into nucleation mechanisms, such as those of Yaghi and co-workers[89] and Lu and co-workers[90], will help to understand the effect of confinement on the formation of stable nuclei, their shape and nucleation rates, which are crucial to reach further achievements in the field of confinement chemistry.

1.3 Molecular Tectonics

Often, the design of supramolecular assemblies begins with the identification of a tecton. A tecton is a molecule which drives molecular assembly *via* various attractive forces regardless whether it belongs in the final structure of the assembly or not.[91] Subsequently, molecular tectonics deals with the design and construction of tectons and the assemblies they form. One of the earliest examples of the formation of a supramolecular assembly by applying the molecular tectonics approach is from 1991 by Wuest and co-workers.[92] The authors are responsible for coining the term tecton and showed that by using a rigid tetrapyridone with various carboxylic acids, a supramolecular assembly with the diamondoid shape containing large cages can be formed. This work established not only the possibility of forming such stable structures, but that these assemblies can be designed by employing tectons with different properties.

In 2000, Macdonald and co-workers first introduced a strategy to control molecular packing and crystal growth of composite materials by utilising a combination of hydrogen bonding interactions and coordination bonds between two tectons to epitaxially grow a new class of modular materials.[93] The careful design of these composite materials began with coordinating first row transition metals with an 2,6-pyridinedicarboxylic acid and imidazole, yielding imidazolium-carboxylate-based coordination complexes (**Figure 1-8a**) which all crystallise in the same space group, *P*2/*c*, and differ in their respective metal centres and unit cell volumes in the region of 2.5–6.5%. These coordination complexes form layers stacked by O–H···O^- hydrogen bonds between water molecules and carboxylates in adjacent layers (**Figure 1-*8*b**). Given the structural uniformity across the coordination complexes, these hydrogen bonded layers served as host lattices for the growth of isostructural layers incorporating alternative metals. This method enabled the synthesis of mixed crystals exhibiting the same layer-type packing but incorporating two different metals. Additionally, composite crystals were synthesised where one coordination complex was used as a seed to epitaxially grow an isostructural complex incorporating a different metal around the seed crystal.

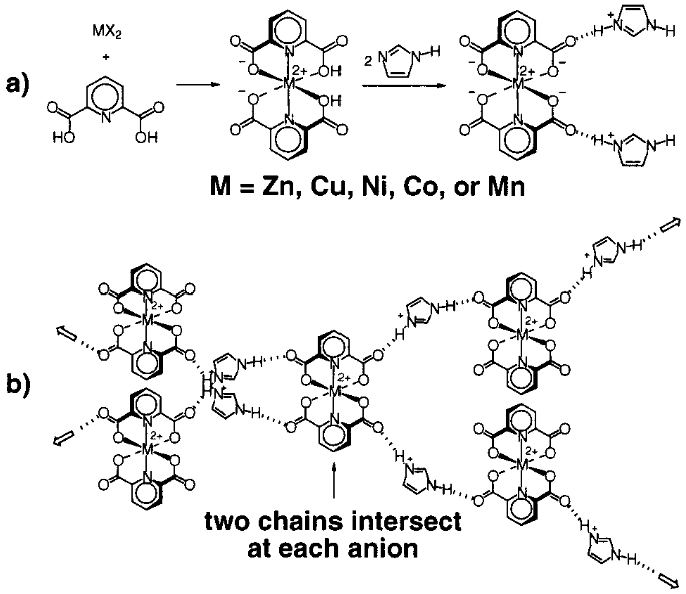

Figure 1-8. a) Coordination of metal centres to the 2,6-pyridinedicarboxylic acid and its hydrogen bonding with imidazole. b) Formation of hydrogen bonded chains *via* the imidazolium cations and carboxylate anions. Reprinted with permission from J. Am. Chem. Soc. 2000, 122, 47, 11692–11702. Copyright 2024 American Chemical Society.

Cyanidoometallates have become a popular type of molecules that could be employed to form supramolecular assemblies. They can coordinate with various metals and form various coordination geometries. For example, at least four different terminal and bridging modes are known for the CN^- anion in cyanocuprates.[94] Thus, they can be employed to design a wide variety of organised structures. A paper in 2013 by the Hosseini group investigated the formation of various crystalline supramolecular assemblies between $KCu(CN)_2$ and six dicationic bisamidinium tectons in solution and in the solid state.[94] Cyanocuprates are capable of forming coordination geometries such as linear$[Cu^1(CN)_2]^-$, trigonal $[Cu^1(CN)_3]^{2-}$ and tetrahedral $[Cu^1(CN)_4]^{3-}$.[95] These anions were combined with complementary cationic tectons, structures of which are shown in **Figure 1-9**. The authors reported seven new coordination networks formed when these two complementary components were mixed together (**Figure 1-9**). Out of the seven networks, one one-dimensional, three two-dimensional and three three-dimensional assemblies formed. The networks are connected mainly through coordination bonds, but encapsulated dicationic tectons were observed to form hydrogen bonding interactions with cyanide moieties.

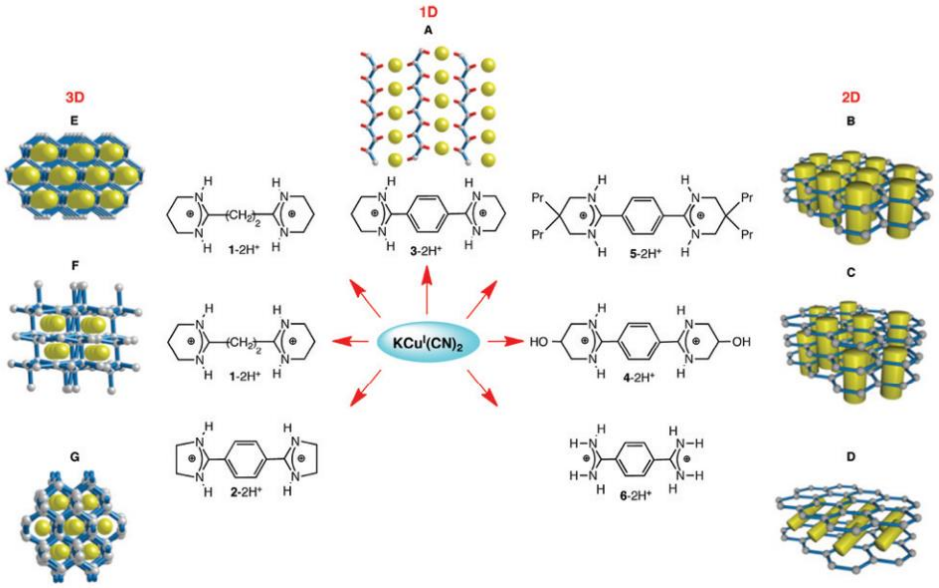

Figure 1-9. Illustration of seven coordination networks formed between $KCu^{I}(CN)_2$ and the various dicationic bisamidinium tectons. Reproduced with permission from ref. 94.

Molecular tectonics can also be applied to crystal engineering. In 2015, the Hosseini group reported on the design of isostructural molecular crystals and their welding using three-dimensional epitaxial growth.[96] The authors demonstrate the use of a dicationic organic tecton paired with an anionic metallatecton to form the isostructural molecular crystals by only changing the metal centre in the metallatecton. **Figure 1-10a** shows the needle-shaped crystals with different colours corresponding to different metals used in the anionic metallatecton. These crystals were then immersed in a drop containing the dicationic tecton, metal source and the ligand and allowed to slowly evaporate. Within 24 hours, a crystal containing a different metal source had grown around the crystal originally placed in the droplet (**Figure 1-10b**). A similar process was repeated to "weld" crystals together. A needle-shaped crystal was cut in half and placed in a droplet containing the aforementioned components. This resulted in the distance between the cut crystal being epitaxially intergrown by the new crystal with a different metal source. Crucially, the crystals were placed in the droplet in a way ensuring that they were positioned along the same axis that the needles grow.

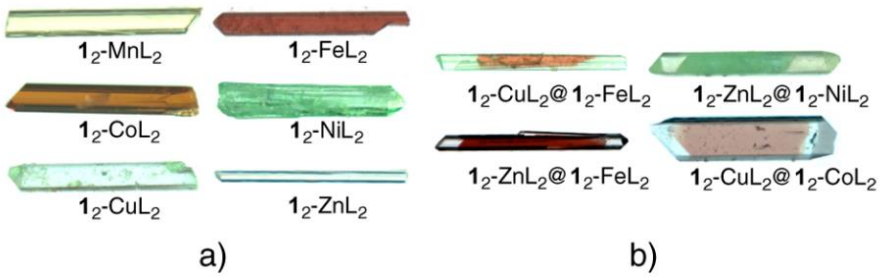

Figure 1-10. a) Needle-shaped crystals obtained by combining the dicationic organic tecton with the metallatecton containing different metals. b) Crystals containing a different metal centre in the metallatecton grown around a preformed crystal. L = 2,4,6-pyridinetricarboxylic acid. Reproduced with permission from ref. 96.

Kim and co-workers showed that epitaxial growth requires the use of crystalline surfaces in order to seed the growth of isostructural compounds.[97] Using HRTEM imaging, the authors showed that on a crystalline Bi_2S_3 surface, the initial nucleation and growth of bismuth particles matched the orientation of the seed lattice with a segment shape. However, the nucleation and growth of bismuth particles on the amorphous $Bi_{12}TiO_{20}$ was free from any heterosurface effects and results in the formation of spherical shape of bismuth clusters. Thus, when employing epitaxial growth, it is important to utilise a seed crystal with similar lattice parameters as that of the target material.

1.3 Metal-Organic Frameworks

1.3.1 Background

Metal-Organic Frameworks (MOFs) are potentially porous coordination polymers, which are formed as a result of a self-assembly process between metal-containing units bridged together by organic linkers. MOFs have various topologies, morphologies, and other physicochemical properties and are used for various industrial and academic purposes. Their most desirable properties include multi-functionality, tunability, and permanent and extensive porosity resulting in surface areas above 6000 $m^2\ g^{-1}$.[98] This has led to their widespread use in various applications such as gas sorption, catalysis, sensing, and separation.[99–102]

MOFs are commonly classified based on their pore sizes. The International Union of Pure and Applied Chemistry (IUPAC) defines three distinct types of pores of below 2 nm, 2 – 50 nm, and above 50 nm as micropores, mesopores, and macropores, respectively. Most MOFs belong to the microporous class, yet lately the interest toward mesoporous MOFs has risen lately due to their

vastly larger pores compared to that of microporous MOFs. Ultramicropores are another type of pore referred to when the pore size is below 0.7 nm, but this type of pore is not defined by the IUPAC.

Prior to a discussion regarding the synthesis and application of MOFs, it is important to give a brief explanation of the common nomenclature used in the field. Reticular chemistry describes the linking of the organic and inorganic building blocks to form periodic nets. Isoreticular is used to describe nets that have the same network topology. Interpenetration of nets is the entanglement of two networks within the same structure without being chemically linked. Expansion of a MOF structure simply means increasing the spacing between the MOF vertices (this is generally achieved by using longer organic linkers). The decoration of a MOF is generally a postsynthetic method that involves replacing or modifying a unit in the MOF framework, for example organic ligand or metal exchange.[103] The postsynthetic metalation (PSM) method involves the incorporation of extraneous metals into the pores of a MOF, either by the addition of the metals to an organic linker, ion exchange in charged frameworks, cation metathesis at the metal nodes of the framework or growth of metal NPs inside the pores.[104] This is generally achieved A secondary building unit (SBU) is a continuous structure made up of metal coordination clusters such as the Zn–O–C motif in MOF-5 (**Figure 1-11**).[105] This concept simplifies the description of these polyhedral networks as various shapes compared to describing them bond-by-bond. MOF isomers consist of networks that have the same stoichiometry of metal-to-ligand, but whose network topology differs.[106]

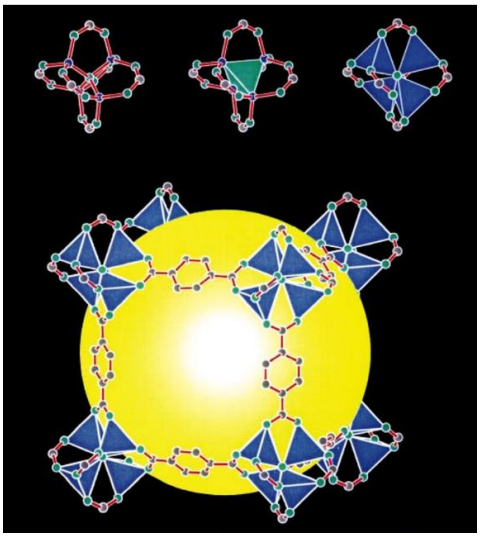

Figure 1-11. Top: Secondary building unit of MOF-5. Bottom: the cavity of MOF-5 framework, which is connected by eight secondary building units linked together by the organic linker 1,4-benzenedicarboxylate. Reproduced with permission from ref. 105.

Commonly appearing network topologies were first identified in 1977 by A. F. Wells.[107] Since, many more have been discovered and to easily describe and identify all, a set of symbols and notations are used. The Wells notation uses two numbers (n, p) to describe the connectivity of a given net. The first number n describes the number of nodes in the smallest circuit within a given net and p describes the connectivity of the nodes. Thus, a (4,4) net describes square nodes that are 4-connected with their neighbouring nodes (**Figure 1-12**). However, this simplifies the given net and is not the most accurate representation of it. *Schläfli* notation is a more complete set of symbols used to describe nets. This method describes the shortest node length and the shortest route back to itself. For example, the same (4,4) net, using the *Schläfli* notation, is $4^4 6^2$. This means that there are four pairs of tetragons and two pairs of hexagons. In this case, the Wells notation overlooks the colinear hexagon pairs.

These notations can become harder to assign to three-dimensional structures, especially when different net topologies are present in one structure. Thus, a bold three-letter code has been developed for commonly appearing three-dimensional nets. For example, the MOF-5 net shown in **Figure 1-11** is generally recognised as the α-polonium net, is called the **pcu** net. Others such as the **qom** (MOF-177 and its isoreticular analogs), **tbo** (MOF-199 and its isoreticular analogs), and **etb** (IRMOF-74 and its isoreticular analogs) are well-recognised net topologies.[108]

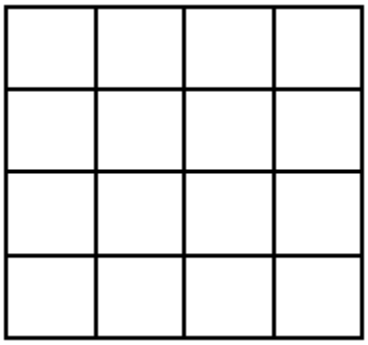

Figure 1-12. Visual representation of the (4,4) net.

The first material termed as a MOF was synthesised as recently as 1995 by Yaghi and Li.[57] It was obtained hydrothermally by reacting the organic linker 4,4'-bipyridine with copper nitrate hemipentahydrate, yielding orange crystals of the MOF. Shortly after, in 1997, the first three-dimensional MOF was reported by Yaghi *and* co-workers by reacting nickel perchlorate hexahydrate with 4,4'-bipyridine *via* the solvothermal method.[109] These landmark reports have been the bases of significant advances in the field of MOF synthesis. At the moment of writing, the MOF subset in the Cambridge Crystallographic Database[110] (CSD, Version 5.45 March 2024 update) contains 125383 hits. This clearly shows that the field has come a long way, but more importantly it showcases the tremendous pace of advances in this area.

1.3.2 Design and synthesis of MOFs

The synthesis of MOFs involves various steps, from the careful and rational design of SBUs to the conditions in which the synthesis is realised. This idea led to the method of designing MOFs in which specific topologies could be targeted and the pore sizes controlled by modifying the connecting organic linkers. Despite the SBU theory, in reality most of the work in this field is empirical. **Figure 1-13a** shows the structure of MOF-5 displaying the octahedral $Zn_4(CO_2)_6$ SBUs along with the organic linker terephthalic acid.[111] This led to the development of isoreticular MOFs as it was hypothesised that the inorganic zinc SBUs could be linked together by other ditopic ligands of varying size.[112] **Figure 1-13b and c** show two MOFs from the IRMOF series – IRMOF-6 and IRMOF-8, respectively. This shows how the original organic linker terephthalic acid was modified into similar ditopic linkers with a different shape and size, resulting in full control of the pore size of the MOF without any changes in its topology. This landmark report paved the way to the systematic design of pore size in MOFs as it was realised that longer linkers can lead to MOFs with exceptionally large pores while maintaining stability in solid state (something that was highly

doubted when MOFs first entered the discussion in the scientific community).[113] Most notably, the expansion of the IRMOF-74 series frameworks resulted in the formation of IRMOF-74XI, which has the pore diameter size of 98Å.[114] Despite all these landmark findings, not all MOFs that have been reported are the result of careful planning and design. Serendipity is somewhat of a common phenomenon, and has resulted in reports of novel MOFs.[115] Having said that, serendipity is not something to rely on and generally careful planning and designing should be undertaken for novel MOF preparation.

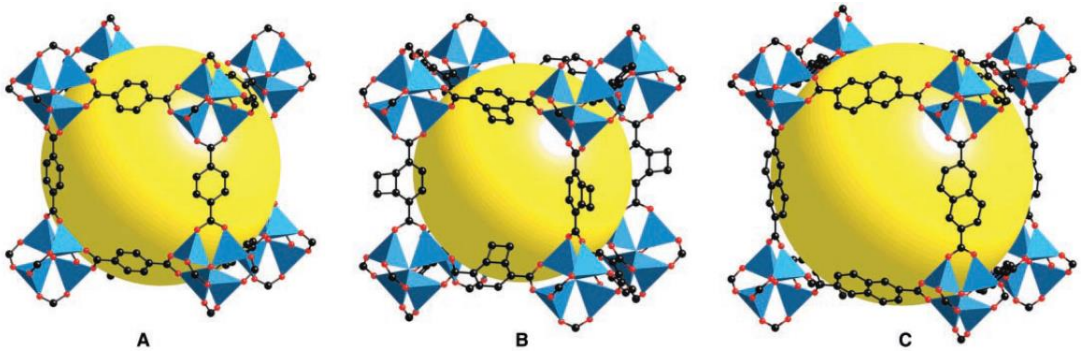

Figure 1-13. Design of a) MOF-5 (IRMOF-1), b) IRMOF-6 and c) IRMOF-8 containing the zinc SBUs linked together by isoreticular ditopic organic ligands. Blue polyhedra: zinc, blue spheres: oxygen, red: oxygen, and black: carbon. Reproduced with permission from ref. 111. The article can be found at https://pubs.acs.org/doi/full/10.1021/jacs.5b10586.

MOFs have been synthesised using metals from s-,[116] p-,[117,118] d-[119] and f-blocks[120], exhibiting a variety of coordination numbers, geometries and oxidation states, which in turn contribute to the formation of MOFs with diverse topologies and properties. Rare earth (RE) metals, encompassing the 15 lanthanides along with yttrium and scandium, offer a particularly intriguing subset for MOF synthesis due to their unique properties arising from their electron configurations in the 4f orbitals. RE metals differ from each other in the number of electrons in the f orbitals, which are shielded from interactions with ligands by electrons in the 5s and 5p orbitals. Consequently, for coordination bonds to form, it will involve the orbital hybridization of the unoccupied higher-energy orbitals (*e.g.* 5d, 6s, 6p). Additionally, coordination bonds will normally be expected to occur for only strongly coordinating ligands.[121] As a result, the coordination geometry is more likely to be dictated by the ligand steric effects and only small energy differences between the resulting coordination geometries occur.[122] These characteristics enable RE metals to form a diverse array of metal nodes and MOFs with unique underlying net

topologies. Howarth and co-workers have discussed the diverse MOF structures that have been obtained using RE metals along with their potential applications.[123] Overall, RE-based MOFs hold significant promise for developing novel MOF functional materials.

In terms of experimental methods used for synthesising MOFs, the most common methods include hydro- and solvothermal, diffusion, electrochemical, microwave, mechanochemical, and sonochemical syntheses.[124,125] Of the aforementioned methods, the solvothermal method is the most widely used as it can yield crystals of sufficient size and quality for single crystal X-ray diffraction analysis. This is generally performed under autogenous pressure in a sealed vessel such as an autoclave or a high-pressure bomb, although milder conditions can permit the use of a sealed vial.[126] The main disadvantage of this method is that it can take from several days to weeks for the reaction to occur and can result in crystals which need to be analysed *via* a Synchrotron source, which is often difficult from the practical point of view. In 2022, Zhou and co-workers used dark-field microscopy (DFM) to atomically trace the growth of MOF single crystals during solvothermal synthesis.[127] The authors used *in situ* interface imaging to study the effects of the organic linker, metal ion, along with other key determining factors, in the formation of single crystals of five common MOFs. While the ligand and the metal ion play important, yet different, three possible reaction mechanisms are proposed: monomer-by-monomer, formation and direct accumulation of SBUs and finally, the formation and fragmentation of SBUs, where a new species formed after the fragmentation acts as the growth unit for the MOF single crystal.

The diffusion method is a relatively common method as well, and was notably used in the original synthesis of MOF-5.[105] Solvent liquid diffusion involves the diffusion of a less dense solvent into the solvent in which the linker and metal source are dissolved in.[124] This results in the formation of a mixture of solvents in which the reactants are less soluble in and can thus result in crystallisation of products. In the case of MOF-5, triethylamine was diffused into a solution of the organic and inorganic linkers in a dimethylformamide/chlorobenzene solution. The p*K*a of the conjugate acid of triethylamine is approximately 10.8, indicating it is a relatively strong base. This results in the deprotonation of the organic linker, facilitating MOF formation and crystallisation.

The electrochemical method is a common industrial route toward synthesising MOFs on a large scale. There are many advantages of this method, such as avoidance of anions, milder conditions, and fast reaction times.[124] There are two methods for electrochemical synthesis – direct and indirect. The term direct implies that electrochemistry is the only method used for the synthesis

of MOFs, unlike the indirect method in which electrochemistry is just one part of the total synthesis of a MOF. The most widely applied method is that of the direct anodic dissolution, in which the formation of the MOF occurs near the surface of the electrode, from which the metal source is provided into the solution including the organic linkers.[128] Other direct and indirect methods include mechanochemistry (notably used to synthesise HKUST-1[129]), reductive deprotonation, galvanic displacement, linker anchoring, electrophoretic deposition, and self-templated synthesis.[128]

1.3.4 Applications of MOFs

Many existing and emerging applications of MOFs are inspired by the emergence of green chemistry. For instance, it was realized roughly two decades ago that MOFs possess huge potential toward gas storage and separation due to their tunability and versatility. Gases such as hydrogen and methane are extremely important due to their potential applications in energy storage. For instance, methane can be used as a more cost-effective fuel source which emits less carbon dioxide than gasoline – an especially topical application when it comes to green chemistry. The first report describing the uptake of hydrogen gas is from 2003 when MOF-5 was successfully used for its adsorption.[111] The MOF-5 series MOFs used in this report exhibited surface areas of 2500-3000 $m^2 g^{-1}$, a value that has been more than doubled since. Thus, hundreds of MOFs have been used to study their gas storage abilities. Most notably, the recently reported NU-1051-Al possesses the largest gravimetric area (7310 $m^2 g^{-1}$) of all known porous materials that satisfy all four BET criteria.[130] At 80 bar and 270 K, the hydrogen storage ability of NU-1051-Al is 0.60 g g^{-1}, one of the highest reported values to date.

According to the ninth principle of green chemistry, catalytic reagents outperform those that are used stoichiometrically.[131] Indeed, minimizing the amount of reagents used by recovering their them after reactions is highly desired not only from a sustainability but also financial standpoint. Various MOFs possess Lewis or Brønsted acidic sites that can be used for the catalysis of various reactions. For instance, the conversion of greenhouse gases such as methane and carbon dioxide to more value-added chemicals has been widely performed.[132] Hydrophobic MOFs have the capability to prevent water, a strong ligand, from occupying the active metal sites that could be used for catalyzing reactions such as oxidation of hydrocarbons, esterification, condensation, and conversion of epoxides.[133] Generally, MOFs are recovered by filtration or centrifugation after reaction completion and subsequently washed and reactivated.[134,135]

Tablet-based drug administration can result in health issues associated with a high concentration loading of the therapeutic species arising from bursting of the binder phase.[136] Consequently, owing to their porosity and chemical tunability, MOFs have emerged as potential carriers for drug delivery as their voids can encapsulate target drugs, which can then be controllably released *via* stimuli-responsiveness.[137] Furthermore, MOFs can be designed to be biodegradable and encapsulate poorly water-soluble therapeutics and gasotransmitter molecules such as nitric oxide and hydrogen sulfide.[138] Thus, drug delivery *via* MOFs could result in the reduction of side effects and increased treatment efficiency compared to other treatments, such as chemotherapy in cancer treatment. In 2008, MIL-53(Fe) was used as a vessel to deliver ibuprofen in a simulated body fluid environment.[139] Full release of the drug for the pores took 3 weeks, indicating that the kinetics of this method need to be improved for practical use. In another study, a Zr-based MOF ZJU-800 was loaded with the diclofenac sodium drug achieving loadings as high as 58.80% weight.[140] The release of the drug was controlled by using pressure and full delivery took between 2 to 8 days depending on the degree of compaction between ZJU-800 and the drug. One of the landmark studies was published by Puigmarti-Luis and co-workers, where the fields of microrobots and MOFs were joined together to create MOF-based small-scale robots (MOFBOTs, **Figure 1-14**).[141] To fabricate MOFBOTs, the authors used gelatin methacryloyl (GelMA) as the chassis prepared by direct-laser writing (**Figure 1-14a**, GelMA polymerization). Subsequently, the GelMA chassis was coated with a presynthesised magnetic and biodegradable Fe@ZIF-8 which also contains the target drug Doxorubicin (DOX) inside its pores. The magnetic nature of Fe@ZIF-8 allows control over the locomotion of the MOFBOTs composites and drug release occurs *via* in vitro enzymatic degradation of the chassis and the pH-triggered degradation of the DOX-loaded Fe@ZIF-8 framework.

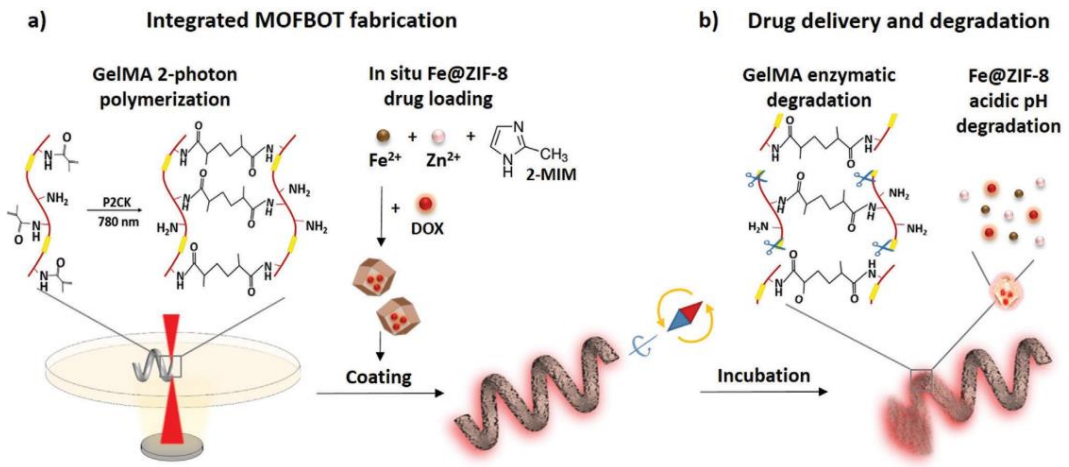

Figure 1-14. Design, synthesis, and application of MOFBOTs. a) Preparation of the chassis, drug loading and coating of the chassis with the MOF. b) Degradation of MOFBOTs. Reproduced with permission from ref. 141.

Nearly half of the human population suffers from water scarcity and the demand for clean water is only increasing.[142] Not only is water essential to humanity, but also to the ecosystems around the planet. Water harvesting by MOFs is advantageous in many ways as they can capture water vapour and release it as a liquid. This means that the MOF-released water is pure and readily consumable. In 2017, a prototype for water harvesting using MOF-801 was placed on a roof at MIT left overnight to absorb water.[143] The following day, relative humidity after solar-assisted water desorption was about 65%, corresponding to water uptake of 0.35 kg kg^{-1}. Thus, this technology would allow to harvest roughly 0.3 liters per 1 kg of MOF of water per day. The highest water uptake of a MOF recorder is for Cr-soc-MOF, which is capable of absorbing water almost twice its weight (1.95 g g^{-1}).[144] However, the main drawbacks of this MOF are structural integrity upon water regeneration and costly synthesis. Alternatively, an aluminium-based MOF-303 has been hydrothermally synthesised with hydrophilic pores and maximum water capture capacity of 0.48 g g^{-1}.[145] Furthermore, this MOF can complete multiple cycles of absorption and desorption per day under dry conditions. This material was commercialised into a water harvesting unit, which is capable of producing 1.3 litres of water per kg of MOF per day.[146]

Food packaging is an essential part of maintaining food safety as it provides a physical barrier between food and microorganisms. Furthermore, it allows for longer food storage and efficient transportation. However, many advances are to be made. Water permeation through food

packaging can damage the shelf life of a given food. In addition, nonbiodegradable plastics are harmful to the environment and cause microplastic pollution. In fact, a recent report showed that microplastics were for the first time found in human placenta.[147] In 2016, the aforementioned water harvesting MOF-801 was incorporated into a membrane of a hydrophobic cyclic olefin copolymer.[148] The resulting mixed-matrix membrane exhibited an almost 11-fold increase in water vapour blocking. In a more recent report, Fe^{III}-HMOF-5 loaded with capsaicin was embedded into a gelatin/chitosan film.[149] Capsaicin is believed to have antibacterial properties and thus could aid in preserving the shelf life of given foods. Indeed, not only did the MOF-embedded film exhibit efficient antimicrobial properties against *Esterichia coli*, but also showed increased tensile strength and water vapour permeability.

The efficient capture and storage of greenhouse gases, such as carbon dioxide, methane and chlorofluorocarbons, is a global ambition due to the negative effects of their presence in the atmosphere. Carbon dioxide is the most commonly produced greenhouse gas and subsequently much research is focused on its sequestration. MOFs provide well-defined pores (in the form of cages and channels) that can be used for gas capture and storage. This process is generally performed in the solid state under high pressure and a flow of gas. Thus, MOFs that retain their crystallinity under these conditions are highly sought after, because subsequent analysis *via* SC-XRD can provide insights into how the gas molecules order inside the pores. Additionally, this aids in the future design of MOFs for the efficient sequestration of desired gases. However, the encapsulation of gases is best studied *via* sorption isotherm experiments. Upon gas sorption, crystalline MOF structures generally lose their single crystallinity, *i.e.* they are no longer suitable for SC-XRD analysis. As a result, there is a relatively limited literature on crystal structures of MOFs containing solid-state nanoclusters of gas molecules.

The earliest report containing direct observation of gas molecules inside a MOF is from 2005 by Kobayashi and co-workers.[150] A pillared layer coordination polymer CPL-1 with microporous channels of 4 × 6 Å was synthesized and used for hydrogen adsorption studies. Synchrotron PXRD analysis of empty CPL-1 at 90 kPa and hydrogen-adsorbed CPL-1 (H_2@CPL-1) at 102 kPa were analysed using the maximum entropy method (MEM)/Rietveld method to determine the single crystal structures. The MEM charge-density distribution maps of H_2@CPL-1 show electron density corresponding to two hydrogen atoms inside the channels of the framework.

The H_2 atoms are slightly displaced from the centre of the pores, closer to the oxygen atoms of the carboxylate group of the organic linker pyrazine-2,3-dicarboxylate.

In 2010, Takeda and co-workers synthesised a series of metal-organic one-dimensional assemblies to study the adsorption of CO_2, H_2, N_2, O_2 and Ar.[151] Single crystalline hosts $[M^{II}_2(bza)_4(Rpyz)]_n$ (bza = benzoate, pyz = pyrazine, M^{II} = Rh^{II} (**a**) or Cu^{II} (**b**), *R* = H (**1.1**), 2-methyl (**1.2**) or 2,3-dimethyl (**1.3**)) were synthesised *via* vapour diffusion and adsorption experiments were carried out under 195 K for CO_2 and 77 K for other gases under varying pressure conditions. For **1.1**, **1.2**, and **1.3**, the maximum absorption capacity of CO_2 is 3 molecules per M_2 unit for **1.1** and **1.2** and 2 molecules for **1.3**. Single crystal structures of **1.1a**, **1.2a** and **1.3a** after CO_2 absorption studies are shown in **Figure 1-15**. The single crystal structures of CO_2-loaded **1.1a-3a** are isostructural to those of **1.1b-3b** and thus only structures **1.1a-3a** are shown here. The guest-absorbed **1.2a** undergoes a pore expansion to accommodate three CO_2 molecules per M_2 unit. The encapsulated CO_2 molecules are arranged in a A–A–B type as seen in **Figure 1-15a**. The parallel arrangement for A–A CO_2 molecules is the most stable arrangement of that two CO_2 molecules can undertake while the perpendicular A–B is the second most stable.[152] **Figure 1-15b** shows that the crystal structure of **1.2a** still contains three CO_2 molecules despite the addition of a methyl group onto the pyrazine ring. A similar structural transformation in which the pore size increase is observed for the CO_2-absorbed **1.2a** compared to its empty counterpart. In addition, the as-synthesised **1.2a** exhibits zigzag-like pore structure and upon CO_2 inclusion the shape of the pores changes to a one-dimensional straight pore with a similar A–A–B type packing of the guest molecules. **Figure 1-15c** shows the CO_2 inclusion structure of **1.3a** which contains the 2,3-dimethylpyrazine organic linker, thus adding an extra methyl group per linker into the pores compared to **1.2a**. The structure reveals a significant reduction in the number of encapsulated CO_2 molecules, from 3 to 0.49 per M_2 unit. The addition of a methyl group prevents the structural transformation that was observed in the case of **1.2a** and the host remains in a zigzag-like arrangement. Overall, Takeda and co-workers conclude that controllability of the dynamic adsorption properties of host molecules can lead to novel diffusivity and dynamic selectivity of guest molecules inside this type of flexible porous hosts.

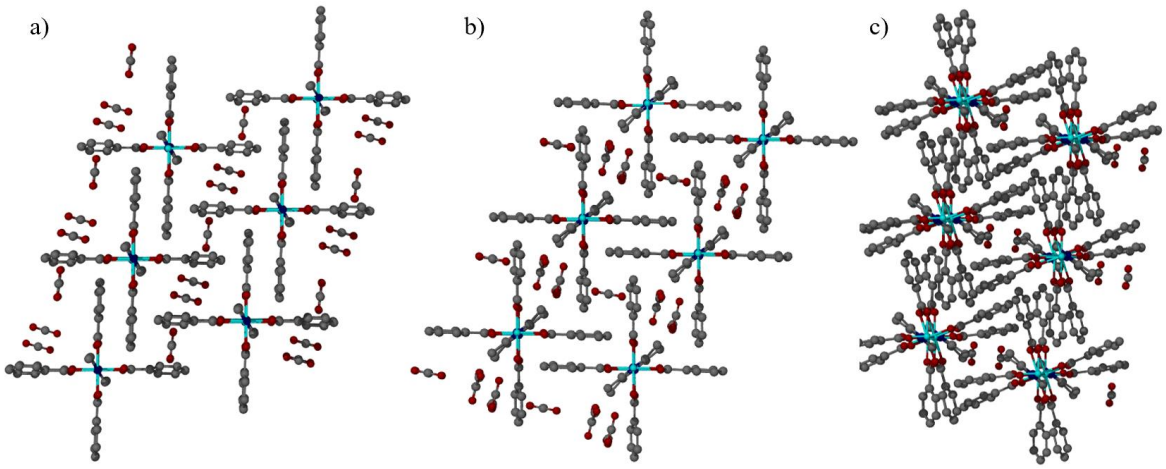

Figure 1-15. Single crystal structures of CO_2-absorbed metal-organic assemblies viewed down the pore axis. a) **1.1a**, b) **1.2a** and c) **1.3a**. Red: O. Gray: C. Light blue: Rh. Hydrogen atoms have been omitted for clarity.[151]

In 2010, Woo and co-workers reported a microporous amine-based MOF $Zn_2(atz)_2(ox)$ (atz = 3-amino-1,2,4-triazole; ox = oxalate) which was used for CO_2 capture.[153] Notably, this was the first example of a crystal structure of a CO_2 adsorbed MOF. Crystallographic studies of the CO_2-absorbed MOF samples showed two unique binding sites inside the pores with 80% and 50% occupancy. **Figure 1-16a** shows packing of $Zn_2(atz)_2(ox)$ with two CO_2 molecules occupying each pore. One CO_2 molecule binds to the free amine group of atz (**Figure 1-16b**, CO_2(I)) while the other CO_2 molecule is positioned closer to the ox moiety (**Figure 1-16b**, leftmost CO_2 molecule, CO_2(II)). The authors demonstrated cooperative binding of the guest molecules *via* SC-XRD and computational modelling studies. The binding energy for CO_2(II) is 4.6 kJ mol^{-1} higher when its adjacent site is occupied compared to when it is unoccupied by CO_2, determined by dispersion-corrected periodic DFT calculations. Further calculations showed an interaction energy of 3.9 kJ mol^{-1} between CO_2(I) and CO_2(II). The authors suggest that enhancing the pore size could result in significantly higher CO_2 loading capabilities as a result of the cooperative binding.

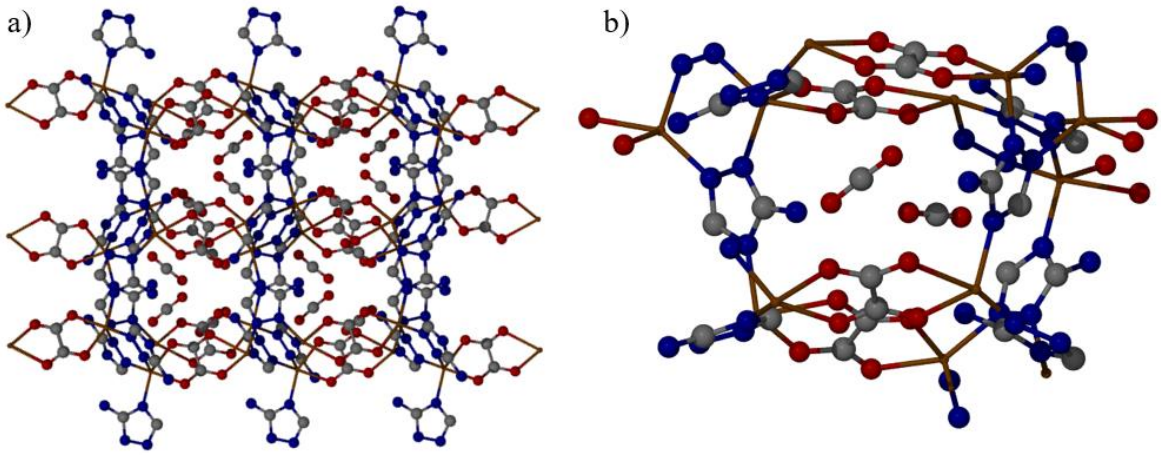

Figure 1-16. Binding of CO_2 inside the micropores of $Zn_2(Atz)_2(ox)$ as determined via SC-XRD. a) Unit cell packing of $Zn_2(atz)_2(ox)$ in the b axis. b) Two crystallographically unique CO_2 molecules inside the cage of $Zn_2(Atz)_2(ox)$. Red: O. Gray: C. Blue: N. Hydrogen atoms have been omitted for clarity.[153]

Iodine and carbon dioxide uptake of a porphyrin-based microporous Co-DpyPtolP-MOF (DpyPtolP = 5,15-di(4-pyridyl)-10,20-di-(4-methylphenyl)porphyrin) (**1.4**) was analysed in 2015 by Lee and co-workers.[154] Material **1.4** retains its crystallinity even after vacuum drying at 250°C to evacuate the solvent molecules. Thus, single crystals of **1.4** were exposed to CO_2 gas under 195K and analysed *via* SC-XRD. The crystal structure of the CO_2-adosrbed framework reveals a linear arrangement of the guest molecules in the one-dimensional pores of the framework. Only a few other examples of solid-state structures of confined CO_2 molecules inside pores or cages have been reported to date.[155,156]

Compound **1.4** was also used to study the uptake of iodine by immersing the MOF crystals in a cyclohexane solution of iodine. SC-XRD analysis of the iodine-adsorbed crystals revealed the formation of polyiodide clusters inside the one-dimensional pores (**Figure 1-17 a** and **b**). More specifically, the central iodine atom has an inversion centre and symmetry expansion generates a I_3^- ion. The $I_3^-\cdots I_3^-$ distance inside the channel is 3.212 Å, which is significantly shorter than the distance of $I_3^-\cdots I_3^-$ chains previously determined in [H_3O(dibenzo-18-crown-6)] at 4.0-4.2 Å.[157] The authors conclude that instead of discrete I_3^- ions, the iodine atoms form a symmetric structure inside the framework pores because the exact identity of the polyiodide clusters is different from pure I_2 or I_3^-. Raman spectroscopy analysis of encapsulated polyiodide clusters showed different signals compared to those of pure I_2 or I_3^-. The latter exhibit signals at 200, 170 and 103cm^{-1} while polyiodide clusters give new signals at 333, 220 and 161 cm^{-1}. This unique behaviour of iodine in

this system in which it does not resemble either I_2 or I_3^- has not been previously observed and could potentially be driven by the geometry of the pores of **1.4**. Previously in 2008, I_3^- species were encapsulated into two indium-based MOFs with tetratopic tetrathiafulvalene linkers.[158] However, in this case the formation of I_3^- was directly confirmed *via* SC-XRD as the latter act as counterions for the reduced organic linkers.

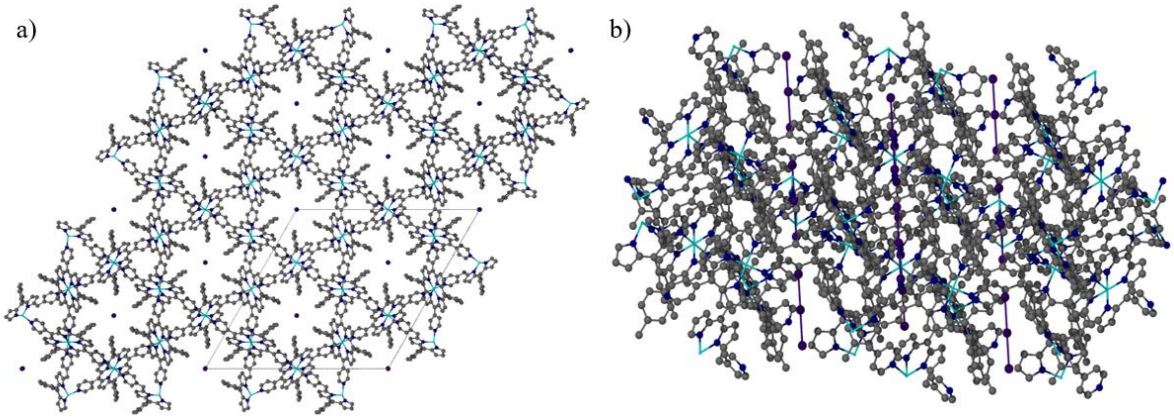

Figure 1-17. Polyiodide chains inside the pores of **1.4**. a) View along the c axis. b) View of the polyiodide chains in the MOF pores. Gray: C. Dark blue: N. Light blue: Co. Purple: I. Hydrogen atoms have been omitted for clarity.[154]

In 2018, Miyasaka and co-workers used a framework-like porous layered ferrimagnet $[\{Ru^{II}(3,5\text{-}F_2PhCO_2)_4\}_2\{TCNQ(MeO)_2\}]\cdot 3(DCM)\cdot 1.5(DCE)$ (**1.5-solv**, 3,5-F_2PhCO$_2$ = 3,5-difluorobenzoate, TCNQ(MeO$_2$) = 2,5-dimethoxy-7,7,8,8-tetracyanoquinodimethane, DCM = dichloromethane and DCE = dichloroethane) for gas sensing applications.[159] As-prepared **1.5-solv** has inter-layer distance of 9.78 Å which contracts to 9.46 Å upon the release of DCM and DCE (**1.5**), a reversible process when reintroduced to vapours of DCM and DCE. Adsorption isotherms of O_2, N_2 and CO_2 show that **1.5** is capable of encapsulating these gases. *In situ* SC-XRD analysis reveals the structures of CO_2- and N_2-adsorbed **1.5** (**1.5**⊃CO_2 and **1.5**⊃N_2). Adsorption of O_2 was measured at 94 (**1.5**⊃O_2-I) and 130K (**1.5**⊃O_2-II, structure solved using the Rietveld refinement technique) due to two gas-adsorbed temperature-dependent phases existing at those temperatures. Thus, *in situ* SC-XRD was employed at those temperatures as well. All structures containing gas guest molecules exhibit further inter-layer distance decrease from the solvent evacuated **1.5**. The structures of **1.5**⊃N_2 and **1.5**⊃O2-II are almost identical and their occupancy numbers are 4 and 5.2, respectively while that of **1.5**⊃CO_2 is 5.0. The smaller occupancy of N_2@**1.5** leads to the framework having the shortest interlayer distance of 8.76 Å while **1.5**⊃CO_2 and **1.5**⊃O_2-II exhibit

nearly identical distances of 9.11 and 9.10 Å. Magnetic measurements of **1.5**⊃CO_2 and **1.5**⊃N_2 show an increase in the Curie temperature (T_C) relative to **1.5**. This change in T_C is likely the result of a reduction in structural deformation that **1.5** exhibits upon transformation from **1.5-solv** to **1.5**, *i.e.* the structural deformation upon gas adsorption results in a structure more similar to **1.5-solv** than **1.5**. Magnetic measurements were repeated for **1.5**⊃O_2, which is a paramagnetic gas unlike CO_2 and N_2. Upon O_2 adsorption, the resulting material exhibits antiferromagnetic (AF) properties because O_2 molecules mediate a transition to the AF state *via* intercalated O_2 spins. In short, by introducing O_2 gas into the pores of the ferrimagnet **1.5**, Miyasaka and co-workers demonstrate facile and fast switching between a ferrimagnet (evacuated **1.5**) and antiferromagnet (O_2-adsorbed **1.5**).

In 2021, Miyasaka and co-workers synthesised a stimuli-responsive D_2A-layered (D = donor and A = acceptor) ferrimagnetic MOF [{$Ru^{II}(F_3PhCO_2)_4$}$_2$TCNQ$(OEt)_2$]·3DCM (**1.5**-DCM, $F_3PhCO_2^-$ = 2,4,6-trifluorobenzoate, TCNQ(OEt_2) = 2,5-diethoxy-7,7,8,8-tetracyanoquinodimethane) which turns paramagnetic upon CO_2 absorption.[160] The ferrimagnetic behaviour comes from a one-electron transfer between the donor and acceptor throughout the material in a pattern of $[D–A^––D^+]_\infty$. Similarly to **1.5**, MOF **1.6**-DCM shows reversible solvent absorption-desorption to form DCM-free **1.6** with thermal stability up to 473K. CO_2-atmosphere-controlled *in situ* SC-XRD analysis was performed at pressures of 3 kPa (**1.6**⊃CO_2-I) and 100 kPa (**1.6**⊃CO_2-II). The single crystal structure of **1.6**⊃CO_2-I reveals a pseudopolymorphic form of **1.6**-DCM with four molar equivalents of CO_2 replacing DCM molecules in the centre of the MOF pores. However, **1.6**⊃CO_2-II crystallizes in a different space group from those of **1.6**-DCM and **1.6**⊃CO_2-I, indicating that the adsorption of CO_2 at 100 kPa induces structural changes of the framework. Indeed, four more CO_2 molecules are encapsulated in **1.6**⊃CO_2-II compared to **1.6**⊃CO_2-I, resulting in an increase in the void space and flattening of the D_2A layers. Furthermore, the electronic state became neutral for **1.6**⊃CO_2-II, which was also confirmed by *in situ* IR spectroscopy showing a broadening and weakening of the $\nu_{C\equiv N}$ band in **1.6**⊃CO_2-II compared to **1.6**-DCM. DFT calculations of different model structures obtained from SC-XRD analysis show that the neutral ground state of **1.6**⊃CO_2-II is the most stable form of the obtained structures, ascribed to a stabilizing interaction between a CO_2 orbital and δ* orbital of the [Ru^{II}_2] and π* orbital of TCNQ$(OEt)_2$. Overall, **1.6** shows reversible ferrimagnetic and paramagnetic behaviour upon CO_2 absorption and desorption. Such gas-responsive materials as **1.5** and **1.6** are promising

and desired towards applications in gas sensing and capture importantly because of the ability to study structural changes *via* SC-XRD which is an important tool towards designing future materials for efficient sensing and capture.

Telfer and co-workers reported on the synthesis of a cost-effective MOF series MUF-16 (MUF-16(Co), MUF-16(Mn) and MUF-16(Ni)) to selectively separate CO_2 from hydrocarbons.[161] The MUF-series MOFs exhibit one-dimensional micropores of 3.6×7.6 Å and the empty framework is shown in **Figure 1-18a**. The guest gas was introduced to a single crystal of the evacuated MUF-16(Mn) under 1.1 bar inside a capillary. **Figure 1-18b** shows the single crystal structure the CO_2-adsorbed MUF-16(Mn) with CO_2 molecules packed along the pore axis. The oxygen atoms of CO_2 are involved in hydrogen bonding interactions with the amino (N–H···O) and phenyl (C–H···O) groups at distances of 2.55, 2.81 and 2.87 Å. Based on the occupancy of 50/50 of the guest molecules, this yields the capture capacity of 0.77 molecules per Mn centre, which is in good agreement with the obtained adsorption isotherm. In addition, the encapsulated guest molecules exhibit attractive C···O intermolecular interactions with the distance of 3.78 Å. The combination of these attractive interactions results in strong selectivity of CO_2 towards the pores of MUF-16 MOFs. Separation studies with hydrocarbon mixtures (CO_2/C_2H_6, CO_2/C_2H_4, CO_2/C_2H_2 and CO_2/CH_4) show that hydrocarbons break through from the column at an early stage due to efficient adsorption of CO_2 by the MOF. This results in the productivity of 1 kg of MOF producing 27 L of hydrocarbons from equimolar solutions of CO_2 and hydrocarbon outperforming all previously reported materials. The facile and cost-effective synthesis coupled with excellent selectivity for CO_2 of the MUF-16 series MOFs thus make them a promising physisorbent for CO_2 capture and separation.

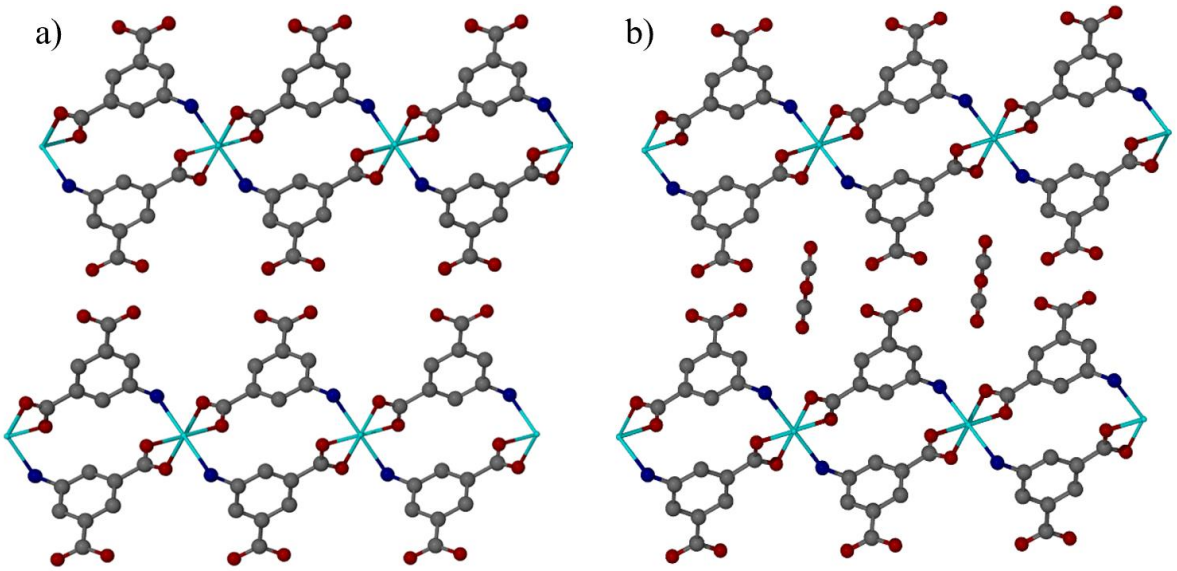

Figure 1-18. Single crystal structures of a) MUF-16(Mn) and b) CO_2@MUF-16(Mn) as viewed along the axis of the pores. Light blue: Mn. Gray: C. Red: O. Dark blue: N. Hydrogen atoms have been omitted for clarity.[161]

Zhou and co-workers reported on the iodine absorption of another redox-active Zr-based MOF with cage sizes in the high microporous (12.6 and 15.8 Å) and low mesoporous (20.6 Å) range.[162] Similarly, I_3^- formed *via* a redox reaction and was relatively easily characterised *via* SC-XRD. Crucially, the case of Co-DpyPtolP-MOF is rather unique as it is the only known crystalline structure of a chain of polyiodide molecules inside a pore that does not form I_2 or I_3^- species. As observed for water clusters in Cr-soc-MOF and the metal-organic nanotube **1.13**, voids of different shapes and sizes result in different behaviour of molecules of the same kind. Thus, this warrants reason for further research in the confinement of various molecules in metal-organic-framework-type materials.

1.3.4 MOFs in confinement chemistry

It is believed that confinement plays a key role in many biological processes, and possibly even in the formation of life.[163–165] For example, according to a theory, mica sheets could have been the source of the origin of life as nanoconfinement between layers of mica sheets could have had the purpose of isolation and protection of the first protocells.[166] These protocells could be regarded as microreactors that provided compartmentalisation for the evolution of living cells.[163] Confinement and compartmentalisation remain essential for the persistence of life on Earth as eukaryotic life

forms consist of confinement from the organ and down to the subcellular levels. Consequently, these systems provide us with biochemical reactions that are consistently performed at amazingly high rates, selectivities, and efficiencies.[167,168]

It is no surprise then that chemistry under confinement in various levels is being studied for various purposes. Confinement can be introduced in many forms using cages, cavitands, micelles, lipid bilayers, liquid droplets, porous siliceous materials, and mineral surfaces.[164,169,170] The purposes of introducing such confinements are various. They can be to study chemical reactions, crystallisation, information in DNA molecules, and single molecule sensing.[169–172] For example, the hydroxyl radicals produced from the Fenton reaction were confined in one-dimensional Fe_3O_4-functionalised nanoreactors having the radius of 20 nm.[173] Compared to the same reaction in a larger vessel, the confinement resulted in a significant increase in the kinetics of terephthalate decomposition upon contact with the short-lived hydroxyl radicals.

The well-defined pore spaces provided by MOFs can readily be used for such confinement chemistry purposes. It was briefly discussed how MOFs are used as catalysts, but they can also be used as templates for the preparation of catalysts. More specifically, MOF pores can be used to control the size of the product that is prepared within. For example, Zhang and co-workers described the use of the zeolitic metal-azolate MAF-6 as the reactor within which tungsten carbide nanoclusters were prepared, which exhibited high catalytic performances toward the hydrogen evolution reaction under acidic conditions.[174] MAF-6 was loaded with $W(CO)_6$ and subsequent pyrolysis yielded the tungsten carbide catalyst in significantly smaller sizes compared to when prepared outside of the MOF pores.

Confinement within the MOF pore walls also allows the control of reactivity and selectivity of chemical reactions. Recently, MUF-77, which comprises of three different organic ligands (**Figure 1-19**) was used for the catalysis of aldol and Henry reactions.[175] Through rational modification of each ligand prior to the synthesis of MUF-77, the environment of the resulting framework's active sites was controlled toward the catalysis of these reactions. First, the MOF is synthesised so that all ligand are connected by SBUs, with the catalytically active ligand protected. Subsequent thermolytic cleavage of the protecting group exposes the prolinyl group used for the catalysis. The other two ligands are modified prior to the synthesis. Longer alkyl chain lengths on the reactivity modulator ligand resulted in slower rate constants of the *m*-Henry reaction and the

replacement of the *bpdc* with the *dppdc* ligand resulted in an increase of the rate constant due to a cooperative effect between the truxene and the *dppdc* ligands.

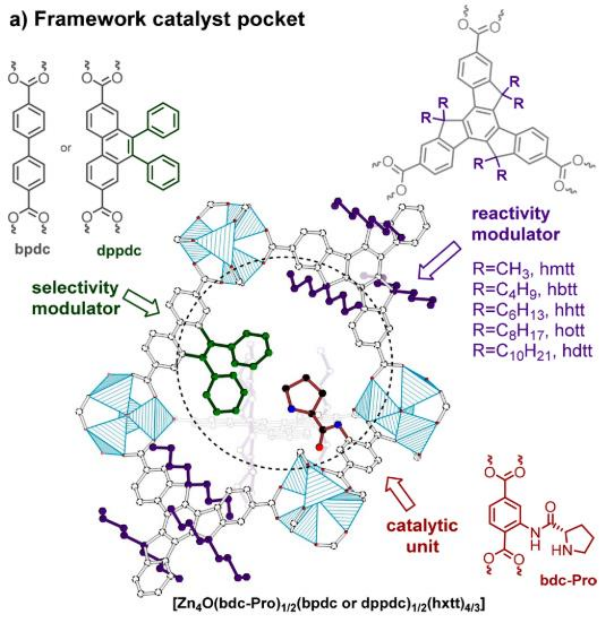

Figure 1-19. Design of MUF-77 with the structures of the selectivity and reactivity modulator and the catalytic unit. Reprinted with permission from ref. 149. Copyright 2019 American Chemical Society.

Confinement of charged species within MOF pores has been demonstrated to result in tunable electrical conductivity.[176] Thin films devices based on HKUST-1 were loaded with a redox-active molecule 7,7,8,8-tetracyanoquinododimethane (TCNQ) by substituting the coordinated water molecules with TCNQ. The conductivity of the resulting thin films loaded with TCNQ was six orders of magnitudes higher compared to that of thin films without the redox-active species. *Ab initio* calculations suggested that this conductivity arose *via* four TCNQ molecules creating a bridge with each other in a unit cell. It is suggested that TCNQ molecules insert unoccupied molecular orbitals into the HOMO-LUMO gap of HKUST-1.

1.5. Molecular Clusters in Metal-Organic Frameworks

Section 1.5 in its entirety has been previously published as a part of a review article entitled "Molecular Clusters in Confined Spaces".[60]

A 2002 article by Levinger pointed out that water under confinement can behave differently compared to its bulk.[177] Confinement of water molecules inside a reverse micelle leads to changes in the vibrational modes in the far-IR region (3–33 cm^{-1}) of reverse micellar water solutions which

can dramatically affect various chemical and biological processes.[178] The absorption features in the far-IR region are only observed in micelles with radii between 15 and 45 Å while the spectra of larger aqueous reverse micelles do not show these absorption peaks, which is consistent with bulk water. As a result, the focus of confinement chemistry shifted to studying confinement effects on various molecules and molecular processes including physicochemical properties, ionic and molecular transport and self-assembly.[179–181] In 2005, a landmark review article by McKenna and Alcoutlabi discussed crystallization under confinement.[182] Importantly, the authors concluded that amorphous solids under confinement can exhibit a decreased glass transition temperature. These results suggest that confinement effects could also affect nucleation and subsequently crystal growth processes. Roughly a decade later, Ward and Jiang reviewed advances in this field.[170] An influential discovery within the decade was the recognition by Ward and co-workers of the phenomenon of size-dependent polymorphism, which can have considerable effects on the production of nanosized active pharmaceutical ingredients.[67] This result highlights the growing importance of confinement chemistry which can be increasingly understood due to advances in techniques such as single crystal X-ray diffraction (SC-XRD) and micro electron diffraction (microED), which allow the study of confinement at ever smaller scales with increasing resolution. Recent review articles about the effects of molecular confinement on chemical reactivity (including kinetics, selectivity, and types of reactions), water purification, cancer theranostics, and supramolecular organization highlight further advances in the field.[183–186] As a result, a substantial collection of studies has accumulated on the topic. This section will focus on recent discoveries in confining molecular clusters in MOFs and extended framework-type materials.

1.5.1 Inorganic Clusters

Metal nanoparticles (NPs) are widely used in the chemical industry, especially catalysis[187], due to their large surface-to-volume ratio compared to their bulk equivalents, which can give them unique properties when compared to their bulk counterparts.[188] As a result, the thermal, magnetic and electronic properties, along with the reactivity, of metal NPs can change with their size. For example, indium NPs with particle size of 10 nm exhibit a 120°C decrease in the melting point compared to larger clusters of 100 nm.[189] Silver NPs emit green, yellow and red/orange light corresponding to 70, 115 and 140 nm particle sizes, respectively. However, one of the main drawbacks of NPs is the difficulty in controlling their size distribution and morphology. Being able to control the aggregate size of NPs can thus be beneficial to various electronic and optical

applications. Additionally, in fields such as optical filters and biosensors, the anisotropy of NP morphology is important.[190] The control over both the size and shape of NPs can be achieved by using framework-type materials with well-defined pore sizes as matrices for the synthesis of NPs. In general, two methods to synthesise NPs inside porous coordination networks are used. The first method involves the conversion of encapsulated metal precursors to NPs within the framework pores. The second method is one-pot synthesis of frameworks in the presence of NPs.

A more unique approach to encapsulated nanoparticles was reported by Chen and co-workers in 2014, and involves ligand design to prepare palladium-incorporated UiO-67 MOF (Pd^0-in-UiO-67).[191] In the first step, the authors coordinated palladium(II) chloride to 2,2'-bipyridine-5,5'-dicarboxylic acid (bpydc) to synthesize the metalloligand **1.7**. Mixing **1.7** with biphenyldicarboxylic acid and zirconium(IV) chloride ($ZrCl_4$) in DMF gives Pd^{II}-in-UiO-67 *via* a solvothermal method. Subsequent treatment of the framework with hydrogen gas at 250°C yields encapsulated palladium metallic NPs; Pd^0-in-UiO-67. TEM imaging reveals an average palladium NP size of 3.0 ± 0.5 nm inside the pores of Pd^0-UiO-67. The encapsulated palladium NPs have been used as catalysts for the oxidation of alcohols and reduction of nitrobenzene. The catalytic efficiency of Pd^0-in-UiO-67 for nitrobenzene reduction is comparable to that of the most active palladium catalyst reported.[191]

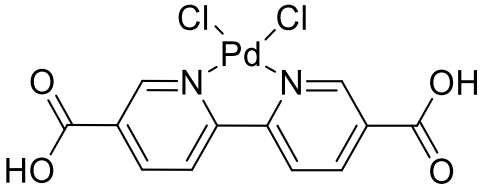

Scheme 1-1. Structure of 2,2'-bipyridine-5,5'-dicarboxylic acid (**1.7**).

A similar approach was taken to synthesise ultrasmall Cu/ZnO_x NPs within another UiO-series MOF UiO-bpy.[192] The solvothermal synthesis of a DMF solution containing $ZrCl_4$, bpydc and formic acid yields UiO-bpy as a white powder. Postsynthetic modification was used to coordinate copper ions to the bipyridine moieties of the framework by simply adding UiO-bpy to a solution containing $CuCl_2$ until the MOF turns green (UiO-bpy-Cu). Additionally, zinc ions can be attached to the zirconium oxide secondary building units by adding $ZnEt_2$ to a solution of UiO-bpy-Cu until the green MOF turns black to form Zn@UiO-bpy-Cu. The MOF can then be reduced at 250°C and 4 MPa under hydrogen atmosphere to form ultrasmall Cu/ZnO_x NPs inside the UiO-bpy pores (CuZn@UiO-bpy). The resulting material has been characterised by diffuse reflectance

UV–vis–NIR spectroscopy and scanning transmission electron microscopy-high angle annular dark-field images. The ZnCu@Uio-bpy material exhibits higher space-time yield and selectivity toward CO_2 hydrogenation to methanol than the commercial ternary $Cu/ZnO/Al_2O_3$. Remarkably, the MOF catalyst exhibits 100% selectivity for methanol under 200–250°C.

In previous examples, secondary building units and organic linkers were used to prepare NPs in MOFs. Additionally, the overall charge, in the case of ionic MOFs, can be used to encapsulate and stabilise metal NPs. For instance, ultrasmall metal clusters can also be prepared inside a negatively charged MOF, in which both the confinement effect and charge act to stabilise the metal clusters. This was achieved by Pardo and co-workers who synthesised an anionic MOF $Ni^{II}_2\{Ni^{II}_4[Cu^{II}_2(Me_3mpba)_2]_3\}\cdot 54H_2O$ (**1.8**) (**Figure 1-20a**) by a transmetallation process of a magnesium-based MOF.[193] Material **1.8** was then reacted with $[Pd^{II}(NH_3)_4]^{2+}$ and subsequently reduced using $NaBH_4$ to yield compound **1.9** (**Figure 1-20b**), which contains $[Pd_4]^{2+}$ clusters inside the pores of the anionic MOF. SC-XRD analysis of **1.9** shows that the tetranuclear palladium clusters are one- and two-coordinated. Furthermore, the inner Pd–Pd bond lengths (2.57 and 2.44 Å) are considerably shorter than the outer Pd–Pd bond lengths (3.16 and 2.91 Å). This drastic difference in bond lengths within a cluster had not been previously observed. The palladium clusters encapsulated in the MOF act as catalysts for the Buchner ring expansion reaction. Remarkably, **1.9** exhibits high catalytic activity and reusability, resulting in a turnover number (TON) of above 2000, which is significantly superior to the state-of-the-art catalyst $Rh_2(OAc)_4$ (TON = 104).[194] The catalytic activity of compound **1.9** also outperforms the catalysts that are used for carbene-transfer-mediated reactions of diazo compounds with some TON values up to 100,000.

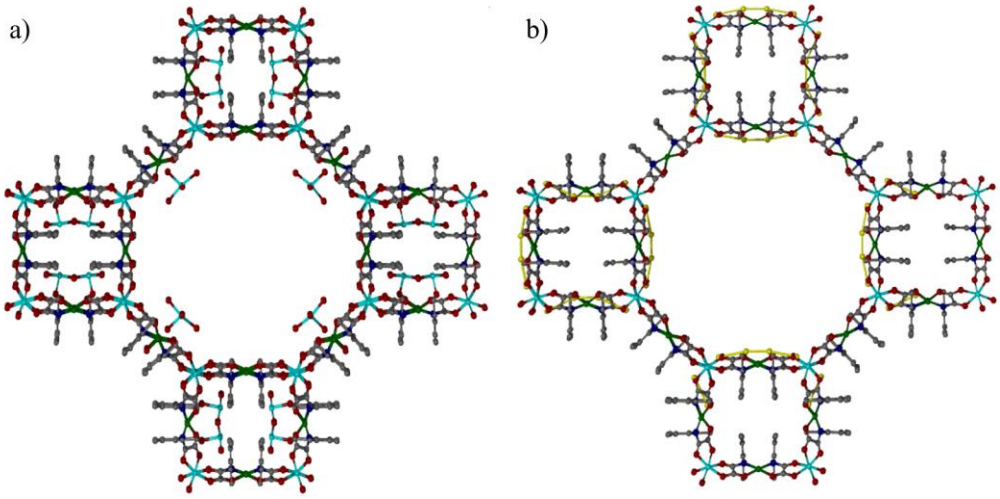

Figure 1-20. Single crystal structures of a) **1.8** and b) **1.9** viewed down the pores. Gray: C. Red: O. Light blue: Ni. Dark green: Cu. Dark blue: N. Yellow: Pd. H atoms omitted for clarity.[193]

In 2019, Zhou and co-workers synthesised metal clusters in HUST-1 MOF *via* the postsynthetic metalation (PSM) method.[195] HUST-1 was synthesised by reacting HUST-1 (**Figure 1-21a**) with nickel halides the authors were able to demonstrate the formation of trinuclear (HUST-3) and heptanuclear (HUST-2) nickel clusters inside the pores by SC-XRD (**Figure 1-21b** and **c**). Nickel ions were also successfully incorporated into the pores of HUST-1, but the characterisation *via* SC-XRD was unsuccessful. The nickel-incorporated MOFs have been used as heterogeneous catalysts for ethylene dimerization. Due to their larger pores, the HUST-series catalysts showed higher catalytic activity and superior butene selectivity than the nickel-containing UiO-67 MOF. Within the HUST-series, HUST-3 exhibits the highest activity toward butene production because nickel centres in the trinuclear clusters have more unsaturated metal sites.

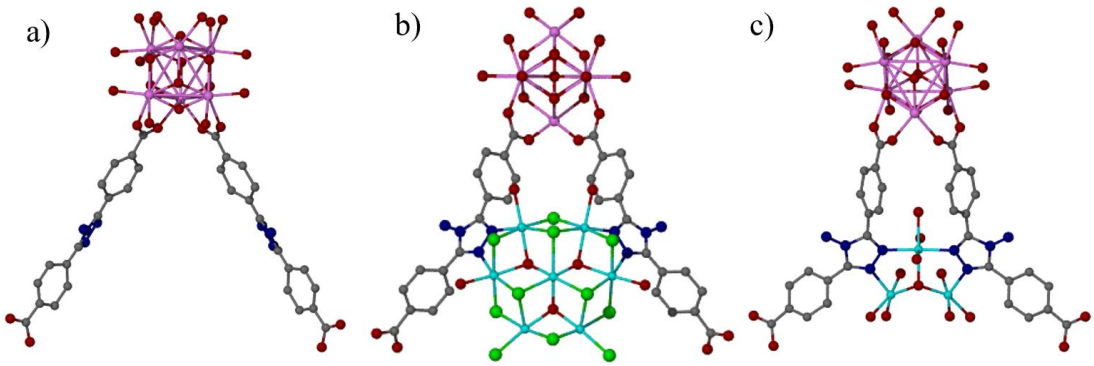

Figure 1-21. Crystal structures of a) HUST-1, b) HUST-2 and c) HUST-3. Red: O. Gray: C. Dark blue: N. Light blue: Ni. Light green: Cl. Pink: Zr. H atoms omitted for clarity.[195]

The main disadvantage of the HUST-series MOFs is the inability to control the size and shape of the metal clusters. Long and co-workers have reported a method to prepare two-dimensional metal sheets inside the MOF $Zr_6O_4(OH)_4(bpydc)_6$ (bpydc = 2,2'-bipyridine-5,5'-dicarboxylate) with the ability to control the size, structure and spatial arrangement of the metal(II) halide sheets.[196] Coordination of the bipyridine organic linkers results in the latter pointing toward the pores of the MOF, facilitating the growth of metal halide sheets. Magnetic susceptibility studies showed that the iron halide sheets exhibit superparamagnetism below 8 K, a phenomenon not observed for bulk iron chloride. This work highlights the ability to control the design of the structures and sizes of metallic clusters inside MOFs, which can be used to synthesise a variety of metal NPs for desired applications.

POMs are a type of metal-oxygen clusters with well-defined topologies and diverse structures and potential applications in catalysis and medicine.[197,198] Liu and co-workers have reported on the encapsulation of a polyoxometalate (POM) cluster $LaW_{10}O_{36}$ cluster inside the pores of MIL-101(Cr).[199] The mesoporous cages of MIL-101(Cr) were filled with LaW_{10} *via* a tandem post-synthetic modification of the MOF by stirring the evacuated MOF in a solution of the polyoxometalate yielding LaW_{10}@MIL-101 material. X-ray fluorescence spectroscopy and inductively coupled plasma optical emission spectroscopy show a homogeneous dispersion of $LaW_{10}O_{36}$ inside both smaller (25 Å diameter) and larger (29 Å diameter) MOF cages. Pyridine-adsorbed IR spectroscopy (Py-IR) can be used to characterise coordinatively unsaturated metal sites by exposing the material to pyridine vapour and subsequently recording its FT-IR spectrum. Py-IR shows that the oxygen atoms of the POM cluster interact with the unsaturated Cr^{3+} metal sites. This is further supported by XPS analysis, in which shifts in the La_3d and Cr_2p spectra correspond to the formation of W=O···Cr coordination bond, which is attributed to the confinement effect of the MIL-101(Cr) framework. The LaW_{10}@MIL-101 acts as a catalyst for oxidative desulfurization of benzothiophene (BT), dibenzothiophene (DBT) and 4,6-dimethyldibenzothiophene (4,6-DMDBT). The catalytic efficiency of LaW_{10}@MIL-101 after 180 min of reaction time is 99.1%, 94.5% and 87.4% for DBT, 4,6-DMDBT and BT, respectively. The catalytic efficiency toward desulfurization of BT and 4,6-DMDBT is the highest reported, along with nearly full desulfurization of DBT (although 100% catalytic efficiency has been reported elsewhere using a similar method of encapsulating POMs in the MIL-101(Cr) framework). Crucially, however, the catalyst can be reused at least seven times without losing significant

activity although a small decrease from 98.2% to 96.8% for DBT conversion after 120 min reaction time is observed. This remarkable stability is attributed to the W=O···Cr coordination bond which anchors the catalyst to the pore, thus preventing leaching.

Wöll and co-workers have encapsulated $Au_{55}(PPh_3)_{12}Cl_6$ clusters inside surface-supported MOF (SURMOF) thin films Cu-QPDC (**1.10**) and Cu-PPDC-CH_3 (**1.11**).[200] Both **1.10** and **1.11** are synthesised onto a hydroxyl-functionalised Si substrates using a layer-by layer method as depicted in **Figure 1-22**. First, a layer of compound **1.10** or **1.11** is sprayed onto the film, followed by a loading of the clusters onto the MOF layer and subsequent spraying of the next MOF layer. This process is repeated until a sandwich-like structure of **1.10** and **1.11** containing $Au_{55}(PPh_3)_{12}Cl_6$ clusters is obtained. Quartz crystal microbalance (QCM) measurements reveal that the loading efficiency of Au_{55} clusters is around 25%. Experimentally obtained PXRD patterns of compound **1.10** fully loaded with $Au_{55}(PPh_3)_{12}Cl_6$ clusters reveal a substantial decrease in the 001 peak compared to the empty **1.10** indicating successful encapsulation of the gold clusters. However, computational modelling using density functional theory (DFT) showed a significantly stronger intensity of the 001 reflection compared to that of the experimentally obtained. Thus, ligand-stripped Au_{55} clusters were placed inside the pore of **1.10** and allowed to move freely in order to systematically search for the best theoretical match between the experimentally and theoretically obtained peak intensities. A good agreement is obtained for a structure in which the Au_{55} clusters are positioned in the corners of the pores of **1.10**. The stripping or partial displacement of PPh_3 ligands is a result of a competitive binding site which stabilises the Au_{55} cluster inside the pores of **1.10**. The catalytic efficiency of the gold nanocluster encapsulated inside **1.10** was evaluated by 4-nitrophenol reduction reaction. UV-Vis absorption spectra show that Au_{55}@**1.10** exhibits superior reduction of 4-nitrophenol to 4-aminophenol compared to bulk $Au_{55}(PPh_3)_{12}Cl_6$.

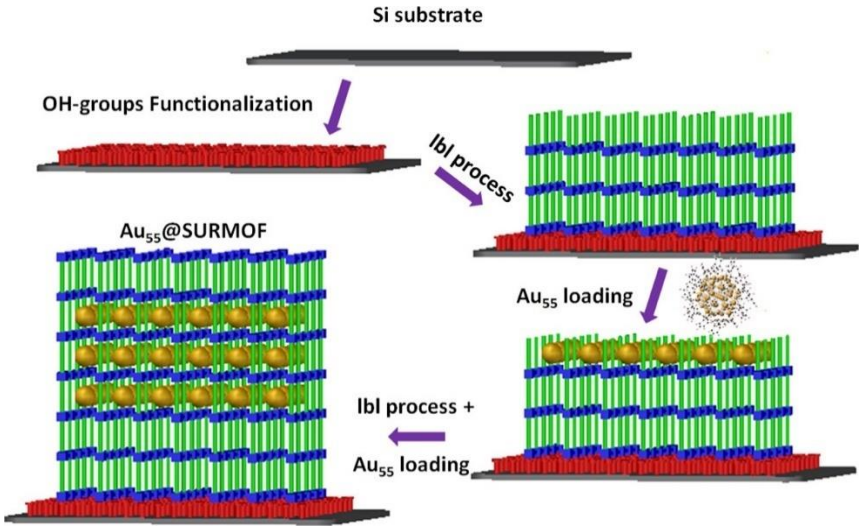

Figure 1-22. Synthetic process of obtaining gold-encapsulated surface-supported MOF thin films. Reprinted with permission from *ACS Appl. Nano Mater.* 2021, 4, 1, 522–528. Copyright 2024 American Chemical Society.

Heavy metal pollution in water has significant negative impacts on animal and human health, ranging from carcinogenic effects to liver damage and cerebral disorders.[201] Chromium(VI) is a highly toxic heavy metal and is more toxic compared to Cr^{III} and Cr^{VI} often exists as a chromate or dichromate oxyanion.[202] In 2020, Li and co-workers synthesised zirconium- and hafnium-based isostructural MOFs (Zr/Hf-MOF-1, Zr/Hf-MOF-2 and Zr/Hf-MOF-3) for the detection of $Cr_2O_7^{2-}$ in aqueous solutions.[203] UV-Vis absorption spectra show that Hf-MOF-2 has the highest maximum capture capacity of $Cr_2O_7^{2-}$ out of the synthesised MOFs. In addition, Hf-MOF-2 which has a neutral framework outperforms other reported cationic MOFs such as FIR-53 and 1-Br.[204,205] Luminescence quenching efficiency is the highest for Zr/Hf-MOF-3, which also have a limit of detection of 0.013 and 0.019 μM, respectively. These values are similar to the best performing MOFs reported. SC-XRD analysis of the $Cr_2O_7^{2-}$-loaded Hf-MOF-2 is shown in **Figure 1-23**. This reveals that $Cr_2O_7^{2-}$ clusters replace the H_2O/OH^- groups coordinated to the Zr_6 or Hf_6 clusters of the MOFs. In addition, the enhanced pore size of the isostructural Zr/ Hf-MOF-2 compared to Zr/Hf-MOF-1 and -3 allow for two more $Cr_2O_7^{2-}$ anions to bind inside each pore. This is the first time $Cr_2O_7^{2-}$ anions have been characterised inside MOF pores by SC-XRD and confirmed the hypothesis that the uptake mechanism of the anion proceeds by coordinating to the SBU oxide clusters.

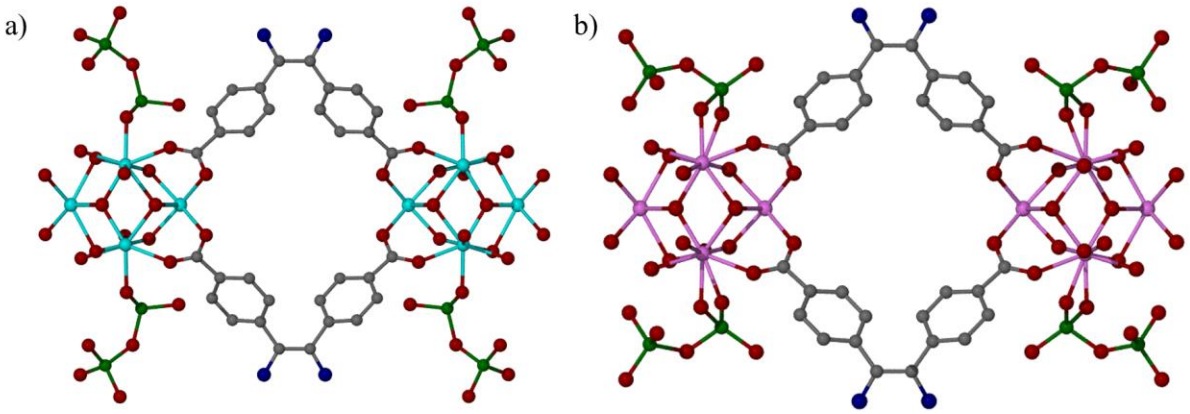

Figure 1-23. Single crystal structures of a) Hf-MOF-2 with $Cr_2O_7^{2-}$ anions viewed along the 001 axis and b) Zr-MOF-2 with $Cr_2O_7^{2-}$ anions viewed along the 001 axis. Gray: C. Red: O. Light blue: Hf. Pink: Zr. Green: Cr. Hydrogen atoms omitted for clarity.[203]

1.5.2 Organic Clusters

The crystalline sponge method (CSM) allows the determination of the structure of guest molecules encapsulated in the pores of a single crystal of a porous coordination network. The advantages of this method are that the guest molecules do not have to be crystalline to allow inclusion and crystal structure determination, and only a trace amount (<0.1 μg) of the guest is required. CSM was originally introduced by Fujita and co-workers who determined the structures of a variety of guest molecules encapsulated in the pores of single crystals of $\{[(ZnI_2)_3(TPT)_2]_x(solvent)\}_n$ MOF (**1.12**) (TPT = 2,4,6-tris(4- pyridyl)-1,3,5-triazine).[206] The absolute structures of chiral molecules, such as santonin and myakosine A were successfully determined. In fact, this is the first reported molecular structure of myakosine A. In addition, the slow diffusion of guest compounds into the pores of the MOF results in well-ordered structures making CSM a very attractive method to study confined molecular clusters.

In 2016, Fujita and co-workers closely examined the steps involved in CSM and analysed the advantages and disadvantages of various guest soaking methods, such as the original, a-grain-of-crystal, slow evaporation and high-throughput.[207] Fujita and co-workers also expanded on factors that affect crystallographic analysis such as guest occupancy, molecular recognition sites, data collection conditions and structure refinement. For instance, the authors recommend using Cu Kα radiation for diffraction data collection as it yields higher I/σ values for high-angle regions compared to Mo Kα radiation. Overall, this work provides optimized steps for reliable and

reproducible X-ray crystallographic analysis of guest molecules when undertaking CSM, a very attractive method for the determination of absolute configuration of a wide array of compounds.

The main drawback of MOF **1.12** in the CSM context is the hydrophobicity of the pores which means that most of the guest molecules that can be encapsulated are hydrophobic. In addition, **1.12** is not stable in many solvents. These drawbacks were remedied by the synthesis of the novel RUM-series MOFs (RUM-1, RUM-2 and RUM-3) based on f-block metals.[208] RUM-1 and RUM-2 are synthesized using 1,3,5-benzenetribenzoic acid (H_3BTB) and differ only by the connectivity of the organic linker to the secondary building units containing gadolinium. The framework in RUM-1 is two-dimensional while RUM-2 is three-dimensional. RUM-3 employs the 4,4',4''-(1,3,5-triazine-2,4,6-triyl)tribenzoic acid (H_3TATB) linker connecting cerium or dysprosium. RUM-1 and RUM-2 are the most stable MOFs in the series, and both are stable in a variety of polar solvents. Due to the microporous size of the MOFs cavities, only small organic molecules such as carvone, ε-caprolactam and pyridine can be encapsulated. This work established the capability of CSM to be successfully applied using various solvents and overcoming hydrophobicity by hydrogen bond interactions *via* water molecules coordinated to the secondary building unit metals in the case of RUM-1 and vacant metal sites in the case of RUM-2 and RUM-3.

However, the CSM concept can also work without using any solvent (*i.e.* without soaking MOF single crystals in a solvent in which the target guest is dissolved). In 2018, Eddaoudi and co-workers reported on the synthesis of a novel Cr-soc-MOF, which is capable of capturing twice its own weight of water (1.95 g g^{-1}).[144] Cr-soc-MOF contains channels of roughly 17 Å and cages of roughly 15 Å in size. SC-XRD analysis of this material after water adsorption reveals that 114 water molecules form a cluster inside the cages (**Figure 1-24a** and **b**). The encapsulated water molecules form hexamers and heptamers which interact more strongly with each other rather than with water molecules located on the cage edges. This suggests that some water molecules could be acting as nuclei to form aggregates of hexamers and heptamers. Furthermore, if nucleation processes are possible in these systems, they could also be used as vessels for nanosized crystallization.

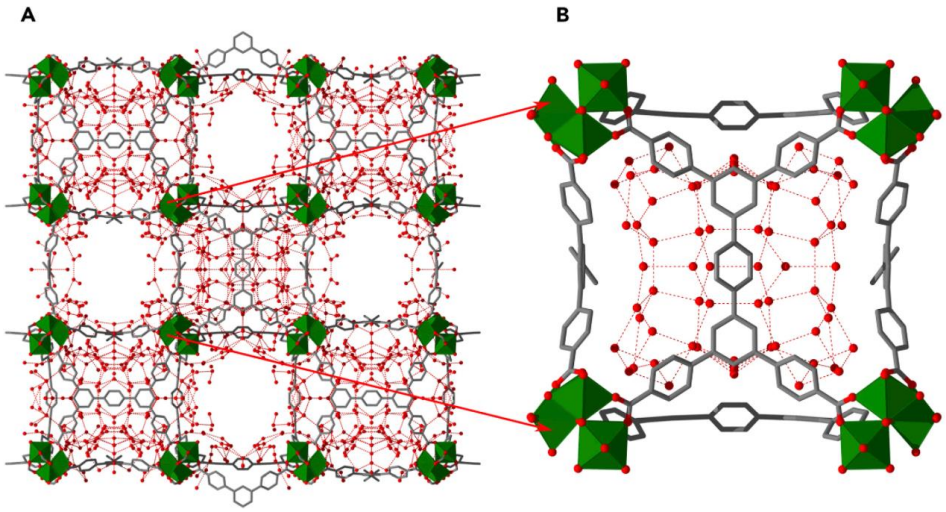

Figure 1-24. a) Single crystal structure depicting the channels and cages of water-absorbed Cr-soc-MOF. b) Position of water molecules inside the cage of Cr-soc-MOF. Hydrogen atoms have been omitted for clarity. Reproduced with permission from ref. 131.

In order to study how confined water clusters behave in a hydrophobic environment, Kitagawa and co-workers synthesised a metal-organic square-shaped nanotube **1.13** (**Figure 1-25a**).[209] Compound **1.13** contains two channels; the larger channel A is hydrophobic and smaller channel B is hydrophilic. Inside channel B, water clusters form a hydrogen-bonding network with the terminal amino groups and sulfate anions. However, water clusters in channel A are vastly different. Inside the hydrophobic channels, there are two types of water clusters, tetramers and octamers (**Figure 1-25b**). The O–O distances are in the range of 2.5–2.7 Å, corresponding to strong hydrogen bonding between water molecules in clusters. In addition, in the *a*-direction, the clusters also form weaker hydrogen bonds as the O–O distances vary from 3.0 to 3.4 Å.

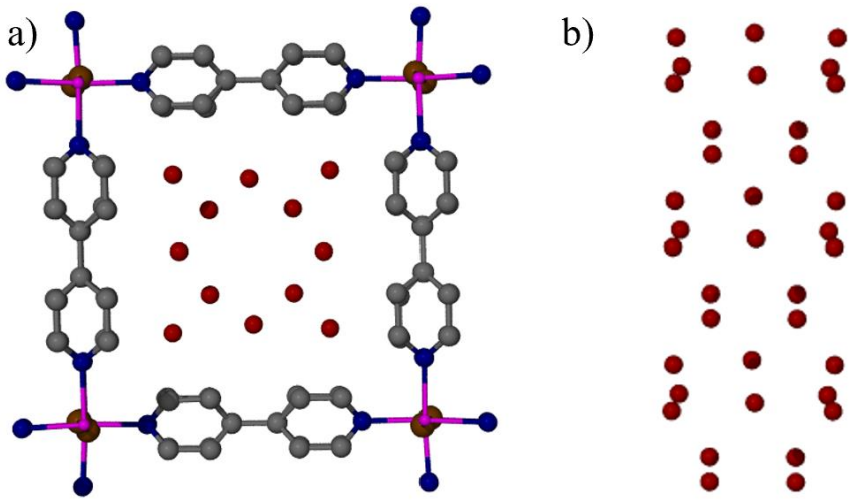

Figure 1-25. a) View down channel A of **1.13** showing the water oxygen atoms and b) Side view of the octa- and tetranuclear water clusters inside channel A of **1.13**. Gray: C. Dark blue: N. Purple: Pt. Brown: Br. Red: O.[209]

Comparing the pores of Cr-soc-MOF and nanotube **1.13** can provide insight into what nanoconfinement effects promote the formation of these specific clusters. For example, there is a slight difference in pore sizes; the size of Cr-soc-MOF cage is 15 Å while the nanotube channel is 14 Å in size. Intuitively, it would expected that larger clusters are formed inside Cr-soc-MOF pores. However, the largest cluster of water molecules consist of heptamers (7 molecules) inside Cr-soc-MOF while octamers (8 molecules) form inside the smaller nanochannel. This implies that the pore geometry plays an important role in the nucleation processes. Indeed, the shape of these voids are drastically different. The endless rectangular channels of the nanotubes result in the formation of two-dimensional water cluster layers of tetramers and octamers, which are relatively planar and form rectangular-shaped clusters. In the case of the cage, the clusters are not layered and rather form three-dimensional clusters. The cages of Cr-soc-MOF rather consist of water hexamers and heptamers inside the cages with single water molecules on the side of the cages, as Eddaoudi and co-workers propose, acting as nuclei. In terms of intermolecular interactions between the frameworks and guest clusters, both Cr-soc-MOF and nanotube material **1.13** contain hydrophobic voids. Thus, it is more likely that water clusters assemble *via* hydrogen bonding interactions and take up clusters that have a good fit within the pores. Kitagawa and co-workers add that the clustering of water molecules arises from the hydrophobic nature of the channels, an effect similar to that observed in carbon nanotubes and ion transport proteins.[209–212]

Recently, Yaghi and co-workers combined DFT calculations with experimental crystallographic structures to reveal the evolution of water clusters inside MOF-303.[89] MOF-303 is composed of 1-*H*-pyrazole-3,5-dicarboxylate (H_2PZDC) linkers connected together by AlO_6 secondary building unit clusters and exhibits the **xhh** topology. MOF-303 is efficient in capturing water (0.48 g g^{-1}) and the water sorption isotherm reveals a three-step adsorption process. Thus, single crystals were synthesised to study one-by-one nucleation of water molecules inside MOF-303. Synchrotron SC-XRD analysis reveals the locations of the first four adsorbed water molecules. The first two water molecules are located between two pyrazole units, which is also the most hydrophilic part of the framework. The third and fourth water molecules interact with the μ_2-OH group and the first two water molecules, respectively. The subsequent nucleation of water molecules onto the "seed" of the first four was investigated *via* DFT calculations. The results reveal that the nucleated water molecules interact with previously bound water molecules rather than with the surrounding MOF. The addition of fifth and sixth water molecules results in the formation of a tetramer cluster, which is transformed into a hexamer by the addition of seventh and eighth water molecules. The addition of water molecules 5-8 signifies the second step in the isotherm and is referred to as the clustering phase. In the final networking phase, water molecules 9 through 14 partly fill the MOF pores to form permanent H-bonded water chains throughout the framework pores, resulting in the total uptake of 0.45 g g^{-1}, which agrees with the experimentally obtained water isotherm. Additionally, the authors replaced the $PZDC^{2-}$ linkers with 2,4-furandicarboxylic acid to probe the importance of the hydrophilic pocket presented by the $PZDC^{2-}$ linker towards the efficient seeding of water molecules. It was found that the initial water molecules bind to the μ_2-OH sites rather than the organic linker sites.

In 2018, Pardo and co-workers isolated single platinum metal ions stabilised by a water cluster inside the pores of a mesoporous MOF.[213] The authors synthesised a nickel-based MOF having the formula $Ni_2^{II}\{Ni^{II}_4[Cu^{II}_2(Me_3mpba)_2]_3\}\cdot 54H_2O$ (**1.14**) (Me_3mpba = *N,N*'-2,4,6-trimethyl-1,3-phenylenebis(oxamate)), which was subsequently treated with $[Pt(NH_3)]_4^{II}$ to yield $[Pt^{II}_2(m\text{-}OH_2)(NH_3)_6)]_{0.65}[Pt^{II}(NH_3)_4]_{0.7}\{Ni^{II}_4[Cu^{II}_2(Me_3mpba)_2]_3\}\cdot 65H_2O$ (**1.15**) and $NaBH_4$ to yield $[Pt^{II}_2(\ \text{-}O)(OH)_2(NH_3)_4]_{0.5}Pt^{I}@Na_3\{Ni^{II}_4[Cu^{II}_2(Me_3mpba)_2]_3\}\cdot 79H_2O$ (**1.16**). XANES analysis of framework **1.16** suggests that the encapsulated platinum ions are oxidised and exhibit a different local environment compared to platinum foil. Furthermore, EXAFS spectra indicate the presence of Pt–O or Pt–N bonds and a high dispersion of platinum ions in the framework of **1.16**.

Indeed, SC-XRD analysis of the framework shows that platinum ions are coordinated to four water molecules and the cluster is stabilised by hydrogen bond interactions between the water molecules and the framework ligands. DFT structure of platinum ions inside the pores of **1.16** also suggests the presence of a second coordination sphere, which consists of three water molecules interacting with the platinum–water cluster and the framework *via* hydrogen bonding. Thus, the pore acts as a confinement matrix to stabilise the platinum metal and the surrounding water clusters. Subsequently, **1.16** was used as a catalyst for the water-gas shift reaction, which generates CO_2 and H_2 from carbon monoxide and water, generally by using platinum or gold ions as catalysts. The catalytic activity of **1.16** was compared to other Pt-supported catalyst and remarkably **1.16** shows the highest activity up to 150° C. Pardo and co-workers suggest that the mechanism of CO_2 formation stems from the encapsulated water molecules, which trigger a double water attack on the CO to yield CO_2 at temperatures as low as 50°C. This superior activity compared to other Pt-supported catalysts arises from the confinement effect of the pore which stabilises the Pt^{I} ions and its surrounding water clusters. The presence of Pt^{I} rather than Pt^{II} or Pt^{0} was confirmed by X-ray photoelectron spectroscopy.

Overall, these results suggest that MOFs can be designed for selective binding of guest molecules. More importantly, the close agreement between SC-XRD measurements and DFT calculations for the seeding event inside the MOF suggests that the shape and environment of MOF pores leads to a specific arrangement of water molecules unique to that MOF. In other words, water molecules assemble to unique polymorphs inside different MOFs. This concept could potentially be applied to crystallize novel polymorphs of small organic molecules inside MOFs by gaining control over the seeding and clustering pathways to form an initial nucleus of critical size, which would subsequently direct the crystal growth phase. So far in this work, various water clusters have been observed for both hydrophilic and hydrophobic MOF pores. The evidence suggests that designing hydrophilic MOF pores could be advantageous in terms of controlling where the initial guest seeds form. Subsequently, using computational modelling, the shape of the corresponding guest nuclei could be predicted to obtain clusters, and eventually polymorphs, with the desired shapes and properties. .

1.5 Conclusions

This chapter provides an overview of the mechanisms and applications involved with crystallisation, along with an in-depth discussion of MOFs and their use as confinement matrices.

Nucleation is believed to play a crucial role in crystallisation and can have a significant impact on its outcomes. However, it is difficult to study nucleation mechanisms as the process itself occurs at such a small scale and timeframe. Thus, by confining nucleation processes within a confinement matrix, such as a MOF, not only does it provide a fixed space where nucleation can be studied, it also allows for the visualisation of said space *via* SC-XRD due to the high crystallinity of MOFs. The high crystallinity of MOFs has been already exploited to study the molecular structure of single molecules that are difficult to crystallise, termed as the crystalline sponge method. So far, many of the MOF materials used as crystalline sponges are microporous and capable of encapsulating only a single unit of a target molecule per asymmetric unit.

By expanding the MOF pores into the mesoporous scale, the nucleation of molecules can consequently be studied within these spaces. Mesoporous MOFs could potentially be obtained by using lanthanoids as metal centres. Due to their large coordination number, they could potentially lead to MOFs containing larger pores as compared to their transition metal counterparts. To reach this goal, some important aspects still need improving, such as the crystallinity of MOFs and full encapsulation of the guest molecules throughout the whole crystal of the MOF. It is very common for MOF single crystals to lose their crystallinity when removed from their mother liquor, rendering their contents impossible to analyse *via* SC-XRD. Thus, the synthesis of stable and highly crystalline MOFs is crucial. Additionally, it is important to ensure that the guest molecules diffuse throughout the whole MOF crystal, which results in a consistent packing arrangement and decreases the disorder associated with the final crystal structure. By overcoming these limitations, MOFs can be easily and effectively used as confinement matrices to study nucleation processes of various molecules.

1.6 Project Aims and Overview

This work aims to further the field of controlled crystallisation, with a focus on studying confinement chemistry and epitaxy. Confinement chemistry will be employed *via* the synthesis of single crystals of MOF materials exhibiting pores that will serve as confinement matrices for the encapsulation of molecular clusters of meaningful sizes. Subsequently, solvent molecules in the MOF pores will be exchanged with target guest compounds, resulting in clusters of guest molecules within the MOF pores. SC-XRD will be employed to analyse the shape and interactions of these guest clusters in order to gain a better understanding of molecular aggregation and potentially nucleation mechanisms at this scale. Additionally, this method of confining guest

clusters inside MOF pore spaces could potentially be used to uncover novel polymorphs as the pores are expected to induce a different packing arrangement of guest molecules as compared to their bulk equivalents. Epitaxy will be employed towards the controlled crystallisation of coordination compounds of transition metals with 1,4,7-trimethyl-1,4,7'-triazacyclononane and 1,4,7-trithiacyclononane ligands. A seed crystal of a coordination compound will be used to epitaxially grow crystals of isostructural materials with a different metal centre. This method could be used for controlled crystallisation of labile copper(II)-based coordination compounds. As a result, this work will contribute to the improvement of controlled crystallisation of organic and inorganic materials.

1.7 References

1 R. W. Hartel, A. V Shastry, R. W. Hartel and A. V Shastry, *Crit. Rev. Food Sci. Nutr.*, 2009, **30**, 49–112.

2 N. E. Chayen and E. Saridakis, *Nat. Methods*, 2008, **5**, 147–153.

3 K. J. Carpenter and W. M. L. Wood, *Adv. Powder Technol.*, 2004, **15**, 657–672.

4 N. Variankaval, A. S. Cote and M. F. Doherty, *AIChE*, 2008, **54**, 1682–1688.

5 P. G. Vekilov, *Nanoscale*, 2010, **2**, 2346–2357.

6 D. Erdemir, A. Y. Lee and A. S. Myerson, *Acc. Chem. Res.*, 2009, **42**, 621–629.

7 J. W. Gibbs, *Am. J. Sci.*, 1878, **3**, 300–320.

8 A. Laaksonen and I. Napari, *J. Phys. Chem. B*, 2001, **105**, 11678–11682.

9 V. M. Fokin and E. D. Zanotto, *J. Non-Cryst. Solids*, 2000, **265**, 105–112.

10 D. Frenkel and P. R. ten Wolde, *Science*, 1997, **277**, 1975–1978.

11 A. Gavezzotti, *Chem. Eur. J.*, 1999, **5**, 567–576.

12 D. Kashchiev, *J. Chem. Phys.*, 2003, **118**, 1837–1851.

13 P. G. Vekilov, *Nature*, 2019, **570**, 450–452.

14 U. Gasser, E. R. Weeks, A. Schofield, P. N. Pusey and D. A. Weitz, *Science*, 2001, **292**, 258–262.

15 J. Zhou, Y. Yang, Y. Yang, D. S. Kim, A. Yuan, X. Tian, C. Ophus, F. Sun, A. K. Schmid, M. Nathanson, H. Heinz, Q. An, H. Zeng, P. Ercius and J. Miao, *Nature*, 2019, **570**, 500–503.

16 J. Li and F. L. Deepak, *Chem. Rev.*, 2022, **122**, 16911–16982.

17 E. H. Lee, *Asian J. Pharm. Sci.*, 2014, **9**, 163–175.

18 J. Thun, L. Seyfarth, C. Butterhof, J. Senker, R. E. Dinnebier and J. Breu, *Cryst. Growth Des.*, 2009, **9**, 2435–2441.

19 J. von Liebig and F. Wohler, *J. Ann. Pharm.*, 1832, **17**, 249–282.

20 J. Thun, L. Seyfarth, J. Senker, R. E. Dinnebier and J. Breu, *Angew. Chem. Int. Ed.*, 2007, **46**, 6729–6731.

21 A. J. Cruz-cabeza, S. M. Reutzel-Edens and J. Bernstein, *Chem. Soc. Rev.*, 2015, **44**, 8619–8635.

22 J. D. Dunitz and J. Bernstein, *Acc. Chem. Res.*, 1995, **28**, 193–200.

23 J. Bernstein, R. J. Davey and J. Henck, *Angew. Chem. Int. Ed.*, 1999, **38**, 2440–3461.

24 A. J. Cruz-Cabeza and J. Bernstein, *Chem. Rev.*, 2014, **114**, 2170–2191.

25 J. P. Brog, C. L. Chanez, A. Crochet and K. M. Fromm, *RSC Adv.*, 2013, **3**, 16905–16931.

26 Fu Jian Hua, J. Rose, F. Tam Ming and Wang Bi Cheng, *Acta Crystallogr. Sect. D*, 1994, **50**, 219–224.

27 W. von Ostwald, *Zeitschrift für Physikalische Chemie*, 1897, **XXII**, 289–330.

28 E. H. Lee, *Asian J. Pharm. Sci*, 2014, **9**, 163–175.

29 C. Rasmuson, *Eur. J. Pharm. Sci.*, 2006, **28**, 377–384.

30 D. Chistyakov, G. Sergeev, *Pharmaceutics*, 2020, **12**(1), 34.

31 J. Bauer, S. Spanton, R. Henry, J. Quick, W. Dziki, W. Porter and J. Morris, *Pharm. Res.*, 2001, **18**, 859–866.

32 L. Yu, S. M. Reutzel, G. A. Stephenson, L. Yu, S. M. Reutzel and G. A. Stephenson, *PSTT*, 1998, **1**, 118–127.

33 S. Bates, G. Zografi, D. Engers, K. Morris, K. Crowley and A. Newman, *Pharm. Res.*, 2006, **23**, 2333–2349.

34 A. A. Bunaciu, E. Gabriela Udriştioiu and H. Y. Aboul-Enein, *Crit. Rev. Anal. Chem.*, 2015, **45**, 289–299.

35 P. N. T. Unwin and R. Henderson, *J. Mol. Biol.*, 1975, **94**, 425–440.

36 R. Henderson, J. M. Baldwin, K. H. Downing, J. Lepault and F. Zemlin, *Ultramicroscopy*, 1986, **19**, 147–178.

37 T. Gonen, Y. Cheng, P. Sliz, Y. Hiroaki, Y. Fujiyoshi, S. C. Harrison and T. Walz, *Nature*, 2005, **438**, 633–638.

38 T. Nakane, A. Kotecha, A. Sente, G. McMullan, S. Masiulis, P. M. G. E. Brown, I. T. Grigoras, L. Malinauskaite, T. Malinauskas, J. Miehling, T. Uchański, L. Yu, D. Karia, E. V. Pechnikova, E. de Jong, J. Keizer, M. Bischoff, J. McCormack, P. Tiemeijer, S. W. Hardwick, D. Y. Chirgadze, G. Murshudov, A. R. Aricescu and S. H. W. Scheres, *Nature*, 2020, **587**, 152–156.

39 D. Shi, B. L. Nannenga, M. G. Iadanza and T. Gonen, *Elife*, 2013, **2**, e01345.

40 C. Nguyen and T. Gonen, *Curr. Opin. Struct. Biol.*, 2020, **64**, 51–58.

41 Y. Dai, V. Terskikh, A. Brinmkmann and G. Wu, *Cryst. Growth Des.*, 2020, **20**, 7484–7491.

42 R. K. Harris, A. M. Kenwright, B. J. Say, R. R. Yeung, R. W. Lancaster, M. U. B. Ohe and K. Harris, *Spectrochim. Acta*, 1990, **46A**, 927–935.

43 H. G. Brittain, K. R. Morris, D. E. Bugay and A. T. M. Serajuddin, *J. Pharm. Biomed. Anal.*, 1993, **11**, 1063–1069.

44 H. Park, H. Nie, A. Dhiman, V. Tomar and Q. T. Zhou, *Mol. Pharmaceutics*, 2020, **17**, 3043–3052.

45 M. L. P. Leitao, M. S. C. C. Canotilho, J. C. Pereira, A. T. Sousa and J. S. Redinha, *J. Therm. Anal. Calorim.*, 2002, **68**, 397–412.

46 G. Coquerel, *Chem. Soc. Rev.*, 2014, **43**, 2286–2300.

47 B. Spingler, S. Schnidrig, T. Todorova and F. Wild, *CrystEngComm*, 2012, **14**, 751–757.

48 C. Orvig, *J Chem Educ*, 1985, **62**, 84.

49 H. Hope, *J. Appl. Crystallogr.*, 1971, **4**, 333–333.

50 C. Bridle and T. R. Lomer, *Acta Crystallogr.*, 1965, **19**, 483–484.

51 X. Li, X. Ou, H. Rong, S. Huang, J. Nyman, L. Yu and M. Lu, *Cryst. Growth Des.*, 2020, **20**, 7093–70.

52 S. Chen, I. A. Guzei and L. Yu, *J. Am. Chem. Soc.*, 2005, **127**, 9881–9885.

53 X. Ou, X. Li, H. Rong, L. Yu and M. Lu, *Chem. Commun.*, 2020, **56**, 9950–9953.

54 A. Ghosh and G. Das, *New J. Chem.*, 2020, **44**, 1354–1361.

55 D. A. Brewster, Y. Bian and K. E. Knowles, *Chem. Mater.*, 2020, **32**, 2004–2013.

56 C. Zhang, R. S. Patil, T. Li, C. L. Barnes and J. L. Atwood, *Chem. Commun.*, 2017, **53**, 4312–4314.

57 O. M. Yaghi and H. Li, *J. Am. Chem. Soc.*, 1995, **117**, 10401–10402.

58 T. Sugiyama and H. Masuhara, *Chem. Asian J.*, 2011, **6**, 2878–2889.

59 W. Beckmann, *Org. Process. Res. Dev.*, 2000, **4**, 372–383.

60 A. Braschinsky and J. W. Steed, *Coord. Chem. Rev.*, 2022, **473**, 214840.

61 B. W. Smith, M. Monthioux and D. E. Luzzi, *Nature*, 1998, **396**, 323–324.

62 F. C. Meldrum and C. O'Shaughnessy, *Adv. Mater.*, 2020, **32**, 2001068.

63 R. R. Meyer, J. Sloan, R. E. Dunin-Borkowski, A. I. Kirkland, M. C. Novotny, S. R. Bailey, J. L. Hutchison and M. L. H. Green, *Science*, 2000, **289**, 1324–1326.

64 M. Alcoutlabi and G. B. McKenna, *Journal of Physics Condensed Matter*, 2005, **17**, R461–R524.

65 J. M. Ha, J. H. Wolf, M. A. Hillmyer and M. D. Ward, *J. Am. Chem. Soc.*, 2004, **126**, 3382–3383.

66 J. M. Ha, B. D. Hamilton, M. A. Hillmyer and M. D. Ward, *Cryst. Growth Des.*, 2009, **9**, 4766–4777.

67 J. M. Ha, B. D. Hamilton, M. A. Hillmyer and M. D. Ward, *Cryst. Growth Des.*, 2012, **12**, 4494–4504.

68 Q. Jiang, C. Hu and M. D. Ward, *J. Am. Chem. Soc.*, 2013, **135**, 2144–2147.

69 J. Desarnaud, D. Bonn and N. Shahidzadeh, *Sci. Rep.*, 2016, **6**, 23–26.

70 D. Fu, Y. Su, X. Gao, Y. Liu and D. Wang, *J. Phys. Chem. B*, 2013, **117**, 6323–6329.

71 Y. Liu, Y. Wu, J. Yao, J. Yin, J. Lu, J. Mao, M. Yao and F. Luo, *ACS Omega*, 2021, **6**, 18235–18247.

72 E. L. Smith, A. P. Abbott and K. S. Ryder, *Chem. Rev.*, 2014, **114**, 11060–11082.

73 X. Lan, X. Wang, W. Du, T. Mu and X. Z. Lan, *Phys. Chem. Chem. Phys.*, 2021, **23**, 13785–13788.

74 J. W. Pridgeon, R. M. Pereira, J. J. Becnel, S. A. Allan, G. G. Clark and K. J. Linthicum, *J. Med. Entomol.*, 2008, **45**, 82–87.

75 X. Zhu, C. T. Hu, B. Erriah, L. Vogt-Maranto, J. Yang, Y. Yang, M. Qiu, N. Fellah, M. E. Tuckerman, M. D. Ward and B. Kahr, *J. Am. Chem. Soc.*, 2021, **143**, 17144–17152.

76 J. F. McConnell, *Cryst. Struct. Commun.*, 1973, **2**, 459–461.

77 H. Krishna Murthy, T. Bhat and M. Vijayan, *Acta Crystallogr., Sect. B: Struct. Crystallogr. Cryst. Chem.*, 1982, **38**, 315–317.

78 V. Lopez-Mejias, J. W. Kampf and A. J. Matzger, *J. Am. Chem. Soc.*, 2012, **134**, 9872–9875.

79 K. Zhang, N. Fellah, V. López-Mejías and M. D. Ward, *Cryst. Growth Des.*, 2020, **20**, 7098–7103.

80 C. E. Nicholson, C. Chen, B. Mendis and S. J. Cooper, *Cryst. Growth Des.*, 2011, **11**, 1–4.

81 J. Liu, C. E. Nicholson and S. J. Cooper, *Langmuir*, 2007, **23**, 7286–7292.

82 Q. Liu, J. Wang, H. Wu, S. Zong, X. Huang, T. Wang and H. Hao, *Ind. Eng. Chem. Res.*, 2020, **59**, 13024–13032.

83 K. Allen, R. J. Davey, E. Ferrari, C. Towler, G. J. Tiddy, M. O. Jones and R. G. Pritchard, *Cryst. Growth Des.*, 2002, **2**, 523–527.

84 A. K. Tiwary, *Drug Dev. Ind. Pharm.*, 2001, **27**, 699–709.

85 J. Wang, W. Cao, L. Zhu, J. Wang and R. Lakerveld, *Chem. Eng Sci.*, 2020, **226**, 115861.

86 Y. Kawabata, K. Wada, M. Nakatani, S. Yamada and S. Onoue, *Int. J. Pharm.*, 2011, **420**, 1–10.

87 G. Ward, P. M. Martin-Soladana, P. Martin, R. Tona, N. Garg, N. Douillet and D. Lai, *Lab Chip*, 2020, **20**, 1815–1826.

88 S. R. Wilson-Whitford, R. W. Jaggers, B. W. Longbottom, M. K. Donald, G. J. Clarkson and S. A. F. Bon, *ACS Appl. Mater. Interfaces*, 2021, **13**, 5887–5894.

89 N. Hanikel, X. Pei, S. Chheda, H. Lyu, W. Jeong, J. Sauer, L. Gagliardi and O. M. Yaghi, *Science*, 2021, **459**, 454–459.

90 C. Lu, B. Maity, X. Peng, N. Ito, S. Abe, X. Sheng, T. Ueno and D. Lu, *Commun. Chem.*, 2022, **5**, 39.

91 P. Brunet, M. Simard and J. D. Wuest, *J. Am. Chem. Soc.*, 1997, **119**, 2737–2738.

92 M. Simard, D. Su and J. D. Wuest, *J. Am. Chem. Soc.*, 1991, **113**, 4696–4698.

93 J. C. MacDonald, P. C. Dorrestein, M. M. Pilley, M. M. Foote, J. L. Lundburg, R. W. Henning, A. J. Schultz and J. L. Manson, *J. Am. Chem. Soc.*, 2000, **122**, 11692–11702.

94 S. Ferlay, P. Dechambenoit, N. Kyritsakas and M. W. Hosseini, *Dalton Trans.*, 2013, **42**, 11661–11671.

95 J. K. Burdett and O. Eisenstein, *Inorg. Chem*, 1992, **31**, 1758–1762.

96 C. R. R. Adolf, S. Ferlay, N. Kyritsakas and M. W. Hosseini, *J. Am. Chem. Soc.*, 2015, **137**, 15390–15393.

97 H. J. Kim, J. H. Kim, J. S. Jeong, C. Y. Moon, S. Nahm, K. M. Nam, J. Park and Y. H. Kim, *Nano Lett.*, 2022, **22**, 3252–3259.

98 H. C. Zhou, J. R. Long and O. M. Yaghi, *Chem. Rev.*, 2012, **112**, 673–674.

99 X. Gao, T. Xu, Z. Jiang, H. Yu, Y. Wang and Y. He, *Dalton Trans.*, 2019, **48**, 16793–16799.

100 T. Zhou, S. Chen, X. Wang, C. Xie and D. Zeng, *ACS Appl. Mater. Interfaces*, 2020, **12**, 48948–48956.

101 P. C. Rao and S. Mandal, *Chem. Asian J.*, 2019, **14**, 4087–4102.

102 B. Liang, X. Zhang, Y. Xie, R. Lin, R. Krishna, H. Cui, Z. Li, Y. Shi, H. Wu, W. Zhou and B. Chen, *J. Am. Chem. Soc.*, 2020, **142**, 17795–17801.

103 C. T. Lollar, J. S. Qin, J. Pang, S. Yuan, B. Becker and H. C. Zhou, *Langmuir*, 2018, **34**, 13795–13807.

104 J. D. Evans, C. J. Sumby and C. J. Doonan, *Chem. Soc. Rev.*, 2014, 43, 5933–5951.

105 H. Li, M. Eddaoudi, M. O'Keeffe and O. M. Yaghi, *Nature*, 1999, **402**, 276–279.

106 F. Luo, C. Yan, L. Dang, R. Krishna, W. Zhou, H. Wu, X. Dong, Y. Han, T. L. Hu, M. O'Keeffe, L. Wang, M. Luo, R. B. Lin and B. Chen, *J. Am. Chem. Soc.*, 2016, **138**, 5678–5684.

107 A. F. Wells, *Three-Dimensional Nets and Polyhedra*, Wiley-Interscience, New York, 1977.

108 H. Furukawa, K. E. Cordova, M. O'Keeffe and O. M. Yaghi, *Science*, 2013, 341, 1230444.

109 H. O. Clo, O. M. Yaghi, H. Li, T. L. Groy and C. L. C. Mater, *Inorg. Chem.*, 1997, **5**, 4292–4293.

110 C. R. Groom, I. J. Bruno, M. P. Lightfoot and S. C. Ward, *Acta Crystallogr., Sect. B: Struct. Sci. Cryst. Eng. Mater.*, 2016, **72**, 171–179.

111 N. L. Rosi, J. Eckert, M. Eddaoudi, D. T. Vodak, J. Kim, M. O'Keeffe and O. M. Yaghi, *Science*, 2003, **300**, 1127–1129.

112 M. Eddaoudi, J. Kim, N. Rosi, D. Vodak, J. Wachter, M. O'Keeffe and O. M. Yaghi, *Science*, 2002, **295**, 469–472.

113 M. O'Keeffe, *Chem. Soc. Rev.*, 2009, **38**, 1215–1217.

114 H. Deng, S. Grunder, K. E. Cordova, C. Valente, H. Furukawa, M. Hmadeh, F. Gandara, A. C. Whalley, Z. Liu, S. Asahina, H. Kazumori, M. O'Keeffe, O. Terasaki, J. F. Stoddart and O. M. Yaghi, *Science*, 2012, **336**, 1018–1024.

115 E. Fernandez-Bartolome, J. Santos, S. Khodabakhshi, L. J. Mcormick, S. J. Teat, C. S. De Pipaon, J. R. Galan-Mascarós, N. Martín and J. Sanchez Costa, *Chem. Commun.*, 2018, **54**, 5526–5529.

116 M. A. Alnaqbi, A. Alzamly, S. H. Ahmed, M. Bakiro, J. Kegere and H. L. Nguyen, *J. Mater. Chem. A*, 2021, **9**, 3828–3854.

117 L. Zhao, Z. Pan, L. Cai, S. Wang, B. Lu, S. Lv, Y. Qiu and G. Wang, *Desalination*, 2024, **576**, 117360.

118 L. Robison, L. Zhang, R. J. Drout, P. Li, C. R. Haney, A. Brikha, H. Noh, B. L. Mehdi, N. D. Browning, V. P. Dravid, Q. Cui, T. Islamoglu and O. K. Farha, *ACS Appl. Bio Mater.*, 2019, **2**, 1197–1203.

119 D. Feng, Z. Y. Gu, J. R. Li, H. L. Jiang, Z. Wei and H. C. Zhou, *Angew. Chem. Int. Ed.*, 2012, **51**, 10307–10310.

120 K. C. Park, P. Kittikhunnatham, J. Lim, G. C. Thaggard, Y. Liu, C. R. Martin, G. A. Leith, D. J. Toler, A. T. Ta, N. Birkner, I. Lehman-Andino, A. Hernandez-Jimenez, G. Morrison, J. W. Amoroso, H. C. zur Loye, D. P. DiPrete, M. D. Smith, K. S. Brinkman, S. R. Phillpot and N. B. Shustova, *Angew. Chem. Int. Ed.*, 2023, **62**, e202216349.

121 T. Moeller, D. F. Martin, L. C. Thompson, R. Ferrús, G. R. Feistel and W. J. Randall, *Chem. Rev.*, 1965, **65**, 1–50.

122 M. Seitz, A. G. Oliver and K. N. Raymond, *J. Am. Chem. Soc.*, 2007, **129**, 11153–11160.

123 F. Saraci, V. Quezada-Novoa, P. R. Donnarumma and A. J. Howarth, *Chem. Soc. Rev.*, 2020, **49**, 7949–7977.

124 M. Safaei, M. M. Foroughi, N. Ebrahimpoor, S. Jahani, A. Omidi and M. Khatami, *TrAC - Trends Anal. Chem.*, 2019, **118**, 401–425.

125 D. J. Tranchemontagne, J. R. Hunt and O. M. Yaghi, *Tetrahedron*, 2008, **64**, 8553–8557.

126 H. Furukawa, Y. B. Go, N. Ko, Y. K. Park, F. J. Uribe-Romo, J. Kim, M. O'Keeffe and O. M. Yaghi, *Inorg. Chem.*, 2011, **50**, 9147–9152.

127 J. Han, X. He, J. Liu, R. Ming, M. Lin, H. Li, X. Zhou and H. Deng, *Chem*, 2022, **8**, 1637–1657.

128 H. Al-Kutubi, J. Gascon, E. J. R. Sudhölter and L. Rassaei, *ChemElectroChem*, 2015, **2**, 462–474.

129 P. Liu, T. Zhao, K. Cai, P. Chen, F. Liu and D. J. Tao, *Chem. Eng. J.*, 2022, **437**, 135364.

130 Z. Chen, P. Li, R. Anderson, X. Wang, X. Zhang, L. Robison, L. R. Redfern, S. Moribe, T. Islamoglu, D. A. Gómez-Gualdrón, T. Yildirim, J. F. Stoddart and O. K. Farha, *Science*, 2020, **368**, 297–303.

131 P. Anastas and N. Eghbali, *Chem. Soc. Rev.*, 2010, **39**, 301–312.

132 Z. Ajoyan, P. Marino and A. J. Howarth, *CrystEngComm*, 2018, **20**, 5899–5912.

133 L. Liu, Z.-P. Tao, H.-R. Chi, B. Wang, S.-M. Wang and Z. Han, *Dalton Trans.*, 2020, **50**, 39–58.

134 P. T. K. Nguyen, H. T. D. Nguyen, H. N. Nguyen, C. A. Trickett, Q. T. Ton, E. Gutiérrez-Puebla, M. A. Monge, K. E. Cordova and F. Gándara, *ACS Appl Mater Interfaces*, 2018, **10**, 733–744.

135 D. Y. Osadchii, A. I. Olivos-Suarez, Á. Szécsényi, G. Li, M. A. Nasalevich, I. A. Dugulan, P. S. Crespo, E. J. M. Hensen, S. L. Veber, M. V. Fedin, G. Sankar, E. A. Pidko and J. Gascon, *ACS Catal.*, 2018, **8**, 5542–5548.

136 M. S. Alqahtani, M. Kazi, M. A. Alsenaidy and M. Z. Ahmad, *Front. Pharmacol.*, 2021, 12, 618411.

137 S. He, L. Wu, X. Li, H. Sun, T. Xiong, J. Liu, C. Huang, H. Xu, H. Sun, W. Chen, R. Gref and J. Zhang, *Acta Pharm. Sin. B*, 2021, 11, 2362–2395.

138 H. D. Lawson, S. P. Walton and C. Chan, *ACS Appl. Mater. Interfaces*, 2021, **13**, 7004–7020.

139 P. Horcajada, C. Serre, G. Maurin, N. A. Ramsahye, F. Balas, M. Vallet-Regí, M. Sebban, F. Taulelle and G. Férey, *J. Am. Chem. Soc.*, 2008, **130**, 6774–6780.

140 K. Jiang, L. Zhang, Q. Hu, D. Zhao, T. Xia, W. Lin, Y. Yang, Y. Cui, Y. Yang and G. Qian, *J. Mater. Chem. B*, 2016, **4**, 6398–6401.

141 A. Terzopoulou, X. Wang, X. Z. Chen, M. Palacios-Corella, C. Pujante, J. Herrero-Martín, X. H. Qin, J. Sort, A. J. deMello, B. J. Nelson, J. Puigmartí-Luis and S. Pané, *Adv. Healthc. Mater.*, 2020, **9**, 2001031.

142 M. M. Mekonnen and A. Y. Hoekstra, *Sci. Adv.*, 2016, **2**, e1500323.

143 S. Kim, Hyunho, Yang, S. R. Rao, S. Narayanan, E. A. Kapustin, H. Furukawa, A. S. Umans, O. M. Yaghi and E. N. Wang, *Science*, 2017, **434**, 430–434.

144 S. M. Towsif Abtab, D. Alezi, P. M. Bhatt, A. Shkurenko, Y. Belmabkhout, H. Aggarwal, Ł. J. Weseliński, N. Alsadun, U. Samin, M. N. Hedhili and M. Eddaoudi, *Chem*, 2018, **4**, 94–105.

145 F. Fathieh, M. J. Kalmutzki, E. A. Kapustin, P. J. Waller, J. Yang and O. M. Yaghi, *Sci. Adv.*, 2018, **4**, 1–10.

146 W. Xu and O. M. Yaghi, *ACS Cent. Sci.*, 2020, **6**, 1348–1354.

147 A. Ragusa, A. Svelato, C. Santacroce, P. Catalano, V. Notarstefano, O. Carnevali, F. Papa, M. C. A. Rongioletti, F. Baiocco, S. Draghi, E. D'Amore, D. Rinaldo, M. Matta and E. Giorgini, *Environ. Int.*, 2021, **146**, 106274.

148 Y. J. Bae, E. S. Cho, F. Qiu, D. T. Sun, T. E. Williams, J. J. Urban and W. L. Queen, *ACS Appl. Mater. Interfaces*, 2016, **8**, 10098–10103.

149 J. Zhao, F. Wei, W. Xu and X. Han, *Appl. Surf. Sci.*, 2020, **510**, 145418.

150 Y. Kubota, M. Takata, R. Matsuda, R. Kitaura, S. Kitagawa, K. Kato, M. Sakata and T. C. Kobayashi, *Angew. Chem. Int. Ed.*, 2005, **44**, 920–923.

151 S. Takamizawa, E. I. Nataka, T. Akatsuka, R. Miyake, Y. Kakizaki, H. Takeuchi, G. Maruta and S. Takeda, *J. Am. Chem. Soc.*, 2010, **132**, 3783–3792.

152 T. Kihara and A. Koide, *Adv. Chem. Phys.*, 1975, **33**, 51.

153 R. Vaidhyanathan, S. S. Iremonger, G. K. H. Shimizu, P. G. Boyd, S. Alavi and T. K. Woo, *Science*, 2010, **330**, 650–653.

154 S. H. Chae, H. C. Kim, Y. S. Lee, S. Huh, S. J. Kim, Y. Kim and S. J. Lee, *Cryst. Growth Des.*, 2015, **15**, 268–277.

155 M. Guillermo, F. Rey and J. Vito, *J. Am. Chem. Soc.*, 2013, **135**, 15986–15989.

156 P. Liao, D. Zhou, A. Zhu, L. Jiang, R. Lin and J. Zhang, *J. Am. Chem. Soc.*, 2012, **134**, 17380–17383.

157 L. Kloo, H. Svensson and M. J. Taylor, *J. Chem. Soc., Dalton Trans.*, 2000, 1061–1065.

158 J. Su, S. Yuan, H. Wang, L. Huang, T. Cagin, J. Zuo, H. Zhou, J. Ge, E. Joseph and J. Qin, *Nat. Commun.*, 2017, **8**, 2008.

159 W. Kosaka, Z. Liu, J. Zhang, Y. Sato, A. Hori, R. Matsuda, S. Kitagawa and H. Miyasaka, *Nat. Commun.*, 2018, **9**, 5420.

160 J. Zhang, W. Kosaka, Y. Kitagawa and H. Miyasaka, *Nat. Chem.*, 2021, **13**, 191–199.

161 O. T. Qazvini, R. Babarao and S. G. Telfer, *Nat. Commun.*, 2021, **12**, 197.

162 J. Su, S. Yuan, T. Wang, C. T. Lollar, J. Zuo, J. Zhang and H. Zhou, *Chem. Sci.*, 2020, **11**, 1918–1925.

163 P. L. Urban, *New. J. Chem.*, 2014, **38**, 5135–5141.

164 D. Muñoz-Santiburcio and D. Marx, *Chem. Sci.*, 2017, **8**, 3444–3452.

165 A. Kato, M. Yanagisawa, Y. T. Sato, K. Fujiwara and K. Yoshikawa, *Sci. Rep.*, 2012, **2**, 283.

166 H. G. Hansma, *Origins Life Evol. Biospheres*, 2014, **44**, 307–311.

167 Y. Shichida and T. Matsuyama, *Philos. Trans. R. Soc., B*, 2009, 364, 2881–2895.

168 B. C. Tripp, K. Smith and J. G. Ferry, *J. Biol. Chem.*, 2001, **276**, 48615–48618.

169 A. B. Grommet, M. Feller and R. Klajn, *Nat. Nanotechnol.*, 2020, **15**, 256–271.

170 Q. Jiang and M. D. Ward, *Chem. Soc. Rev.*, 2014, **43**, 2066–2079.

171 Y. Lin, Y. L. Ying, R. Gao and Y. T. Long, *Chem. Eur. J.*, 2018, **24**, 13064–13071.

172 W. Reisner, J. N. Pedersen and R. H. Austin, *Rep. Prog. Phys.*, 2012, **75**, 106601.

173 S. Zhang, M. Sun, T. Hedtke, A. Deshmukh, X. Zhou, S. Weon, M. Elimelech and J. H. Kim, *Environ. Sci. Technol.*, 2020, **54**, 10868–10875.

174 Y. T. Xu, X. Xiao, Z. M. Ye, S. Zhao, R. Shen, C. T. He, J. P. Zhang, Y. Li and X. M. Chen, *J. Am. Chem. Soc.*, 2017, **139**, 5285–5288.

175 T. Y. Zhou, B. Auer, S. J. Lee and S. G. Telfer, *J. Am. Chem. Soc.*, 2019, **141**, 1577–1582.

176 A. A. Talin, A. Centrone, A. C. Ford, M. E. Foster, V. Stavila, P. Haney, R. A. Kinney, V. Szalai, F. El Gabaly, H. P. Yoon, F. Léonard and M. D. Allendorf, *Science (1979)*, 2014, **343**, 66–69.

177 N. E. Levinger, *Science*, 2002, **298**, 1722–1723.

178 J. E. Boyd, A. Briskman, C. M. Sayes, D. Mittleman and V. Colvin, *Journal of Physical Chemistry B*, 2002, **106**, 6346–6353.

179 H. J. G. E. Gardeniers, *Anal. Bioanal. Chem.*, 2009, **394**, 385–397.

180 H. X. Zhou, *Arch. Biochem. Biophys.*, 2008, **469**, 76–82.

181 M. Wang, Y. Hou, L. Yu and X. Hou, *Nano Lett.*, 2020, **20**, 6937–6946.

182 M. Alcoutlabi and G. B. Mckenna, *J. Phys: Condens. Matter*, 2005, **17**, R461–R524.

183 K. ichi Otake and H. Kitagawa, *Small*, 2021,**17**(22), 2006189.

184 J. Qian, X. Gao and B. Pan, *Environ. Sci. Technol.*, 2020, **54**, 8509–8526.

185 C. Kang and D. Kim, *Arch. Pharm. Res.*, 2020, **43**, 110–117.

186 G. Tabacchi, *ChemPhysChem*, 2018, **19**, 1249–1297.

187 C. Gao, F. Lyu and Y. Yin, *Chem Rev*, 2021, 121, 834–881.

188 V. Mody, R. Siwale, A. Singh and H. Mody, *J Pharm Bioallied Sci*, 2010, **2**, 282.

189 M. Zhang, M. Y. Efremov, F. Schiettekatte, E. A. Olson, A. T. Kwan, S. L. Lai, T. Wisleder, J. E. Greene and L. H. Allen, *Phys. Rev. B: Condens. Matter Mater. Phys.*, 2000, **62**, 10548–10557.

190 C. Lu, S. Zhou, F. Gao, J. Lin, J. Liu and J. Zheng, *TrAC, Trends Anal. Chem.*, 2022, **148**, 116533.

191 L. Chen, H. Chen, R. Luque and Y. Li, *Chem. Sci.*, 2014, **5**, 3708–3714.

192 B. An, J. Zhang, K. Cheng, P. Ji, C. Wang and W. Lin, *J. Am. Chem. Soc.*, 2017, **139**, 3834–3840.

193 F. R. Fortea-Pérez, M. Mon, J. Ferrando-Soria, M. Boronat, A. Leyva-Pérez, A. Corma, J. M. Herrera, D. Osadchii, J. Gascon, D. Armentano and E. Pardo, *Nat. Mater.*, 2017, **16**, 760–766.

194 A. J. Anciaux, A. Demonceau, A. F. Noels, A. J. Hubert, R. Warin and P. Teyssié, *J. Org. Chem.*, 1981, **46**, 873–876.

195 X. N. Wang, P. Zhang, A. Kirchon, J. L. Li, W. M. Chen, Y. M. Zhao, B. Li and H. C. Zhou, *J. Am. Chem. Soc.*, 2019, **141**, 13654–13663.

196 M. I. Gonzalez, A. B. Turkiewicz, L. E. Darago, J. Oktawiec, K. Bustillo, F. Grandjean, G. J. Long and J. R. Long, *Nature*, 2020, **577**, 64–68.

197 A. Bijelic, M. Aureliano and A. Rompel, *Angew. Chem. Int. Ed.*, 2019, **58**, 2980–2999.

198 M. Samaniyan, M. Mirzaei, R. Khajavian, H. Eshtiagh-Hosseini and C. Streb, *ACS Catal.*, 2019, **9**, 10174–10191.

199 Y. Lu, C. Yue, B. Liu, M. Zhang, Y. Li, W. Yang, Y. Lin, Y. Pan, D. Sun and Y. Liu, *Microporous Mesoporous Mater.*, 2021, **311**, 110694.

200 J. Liu, S. Heidrich, J. Liu, B. Guo, M. Zharnikov, U. Simon, W. Wenzel and C. Wöll, *ACS Appl. Nano Mater.*, 2021, **4**, 522–528.

201 A. E. Burakov, E. V Galunin, I. V Burakova, A. E. Kucherova, S. Agarwal, A. G. Tkachev and V. K. Gupta, *Ecotoxicol. Environ. Saf.*, 2018, **148**, 702–712.

202 K. Harsha, P. Senthil and R. C. Panda, *J. Mol. Liq.*, 2019, **290**, 111197.

203 K. Wu, J. Zheng, Y. Huang, D. Luo, Y. Y. Li, W. Lu and D. Li, *J. Mater. Chem. C*, 2020, **8**, 16974.

204 X. Lv, L. Shi, K. Li, B. Li and H. Li, *ChemComm*, 2017, **53**, 1860–1863.

205 H. Fu, Z. Xu and J. Zhang, *Chem. Mater.*, 2015, **27**, 205–210.

206 Y. Inokuma, S. Yoshioka, J. Ariyoshi, T. Arai, Y. Hitora, K. Takada, S. Matsunaga, K. Rissanen and M. Fujita, *Nature*, 2013, **495**, 461–466.

207 M. Hoshino, A. Khutia, H. Xing, Y. Inokuma and M. Fujita, *IUCrJ*, 2016, **3**, 139–151.

208 W. de Poel, P. Tinnemans, A. L. L. Duchateau, M. Honing, F. P. J. T. Rutjes, E. Vlieg and R. de Gelder, *Chem. - Eur. J.*, 2019, **25**, 14999–15003.

209 K. ichi Otake, K. Otsubo, T. Komatsu, S. Dekura, J. M. Taylor, R. Ikeda, K. Sugimoto, A. Fujiwara, C. P. Chou, A. W. Sakti, Y. Nishimura, H. Nakai and H. Kitagawa, *Nat. Commun.*, 2020, **11**, 843.

210 B. A, G. Hummer, J. C. Rasaiah and J. P. Noworyta, *Nature*, 2001, **414**, 188–190.

211 Y. Umena, K. Kawakami, J. Shen and N. Kamiya, *Nature*, 2011, 0–6.

212 H. Sui, B. Han, J. K. Lee, P. Walian and B. K. Jap, *Nature*, 2001, **414**, 872–878.

213 M. A. Rivero-crespo, M. Mon, J. Ferrando-soria, C. W. Lopes, M. Boronat, A. L. Ø, A. Corma, J. C. Hern, L. Miguel, J. J. Calvino, E. V Ramos-fernandez, D. Armentano and E. Pardo, *Angew. Chem. Int. Ed.*, 2018, **57**, 17094–17099.

Chapter 2 – Capturing Nuclei in Cluster Confining MOFs

2.1 Introduction

Owing to their crystallinity and porosity, metal organic frameworks (MOFs) have been employed in a confinement context as crystalline sponges, a method developed by Fujita and co-workers in 2013, as a way to determine the molecular structures of difficult-to-crystallize materials encapsulated inside the pores of MOF single crystals.[1,2] The method involves soaking a single crystal of a MOF inside a solution containing the desired guest which diffuses into the cavities of the framework.[3] Single crystal structure determination on the resulting MOF crystal subsequently results in the determination of the structure of the included guest molecule. Crystalline sponge methods, however, focus on molecular structure, rather than the crystal structure of aggregates of guest molecules. In the context of confinement of molecular aggregates, however, MOFs are potentially highly useful. First, they are capable of confining a wide range of compounds inside their tunable pores and secondly, they offer a way to crystallographically isolate and structurally characterise the shape, size and packing arrangement of encapsulated aggregates and compare their structural and physicochemical properties to the bulk. For instance, Long and co-workers have reported precise control over the shape and size of metal halide sheets grown in the pores of a bipyridine-based MOF.[4] Additionally, Eddaoudi and co-workers have reported a cluster of 114 water molecules in a cubic cage of a MOF.[5] Such large aggregates approach the size of critical nuclei. For example, a recent study of ice nucleation based on observing the crystallization temperatures of materials within microemulsions followed by measurement of the microemulsion droplet size suggests that the critical nucleus contains 70-210 water molecules radii of approximately 1.2-1.8 nm.[6] For molecular compounds the critical nucleus size can be significantly smaller, *e.g.* 5–50 for typical crystallization conditions of several proteins.[7]

This work aims to synthesise a crystalline MOF capable of entrapping molecular clusters of significant size. To create the required void space, the organic linker must be carefully selected as it, in part, controls the size and shape of the framework pores. Throughout the published history of MOFs, 1,4-benzenedicarboxylate (BDC) and its derivatives are one of the most widely reported linkers for MOF design and synthesis.[8,9] However, using BDC as an organic linker to construct MOFs commonly results in the formation of microporous frameworks containing voids too small to entrap clusters of molecules.[10–12] Therefore, this work focuses on the expanded derivative of BDC, 4,4'-biphenyldicarboxylic acid (H_2BPDC), which, as a longer linker can be used to synthesise MOFs with larger pores. Herein, the

synthesis, structure and guest cluster exchange properties of mesoporous lanthanoid Cluster Capture MOFs (CCM-1–4) able to capture meaningfully large clusters of small molecules is described. Additionally, the ability of the CCM-series MOFs to entrap arrays of molecular guests and undergo exchange of sub-critical nucleus-sized molecular clusters in the solid state will be demonstrated.

2.2 Synthesis of Metal-Organic Frameworks

Owing to their high coordination number, lanthanoids can yield novel MOF structures consisting diverse metal nodes and underlying net topologies.[13] While structure prediction becomes difficult with lanthanoids, they can potentially result in MOFs exhibiting larger pores than those based on transition metal SBUs. In 2008, a series of isomorphous lanthanide MOFs based on 4,4'-biphenyldicarboxylic acid (H_2BPDC) as the organic linker were reported by You and co-workers.[14] Among the lanthanides used to synthesise these MOFs were europium(III), samarium(III), lanthanum(III), cerium(III), gadolinium(III) and neodymium(III). Four years later, in 2012, the same neodymium-based MOF reported by You and co-workers (reference code AFOVOH in the Cambridge Structural Database) was also published by Łyszczek and Mazur (reference code WAYKAK).[15] Both AFOVOH and WAYKAK are isomorphous and only differ in the nature of the solvent that is coordinated to the metal centre. In AFOVOH and WAYKAK, formic acid and DMF, respectively, coordinate to the vacant coordination site on the neodymium(III) metal centre. In addition, a praseodymium(III)-based isomorphous framework was also synthesised by Sessler and co-workers in 2016.[16] As these MOFs contain well-defined mesopores, we aimed to synthesise these materials for use as crystalline confining matrices.

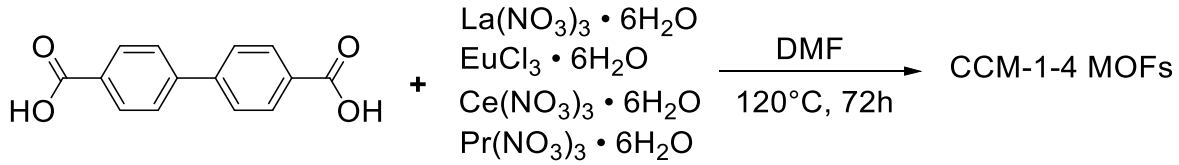

Scheme 2-1. General synthetic procedure for the preparation of CCM-1-4 MOFs.

The synthesis of the CCM-series MOFs was undertaken using the solvothermal method. A DMF solution containing a 1:1 ratio of lanthanum(III) nitrate hexahydrate and H_2BPDC metal-to-ligand was made up into a Teflon-lined acid digestion vessel, which was subsequently placed in an isothermal oven and heated at 120°C for 72 hours (**Scheme 2-1**) resulting in the crystallization of $La(BPDC)_{1.5}(DMF)_3$ (CCM-1, **Figure 2-26a**). Analogous reactions with europium(III) chloride hexahydrate, cerium(III) nitrate hexahydrate and praseodymium(III)

nitrate hexahydrate resulted in isomorphous MOFs with formulae $Eu(BPDC)_{1.5}(DMF)_3$, $Ce(BPDC)_{1.5}(DMF)_3$ and $Pr(BPDC)_{1.5}(DMF)_3$ (CCM-2-4, **Figure 2-26b**–**d**, respectively). The synthesis of CCM-1 MOF was performed with trifluoroacetic acid (TFA) as a modulator.[17] In general, modulators used in MOF syntheses are monocarboxylic acids. *In situ* synchrotron diffraction studies have shown that the role of modulators is to compete for the coordination sites of the metal centres in MOFs which consequently aids in the nucleation and crystal growth processes as the modulators are replaced with organic linkers.[18,19] The as-synthesised crystals were characterised with single crystal X-ray diffraction (SC-XRD), powder X-ray diffraction (PXRD), FT-IR spectroscopy, elemental analysis, thermogravimetric analysis (TGA) and solution-state NMR spectroscopy. Specific details regarding the synthesis of these MOFs can be found in the experimental details (Section 2.6).

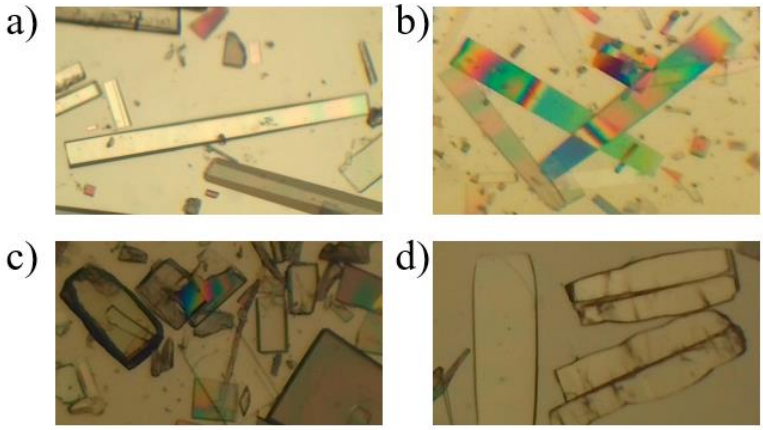

Figure 2-26. Images of single crystals of a) CCM-1, b) CCM-2, c) CCM-3 and d) CCM-4. Images taken using a polarising microscope.

2.3 Characterisation of MOFs

2.3.1 Non-Crystallographic Characterisation Methods

Figure 2-27 shows the IR spectra of MOFs CCM-1–4, along with the spectrum of the organic linker H_2BPDC. In each of the CCM-series MOFs, the broad band corresponding to the O–H stretching of the carboxylic acid (3055–2547 cm^{-1}, purple trace) has disappeared indicating the deprotonation of the carboxylic acid as a result of coordination to the lanthanoid metal centre. The C–H stretching (2929 and 2864 cm^{-1} shown for CCM-1) of the DMF molecules inside the pores of the MOFs appears for all CCM-series MOFs. Additionally, the band at 1669 cm^{-1} corresponding to the asymmetric C=O stretching of the H_2BPDC linker is replaced with a wider band centred at 1654 cm^{-1} corresponding to both coordinated and non-coordinated DMF molecules inside the pores of the frameworks.[20]

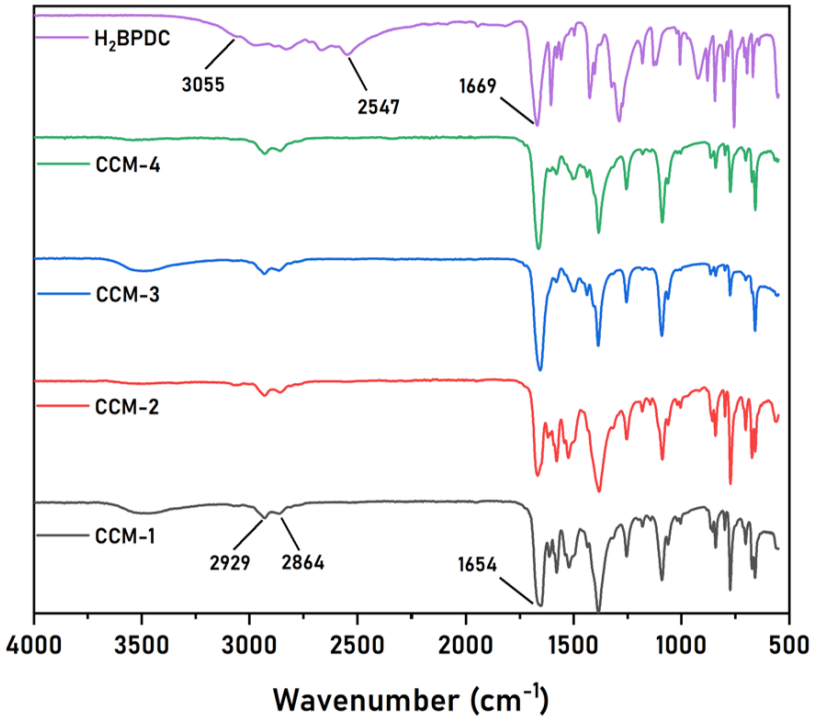

Figure 2-27. FT-IR spectra of the as-synthesised MOFs and the organic linker H_2BPDC. Bands indicated at 2864 and 2929 cm^{-1} are indicative of the DMF C–H stretching. In the purple spectrum of the H_2BPDC organic linker, the band at 1669 cm^{-1} is indicative of the asymmetric C=O stretching while the bands at 2547 and 3055 cm^{-1} encapsulate the wide band corresponding to the carboxylic acid OH stretching.

Figure 2-28a shows the experimental and simulated PXRD traces of the as-synthesised MOFs. Good agreement in the 2θ angles, especially between 6–8°, indicates that the unit cells of these frameworks are very similar. The similarities in the experimental powder patterns of CCM-1–4 MOFs indicates that they possess very similar unit cells and are likely isomorphous. Additionally, very good agreement between the simulated and experimental traces also indicates high bulk purity. There are, however, slight differences in the low angle peaks between the simulated and experimental PXRD patterns of the CCM-MOFs. This is a result of the plank-shaped morphology of the crystals which are known to exhibit preferred orientation. In this case, the morphology of the plank-shaped crystals results in the reflections along the crystallographic [100] direction to be intensified and those in the [001] direction diminished. TGA was also performed on all as-synthesised MOFs. **Figure 2-28b** shows four TGA traces of the CCM-series frameworks. The traces collected under N_2 atmosphere reveal that a varying amount solvent resides in the pores of each MOF. CCM-4 exhibits the largest amount of solvent loss at roughly 40% while CCM-3 exhibits a 10% weight loss corresponding to the solvent molecules. The encapsulated DMF molecules in CCM-4 make up 31% of the total weight of

the material, thus indicating there was surface DMF present in this sample. On the other hand, the 10% weight loss in CCM-3 is equivalent to the loss of one DMF molecule per asymmetric unit. Each framework is stable up to 400°C with CCM-4 exhibiting the highest framework stability. Based on the TGA results the framework stability can be ranked from lowest to highest as follows: CCM-3, CCM-2, CCM-1 and CCM-4. All of the frameworks fully decompose by 600°C, in good agreement with the values reported in the literature.[14] The weakest thermal stability of the europium-based MOF CCM-2 also corroborates well with another recent work by Howarth and co-workers.[21] The authors studied how the nature of rare earth metal in rare-earth-based-UiO-66 MOFs (RE-UiO-66) affects the structural parameters and thermal stability and found that the europium(III)-based RE-UiO-66 exhibits the lowest thermal stability. Unfortunately, lanthanum(III)- and cerium(III)-based RE-UiO-66 MOFs were not discussed.

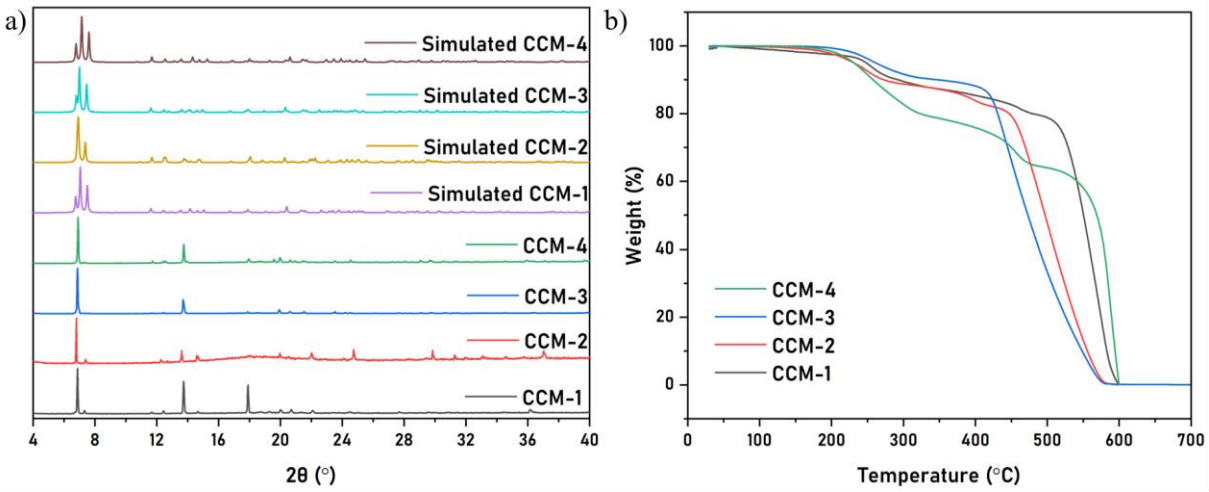

Figure 2-28. a) Experimental and simulated PXRD traces of MOFs CCM-1–4. b) TGA traces of CCM-1 (black line), CCM-2, (red line), CCM-3 (blue line) and CCM-4 (green line) measured between room temperature and 700°C under N_2 atmosphere.

Solution-state ^{1}H NMR spectroscopy was also employed to further characterise CCM-1–4 MOFs (**Figure 2-29**). Acid digestion was used to ensure the dissolution of MOFs in the d_6-DMSO solvent. This was performed by adding one drop of concentrated hydrochloric acid to the mixture of MOF single crystals in d_6-DMSO. The presence of signals attributed to the aromatic ring CH protons of the $BPDC^{2-}$ linker in the range of 7.82–7.86 and 8.00–8.04 ppm in each spectrum further indicates the successful formation of MOFs. Finally, elemental analysis was performed on MOF crystals that were dried in a 70°C isothermal oven overnight. Good agreement between the expected and experimental elemental compositions, as reported in **Section 2.6.2**, suggests the desired MOFs with good bulk purity were prepared.

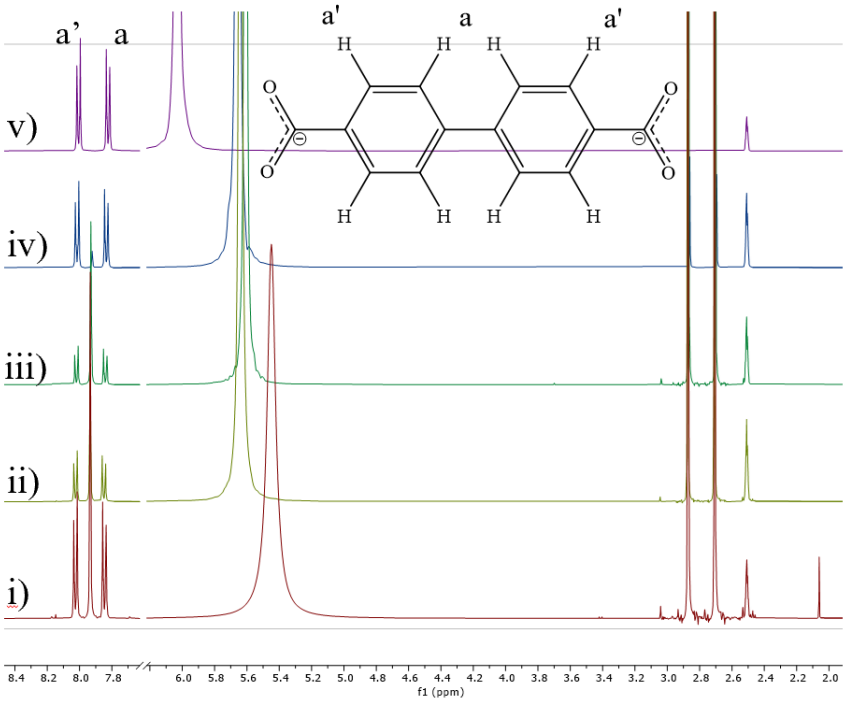

Figure 2-29. Solution state ^{1}H NMR spectra of i) H_2BPDC, ii) CCM-1, iii) CCM-2, iv) CCM-3 and v) CCM-4. The linker (5 mg) was dissolved in d_6-DMSO (0.7 mL) by heating the mixture. The CCM-MOF crystals (5mg) were dissolved in d_6-DMSO (0.7 mL) by adding one drop of concentrated HCl to the mixture. The spectra show the location of the aromatic ring hydrogen atoms of the H_2BPDC linker. Additional solvent residual peaks are also present at lower chemical shifts. The resonances in the range of 2.0–3.0 ppm are attributed to DMF and solvent residual peaks.

2.3.2 Single Crystal X-Ray Diffraction Analysis

Low-temperature (120 K) SC-XRD analysis reveals that the single crystals obtained from the reaction with lanthanum(III) nitrate hexahydrate comprise the expected mesoporous lanthanum MOF CCM-1. The product crystallizes in the Sohncke space group *C*2 implying a chiral packing arrangement despite the achiral nature of the components, making it a potentially attractive MOF for enantioselective applications.[22] **Figure 2-30a** shows the structure of CCM-1 along the crystallographic *c* axis. The framework consists of lanthanum(III) metal centres octa-coordinated in a square antiprismatic coordination geometry to six BPDC ligands and one DMF solvent molecule. The secondary building units (SBUs) form metal nodes connected to each other in a zig-zag chain, a common phenomenon for rare-earth metal-organic frameworks assembled by carboxylic acid organic linkers.[13,23] This type of metal node connectivity results in two different cross-sections of the pores in CCM-1. The void volume, using a probe radius of 1.2 Å, of CCM-1 is 1608 Å^3 (51.1% of the unit cell).

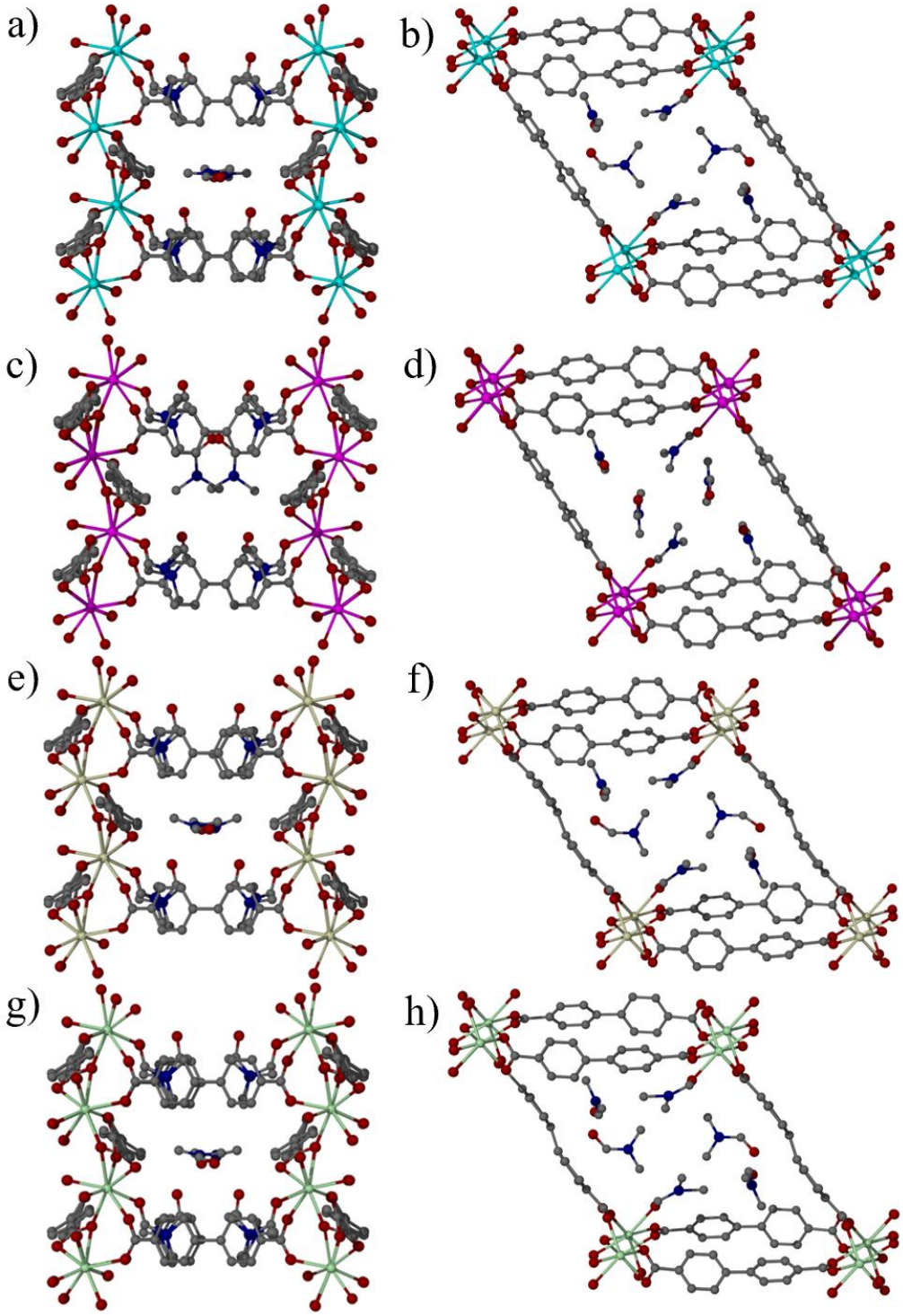

Figure 2-30. SC-XRD structures from up to down: CCM-1, CCM-2, CCM-3 and CCM-4. Top and bottom rows depict the crystallographic *c* and *b* axes, respectively. Grey: C. Blue: N. Red: O. Light blue: La. Pink: Eu. Beige: Ce. Light green: Pr. Hydrogen atoms omitted for clarity.

The solvothermal reaction using europium(III) chloride hexahydrate as the metal source yields rod-shaped transparent single crystals which emitted a pinkish luminescence under UV light, distinctive to europium-based materials.[24] SC-XRD analysis reveals a material with an

isomorphous framework to CCM-1, with a formula $Eu(BPDC)_{1.5}(DMF)_3$, termed CCM-2, **Figure 2-30 c** and **d**. As expected, the coordination bond lengths in CCM-2 are shorter than those in CCM-1 due to a smaller ionic radius of europium(III).[25] The coordination bond lengths range from 2.416(4)–2.710(4) Å and 2.322(4)–2.647(4) Å for CCM-1 and CCM-2, respectively. Topologically, CCM-2 exhibits identical rod-shaped connectivity of metal centres (**Figure 2-30c**) and as a result the pore cross section of CCM-2 is similar to those of CCM-1 (**Table 2-1**). **Figure 2-31** shows how the cross-sectional distances were measured. To start with, the metal centres coloured in green are parallel with each other and the distance of the metal centre across the pore was measured and reported in **Table 2-1** for each of the CCM-1–4 MOF. This was repeated with the metal centres coloured orange, resulting in two cross-sectional values for each MOF. Even though the MOF frameworks exhibit nearly identical structures, the packing of DMF molecular clusters in CCM-1 and CCM-2 differs slightly. Inside the pores of both CCM-1 and CCM-2, DMF forms hexamers in 4–2–4–2 repeating layers. In CCM-1, DMF dimers are orientated in a perpendicular fashion to the tetramers, *i.e.* along the *c* axis pore (**Figure 2-30 a** and **b**). However, in CCM-2 the solvent dimers are disordered and can be modelled to point along the *b* axis pore or perpendicularly to the tetramer. In this case, the former is shown as this way the encapsulated DMF molecules form a more discrete hexamer as compared to the DMF cluster in CCM-1. You and co-workers report only one DMF molecule per asymmetric unit for every reported MOF, suggesting that the other DMF molecules were too severely disordered for accurate crystallographic determination.[14] On the other hand, Sessler and co-workers were able to crystallographically determine the tetramers similar to those in CCM-1–4 MOFs while the dimers were not modelled, likely due to the severe disorder.[16]

Table 2-1. Cross-sectional pore sizes of CCM-1–4 MOFs.

MOF	Pore size (Å)
CCM-1	15.0 × 26.4 and 12.4 × 26.0
CCM-2	15.3 ×26.1 and 12.9 × 25.5
CCM-3	15.1 × 26.3 and 12.6 × 25.9
CCM-4	14.8 × 26.4 and 12.2 × 26.0

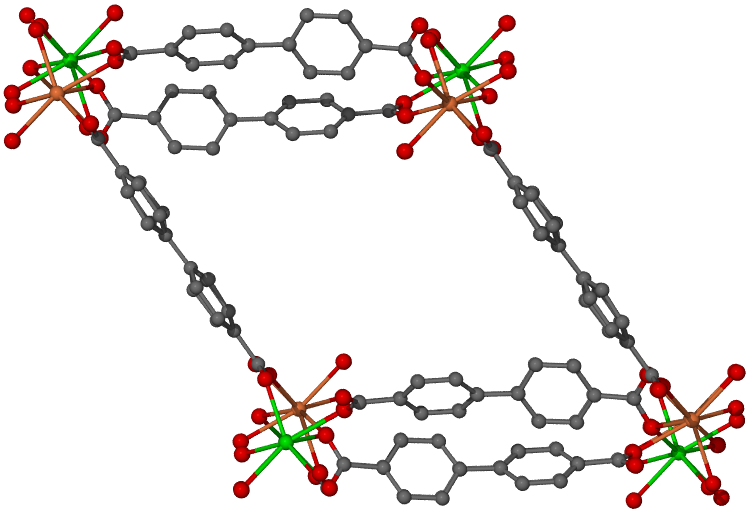

Figure 2-31. Image of the pore of a CCM-series MOF. Green-coloured lanthanum(III) metal centres indicate the metal centres used to measure one cross-section and orange-coloured metal centres were used to calculate the second cross-section.

The reaction containing cerium(III) nitrate hexahydrate as the metal source yields green plank-shaped single crystals. SC-XRD analysis reveals another isomorphous framework to those of CCM-1 and CCM-2, with a formula $Ce(BPDC)_{1.5}(DMF)_3$, termed CCM-3 and shown in **Figure 2-30 e** and **f**. The coordination bond lengths in CCM-3 range from 2.386(6)–2.684(5) Å. As expected, this range in coordination bond length is in between those determined in CCM-1 and CCM-2 as the ionic radius of cerium(III) is in between that of lanthanum(III) and europium(III).[25] The pore size of CCM-3 is 15.1 × 26.3 Å and 12.6 × 25.9 Å, also similar to that of CCM-1 and CCM-2. However, the main difference in the frameworks is the orientation of the $BPDC^{2-}$ linkers. In CCM-3, the linkers are slightly bent as opposed to being relatively directly aligned between the metal centres as they are in CCM-1 and CCM-2. This indicates that the CCM-series MOFs are capable of exhibiting some structural flexibility which can aid in encapsulating guest molecules with different geometries. The solvent DMF molecules in CCM-3 are orientated in a very similar way to those in CCM-1. Along the crystallographic *b* axis (**Figure 2-30 b** and **f**) the DMF clusters seem to be identical. However, as shown in **Figure 2-30e**, two of the amide methyl groups are slightly tilted in CCM-3 while they remain planar in CCM-1 (**Figure 2-30a**). It is difficult to ascertain the reason why these methyl groups are tilted as there are no apparent intermolecular interactions between these methyl groups and the nearby DMF molecules or the framework moieties.

Finally, dark green single crystals of a praseodymium(III)-based MOF were obtained from a solvothermal synthesis containing H_2BPDC and praseodymium(III) nitrate hexahydrate

in a 1:1 ratio in DMF. This MOF has been previously synthesised by Sessler and co-workers using a similar solvothermal method.[16] However, guest exchange studies were not performed on the framework. **Figure 2-30g** and **h** show the crystal structure of the praseodymium(III)-based MOF, termed CCM-4, along the crystallographic *c* and *b* axes, respectively. The asymmetric unit of CCM-4 has a formula of $Pr(BPDC)_{1.5}(DMF)_3$ and also exhibits the slightly bent conformation of the $BPDC^{2-}$ ligands such as CCM-3. The coordination bond length in CCM-4 ranges from 2.373(4)–2.703(4) Å. Thus, within the CCM-series MOFs, the shortest coordination bond length is in CCM-2, followed by CCM-4, CCM-3 and CCM-1. The pore size of CCM-4 is 14.8 × 26.4 Å and 12.2 × 26.0 Å. The solvent DMF molecules inside the pores of CCM-4 are orientated in a very similar way to those in CCM-3 with the main difference being that the amide methyl groups are more planar than those in CCM-3. Overall, single crystal structure analysis shows the successful formation of four lanthanoid MOFs with significant pore size.

2.3.3 Topological Analysis of CCM-1

As revealed by powder and single crystal X-ray diffraction, compounds CCM-1–4 possess essentially identical three-dimensional frameworks. Therefore, the analysis of CCM-1 will be taken as an example to describe the topology of all as-synthesised MOFs. The topological analysis was undertaken using the software ToposPro.[26] The CCM-series MOF topologies were assessed using both the standard and point of extension methods.[27] In the standard method, each organic linker and metal atom is treated as a separate node. On the other hand, the point of extension method treats a metal cluster as a node and the points of connection to the organic linker as separate nodes. For instance, for the organic linker H_2BPDC, these points of connection are the two carboxylate carbon atoms. For the topological analysis, all hydrogen and solvent atoms were removed from the single crystal structure. All details regarding the processing and analysis of the single crystal structures to determine the underlying nets are described under the general experimental **Section 2.6**.

Using the standard method, the topological analysis yields the underlying net **fsy**, shown in **Figure 2-32a** along the crystallographic (001) direction. In this case, the underlying network belongs to the *Cmmm* space group which means it is achiral. This is different from the space group assigned to all of the CCM-series MOFs, which belong to the *C*2 space group and are chiral. This difference arises from the way molecules are arranged in the framework structure since the underlying net does not describe the molecular packing but rather its connectivity.

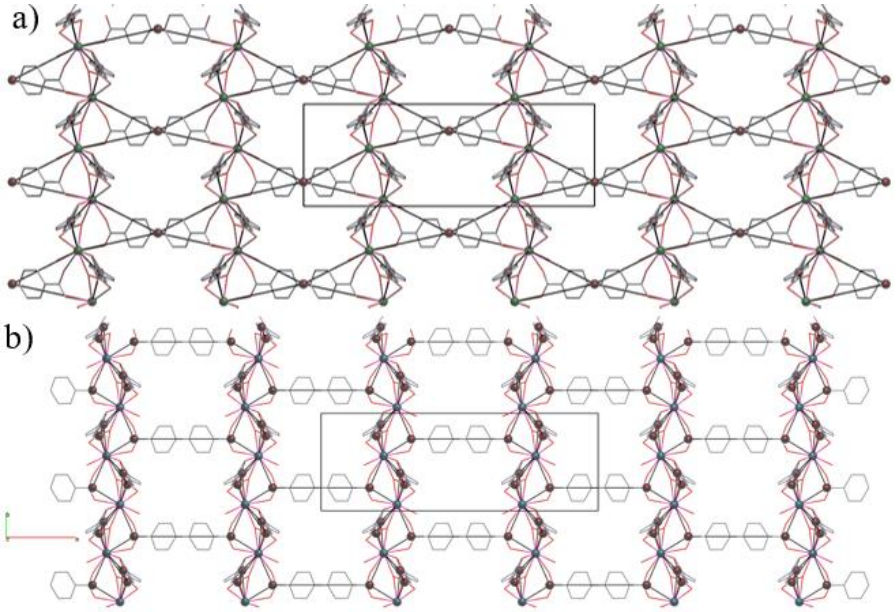

Figure 2-32. The topology of CCM-1 overlaid with the single crystal structure using the a) standard method showing the **fsy** net and b) point of extension method showing the **tsy** net. Unit cell and crystallographic directions are also depicted. The single crystal structure is depicted as wireframe while the topological connectivity is depicted in the ball and stick models. Grey: C. Red: O. Pink: La. Brown ball: Ligand node. Green ball: Metal node in **fsy**. Blue ball: Metal node in **tsy**.

Employing the point of extension method, the topological analysis yields the **tsy** underlying net which is a 3-nodal and 4^2,6-coordinated net, shown in **Figure 2-32b**. This topology also belongs to the *Cmmm* space group and is related to the **fsy** net. The advantage of using the point of extension method is that it is generally used for the analysis of rod-like metal-organic frameworks and can be more efficiently used to find isomorphous structures. As opposed to the standard method where the organic ligand is made into one four-connected (4-c) node, the point of extension simplifies the organic ligand into two 3-c nodes. Additionally, the SBUs are simplified into nodes that show the coordination to the carboxylates of the $BPDC^{2-}$ ligand. This results in a simpler and more accurate depiction of the underlying topology. There are 99 records in the CSD structural database that exhibit the **fsy** topology and when all are analysed on ToposPro, they yield 190 cluster depictions, *i.e.* 190 ways to they can be arranged using the **fsy** topology, meaning there are 190 underlying topologies describing these 99 records. Out of these 190, 86 can be described using the **tsy** topology. This does not mean that there are 86 lanthanum rod-MOFs that are isostructural to CCM-1. Rather, there are 86 structures that are potentially chemically different from the CCM-series MOFs but their underlying nets are isomorphous with one another.

In order to find all isostructural rod-like MOFs the 86 resulting structures were filtered by space group. More specifically, all results in the *C*2 space group of the CCM-series MOFs were extracted. Out of the 86 hits, eight are in *C*2 and have been reported in three articles.[14–16] Crucially, this method of analysing topologies and subsequently finding isomorphous materials is seemingly more powerful than doing a simple unit cell search on the CSD. When a search query using the unit cell parameters of CCM-1 is undertaken using the CSD structural database, only three results are obtained: AFOVAT, QOQPIW and WAYKAK. Of these, only AFOVAT and WAYKAK are isomorphous MOFs to those of CCM-series frameworks while QOQPIW is a diimine molecule unrelated to MOFs.[28] Thus, based on the CSD query there appear to be only two isostructural materials to the CCM-series MOFs.

2.4 Analysis of Guests in MOFs

2.4.1 Solvent Clusters in CCM-Series MOFs

The capability of analysing single crystal structures of guest molecules inside the CCM-series MOFs can lead to insights into how packing arrangement of materials changes when removed from conventional crystallization conditions. In the crystal structure of CCM-1, no formyl hydrogen atoms participate in hydrogen bonding with either the framework or solvent molecules. In CCM-2, the encapsulated DMF molecules participate in hydrogen bonding with the MOF framework. In particular, a C···O distance of 3.373(6) Å between a DMF and the framework is observed, while the same oxygen atom also partakes in another weak intermolecular hydrogen bond interaction, 3.387(13) Å, with a neighbouring DMF methyl hydrogen atom (**Figure 2-31a, red dashed line)**.

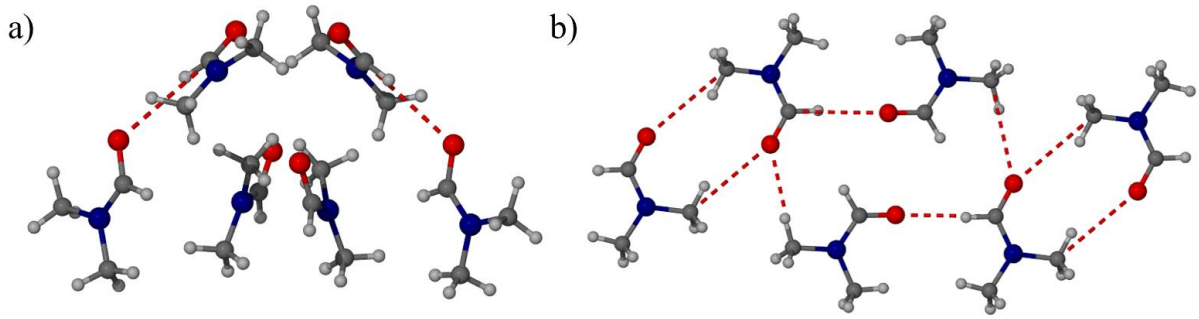

Figure 2-33. Single crystal structures showing hydrogen bond interactions between DMF molecules in a) bulk DMF and b) CCM-2. Hydrogen bonds are shown in red dashed lines. Gray: C. Red: O. Blue: N. White: H.

Bulk DMF is known to crystallize in one polymorphic form containing dimeric and tetrameric hydrogen bonded cyclamers, shown in **Figure 2-33b**.[29] One of two formyl hydrogen

atoms is involved in hydrogen bonding with the oxygen atom of the formyl C=O while other hydrogen bonding interactions form between the methyl hydrogen atoms and the two formyl C=O moieties. The single crystal structures of CCM-1 and CCM-2 show that the asymmetric unit of each MOF contains three symmetry-independent DMF molecules which make up groups of hexamers along the cavity of the pore. These hexamers can be also observed in **Figure 2-30 b** and **d**. In fact, in each of the CCM-series MOFs these hexamers can be observed while the crystal structure of bulk DMF (reference code KAQPUN in the CCDC repository) consists of dimers that also form hexamers.[29,30] Overall, DMF encapsulated in CCM MOFs does not form any hydrogen bonded clusters in contrast to the bulk behaviour. This could be due to the weak nature of the DMF intermolecular hydrogen bonds which are not strong enough to add directionality to the encapsulated DMF clusters.

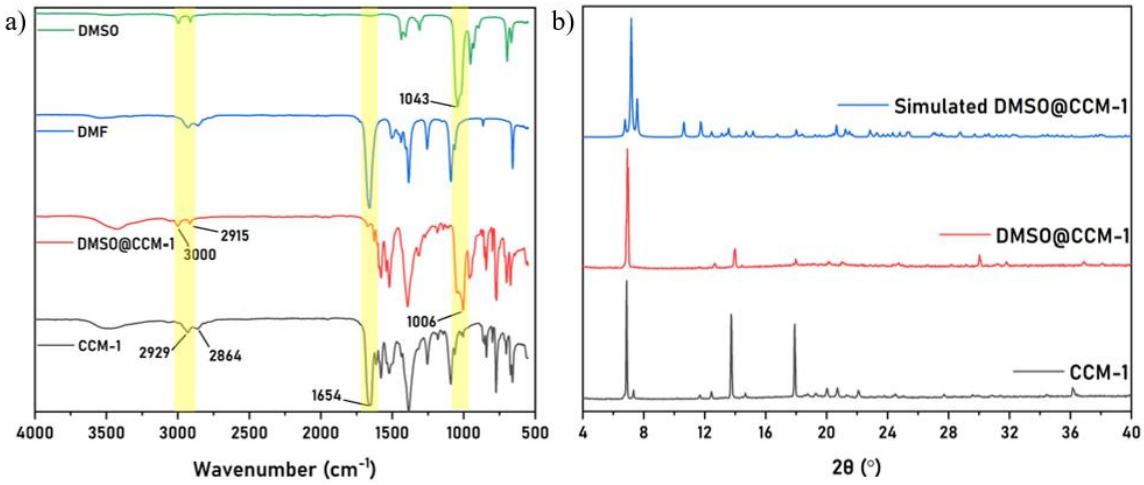

Figure 2-34. a) IR spectra of CCM-1, DMSO@CCM-1, pure DMF and pure DMSO. b) PXRD patterns of CCM-1 (as-synthesised DMF solvate), DMSO@CCM-1 and the simulated PXRD pattern of DMSO@CCM-1 from the single crystal structure. Yellow shading on the IR spectra illustrates the difference in specific bands.

MOFs are widely used to encapsulate a variety of molecules, from small organics to metals, gases and enzymes.[30–33] This is generally achieved in two ways. The solvent molecules can be evacuated from the pores of the as-synthesized MOFs and the resulting empty framework exposed to the guest molecules in the vapour or liquid phase. This method is used for water harvesting, for example.[34] Alternatively, the material can undergo direct guest exchange by exposure to the target guest.[35,36] The first method generally results in the MOF materials losing crystallinity during the solvent evacuation phase. As CCM-1 behaves in this manner, we tested the direct guest exchange capabilities of this material initially with small molecule solvents as target guests. Single crystals of CCM-1 were soaked in a range of potential

guest solvents at room temperature. Within 24 hours crystallinity is lost or the CCM-1 crystals become cracked in most solvents, with the exception of DMSO. The FT-IR spectrum of the crystals soaked in DMSO (DMSO@CCM-1, **Figure 2-34a**) for 24 hours indicates that DMF is exchanged with the new solvent. Notably, the band corresponding to the DMF C=O stretching (1654 cm^{-1}) almost disappears after 24 hours of soaking in DMSO. Instead, a strong band centred at 1006 cm^{-1} appears, corresponding to the S=O stretching of coordinated DMSO molecules.[37] Neat DMSO exhibits the S=O stretching at 1043 cm^{-1}, which manifests itself on the spectrum as a shoulder to the 1006 cm^{-1} band implying the presence of both metal-coordinated and free DMSO within the exchanged crystal. Additionally, the C–H stretching corresponding to the DMSO methyl groups appear at 3000 and 2915 cm^{-1} while those of DMF disappear. The material maintains a high degree of crystallinity after guest exchange as seen on **Figure 2-34b** (red trace). Additionally, the powder pattern of DMSO@CCM-1 is nearly identical to that of CCM-1 (**Figure 2-34b**, black trace) indicating that the framework does not undergo any significant structural changes upon the guest exchange. The simulated powder pattern of DMSO@CCM-1 exhibits additional peaks which are not observed in the experimentally obtained pattern due to preferred orientation. This leads to the reflections along the [*001*] axis diminishing in the experimentally obtained pattern, as also observed for the as-synthesised CCM-1–4 MOFs.

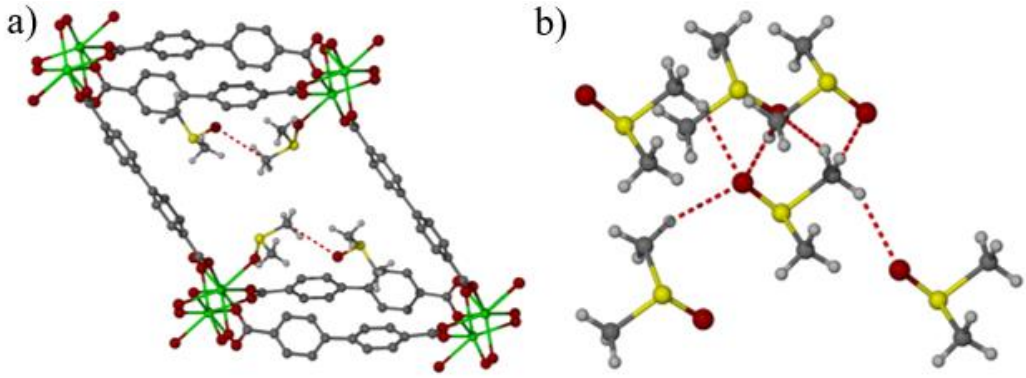

Figure 2-35. Single crystal structures of a) DMSO@CCM-1 along the *b* axis and b) hydrogen bonding in bulk DMSO.[38] Grey: C. Red: O. Yellow: S. White: H. Hydrogen atoms of the CCM-1 framework omitted for clarity.

SC-XRD analysis of DMSO@CCM-1 reveals the CCM-1 framework with encapsulated DMSO molecules yielding a structure with the formula $La(BPDC)_{1.5}(DMSO)_2$. **Figure 2-35a** shows the view along the crystallographic *b* axis of DMSO@CCM-1. Unlike the as-synthesised CCM-1, DMSO@CCM-1 contains two coordinated and two non-coordinated DMSO molecules inside the rhombic pores. While DMSO is ambivalent, it coordinates to the La^{3+}

metal centre *via* the oxygen atom of the S=O moiety. Lanthanum cations are hard acids and DMSO is known to coordinate to hard acids through the oxygen atoms and soft acids through the sulfur atom.[39,40] Two of the four DMSO molecules along the *c* axis were severely disordered and as a result were masked using the SQUEEZE tool. **Figure 2-35b** shows the tetramers of DMSO molecules inside CCM-1 pores. Similarly to the DMF structure, the oxygen atoms of DMSO point along the pore direction. Overall, successful exchange of DMF with DMSO proves that CCM-1 is capable of guest exchange.

The bulk DMSO crystal structure was first solved in 1966 but was redetermined more precisely at 100 K in 2017 by Reuter.[38,41] In the bulk, each DMSO molecule engages in four C–H···O hydrogen bonds ranging from 3.33–3.46 Å in C···O distance (**Figure 2-35b**). The molecules pack in a tube-like arrangement along the crystallographic *b* axis. This is significantly different from the packing of DMSO molecules inside CCM-1 which are arranged in a channel along the *b* axis. One hydrogen bond (C–H···O) between the methyl hydrogen atom of a coordinated DMSO and the oxygen atom of a non-coordinated has a C···O distance of 3.249(1) Å. There is a symmetry equivalent hydrogen bonding interaction inside the pore between the second pair of coordinated and non-coordinated DMSO molecules, resulting in two hydrogen bond interactions per pore. However, a hydrogen bonded tetramer does not form between these DMSO molecules. Further analysis of DMSO@CCM-1 is not possible due to high disorder. As with DMF, the structure of included DMSO suggests an alternative packing arrangement to the bulk DMSO structure and hence gives insight into potential alternative DMSO polymorphs.

2.4.2 Partially Exchanged Guest Clusters

The capability of CCM-1–4 MOFs to undergo guest exchange as a single-crystal-to-single-crystal transition (SCSCT) was tested with a variety of non-solvent liquid guests, as detailed in **Table 2-2**. The crystal quality of the immersed MOFs was first inspected visually for the first 24 hours under a polarising microscope. If a crystal did not exhibit cracking or pseudomorphosis, it was taken out of the guest liquid for FT-IR spectroscopy analysis, exemplified by the PMD@CCM-1 crystals shown in **Figure 2-36 a** and **b**. If the FT-IR spectroscopy analysis indicated the occurrence of guest exchange, the crystals were subsequently taken for SC-XRD analysis. However, most crystals display cracking (**Figure 2-36 c** and **d**) within a few hours without showing full or even partial exchange. Finally, longer soaking times result in loss of crystallinity. For instance, single crystals of CCM-1 soaked in PYZ for 48 hours exhibit cracking and are not suitable for single crystal analysis. **Figure 2-36e**

shows PYZ@CCM-1 single crystals after 48 hours of soaking and the resulting diffraction pattern exhibiting poor low angle scattering and twinning.

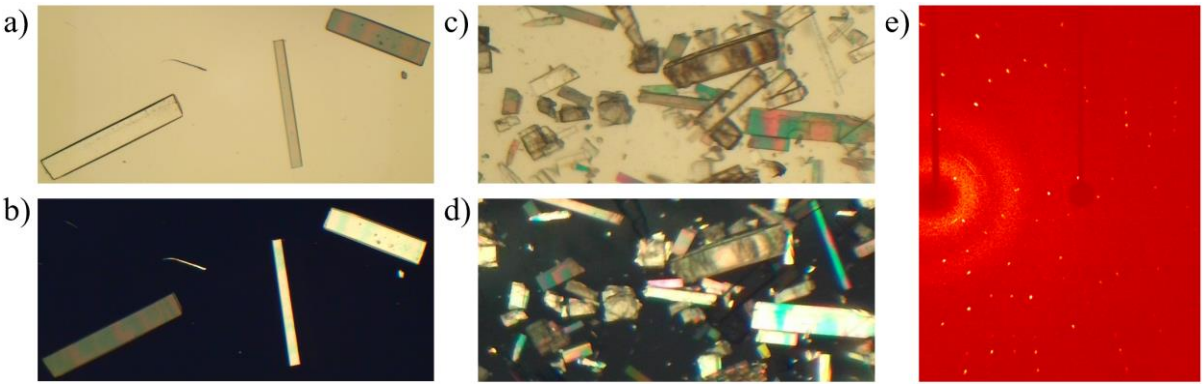

Figure 2-36. Images of single crystals of a) and b) PMD@CCM-1 and c) and d) 4-picoline@CCM-1. Images taken using a polarising microscope. e) The diffraction pattern of PYZ@CCM-1 crystals exhibiting twinning and poor low angle scattering.

For MOF crystals immersed in 1-ethylpyrazole (EtPyz@CCM-1), 2,3-dihydrofuran (DHF@CCM-2), pyrimidine (PMD@CCM-2), 2-pyrrolidinone (2-PDN@CCM-2), 3-aminopyrazole (AmPyz@CCM-2), SC-XRD confirmed only partial exchange for all guest molecules, supported by FT-IR (**Figure 2-37a**) and NMR spectroscopy analysis (**Figure 2-49-27**). The high degree of crystallinity that is retained after soaking the MOF crystals in each of these guests is shown in **Figure 2-37b**. Small changes in the peak positions of the XRD patterns are due to the small changes that the MOF undergoes to accommodate guest molecules inside the pores. The stoichiometric ratio as revealed by SC-XRD for each material is $La(BPDC)_{1.5}(EtPyz)_1(DMF)_1$ $Eu(BPDC)_{1.5}(DHF)_2(DMF)_1$, $Eu(H_2BPDC)_{1.5}(PMD)_2(DMF)_1$, $Eu(H_2BPDC)_{1.5}(2\text{-}PDN)_{0.63}\text{-}(DMF)_{1.37,}$ and $Eu(BPDC)_{1.5}(3\text{-}AmPyz)_3$, respectively. These stoichiometric ratios include masked solvent molecules that are not shown in single crystal structures herein because of severe disorder. In the case of EtPyz@CCM-1, a full formula is not given because a stable refinement of the masked electrons could not be achieved. The masked molecules make up for 121 electrons and the closest match to this can be calculated for 2.5 EtPyz molecules which contain 115 electrons. So, in this case only the accurately refined part of the structure is reported.

Table 2-2. List of liquid guest molecules attempted to encapsulate inside the CCM-series MOFs along with the structures and abbreviations of the molecules that were successfully encapsulated and characterised inside the MOF pores. Table legend: Green: Successful full guest exchange resulting in a single crystal structure. Yellow: Partial guest exchanged confirmed with SC-XRD analysis. Red: Regardless of any potential guest exchange indications, the crystal quality of the soaked MOF deteriorated to the point where SC-XRD could not be performed on the resulting material. Note: this list does not involve the solvents or binary mixtures that were tried.

Guest	Result
2-ethylpyridine	
Pyrazine	
Pinacol	
Benzophenone	
2-Chlorobenzonitrile	
3-Bromopyridine	
3-Amino-1-propanol	
3,5-Dimethylanisole	
2-Pyrrolidinone	
o-vanillin	
Pyridazine	
Pyrimidine	
1,2,3-Triazole	
Dipropyl carbonate	
Cyclopentanone	
4-Pyrimidone	
Cyclohexanone	
2-Bromopyridine	
4-Picoline	
Benzonitrile	
1-Methylimidazole	
1-Ethylpyrrolidinone	
1-Methylpyrrolidinone	
4-Ethylpyridine	
Crotononitrile	
3-Aminopyrazole	
2,3-dihydrofuran	
1-ethylpyrazole	
1-Vinyl-2-Pyrrolidinone	
Ethyl nicotinate	
1-Methylpyrazole	
Caprolactone	

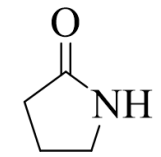

2-PDN (2-Pyrrolidinone)

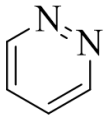

PYZ (pyridazine)

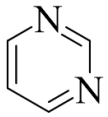

PMD (Pyrimidine)

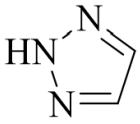

TAZ (1,2,3-Triazole)

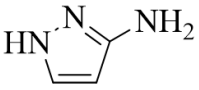

3-AmPyz (3-Aminopyrazole)

DHF (2,3-Dihydrofuran)

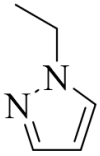

EtPyz (1-Ethylpyrazole)

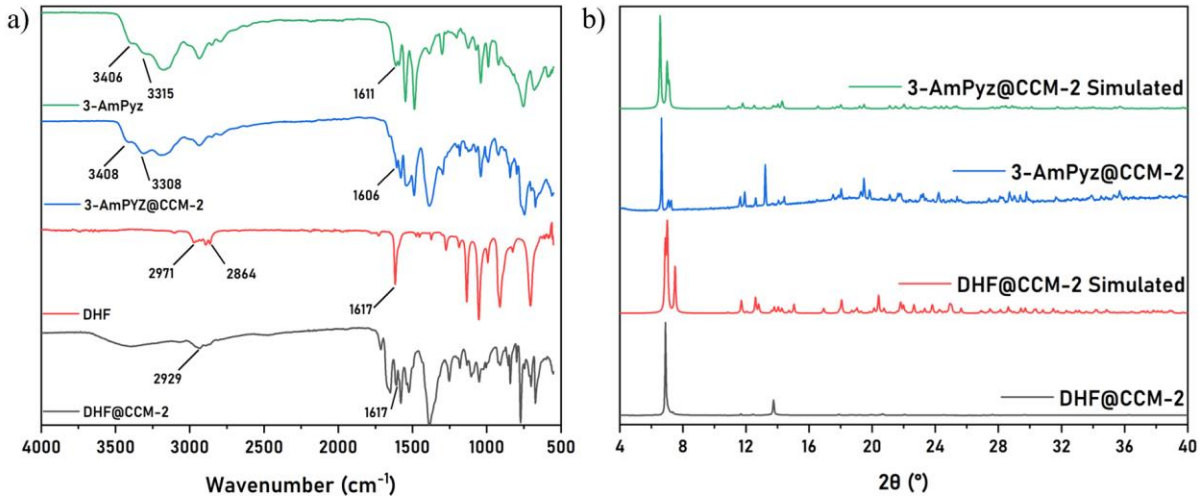

Figure 2-37. a) FT-IR spectra of partially exchanged CCM-MOFs: 3-dihydrofuran@CCM-2 (black line), 2,3-dihydrofuran (red line), 3-aminopyrazole@CCM-2 (blue line) and 3-aminopyrazole (green line). b) Experimental PXRD patterns of 2,3-dihydrofuran@CCM-2 (black line) and 3-aminopyrazole@CCM-2 (blue line) and their simulated counterparts (red and green lines, respectively).

The IR spectra of DHF@CCM-2 (black line) shows the presence of the C=O stretching at 1654 cm^{-1} assigned to the coordinated DMF molecules. As the intensity of this band is lower as compared to the as-synthesised CCM-2 MOF, it indicates that partial exchange of DMF for DHF has occurred. The presence of DMF is also supported by the ^{1}H NMR spectrum of the dissolved and acid treated crystals, which contains resonances at 2.70, 2.86 and 7.92 ppm corresponding to DMF (**Figure 2-50**). The ^{1}H NMR spectrum also does not contain any visible resonances that could be assigned to the DHF protons, however a large peak centred at 5.78 ppm corresponding to dichloromethane (DCM) is present. The presence of DCM is due to the washing step that is undertaken before the NMR spectroscopy analysis of every guest@MOF material to ensure that surface guest molecules are washed away. It is possible that during this washing step (performed three times with 2 mL of DCM) the encapsulated DHF molecules were displaced by the solvent. Thus, in the case of DHF@CCM-2, NMR spectroscopy analysis was not successfully used to determine the presence of DHF inside the pores of the framework. The IR spectrum of DHF@CCM-2 exhibits a peak at 1617 cm^{-1} attributed to C=C stretching that is also observed in the spectrum of pure DHF (**Figure 2-37a**, black and red lines). The C–H stretching bands observed in the range 2971–2864 cm^{-1} for DHF are obscured by the C–H stretching of DMF in the DHF@CCM-2 spectrum. These results indicate that DHF could be inside the pores of CCM-2 but has not displaced the coordinated DMF molecules as there are no obvious shifts in the DHF bands. Still, as DHF@CCM-2 showed potential exchange in the

FT-IR spectroscopy analysis while retaining high crystallinity (**Figure 2-37b**, black trace), the crystals were taken for SC-XRD analysis.

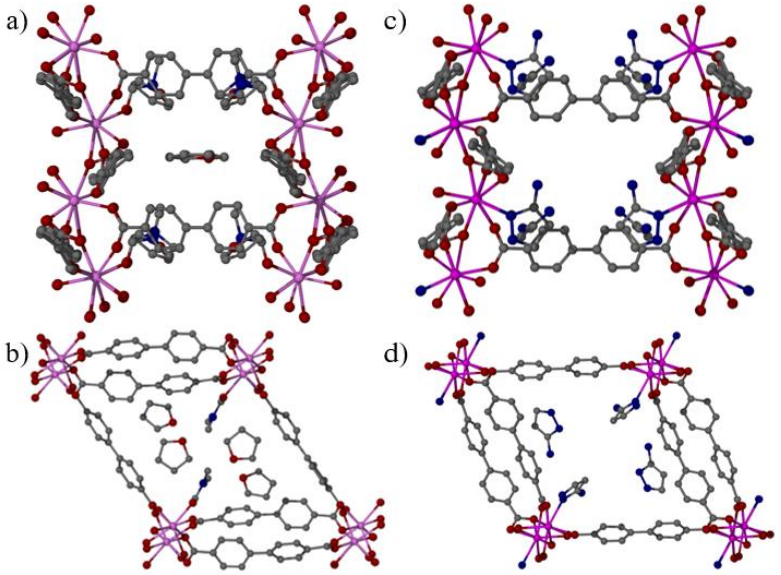

Figure 2-38. SC-XRD structures of DHF@CCM-1 along the a) *c* axis and b) *b* axis and 3-AmPyz@CCM-2 along the c) *c* axis and d) *b* axis. Grey: C. Red: O. Blue: N. Pink: Eu. Hydrogen atoms omitted for clarity.

Figure 2-38 shows the single crystal structure of DHF@CCM-2. The non-coordinated DMF molecules have exchanged with 2,3-dihydrofuran while the coordinated DMF molecules remain inside the pores. When solving the DHF@CCM-2 single crystal structure the non-coordinated DHF molecules were heavily constrained. As a result, the position of the DHF oxygen atoms in these structures are not reliable and any analysis of intermolecular interactions could not be undertaken. The inability of 2,3-dihydrofuran to displace the coordinated DMF molecules is likely due to the more polar nature of the DMF amide which results in stronger coordination to both lanthanum and europium metal centres.

Encapsulation of 3-aminopyrazole inside the pores of CCM-2 is evidenced by the loss of luminescence upon placing single crystals of CCM-2 inside the liquid of 3-aminopyrazole. As-synthesized CCM-2 exhibits pink luminescence under UV exposure due to the f–f transitions common in europium(III).[42] However, when single crystals of CCM-2 are added to the neat liquid of 3-AmPyz, the luminescence is quenched (**Figure 2-39 a** and **b**). This is quantified in the emission spectra of CCM-2 and AmPyz@CCM-2 (**Figure 2-39 c** and **d**) measured in the range of 570–720 nm. There are multiple mechanisms for luminescence quenching, such as framework collapse, inner filter effect (IFE), photoinduced electron transfer (PET) and Förster resonance energy transfer.[43] Framework collapse can be ruled out as PXRD

and SC-XRD analyses clearly show that the CCM-2 framework is retained after soaking in 3-AmPyz. To determine the exact mechanism of luminescence quenching from the other three mechanisms, further experiments including measurement of the 3-AmPyz excitation spectra, DFT calculations of the molecular orbital levels of the donor and acceptor and finally fluorescence lifetime determinations, are required. As this is outside of the scope of this project, these experiments were not further pursued.

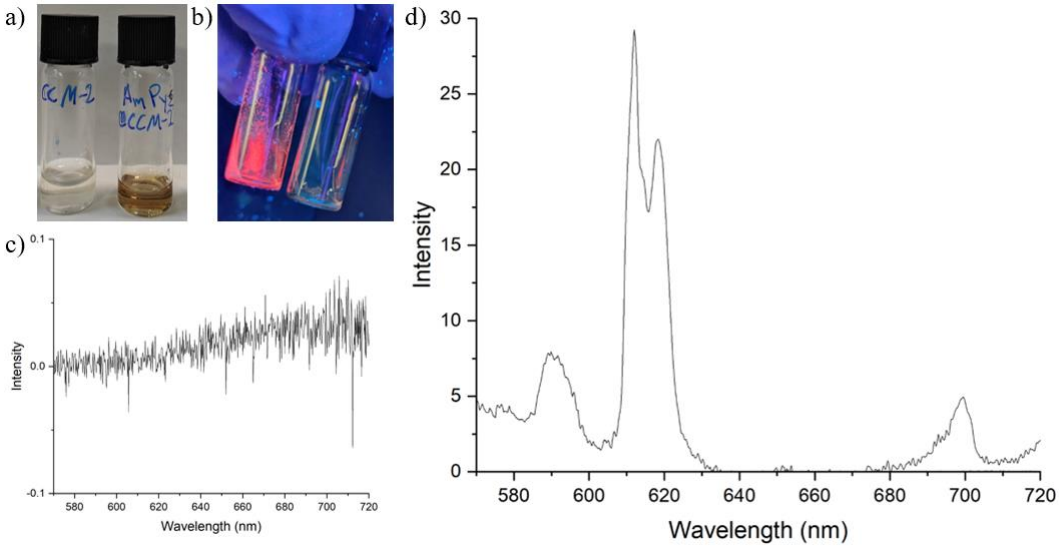

Figure 2-39. a) Image of CCM-2 in the mother liquor (left) and CCM-2 inside 3-aminopyrazole. b) CCM-2 in the mother liquor (left) and CCM-2 inside 3-aminopyrazole (right) under UV light. Emission spectra of c) AmPyz@CCM-2 and d) CCM-2.

SC-XRD analysis of AmPyz@CCM-2 single crystals was undertaken. The crystal structure of AmPyz@CCM-2 confirms that 3-aminopyrazole was successfully encapsulated into the CCM-2 framework, shown in **Figure 2-38 c** and **d**. The asymmetric unit contains one coordinated and one uncoordinated 3-AmPyz molecule. The uncoordinated guest is refined with 0.5 occupancy and another uncoordinated guest could not be definitively identified and was subsequently treated using the PLATON SQUEEZE tool.[44] The void channel containing the masked solvent is shown in **Figure 2-38c**. SC-XRD analysis reveals no intermolecular interactions between neighbouring guest molecules. However, a N–H···O hydrogen bond interaction between the coordinated 3-AmPyz and the oxygen atom of a H_2BPDC linker with a distance of 2.999(7) Å (N···O) is observed. The coordinated 3-AmPyz is slightly disordered and refinement of the minor component proved poorly behaved. It is likely that this minor component arises from residual DMF. This is borne out by the FT-IR spectrum of 3-AmPyz@CCM-2 (**Figure 2-37a**, blue trace) which contains a very small DMF C=O stretching band. The ^{1}H NMR spectrum of dissolved crystals of 3-AmPyz@CCM-2 also contains

resonances at 2.72, 2.89 and 8.03 attributed to DMF (**Figure 2-49**). Thus, full exchange of 3-AmPyz for DMF was not achieved.

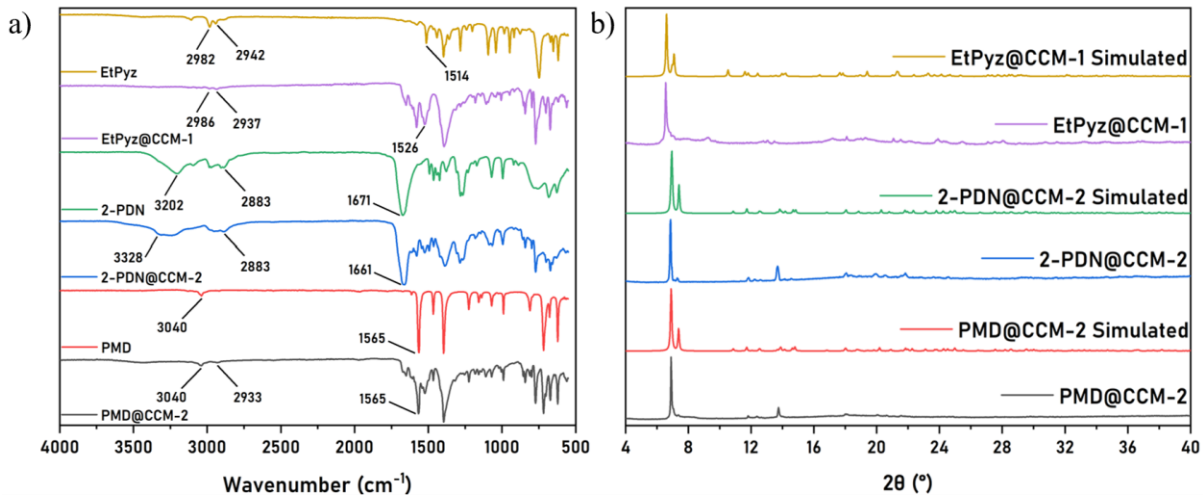

Figure 2-40. a) FT-IR spectra of partially exchanged CCM-MOFs: pyrimidine@CCM-2 (black line), neat pyrimidine (red line) 2-pyrrolidinone@CCM-2 (blue line), neat 2-pyrrolidinone (green line), 1-ethylpyrazole@CCM-1 (purple line) and neat 1-ethylpyrazole (olive yellow line). b) Experimental PXRD patterns of pyrimidine@CCM-2 (black line), 2-pyrrolidone@CCM-2 (blue line) and 1-ethylpyrazole@CCM-1 (purple line) and their simulated counterparts (red, green and olive yellow lines, respectively).

The IR spectrum of PMD@CCM-2 crystals exhibits an band at 1565 cm^{-1}, identical to that in the pure PMD spectrum (**Figure 2-40a**, black and red lines) and is attributed to C=C stretching. Additionally, another identical band centred at 3040 cm^{-1}, attributed to C–H stretching of PMD, in both spectra indicates that PMD could be in the pores of CCM-2. There is a small band centred at 2933 cm^{-1} arising due to the C–H stretching of DMF molecules still in the pores of the framework. These results indicate that PMD could be in inside the pores of CCM-2 but likely has only displaced the non-coordinated DMF molecules as the vibrational bands attributed to PMD do not exhibit any shifts in wavenumber. As these crystals exhibit good crystallinity after 24 hours of soaking (**Figure 2-40b**, black trace), they were used for SC-XRD analysis. In fact, the single crystal structure of PMD@CCM-2 shows that non-coordinated DMF molecules are fully exchanged with those of half-occupied and disordered pyrimidine molecules while coordinated DMF remains inside the pores (**Figure 2-41a and b**). Thus, there is good agreement between the FT-IR spectra and SC-XRD results of the PMD@CCM-2 crystals. Another pyrimidine molecule could not be modelled due to severe disorder and was subsequently masked. Overall, these results suggest that non-coordinated DMF are exchanged first, consistent with a stronger Eu–O_{DMF} bond compared to the Eu–N_{PMD}

bond. The pore along the crystallographic *c* axis (**Figure 2-41b**) contains an electron mass of 44 electrons which corresponds to one pyrimidine molecule but was treated with the SQUEEZE tool due to severe disorder.

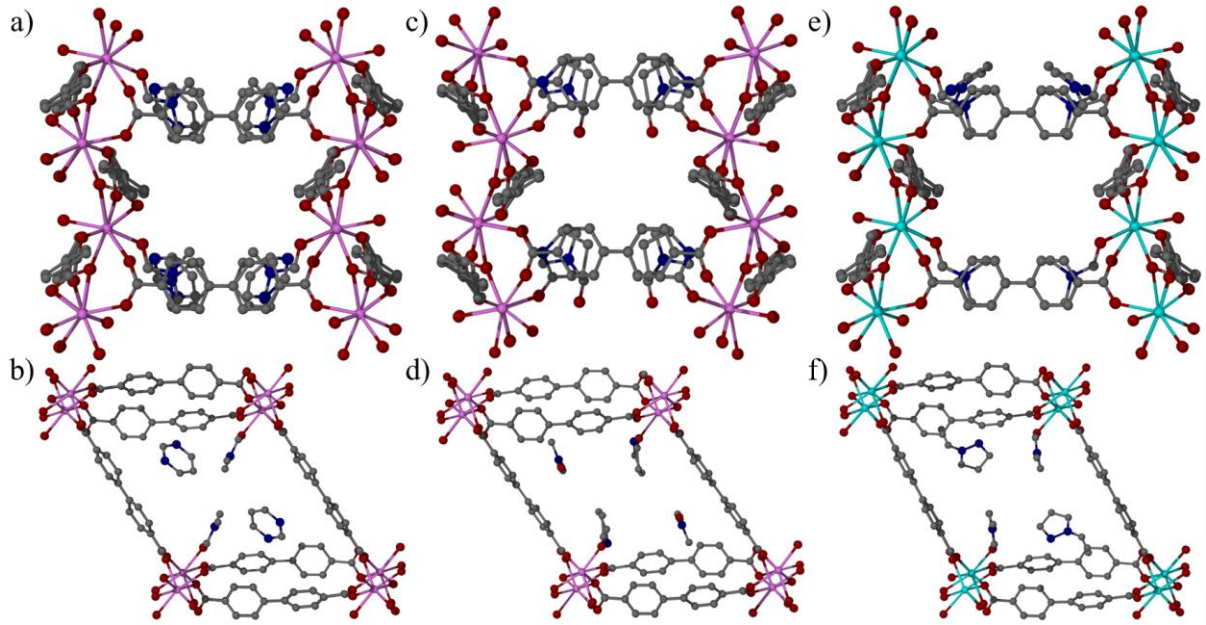

Figure 2-41. SC-XRD structures of 2-PDN@CCM-2 along the crystallographic a) *c* and b) *b* axes, PMD@CCM-2 along the crystallographic c) *c* and d) *b* axes and EtPyz@CCM-1 along the crystallographic e) *a* and f) *b* axes. Grey: C. Red: O. Dark blue: N. Pink: Eu. Light blue: La. Hydrogen atoms omitted for clarity.

The FT-IR spectrum of 2-PDN@CCM-2, on the other hand, indicates that 2-PDN molecules could be coordinated to the europium(III) metal centres. For instance the C=O stretching of 2-PDN which is centred at 1671 cm^{-1} in pure 2-PDN shifts to a lower wavenumber 1661 cm^{-1} in 2-PDN@CCM-2 (**Figure 2-40a**, blue and green lines). The presence of the band ranging from 3228 to 2883 cm^{-1} further supports the encapsulation of 2-PDN inside the pores of CCM-2. However, the presence of these bands could also cover the presence of the DMF C – H stretching usually present around 2932 cm^{-1}. Due to these crystals also retaining crystallinity (**Figure 2-40b**, blue trace), they were taken for SC-XRD analysis.

The single crystal structure of 2-PDN@CCM-2 displays the opposite behaviour to that of PMD@CCM-2 and fully exchanges with the coordinated DMF molecules while the non-coordinated DMF still remains inside the pores (**Figure 2-41 c and d**). More specifically, the coordinated 2-PDN is only partially substituted and was refined to the ratio 0.67:0.33 2-PDN:DMF. The coordination of 2-PDN over PMD to the europium(III) metal centre is likely due to the oxophilic nature of europium(III) which is more likely to form coordination bonds

with the cyclic amide oxygen atom of the 2-PDN rather than the pyrimidine nitrogen atom. From the viewpoint of Pearson's HSAB theory[45], these results correlate very well given that trivalent lanthanides are considered hard acids and oxygen is a harder base than nitrogen. This is further corroborated by the oxophilicity scale[46] which states that lanthanides are among the most oxophilic elements due to their small electronegativity resulting in strong binding with oxygen atoms. The pore along the *c* axis (**Figure 2-41a**) contains 24 electrons which is roughly a quarter of the electron count of a DMF and 2-PDN. As a result, it could not be accurately refined and was treated with the SQUEEZE tool.

Finally, the FT-IR spectrum of EtPyz@CCM-1 exhibits three peaks in similar positions to that of pure EtPyz – 2986, 2937 and 1526 cm^{-1} as compared to 2982, 2942 and 1514 cm^{-1} (**Figure 2-40a**, purple and olive yellow lines). This indicates that EtPyz could also potentially be coordinated to the metal centres in CCM-1. As the PXRD pattern of EtPyz@CCM-1 shows good crystallinity, these crystals were analysed *via* SC-XRD. **Figure 2-41 e** and **f** show the single crystal structure of EtPyz@CCM-1 along the crystallographic *a* and *b* axes, respectively. The coordinated DMF molecules are not displaced by 1-ethylpyrazole, which is consistent with the results that nitrogen donor guests tend not to displace coordinated DMF molecules while oxygen donor guests are more effective. Along the crystallographic *a* axis, the SQUEEZE tool was applied to mask the severely disordered electron cloud worth 121 electrons (115 electrons account for 2.5 molecules of 1-ethylpyrazole) that did not yield a stable refinement.

Overall, these results indicate that CCM-MOFs can be successfully used as confinement matrices to trap molecular clusters that can be viewed *via* SC-XRD diffraction. The aim of this work is to reach full exchange of guest molecules for the initial solvent, so in the cases of partially substituted guest molecules further analysis of the limited guest clusters was not undertaken. Additionally, guest cluster analysis could not be undertaken due to severe disorder that could not be accurately refined.

2.4.3 Fully Exchanged Guest Clusters

Among many other trialled guests (**Table 2-2**), pyridazine (PYZ) exhibited successful SCSCT with the FT-IR spectrum indicating almost complete exchange of the guest (**Figure 2-42a**, red trace) as exemplified by a significant decrease in the intensity of the DMF C=O stretch at 1654 cm^{-1} accompanied by the emergence of the PYZ C–H stretching mode at 3060 cm^{-1}. The persistence of the low angle peak that is also present in the powder pattern of the as-synthesised CCM-1 (**Figure 2-42b**, black line) indicates that the framework structure is retained after

soaking. A high degree of crystallinity is retained after 24 hours of soaking in neat PYZ and as consequently PYZ@CCM-1 was analysed by SC-XRD.

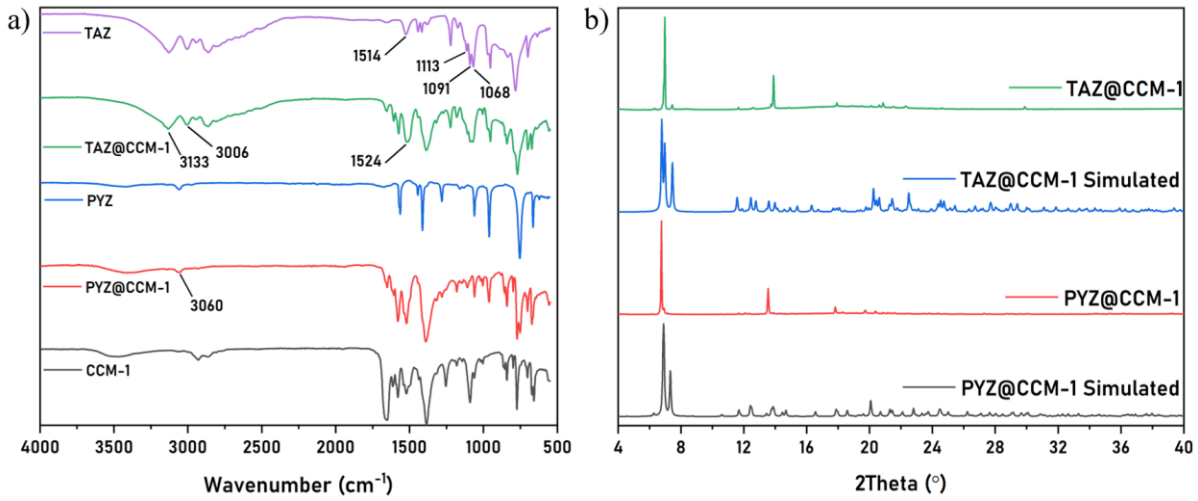

Figure 2-42. a) FT-IR spectrum of CCM-1 (black line), pyridazine@CCM-1 (red line), pure pyridazine (blue line), 1,2,3-triazole@CCM-1 (green line) and pure 1,2,3-triazole (purple line). b) PXRD patterns of simulated pyridazine@CCM-1 (black line), experimentally obtained pyridazine@CCM-1, simulated 1,2,3-triazole@CCM-1 and experimentally obtained 1,2,3-triazole@CCM-1. The band indicated at 3060 cm^{-1} is attributed to the C–H stretching of PYZ while those at 3133 and 3006 cm^{-1} are attributed to the C–H stretching of TAZ. The bands at 1514 and 1524 cm^{-1} are attributed to C=C stretching of TAZ while the bands at 1068, 1091 cm^{-1} belong to N–H bending and 1113 cm^{-1} is attributed to C–H bending of TAZ.[47,48]

The exchange is further supported by the ^{1}H NMR spectrum of the dissolved crystals, which shows the presence of PYZ resonances (**Figure 2-43**). The ratio of PYZ molecules to DMF could not be established due to the low intensity of the resonances associated with PYZ. Additionally, it is possible some residual DMF is still on the surface of the MOF crystals despite the DCM wash. Thus, even if the ratio could be established it might not be an accurate description of the pore contents. **Figure 2-42b** shows the PXRD pattern of pyridazine-soaked CCM-1 single crystals after 24 hours of soaking in the neat guest liquid (red line).

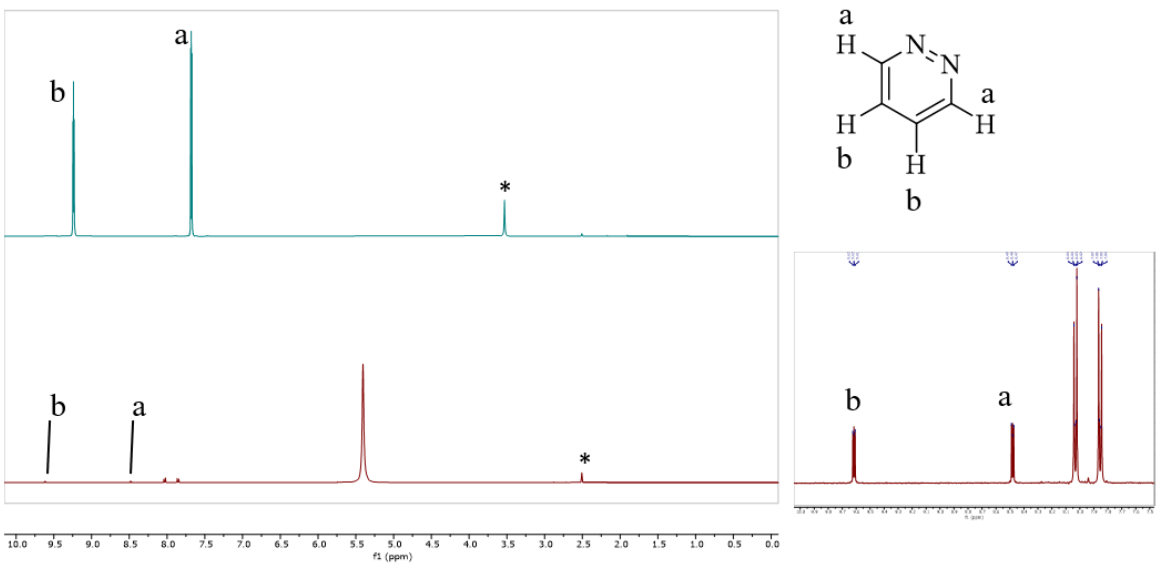

Figure 2-43. ^{1}H NMR spectra of pure pyridazine (blue line) and PYZ@CCM-1 (red line). Zoom into the range of 7.5–10 ppm shows the small PYZ resonances. The intense peak located at 5.40 ppm on the PYZ@CCM-1 spectrum is due to the protonation of the N=N fragment of pyrimidine due to the presence of TFA acid. Spectra collected in d_6-DMSO.

The SC-XRD structure of pyridazine-encapsulated CCM-1 (PYZ@CCM-1) is shown in **Figure 2-44** and yields the formula $La_3(H_2BPDC)_{4.5}(PYZ)_9(DMF)$. The crystal structure of PYZ@CCM-1 contains two types of pores – those which are fully exchanged with pyridazine and those which are partially exchanged. The asymmetric unit contains nine PYZ molecules and one DMF solvent molecule while two thirds of the pores are fully exchanged and one third contains coordinated DMF molecules along with non-coordinated PYZ in a 1:2 ratio (DMF:PYZ, **Figure 2-44**, rightmost pore). In the pores containing DMF, all four non-coordinated DMF molecules have been replaced with PYZ while the two coordinated DMF molecules remain. This suggests that as with pyrimidine, it is the non-coordinated DMF molecules that can be exchanged first with PYZ. In the pores where PYZ coordinates to the framework metal centres, the guest molecule occupies both coordination centres. This suggests that it is likely the non-coordinated DMF molecules are firstly exchanged, then followed by the exchange of the coordinated DMF molecules for PYZ. The La–N distance ranges from 2.634(6) to 2.679(6) Å for PYZ, slightly longer than the La–O distance of 2.543(6) Å for the coordinated DMF molecules. The slightly shorter, and likely stronger, coordination of DMF over pyridazine by the oxophilic metal centre may explain why full exchange of the solvent with the guest was not achieved. Alternatively, it might require more soaking time of CCM-1 single crystals in the neat PYZ liquid to fully exchange all coordinated DMF molecules.

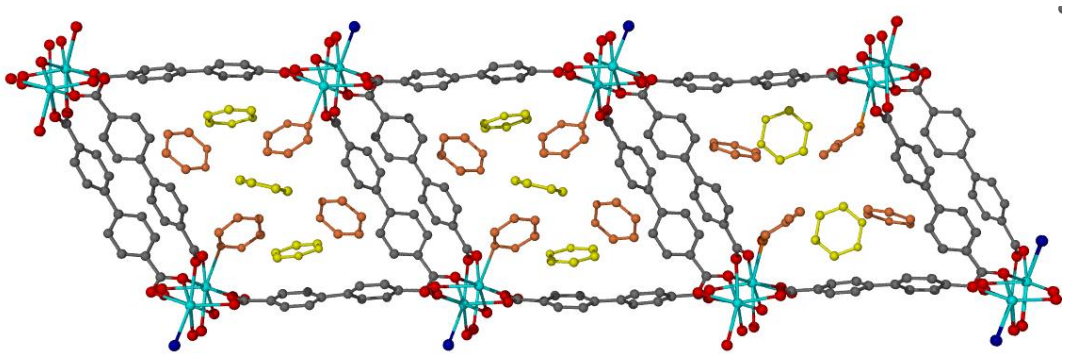

Figure 2-44. SC-XRD image of PYZ@CCM-1 along the crystallographic *b* axis showing fully and partially exchanged pores. Grey: C. Blue: N. Red: O. Green: La. H atoms omitted for clarity. Orange and yellow coloured molecules signify guest molecules parallel with each other in order to highlight the layers of molecules.

Given the ordered nature of the guests in PYZ@CCM-1, it was subsequently studied whether confinement changes the bulk structure of the encapsulated molecules. Three crystal structures at varying pressures of the same polymorph of pyridazine have been reported. The earliest was communicated by Blake and Rankin who obtained their sample by melting pyridazine and slowly cooling it to obtain a single crystal (reference code VOBJEB).[49] The other two structures were reported in 2010 by Katrusiak and co-workers, who published the crystal structures of PYZ at 0.27 and 0.61 GPa (reference codes VOBJEB01 and VOBJEB02, respectively).[50] Despite the different conditions for all reported structures, the packing arrangement of PYZ molecules in the lattice does not change. PYZ stacks in nearly planar sheets and forms mainly C–H···N interactions. For the crystal structures collected at 0.27 and 0.61 GPa, the C–H···N distances range from 3.377(8) to 3.639(8) Å with respective angles ranging from 154 to 140°. In the bulk, each PYZ molecule participates in four C–H···N interactions with two neighbouring PYZ molecules, averaging to two C–H···N interactions per nitrogen atom. Additionally, π–π interactions are present between PYZ molecules of adjacent sheets. Meanwhile, there are no short N···N interactions as they are longer than those of C···N and π–π, indicating that the latter could play a more influential role in the nucleation and crystallization of PYZ.

Pyridazine molecules confined in CCM-1 form alternating clusters of trimers and tetramers forming an unusual seven-molecule repeating unit along the MOF channel along the *b* axis (**Figure 2-44**, yellow and orange molecules). This arrangement is significantly different from the bulk structure and represents a novel packing arrangement. This difference is unsurprising given the coordinated nature of some of the PYZ molecules but highlights the

ability of the MOF to profoundly influence the molecular aggregation. Indeed seven-molecule repeat units are very uncommon in small molecular crystal structures as the most stable crystal structures are formed in systems with strong intermolecular interactions resulting in minimal free space and high symmetry.[51] Strikingly, however, these confined clusters of trimers and tetramers exhibit similar interactions to those in the bulk. For instance, the shortest interactions are those of C···N with a range of 3.319(12) to 3.635(13) Å with respective angles ranging from 134 to 151°. In PYZ@CCM-1, the PYZ tetramer forms between two coordinated and two non-coordinated PYZ molecules. For the tetramer, there are no face-to-face interactions between the pyridazine molecules. This is likely to be due to the presence of coordination bonds between two of these pyridazine molecules and the lanthanum(III) metal centres, resulting in the guest molecules packing at an angle along the *b* axis pore. The two non-coordinated pyridazine molecules have the 1,2-nitrogen atoms pointing toward the centre of the pore. However, there do not appear to be any π–π interactions between the pyridazines and the framework or the guest molecules. Classical nucleation theory posits that the molecular packing inside nuclei of critical size reflects the lattice arrangement in the resulting polymorph.[52] Thus, this novel packing arrangement PYZ inside CCM-1 begins to suggest a model for an alternative bulk packing arrangement.

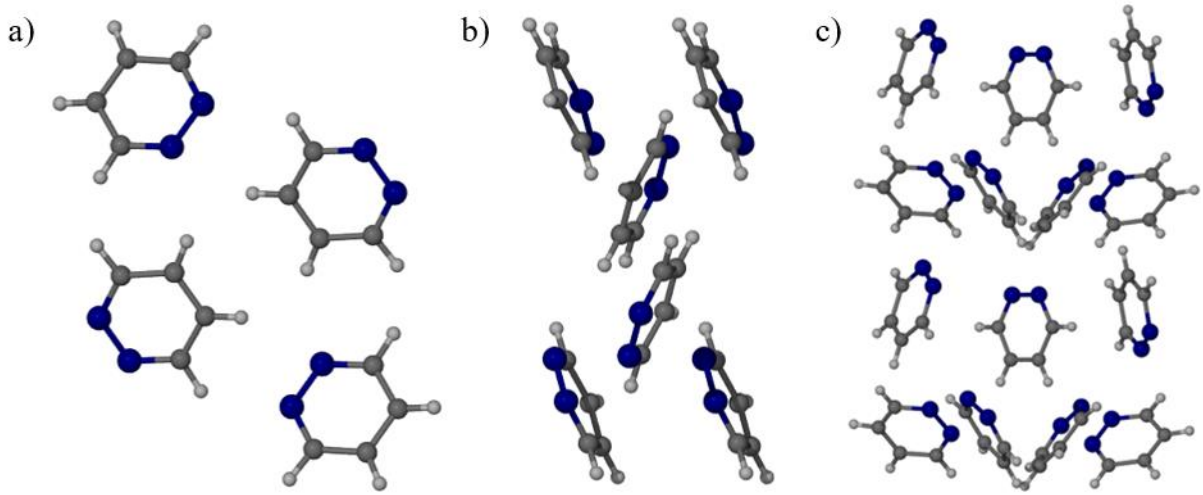

Figure 2-45. Unit cell of bulk pyridazine (CSD reference code: VOBJEB[49] along the crystallographic a) *a* and b) *c* axes. c) Pyridazine trimer and tetramer clusters inside one continuous channel of PYZ@CCM-1. Grey: C. Blue: N. White: H.

The SCSCT guest exchange reaction was also attempted with 1,2,3-triazole (TAZ) by immersing single crystals of CCM-1 in the liquid guest at room temperature. After 24 hours, the FT-IR spectrum of guest-soaked CCM-1 exhibits a significant decrease in the intensity of the C=O stretching band corresponding to the included DMF (**Figure 2-42a**, green line). This

band is replaced with broad peaks in the 2500–3500 cm^{-1} range, characteristic of N–H (3133 cm^{-1}) and C–H (3006 cm^{-1}) stretches of TAZ. In the pure TAZ spectrum, the peaks at 1068, 1091 and 1113 cm^{-1} were assigned to two δ(CH) and one δ(NH) (in-plane bending) modes, respectively (**Figure 2-42a**, purple line).[47] The peak assigned to the N=N stretching in pure TAZ at 1514 cm^{-1} exhibits a widening and shifts to 1524 cm^{-1} in TAZ@CCM-1, indicative of a coordination bond forming between the aromatic nitrogen and lanthanum metal centre. The exchange of DMF with TAZ is further corroborated by the ^{1}H NMR spectrum of the dissolved MOF which shows the presence of the protons of the TAZ ring at 7.86 ppm. The PXRD pattern of TAZ-soaked crystals of CCM-1 (**Figure 2-42b**, green line) exhibits high crystallinity and consequently the crystals were analysed by SC-XRD. The resulting crystal structure shows that TAZ has fully exchanged with DMF, yielding TAZ@CCM-1 with a formula of $La(BPDC)_{1.5}(TAZ)_4$ containing four TAZ molecules in the asymmetric unit and resulting in the formation of octamers along the crystallographic *b* axis. Of the four unique TAZ molecules, two are identified as 1*H*-TAZ and the two others as 2*H*-TAZ tautomers.[53] Tautomeric polymorphism is not uncommon as 51% of crystal structures reported in the CSD are capable of containing more than one tautomeric form.[54] The N–N–N angles of the 1*H*-TAZ molecules are 103(2)° and 107.4(8)° and those of 2*H*-TAZ molecules are 109.5(14)° and 107.9(6)°. In bulk TAZ, the N–N–N angle is 115.9(3)° for 2H-TAZ and 106.5(2)° for *1H*-TAZ.[53] The larger N–N–N angle of the encapsulated 2*H*-TAZ molecules supports the tautomer assignment. CCM-1 undergoes some structural changes to accommodate TAZ inside the pores including a phase change to the centrosymmetric $P2_1/n$, as opposed to the chiral *C*2 of as-synthesised CCM-1. Along the *b* axis, both frameworks look similar, but significant changes are observed along the *a* axis (**Figure 2-46**). Along the *a* axis of CCM-1, the SBUs and organic linkers are parallel to one another while in TAZ@CCM-1 they appear to shift down so that all TAZ molecules can occupy the pores. The encapsulation of TAZ molecules in CCM-3 (TAZ@CCM-3) MOF was also attempted. In CCM-3, an identical molecular cluster of TAZ formed as that in CCM-1, suggesting that the molecular clusters do not form randomly in these MOFs, but indeed the assembly is guided by intermolecular interactions.

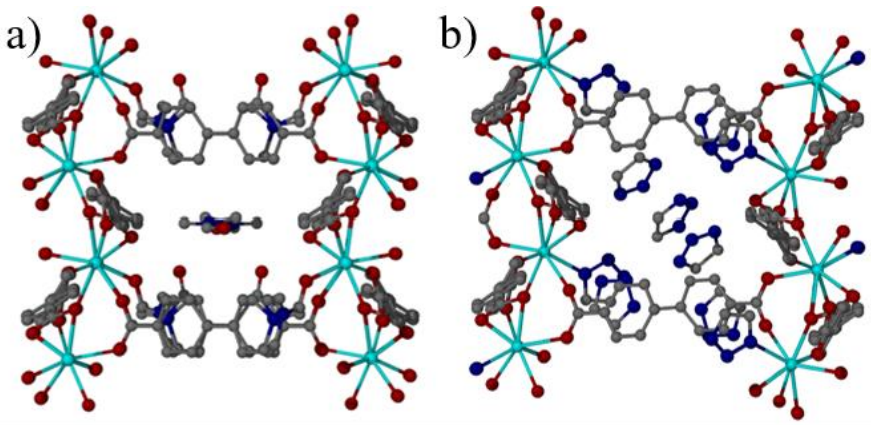

Figure 2-46. Single crystal structures along the crystallographic *a* axis of a) CCM-1 and b) TAZ@CCM-1. Grey: C. Red: O. Dark blue: N. Light blue: La. Hydrogen atoms omitted for clarity.

As a result of physical changes to the framework upon the encapsulation of TAZ, the underlying topology of TAZ@CCM-1 MOF was also studied *via* ToposPro. Similarly to CCM-1–4 frameworks, TAZ@CCM-1 was analysed using the point of extension method. While some structural differences were observed in the MOF containing TAZ clusters, the underlying topology did not change. **Figure 2-47** shows the underlying topology (green cylinder) overlaid with the single crystal structure of the framework. The organic linkers are slightly rotated along the horizontal plane as compared to CCM-1 in order to occupy the guest molecules, but no ohter significant changes are observed.

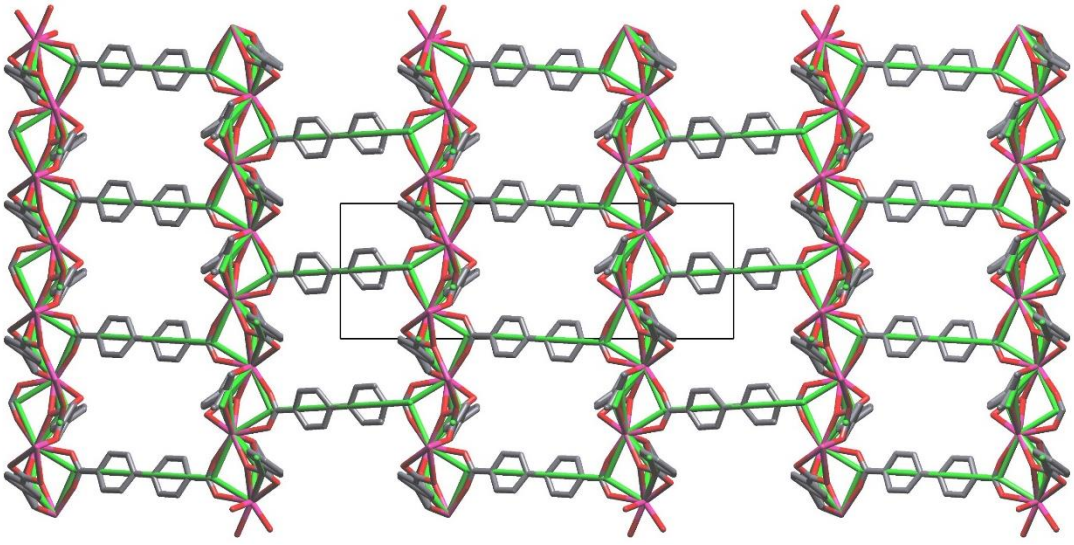

Figure 2-47. Underlying topology of TAZ@CCM-1 as determined by the point of extension method overlaid with the single crystal structure. Black: Unit cell. Gray: C. Red: O. Pink: La. Green: Underlying net exhibiting the **tsy** topology.

The structure of the encapsulated TAZ molecules shows that there are stabilising intermolecular hydrogen bonding and π–π interactions. A hydrogen bonding network can be built starting from the coordinated TAZ molecule (T1, **Figure 2-48a**), which participates in two hydrogen bonding interactions with neighbouring TAZ molecules (T2 and T3) acting as both the donor and acceptor. The hydrogen bond between T1 and T3 exhibits a N1–H···N3 distance of 3.071(11) Å along with an angle of 167.0(3)°. The other hydrogen bond, N2–H···N1 exhibits an N···N distance of 2.799(10) Å and an angle of 161.1(4)°. Both T2 and T3 subsequently interact with T4 through two hydrogen bonds, forming a hydrogen bonded tetramer. This tetramer subsequently grows into a hexamer by the addition of T5 and T6 by both hydrogen bonding and π–π interactions with T2 and T3. Finally, the octamer is completed by the addition of terminal T7 and T8, both of which hydrogen bond strictly with T5 and T6.

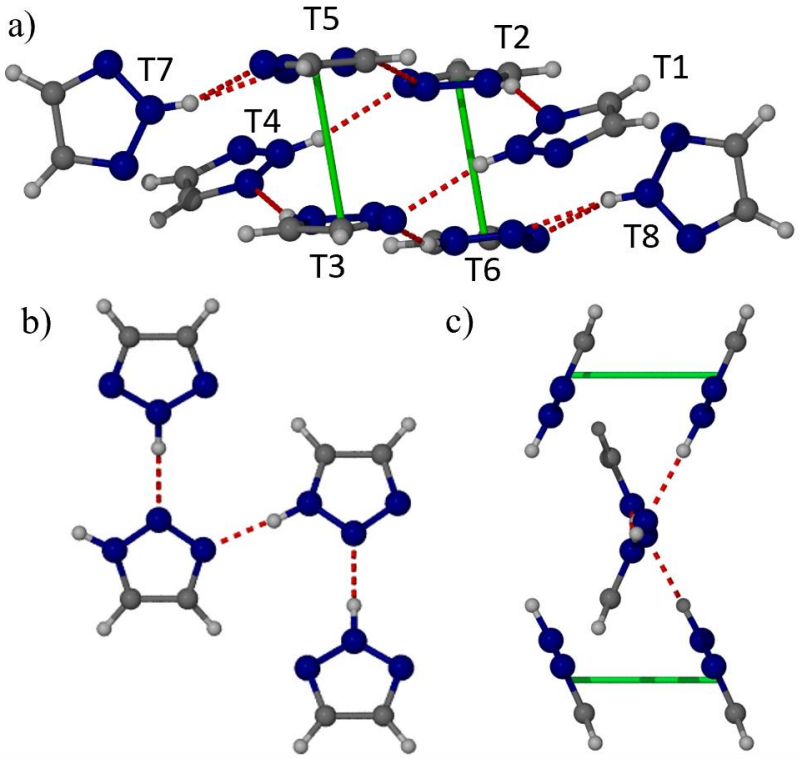

Figure 2-48. SC-XRD structures of a) the TAZ octamer in TAZ@CCM-1 while b) and c) show the bulk arrangement of TAZ. Hydrogen bonds and π–π interactions are shown as red dashed and green solid lines, respectively. Grey: C. Blue: N.

In the bulk, TAZ crystallizes as a 1:1 molecular complex of its two tautomers, *1H*-1,2,3-triazole (*1H*-TAZ) and *2H*-1,2,3-triazole (*2H*-TAZ).[53] Apart from containing the pyrrolic hydrogen atom in either *1H* or *2H* positions, the two tautomers also differ by their ring angles. Both tautomers pack in a herringbone arrangement with adjacent rings having a dihedral angle of 49(1)°. The shortest intermolecular interaction is the N–H···N hydrogen bond between two

adjacent 1H-TAZ molecules with 2.779(2) Å (**Figure 2-48b**, hydrogen bond between two *1H*-TAZ molecules). The second shortest intermolecular interaction is between two adjacent *1H*-TAZ and *2H*-TAZ molecules with the N–H···N hydrogen bond having the distance of 2.935(3) Å. Additional π–π interactions between adjacent *1H*-TAZ molecules with the length of 3.7 Å further act to stabilise the crystal lattice (**Figure 2-48c**, solid green lines).

Crucially, both hydrogen bonding and π–π interactions are present in both bulk TAZ and confined TAZ clusters inside TAZ@CCM-1. Additionally, the ratio of 1*H*- and 2*H*-TAZ in both bulk and confined clusters is 1:1. The most significant difference between these bulk and confined clusters is their shape and size. While in both bulk and confined crystal structures the main stabilising forces are hydrogen bonds and π–π interactions, in CCM-1 the cluster shape is also guided by the external framework. The same intermolecular interactions guide the formation of an octanuclear cluster of TAZ with a unique shape, which suggests that it could be potentially form the basis of novel polymorphs.

2.5 Conclusions and Future Work

In conclusion, lanthanoid-based MOFs CCM-1–4 have been used to describe the formation of molecular clusters inside the framework channels. While partially exchanged systems could not be compared to their bulk equivalents, they potentially highlight the mechanism of guest exchange, based on the oxophilicity of the guest molecule. These insights could thus be applied to the design of MOFs metal centres to selectively coordinate desired guest molecules for applications in catalysis or capture of volatile organics. The inclusion of pyridazine into the framework results in the formation of layers of trimers and tetramers. Additionally, the arrangement of TAZ clusters in CCM-1 significantly differ from that of the bulk material. Under confinement in the CCM-1 MOF, it seems like the generally weaker hydrophobic interactions guide the formation of clusters while in bulk the directionality is gained from hydrogen bonds resulting in herringbone-style packing. This could indicate that during the nucleation steps, it might not necessarily be the strongest interactions that form the pre-critical nuclei that eventually give rise to the bulk crystal. Finally, while the environment within the present MOFs is of course very different to the bulk guests and the cavity size is relatively small compared to the size of a critical nucleus, these initial results nevertheless show that clusters of significant size and very different packing arrangements to the bulk guests can be generated by confinement. This kind of approach represents a possible step along the pathway to stabilising hitherto unobserved polymorphs, particularly those calculated by CSP approaches[55,56], and shedding light on molecular clusters of sub-critical size. Confining the

molecular cluster in a matrix which has controllable shape and size can lead to the formation of oligomers exhibiting novel shapes and sizes. Carpenter and Grünwald recently discussed the capability of small and rigid molecules to form oligomers which play a decisive role in polymorph control.[56]

Future work could focus on coupling the obtained crystal structures of molecular aggregates within MOF pores with DFT calculations in order to better understand the potential mechanisms behind the formation of the confined aggregates. Further future work could also focus on expanding MOF pore sizes while maintaining their shape in order to study the resulting similarities and differences in the cluster formation within the larger pores as compared to those reported herein. Longer term aims could also focus on probing the polymorph landscape of target molecules with crystal structure prediction methods, which are accurate in predicting thermodynamically stable polymorphs.[57] Subsequently, the shape of confined nuclei can be compared to potential new polymorphs that resemble or match the shape of the confined clusters. Finally, the crystallisation of novel polymorphs from the nuclei encapsulated within MOFs could be achieved by layering the MOF onto a surface and adding a droplet of the target molecule onto the MOF.

2.6 Experimental Details

2.6.1 Synthesis of MOFs

General Synthesis Procedure

All MOFs in this chapter 2 were synthesised by similar synthetic procedures. In a vial, a lanthanum salt (0.14 mmol) was mixed together with DMF (7 mL). A supersaturated stock solution of the organic linker, 4,4'-biphenyldicarboxylic acid (H_2BPDC, 41.3 mM, 50 mL), with the was prepared in DMF and 5.04 mL of it was added to the metal salt solution. Prior to the addition of the organic linker, the stock solution was heated to ensure full dissolution of the linker. After the two solutions had been combined, the resulting mixture was sonicated for 5-10 minutes. In the case of CCM-1, trifluoroacetic acid (0.21 mL) was added to the mixture prior to the sonication step. After sonication, the mixture was transferred into a Teflon-lined acid digestion vessel which was placed in an isothermal oven at 120°C for 72 hours and was cooled to room temperature over the course of 6 hours. After this, the acid digestion vessel was removed from the oven and single crystals with a plank shape were observed at the bottom of the vessel. After decanting the mother liquor, the crystals were carefully removed and placed in fresh DMF where the crystallinity could be retained for months.

2.6.2 Characterisation of Compounds

The samples for ^{1}H and $\{^{1}H\}^{13}$C NMR spectroscopy analysis were prepared as follows. For the organic linker, a saturated solution of H_2BPDC (10mg) was prepared in deuterated *d*$_6$–DMSO (0.7 mL). The saturated solution was heated until all of the solute dissolved. Subsequently, the sample was analysed by ^{1}H and $\{^{1}H\}^{13}$C NMR spectroscopy. For CCM-1–4 samples, MOF material (10 mg) was added to *d*$_6$–DMSO (0.7 mL). Subsequently, one drop of concentrated hydrochloric acid was added to this mixture. The vial was gently shaken until the MOF sample dissolved. Subsequently, the sample was taken for NMR analysis. As acid digestion results in the collapse of the MOF framework, the ^{1}H and $\{^{1}H\}^{13}$C NMR spectroscopy results reported herein are of the free ligand rather than the MOF framework itself. The formulae of MOFs as determined by their elemental analysis compositions slightly differ from their crystallographic formulae. MOF crystals were dried using the Abderhalden's drying pistol at 110°C for one day prior to elemental analysis to ensure the removal of surface DMF. However, this process could have also resulted in the loss of some encapsulated DMF molecules, which could have become replaced by atmospheric water molecules. The synthesis and characterisation of CCM-1–3 MOFs was first reported in 2008.[14] The authors did not provide any NMR spectroscopy characterisation, so any comparison of the NMR spectroscopy

data cannot be discussed. However, as stated in the text, the TGA results closely match the literature reported values. The synthesis of CCM-4 was reported eight years later by Sessler and co-workers.[16] A partial ^{1}H NMR spectrum is reported therein and matches the ^{1}H NMR spectroscopy results provided herein for the same compound.

CCM-1

The compound was obtained as transparent plank-shaped single crystals (55 mg, 55% based on crystallographic formula).

^{1}H NMR (400 MHz, DMSO–d_6): δ = 7.83–7.86 (4H, dt, J = 8.6 Hz, 1.8 Hz, Ar–H), 8.01–8.04 (4H, dt, J = 8.6 Hz, 1.8 Hz, Ar–H)

{^{1}H}^{13}C NMR (100.6 MHz, DMSO–d_6): δ = 127.62, 130.48, 130.79, 143.54, 167.46.

Elemental analysis calculated for $C_{21}H_{12}O_6La(H_2O)_3(C_3H_7NO)_3$. Expected: C 46.64, H 5.09, N 5.44%. Found: C 46.47, H 4.97, N 5.72%. The formula determined from elemental analysis contains three additional water and one less DMF molecule compared to the crystallographic formula.

CCM-2

Compound was obtained as transparent plank-shaped single crystals that show pink luminescence under UV light (48 mg, 47% based on crystallographic formula)

^{1}H NMR (400 MHz, DMSO–d_6): δ = 7.84–7.86 (4H, dt, J = 8.6 Hz, 1.8 Hz, Ar–H), 8.01–8.04 (4H, dt, J = 8.6Hz, 1.8 Hz, Ar–H).

{^{1}H}^{13}C NMR (100.6 MHz, DMSO–d_6): δ = 127.63, 130.49, 130.79, 143.54, 167.46.

Elemental analysis calculated for $C_{21}H_{12}O_6Eu(H_2O)(C_3H_7NO)$. Expected: C 47.77, H 3.51, N 2.32%. Found: C 47.90, H 3.09, N 2.29%. The formula determined from elemental analysis contains one more water molecule and three less DMF molecules compared to the crystallographic formula.

CCM-3

Compound was obtained as light green plank-shaped single crystals (50 mg, 50% based on crystallographic formula)

^{1}H NMR (400 MHz, DMSO–d_6): δ = 7.83–7.85 (4H, dt, J = 8.6 Hz, 1.8 Hz, Ar–H), 8.01–8.03 (4H, dt, J = 8.6 Hz, 1.8 Hz, Ar–H).

{^{1}H}^{13}C NMR (100.6 MHz, DMSO–d_6): δ = 127.63, 130.49, 130.78, 143.54, 167.47.

Elemental analysis calculated for $C_{21}H_{12}O_6Ce(H_2O)(C_3H_7NO)_2$. Expected: C 48.79, H 4.25, N 4.21%. Found: C 48.70, H 3.69, N 4.25%. The formula determined from elemental analysis

contains one more water molecule and two less DMF molecules compared to the crystallographic formula.

CCM-4

Compound was obtained as dark green plank-shaped single crystals (43 mg, 43% based on crystallographic formula)

^{1}H NMR (400 MHz, DMSO–d_6): δ =7.82–7.85 (4H, dt, J = 8.6 Hz, 1.8 Hz, Ar–H), 8.00–8.03 (4H, dt, J = 8.6 Hz, 1.8 Hz, Ar–H).

{^{1}H}^{13}C NMR (100.6 MHz, DMSO–d_6): δ = 127.63, 130.49, 130.77, 143.53, 167.47.

Elemental analysis calculated for $C_{21}H_{12}O_6Pr(C_3H_7NO)$. Expected: C 50.19, H 3.33, N 2.44%. Found: C 49.97, H 3.10, N 2.41%. The formula determined from elemental analysis contains three less DMF molecules compared to the crystallographic formula.

2.6.3 General Guest Exchange Procedure

The guest exchange of CCM-series MOFs was undertaken using neat liquid guests. More specifically, single crystals of as-synthesised MOFs were placed in 0.2–0.5 mL of the desired guest liquid and left to soak for at least 24 hours. During this time, the single crystals were monitored *via* FT-IR spectroscopy and polarised optical microscopy to assess guest exchange and crystallinity of the material. PXRD was not used prior to SC-XRD analysis due to the limited amount of single crystals placed in the neat liquid (generally less than 10 mg). In most cases, guest exchange was observed *via* FT-IR spectroscopy but crystallinity was lost over the course of 24 hours or prior to full guest exchange. In these cases, cracking of the crystals or loss of birefringence was observed, indicating loss of crystallinity which made SC-XRD analysis impossible. When crystallinity was retained for 24 hours along with indications of guest exchange *via* FT-IR spectroscopy, the guest@CCM-MOF single crystals were taken to SC-XRD analysis.

2.6.4 Crystallographic Data

Table 2-3. Crystal data for CCM-1–4 MOFs.

	CCM-1	**CCM-2**	**CCM-3**	**CCM-4**
Empirical formula	$C_{27}H_{26}LaN_2O_8$	$C_{30}H_{33}EuN_3O_9$	$C_{27}H_{26}CeN_2O_8$	$C_{27}H_{26}PrN_2O_8$
Formula weight	645.41	731.55	646.62	647.41
Temperature/K	120	120	120	120
Crystal system	Monoclinic	monoclinic	monoclinic	monoclinic
Space group	*C*2	*C*2	*C*2	*C*2
a/Å	27.4499(7)	28.2070(14)	27.729(2)	27.0006(8)
b/Å	8.7721(2)	8.5487(4)	8.7264(7)	8.7440(3)
c/Å	14.3226(4)	14.2248(7)	14.2776(11)	14.2342(4)
α/°	90	90	90	90
β/°	114.2443(10)	115.4485(16)	114.521(2)	113.7839(10)
γ/°	90	90	90	90
Volume/$Å^3$	3144.61(14)	3097.3(3)	3143.2(4)	3075.19(17)
Z	4	4	4	4
$\rho_{calc}g/cm^3$	1.363	1.569	1.366	1.398
μ/mm^{-1}	1.403	2.081	1.492	1.629
F(000)	1292.0	1476.0	1296.0	1300.0
Crystal size/mm^3	0.15 × 0.09 × 0.01	0.34 × 0.11 × 0.02	0.19 × 0.1 × 0.01	0.11 × 0.05 × 0.02
Radiation	MoKα (λ = 0.71073)	Mo Kα (λ = 0.71073)	Mo Kα (λ = 0.71073)	Mo Kα (λ = 0.71073)
2Θ range for data collection/°	4.92 to 59.998	5.026 to 59.998	4.94 to 53.998	4.942 to 61.998
Index ranges	-38 ≤ h ≤ 38, -12 ≤ k ≤ 12, -20 ≤ l ≤ 20	-39 ≤ h ≤ 39, -11 ≤ k ≤ 12, -20 ≤ l ≤ 20	-35 ≤ h ≤ 35, -11 ≤ k ≤ 11, -18 ≤ l ≤ 18	-39 ≤ h ≤ 39, -12 ≤ k ≤ 12, -20 ≤ l ≤ 20
Reflections collected	63301	46463	38321	59948
Independent reflections	9193 [R_{int} = 0.1679, R_{sigma} = 0.0820]	8948 [R_{int} = 0.0348, R_{sigma} = 0.0258]	6868 [R_{int} = 0.0496, R_{sigma} = 0.0369]	9819 [R_{int} = 0.0461, R_{sigma} = 0.0332]
Data/restraints/parameters	9193/180/434	8948/25/432	6868/197/470	9819/183/473
Goodness-of-fit on F^2	1.029	1.136	1.119	1.102
Final R indexes [I>=2σ (I)]	R_1 = 0.0368, wR_2 = 0.0950	R_1 = 0.0374, wR_2 = 0.0957	R_1 = 0.0397, wR_2 = 0.1023	R_1 = 0.0333, wR_2 = 0.0867
Final R indexes [all data]	R_1 = 0.0429, wR_2 = 0.0961	R_1 = 0.0382, wR_2 = 0.0965	R_1 = 0.0451, wR_2 = 0.1056	R_1 = 0.0370, wR_2 = 0.0891

Table 2-4. Crystal data for guest@MOF materials with partial guest exchange.

	DHF@CCM-2	**AmPyz@CCM-2**	**2-PDN@CCM-2**	**PMD@CCM-2**	**EtPyz@CCM-1**
Empirical formula	$C_{32}H_{31}EuNO_9$	$C_{25.5}H_{19.5}EuN_{4.5}O_6$	$C_{26.13}H_{21.87}EuN_{1.5}O_{7.5}$	$C_{26}H_{21}EuN_2O_7$	$C_{39}H_{47}LaN_8O_7$
Formula weight	725.54	636.91	628.84	625.41	878.75
Temperature/K	120	120	120	120	120
Crystal system	monoclinic	monoclinic	monoclinic	monoclinic	monoclinic
Space group	*I2*	*C2*	*C2*	*C2*	*I2*
a/Å	14.1106(4)	30.1268(12)	28.1135(8)	28.3639(6)	14.2414(3)
b/Å	8.6017(3)	8.5230(3)	8.5945(2)	8.5824(2)	8.8400(2)
c/Å	25.3269(9)	14.1221(6)	14.1710(4)	14.1169(3)	26.7225(5)
α/°	90	90	90	90	90
β/°	95.8120(10)	116.6914(11)	115.3908(9)	115.5278(7)	91.190(2)
γ/°	90	90	90	90	90
Volume/Å^3	3058.25(18)	3239.7(2)	3093.27(14)	3101.00(12)	3363.48(12)
Z	4	4	4	4	4
ρ_{calc}g/cm^3	1.576	1.306	1.350	1.340	1.735
μ/mm^{-1}	2.106	1.974	2.067	2.061	1.339
F(000)	1460.0	1260.0	1249.0	1240.0	1800.0
Crystal size/mm^3	0.238 × 0.109 × 0.02	0.14 × 0.13 × 0.01	0.17 × 0.16 × 0.01	0.08 × 0.02 × 0.01	0.164 × 0.051 × 0.014
Radiation	Mo Kα (λ = 0.71073)	MoKα (λ = 0.71073)	Mo Kα (λ = 0.71073)	Mo Kα (λ = 0.71073)	Mo Kα (λ = 0.71073)
2Θ range for data collection/°	5.004 to 66.39	5.014 to 59.99	5.004 to 59.996	5.398 to 60	4.854 to 57.398
Index ranges	-20 ≤ h ≤ 21, -13 ≤ k ≤ 13, -38 ≤ l ≤ 38	-42 ≤ h ≤ 42, -11 ≤ k ≤ 11, -19 ≤ l ≤ 19	-39 ≤ h ≤ 39, -12 ≤ k ≤ 11, -19 ≤ l ≤ 19	-39 ≤ h ≤ 39, -12 ≤ k ≤ 12, -19 ≤ l ≤ 19	-19 ≤ h ≤ 19, -11 ≤ k ≤ 11, -36 ≤ l ≤ 36
Reflections collected	60005	41930	36978	56721	54704
Independent reflections	11690 [R_{int} = 0.0390, R_{sigma} = 0.0293]	9416 [R_{int} = 0.0465, R_{sigma} = 0.0407]	8958 [R_{int} = 0.0292, R_{sigma} = 0.0276]	9017 [R_{int} = 0.0491, R_{sigma} = 0.0339]	8682 [R_{int} = 0.0626, R_{sigma} = 0.0447]
Data/restraints/parameters	11690/933/477	9416/163/390	8958/56/389	9017/86/370	8682/286/365
Goodness-of-fit on F^2	1.141	1.085	1.088	1.082	1.043
Final R indexes [I>=2σ (I)]	R_1 = 0.0289, wR_2 = 0.0646	R_1 = 0.0346, wR_2 = 0.0871	R_1 = 0.0247, wR_2 = 0.0607	R_1 = 0.0296, wR_2 = 0.0691	R_1 = 0.0330, wR_2 = 0.0744
Final R indexes [all data]	R_1 = 0.0310, wR_2 = 0.0653	R_1 = 0.0396, wR_2 = 0.0898	R_1 = 0.0255, wR_2 = 0.0610	R_1 = 0.0317, wR_2 = 0.0699	R_1 = 0.0367, wR_2 = 0.0761

Table 2-5. Crystal data for guest@MOF materials that exhibited full guest exchange.

	PYZ@CCM-1	**TAZ@CCM-1**	**TAZ@CCM-3**
Empirical formula	$C_{96}H_{73}La_3N_{16}O_{19}$	$C_{29}H_{24}LaN_{12}O_6$	$C_{54}H_{42}Ce_2N_{18}O_{12}$
Formula weight	2171.43	775.51	1415.29
Temperature/K	120	120.	100
Crystal system	monoclinic	monoclinic	monoclinic
Space group	*C2*	*$P2_1/n$*	*$P2_1/n$*
a/Å	28.3667(15)	14.2957(3)	14.28301(12)
b/Å	8.8133(5)	8.7355(2)	8.72906(8)
c/Å	39.795(2)	25.4778(5)	25.5279(3)
α/°	90	90	90
β/°	104.138(2)	96.3440(10)	96.0891(9)
γ/°	90	90	90
Volume/$Å^3$	9647.6(9)	3162.19(12)	3164.78(4)
Z	4	4	2
$\rho_{calc}g/cm^3$	1.495	1.629	1.485
μ/mm^{-1}	1.380	10.983	1.382
F(000)	4336.0	1548.0	1408.0
Crystal size/mm^3	0.19 × 0.07 × 0.01	0.202 × 0.198 × 0.103	0.168 × 0.051 × 0.015
Radiation	Mo Kα (λ = 0.71073)	Cu Kα (λ = 1.54178)	Synchrotron (λ = 0.6889)
2Θ range for data collection/°	4.222 to 60	10.712 to 157.486	3.038 to 63.854
Index ranges	$-39 \le h \le 39$, $-12 \le k \le 12$, $-55 \le l \le 55$	$-18 \le h \le 17$, $-9 \le k \le 10$, $-32 \le l \le 32$	$-21 \le h \le 20$, $-13 \le k \le 13$, $-38 \le l \le 36$
Reflections collected	124821	30605	52774
Independent reflections	28029 [R_{int} = 0.0643, R_{sigma} = 0.0626]	6680 [R_{int} = 0.0794, R_{sigma} = 0.0536]	10926 [R_{int} = 0.0580, R_{sigma} = 0.0535]
Data/restraints/parameters	28029/131/1268	6680/434/471	10926/426/470
Goodness-of-fit on F^2	1.039	1.109	1.170
Final R indexes [I>=2σ (I)]	R_1 = 0.0567, wR_2 = 0.1361	R_1 = 0.0585, wR_2 = 0.1483	R_1 = 0.1375, wR_2 = 0.3610
Final R indexes [all data]	R_1 = 0.0681, wR_2 = 0.1435	R_1 = 0.0648, wR_2 = 0.1523	R_1 = 0.1412, wR_2 = 0.3620

2.6.5 Guest@MOF ^{1}H NMR Spectroscopy Data

General Methodology for NMR Spectroscopy Data Collection

Guest@MOF single crystals were gently washed with dichloromethane (2 mL) three times to remove any guest molecules on the surface of the MOF. The single crystals were left to dry in air for 10 minutes and subsequently dissolved in d_6-DMSO by adding one drop of concentrated HCl to the mixture. ^{1}H NMR spectroscopy data was subsequently collected.

3-AmPyz@CCM-2

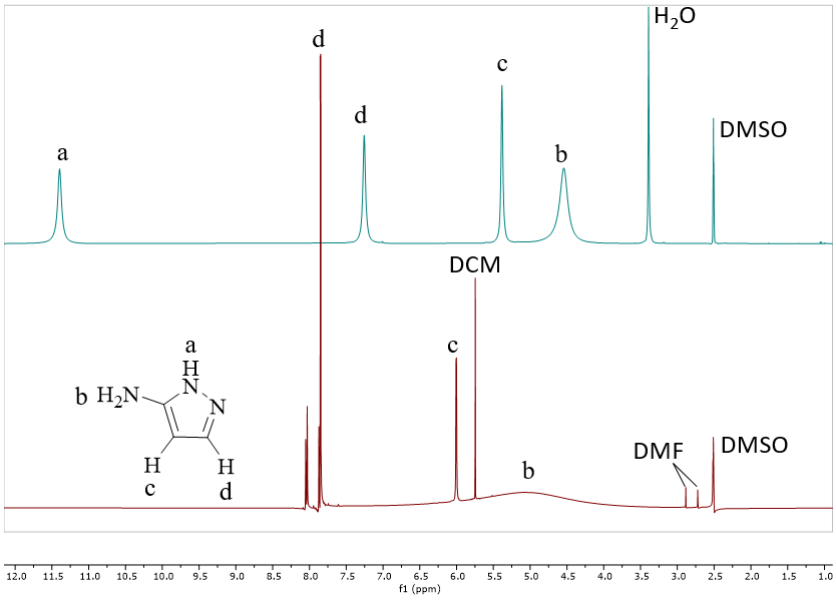

Figure 2-49. ^{1}H NMR spectra of pure 3-aminopyrazole (blue line) and AmPyz@CCM-2 (red line). Solvent residual peaks have been labelled for the solvents that they represent and from herein will only be denoted with an asterisk. Spectra collected using d_6-DMSO as the solvent. Resonance a does not show up on the AmPyz@CCM-2 spectrum due to the presence of TFA acid.

DHF@CCM-2

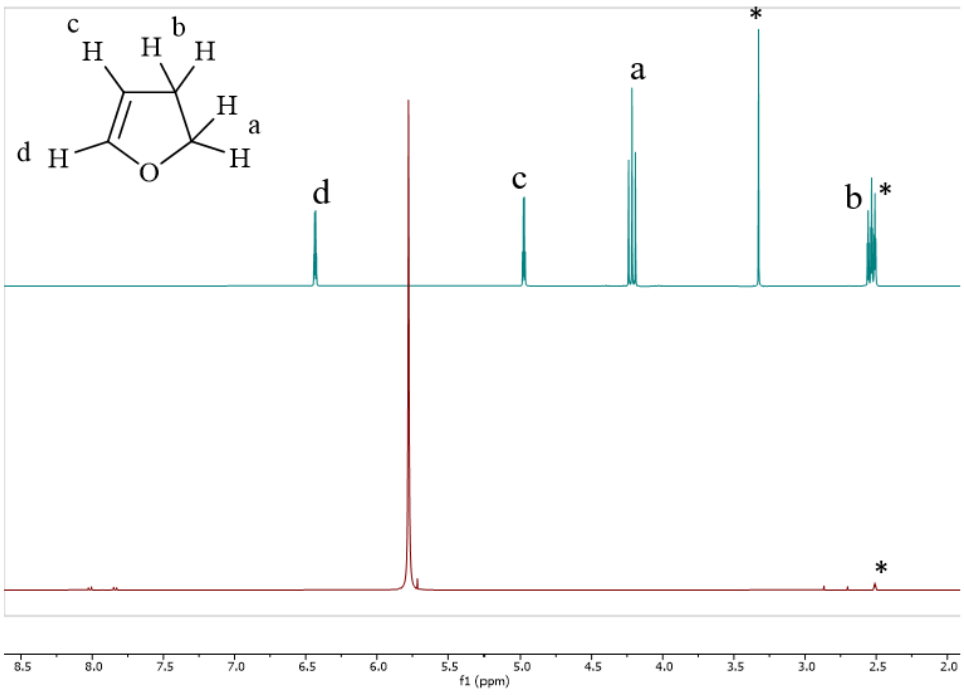

Figure 2-50. ^{1}H NMR spectra of pure 2,3-dihydrofuran (blue line) and DHF@CCM-2 (red line). Spectra recorded in d_6-DMSO. Solvent residual peaks have been labelled with an asterisk.

PMD@CCM-2

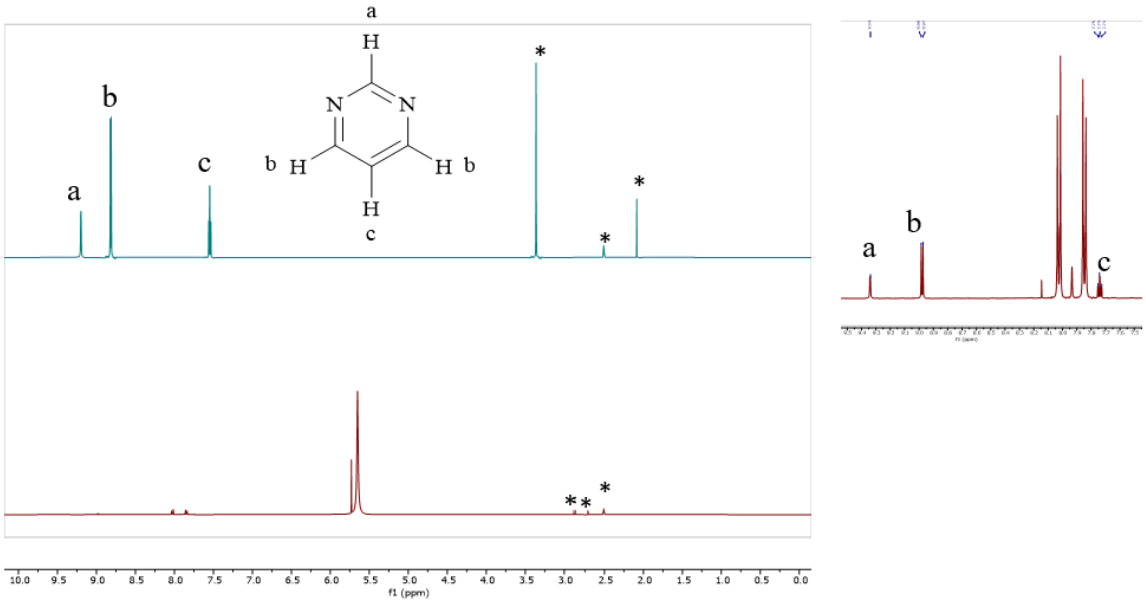

Figure 2-51. ^{1}H NMR spectra of pure pyrimidine (blue line) and PMD@CCM-2 (red line). Spectra collected in d_6-DMSO. Inset on the right: zoomed in image of the region 7.5–9.5 ppm of PMD@CCM-2 spectrum showing resonances corresponding to PMD.

2-PDN@CCM-2

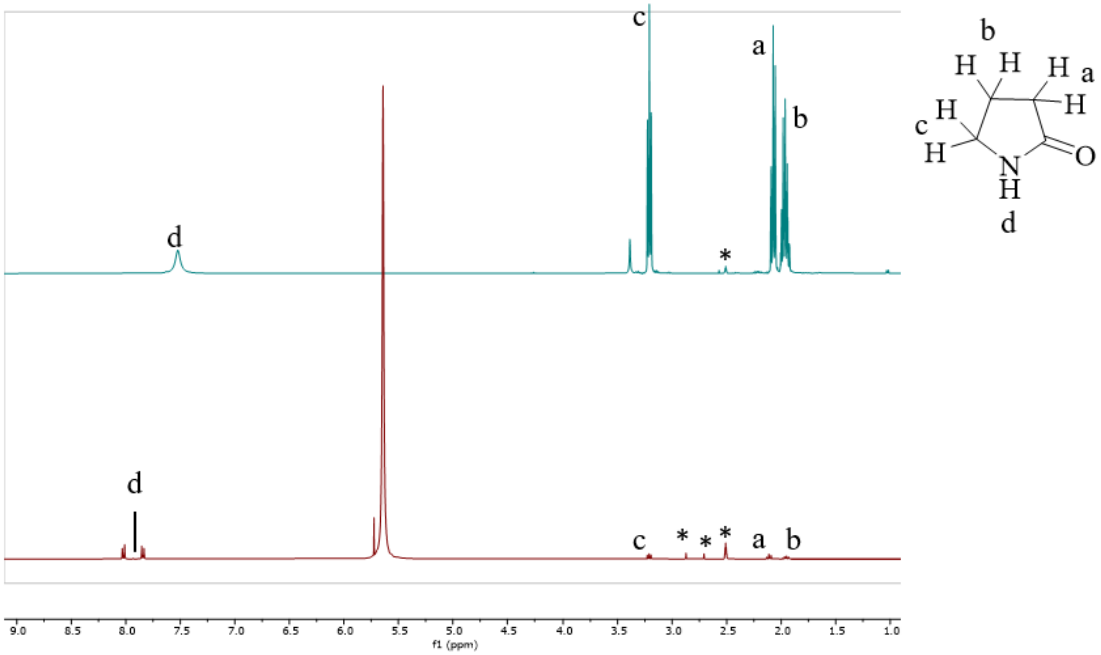

Figure 2-52. ^{1}H NMR spectra of pure 2-pyrrolidinone (blue line) and 2-PDN@CCM-2 (red line). Spectra collected in d_6-DMSO.

EtPyz@CCM-1

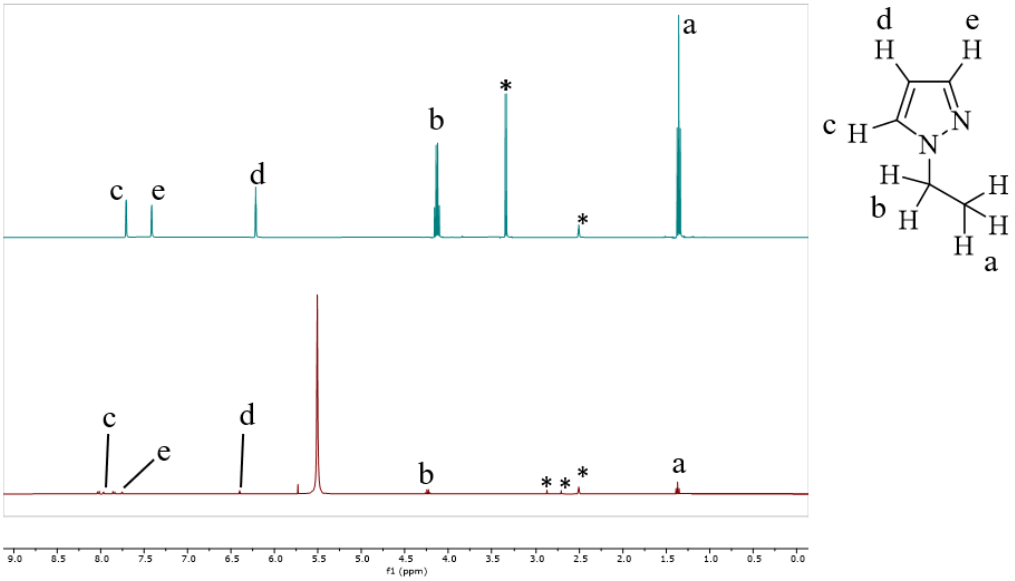

Figure 2-53. ^{1}H NMR spectra of pure 1-ethylpyrazole (blue line) and EtPyz@CCM-1 (red line). Spectra collected in d_6-DMSO.

TAZ@CCM-1

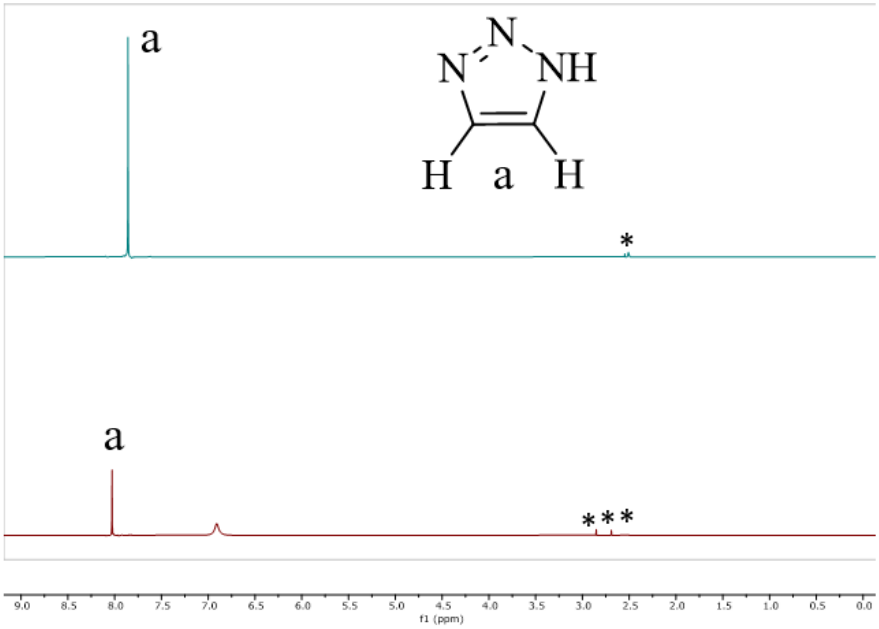

Figure 2-54. ^{1}H NMR spectra of pure 1*H*-1,2,3-triazole (blue line) and TAZ@CCM-1 (red line). The intense peak located at 5.40 ppm on the TAZ@CCM-1 spectrum is due to the protonation of the N=N fragment of TAZ due to the presence of TFA acid. Spectra collected in d_6-DMSO.

2.8 References

1 Y. Inokuma, S. Yoshioka, J. Ariyoshi, T. Arai, Y. Hitora, K. Takada, S. Matsunaga, K. Rissanen and M. Fujita, *Nature*, 2013, **495**, 461–466.

2 M. Hoshino, A. Khutia, H. Xing, Y. Inokuma and M. Fujita, *IUCrJ*, 2016, **3**, 139–151.

3 L. M. Hayes, C. E. Knapp, K. Y. Nathoo, N. J. Press, D. A. Tocher and C. J. Carmalt, *Cryst. Growth Des.*, 2016, **16**, 3465–3472.

4 M. I. Gonzalez, A. B. Turkiewicz, L. E. Darago, J. Oktawiec, K. Bustillo, F. Grandjean, G. J. Long and J. R. Long, *Nature*, 2020, **577**, 64–68.

5 S. M. Towsif Abtab, D. Alezi, P. M. Bhatt, A. Shkurenko, Y. Belmabkhout, H. Aggarwal, Ł. J. Weseliński, N. Alsadun, U. Samin, M. N. Hedhili and M. Eddaoudi, *Chem*, 2018, **4**, 94–105.

6 J. Liu, C. E. Nicholson and S. J. Cooper, *Langmuir*, 2007, **23**, 7286–7292.

7 S. D. Durbin and G. Feher, *Annu. Rev. Phys. Chem.*, 1996, **47**, 171–204.

8 M. Eddaoudi, J. Kim, N. Rosi, D. Vodak, J. Wachter, M. O'Keeffe and O. M. Yaghi, *Science (1979)*, 2002, **295**, 469–472.

9 W. Fan, X. Zhang, Z. Kang, X. Liu and D. Sun, *Coord. Chem. Rev.*, 2021, 443, 213968.

10 H. Li, M. Eddaoudi, T. L. Groy and O. M. Yaghi, *J. Am. Chem. Soc.*, 1997, **120**, 8571–8572.

11 D. Liu, J. P. Lang and B. F. Abrahams, *J. Am. Chem. Soc.*, 2011, **133**, 11042–11045.

12 F. Luo, C. Yan, L. Dang, R. Krishna, W. Zhou, H. Wu, X. Dong, Y. Han, T. L. Hu, M. O'Keeffe, L. Wang, M. Luo, R. B. Lin and B. Chen, *J. Am. Chem. Soc.*, 2016, **138**, 5678–5684.

13 F. Saraci, V. Quezada-Novoa, P. R. Donnarumma and A. J. Howarth, *Chem. Soc. Rev.*, 2020, **49**, 7949–7977.

14 Y. F. Han, X. H. Zhou, Y. X. Zheng, Z. Shen, Y. Song and X. Z. You, *CrystEngComm*, 2008, **10**, 1237–1242.

15 R. Łyszczek and L. Mazur, *Centr. Eur. J. Chem.*, 2012, **10**, 1165–1174.

16 J. Lee, N. W. Waggoner, L. Polanco, G. R. You, V. M. Lynch, S. K. Kim, S. M. Humphrey and J. L. Sessler, *Chem. Commun.*, 2016, **52**, 8514–8517.

17 A. J. R. Thom, E. Regincós Martí, I. Pakamorė, C. Wilson and R. S. Forgan, *Z. Anorg. Allg. Chem.*, 2022, **648**, e202200171.

18 G. Zahn, P. Zerner, J. Lippke, F. L. Kempf, S. Lilienthal, C. A. Schröder, A. M. Schneider and P. Behrens, *CrystEngComm*, 2014, **16**, 9198–9207.

19 R. S. Forgan, *Chem. Sci.*, 2020, 11, 4546–4562.

20 G. B. Deacon and R. J. Phillips, *Coord. Chem. Rev.*, 1980, **33**, 227–250.

21 P. R. Donnarumma, C. Copeman, M. Richezzi, J. Sardilli, H. M. Titi and A. J. Howarth, *Cryst. Growth Des.*, 2024, **24**, 1619–1625.

22 W. Gong, Z. Chen, J. Dong, Y. Liu and Y. Cui, *Chem. Rev.*, 2021, 122, 9078–9144.

23 A. Schoedel, M. Li, D. Li, M. O'Keeffe and O. M. Yaghi, *Chem. Rev.* , 2016, **116**, 12466–12535.

24 K. Binnemans and C. Görrler-Walrand, *Chem. Phys. Lett.*, 1995, **235**, 163–174.

25 M. Rahm, R. Hoffmann and N. W. Ashcroft, *Chem. - Eur. J.*, 2016, **22**, 14625–14632.

26 V. A. Blatov, A. P. Shevchenko and D. M. Proserpio, *Cryst. Growth Des.*, 2014, **14**, 3576–3586.

27 C. Bonneau, M. O'Keeffe, D. M. Proserpio, V. A. Blatov, S. R. Batten, S. A. Bourne, M. S. Lah, J. G. Eon, S. T. Hyde, S. B. Wiggin and L. Öhrström, *Cryst. Growth Des.*, 2018, **18**, 3411–3418.

28 H. Kim, Y. Nguyen, A. J. Lough and J. Chin, *Angew. Chem. Int. Ed.*, 2008, **47**, 8678–8681.

29 H. Borrmann, I. Persson, M. Sandström and C. M. V Stålhandske, *J. Chem. Soc., Perkin Trans. 2*, 2000, **2000**, 393–402.

30 M. B. Majewski, A. J. Howarth, P. Li, M. R. Wasielewski, J. T. Hupp and O. K. Farha, *CrystEngComm*, 2017, **19**, 4082–4091.

31 Y. Yu, W. Zhang and D. Mei, *J. Phys. Chem. C*, 2022, **126**, 1204–1214.

32 N. Hanikel, M. S. Prévot and O. M. Yaghi, *Nat Nanotechnol*, 2020, **15**, 348–355.

33 Y. Q. Hu, M. Q. Li, Y. Wang, T. Zhang, P. Q. Liao, Z. Zheng, X. M. Chen and Y. Z. Zheng, *Chem. Eur. J.*, 2017, **23**, 8409–8413.

34 S. Kim, Hyunho, Yang, S. R. Rao, S. Narayanan, E. A. Kapustin, H. Furukawa, A. S. Umans, O. M. Yaghi and E. N. Wang, *Science*, 2017, **434**, 430–434.

35 D. Balestri, P. P. Mazzeo, R. Perrone, F. Fornari, F. Bianchi, M. Careri, A. Bacchi and P. Pelagatti, *Angew. Chem. Int. Ed.*, 2021, **60**, 10194–10202.

36 W. Wang, X. H. Xiong, N. X. Zhu, Z. Zeng, Z. W. Wei, M. Pan, D. Fenske, J. J. Jiang and C. Y. Su, *Angew. Chem. Int. Ed.*, 2022, **61**, e202201766.

37 J.-C. G. Bünzli, J.-P. Metabanzoulou, P. Froidevaux and L. Jin, *Inorg. Chem*, 1990, **29**, 3875–3881.

38 H. Reuter, *Acta Crystallogr., Sect. E: Crystallogr. Commun.*, 2017, **73**, 1405–1408.

39 G. Kastner and H. Reuter, *Main Group Met. Chem.*, 1999, **22**, 605–609.

40 F. D. Rochon and R. Melanson, *Can. J. Chem.*, 1975, **53**, 2371–2374.

41 R. Thomas, C. Brink Shoemaker and K. Eriks, *Acta Cryst.*, 1966, **21**, 12–20.

42 K. Binnemans, *Coord. Chem. Rev.*, 2015, 295, 1–45.

43 A. H. Malik and P. K. Iyer, *ACS Appl. Mater. Interfaces*, 2017, **9**, 4433–4439.

44 A. L. Spek, *Acta Crystallogr.. Sect. C: Struct. Chem.*, 2015, **71**, 9–18.

45 R. G. Pearson, *J. Am. Chem. Soc.*, 1963, **85**, 3533–3539.

46 K. P. Kepp, *Inorg. Chem.*, 2016, **55**, 9461–9470.

47 B. E. Borello, A. Zecchina and E. Guglielminotti, *J. Chem. Soc. B*, 1969, **8**, 307–311.

48 F. Billes, H. Mikosch and S. Holly, *J. mol. Structur.: THEOCHEM*, 1998, **423**, 225–234.

49 A. J. Blake and D. W. H. Rankin, *Acta Cryst.*, 1991, **C47**, 1933–1936.

50 M. Podsiadlo, K. Jakobek and A. Katrusiak, *CrystEngComm*, 2010, **12**, 2561–2567.

51 K. M. Steed and J. W. Steed, *Chem. Rev.*, 2015, **115**, 2895–2933.

52 R. J. Davey, S. L. M. Schroeder and J. H. Ter Horst, *Angew. Chem., Int. Ed.*, 2013, **52**, 2166–2179.

53 R. Goddard, O. Heinemann and C. Krüger, *Acta Cryst.*, 1997, **C53**, 1846–1850.

54 A. Woods-Ryan, C. L. Doherty and A. J. Cruz-Cabeza, *CrystEngComm*, 2023, **25**, 2845–2858.

55 A. R. Oganov, C. J. Pickard, Q. Zhu and R. J. Needs, *Nat. Rev. Mater.*, 2019, 4, 331–348.

56 J. E. Carpenter and M. Grünwald, *J. Am. Chem. Soc.*, 2021, **143**, 21580–21593.

57 J. Hoja, H.-Y. Ko, M. A. Neumann, R. Car, R. A. Distasio and A. Tkatchenko, *Sci. Adv.*, 2019, **5**, eaau3338.

Chapter 3 – Naphthalenediimide-Based Metal-Organic Frameworks for the Capture of Molecular Clusters

3.1 Introduction

In the design of metal-organic frameworks (MOFs), organic linkers, in conjunction with strategically chosen secondary building units (SBUs), are essential for targeting framework underlying topologies, shapes and sizes.[1] Predominantly, organic linkers with carboxylate functional groups serve as the most common linkers of choice and exhibit versatility in their design – commonly ranging from ditopic to hexatopic linkers.[1] While a large proportion of MOFs are made up by an organic linker bridging together metal SBUs, the synthesis of MOFs containing a mixture of organic linkers[2], and a mixture of metals[3], has also been popularised – an effective approach towards synthesising multifunctional MOFs. Additionally, the isoreticular expansion method is a prominent part of reticular chemistry that is used towards synthesising isomorphous MOFs with increasing pore sizes.[4,5] While all of the above factors play a role in the properties that a MOF can exhibit, this study aimed to expand on the tunability of MOF pores, in the context of studying molecular clusters in framework voids. This can be achieved by utilising a structurally different linker from that of 4,4'-biphenyldicarboxylic acid (H_2BPDC) discussed in the previous chapter. In the CCM-series MOFs, it was observed that the pore size limits the size of the molecular clusters confined within. However, it was impossible to study the effect of the pore shape due to the isomorphous structure of the CCM-1–4 MOFs. Thus, this chapter aims to design a MOF with a different underlying topology and larger pores to expand in order to study how the size and shape of MOF pores affects the formation of molecular clusters and to expand the size of confined clusters.

Among the organic linkers that are structurally and geometrically different from H_2BPDC, *N*,*N*'-bis(5-isophthalic acid)naphthalenediimide (**3.3**) stands out. Larger in size, **3.3** could potentially yield MOFs with larger pores than those of CCM-series frameworks. This work describes the synthesis and characterisation of a novel interpenetrated MOF, designated as CCM-5, which incorporates **3.3** combined with mono- and dinuclear zinc(II) SBUs. While in general interpenetration tends to increase the packing efficiency of a framework and results in microporous MOFs[6] and can be designed for efficient capture of small gases[7], CCM-5 exhibits partial interpenetration and as a result contains pores capable of encapsulating molecular clusters. Three lanthanum(III)-based MOFs (CCM-6–8) with the linker **3.3** are also

reported in this work. While the structure of the frameworks could be precisely modelled, any attempts at modelling the solvent molecules in the pores were unsuccessful.

3.2 Synthesis and Characterisation of CCM-5

3.2.1 Synthesis and Characterisation of the Organic Linker

The synthesis of the organic linker **3.3** was accomplished by following a literature procedure with slight modifications involving refluxing the reactants in DMF, as shown in **Scheme 3-1**.[8] This work employs the wet chemistry approach, although liquid-assisted grinding has also been documented as an alternative for the synthesis of **3.3**.[9] In a typical synthesis, 20 mL of DMF, 4.2 mmol of 5-aminoisophthalic acid and 2.0 mmol of naphthalene-1,4,5,8-tetracarboxylic acid dianhydride are mixed. Upon the addition of both starting materials, the mixture turns red and is subsequently heated up to 110°C. The reaction mixture is refluxed for 6–8 hours after which an off-white-coloured solid precipitates out of the solution. Further precipitation is induced by adding deionised water and the final precipitate is isolated by vacuum filtration. The precipitate is then washed with ethanol and dried under vacuum using an Abderhalden's drying pistol at 110 °C for 2 days, resulting in a white product. The product was characterised using FT-IR and NMR spectroscopy, elemental analysis and SC-XRD.

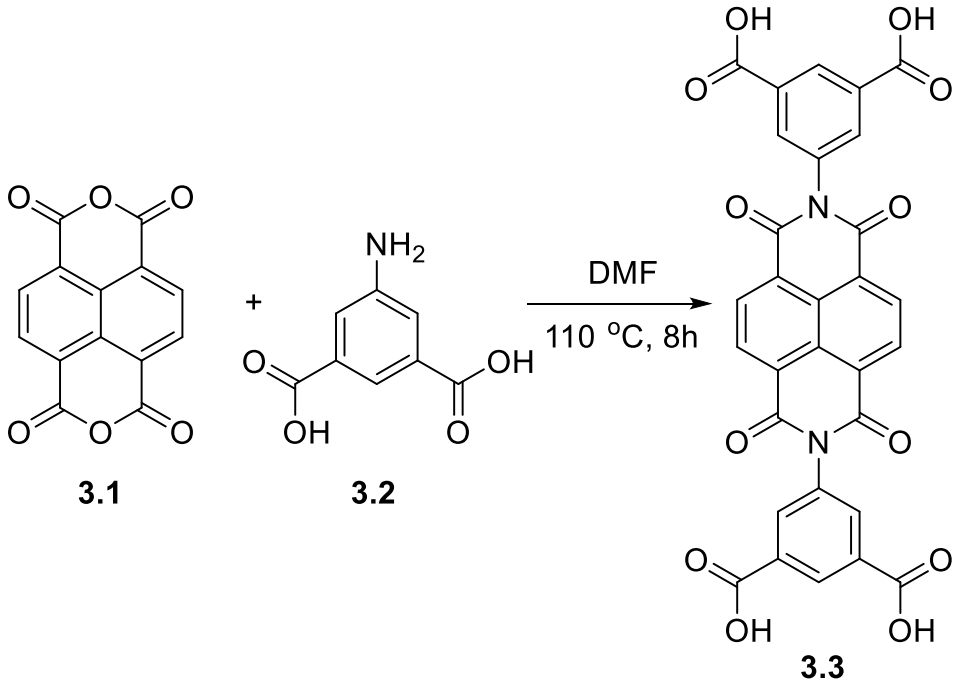

Scheme 3-1. General synthetic procedure for the synthesis of N,N'-bis(5-isophthalic acid)naphthalenediimide (**3.3**) from **3.1** and **3.2**.

Figure 3-55 shows the FT-IR spectra of **3.1**, **3.2** and **3.3**. The spectrum of **3.3** exhibits a wide band ranging from 3080 to 2529 cm^{-1} which is attributed to the O–H stretching of the carboxylic acid groups. Additionally, the band at 1034 cm^{-1} on the spectrum of **3.1**, which is attributed to the C–O stretching of the dianhydride, disappears. It is replaced with the band centred at 1348 cm^{-1} on the **3.3** spectrum which belongs to the C–N stretching of the naphthalenediimide moiety and is observed at a slightly higher wavenumber of 1402 cm^{-1} in the spectrum of **3.2**. A strong band centred at 1667 cm^{-1} in **3.3** is attributed to the asymmetric stretching of the carboxylic acid C=O and the shoulder (1707 cm^{-1}) of this band belongs to the C=O stretching of the carbonyl groups on the NDI moiety. Overall, the IR spectrum of **3.3** indicates successful synthesis of the organic linker. Additionally, the spectrum of **3.3** agrees well with the values reported in the literature, further corroborating its successful synthesis.[10] Additionally, elemental analysis of the dried product closely matches with its expected composition (see experimental section).

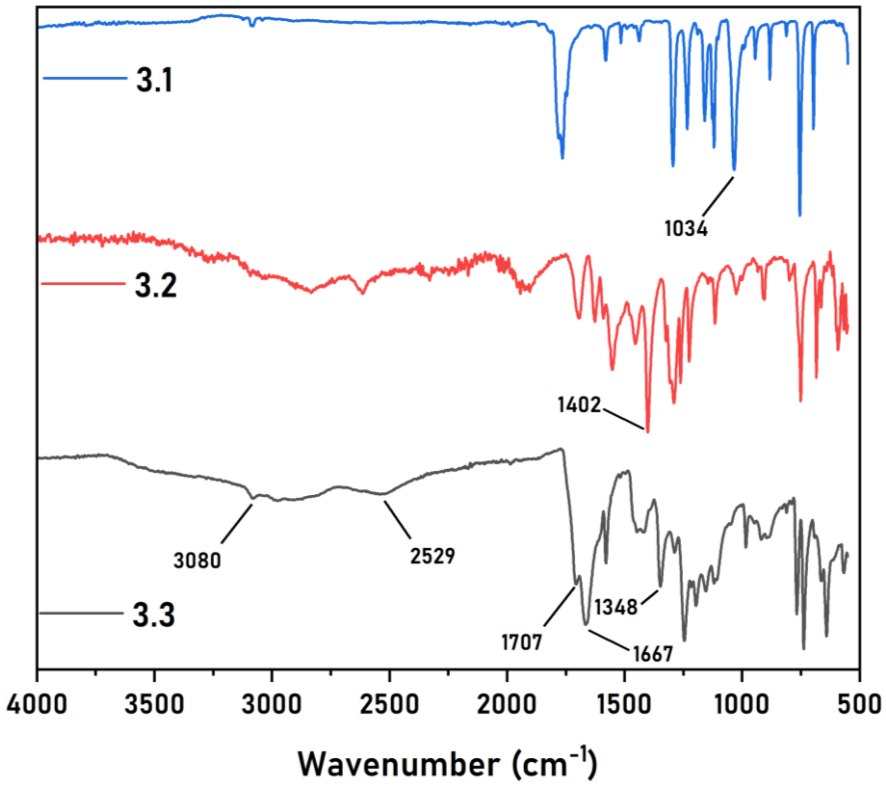

Figure 3-55. FT-IR spectra of **3.1** (blue line), **3.2** (red line) and **3.3** (black line).

To further support these observations, NMR spectroscopy was undertaken. **Figure 3-56** depicts the ^{1}H NMR spectrum of the organic linker collected in deuterated DMSO. Solvent residual resonances are labelled with an asterisk and appear at their expected chemical shifts – resonances attributed to ethanol are located at 1.06, 3.44 and 4.63 ppm while those of water

and DMSO are located at 3.33 and 2.50 ppm. A notable feature in the NMR spectrum is the absence of the resonance at 5.62 ppm belonging to the amine NH protons of 5-aminoisophthalic acid (see experimental section 3.6.1, **Figure 3-76**, blue trace). This absence signifies the successful coupling reaction between **3.1** and **3.2**. Furthermore, three distinct resonances in the aromatic region are observed at 8.35, 8.59 and 8.75 ppm and yield an integration ratio of 4:2:4. This ratio aligns with the expected ratios of the hydrogen atoms on the benzene and naphthalene rings. The singlet at 8.75 is assigned to the protons on the naphthalene ring while the triplet and doublet at 8.35 and 8.59 ppm belong to the benzene protons labelled as **a** and **c**, respectively. **Figure 3-77** further illustrates these aromatic region resonances, providing detailed peak positions and integration values. A small peak located at 13.51 belongs to the proton on the carboxylic acid. These observations support the conclusions drawn from the FT-IR spectra and align closely with the reported values.[11]

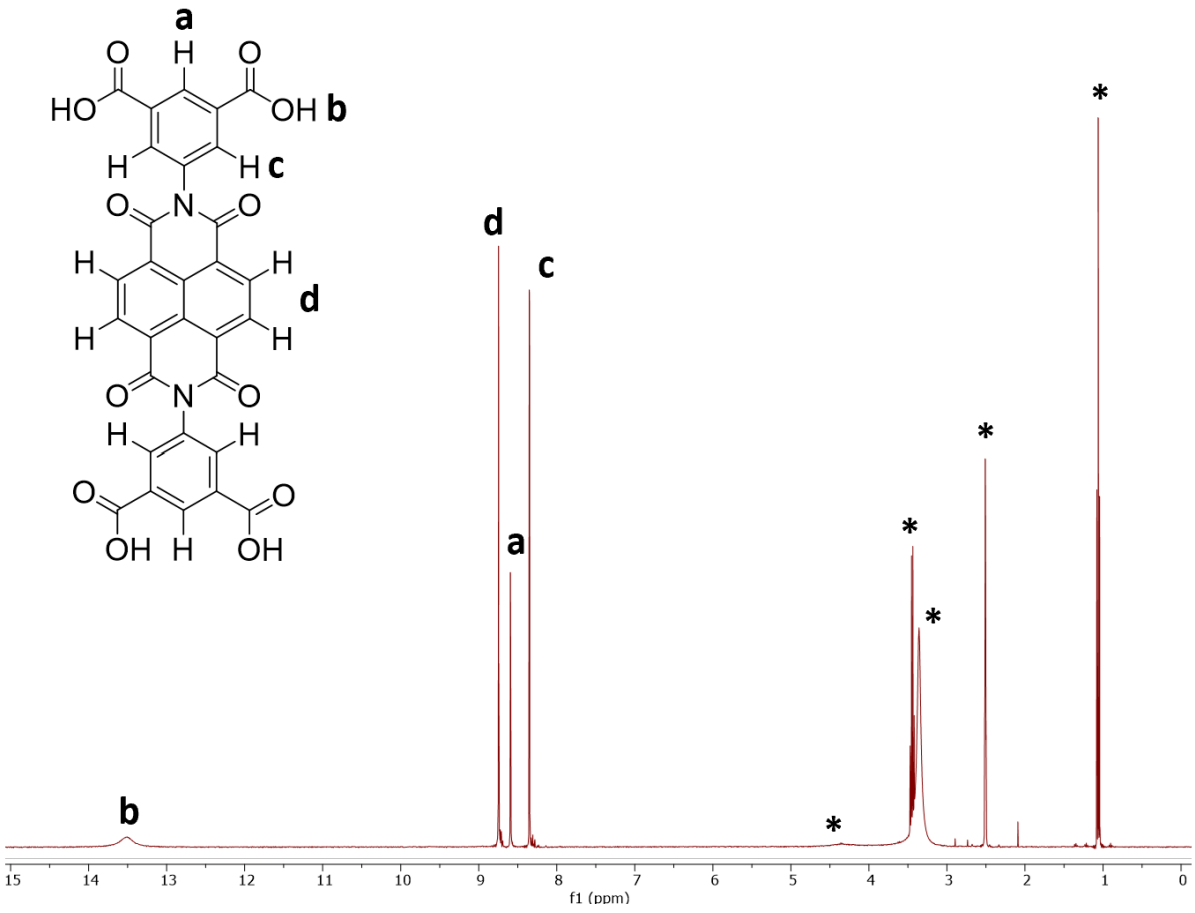

Figure 3-56. ^{1}H NMR spectrum of **3.3**. Spectrum acquired in d_6-DMSO and all solvent peaks have been labelled with an asterisk.

The single crystal structure of **3.3** was reported in 2015 when single crystals of the compound were obtained from DMF.[12] As the exact method was not specified in the work from 2015 and recrystallisation from DMF did not yield single crystals, a different approach was

undertaken. In this work, single crystals of **3.3** were obtained using the vapour diffusion method. For this process, a saturated 0.5 mL DMSO solution containing **3.3** was prepared in a vial. This vial was then placed in a larger, capped vial containing 2 mL of deionised water. Over the course of several days, slow diffusion of water into the DMSO solution resulted in the formation of colourless needle-shaped crystals. SC-XRD analysis of these crystals reveals that the asymmetric unit contains six DMSO molecules and one molecule of **3.3**. Owing to the high disorder of two DMSO molecules, they were masked in the crystal structure.[13] The highly disordered solvent molecules are located between the planar parts of adjacent molecules of **3.3** while the other four are linked to the main molecule by O–H···O hydrogen bonds, shown as red dashed lines in **Figure 3-57a**. These hydrogen bonds are the main stabilising interactions in this crystal structure as adjacent molecules of **3.3** are spaced too far apart for any hydrogen bonding or π–π interactions to be present. It is likely that these hydrogen bonding interactions are responsible for the packing arrangement because when **3.3** is crystallised from DMF, the naphthalenediimide moieties participate in π–π stacking with a distance of 3.3 Å.[12] **Figure 3-57b** illustrates the conformation of **3.3** with the terminal benzene-derived rings perpendicular to the naphthalenediimide moiety. Overall, these results further support the successful synthesis of the organic linker.

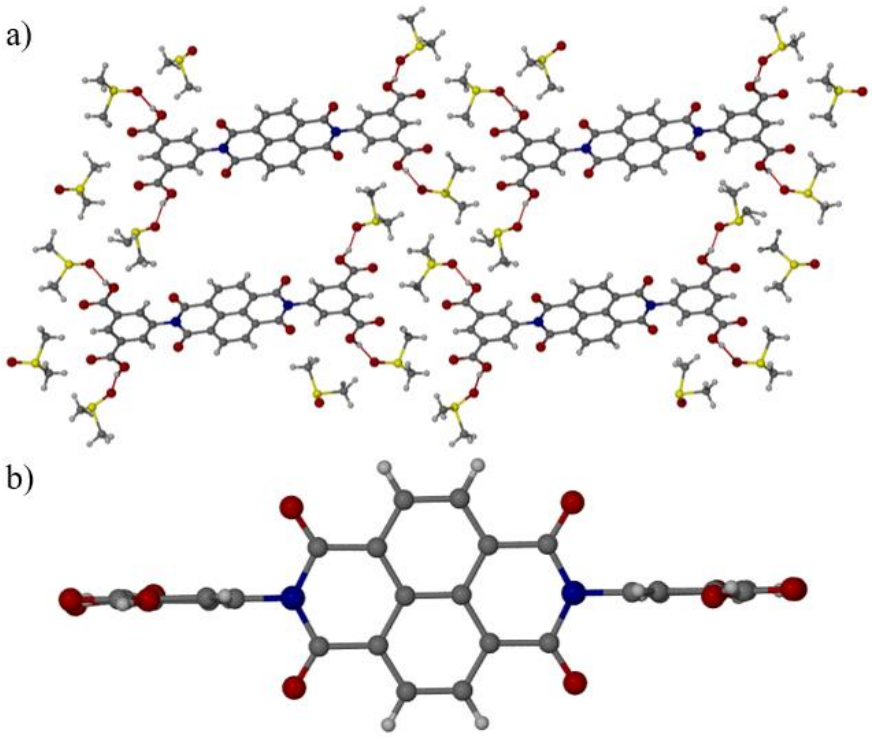

Figure 3-57. Single crystal structure of **3.3** showing a) the view of the unit cell along the *b* axis and b) conformation of the organic linker. Red dashed lines indicate hydrogen bonding interactions Grey: C. White: H. Red: O. Blue: N. Yellow: S.

3.2.2 Synthesis and Characterisation of CCM-5 MOF

Similarly to the synthesis of CCM-1–4 MOFs, the synthesis of a MOF derived from **3.3** and zinc(II) was undertaken using the solvothermal method. In the general procedure, a 10 mL solution of DMF containing zinc(II) nitrate hexahydrate and **3.3** in a desired ratio was prepared in a vial. To this mixture, 0.1 mL of TFA was added and the mixture was sonicated for 5 minutes and poured into an acid digestion vessel. The vessel was placed in an isothermal oven at 120°C for 72 hours, followed by slowly cooling it to room temperature over the course of 6 hours. A range of ratios of zinc(II) : **3.3** were tried – from 2:1 to 4:1 of metal-to-ligand. Each reaction yielded a product which was characterised *via* PXRD. The products from the 3:1 and 4:1 zinc(II):**3.3** reactions appeared relatively crystalline (experimental section 3.6.2, **Figure 3-78**). However, the 3:1 reaction did not produce any single crystals while that of 4:1 did (**Figure 3-58** a and b). More specifically, the 4:1 reaction resulted in the formation of dark poorly crystalline material along with brown-coloured plate-like single crystals designated as CCM-5. The as-synthesised crystals were characterised *via* PXRD, SC-XRD, thermogravimetric analysis, FT-IR and NMR spectroscopy.

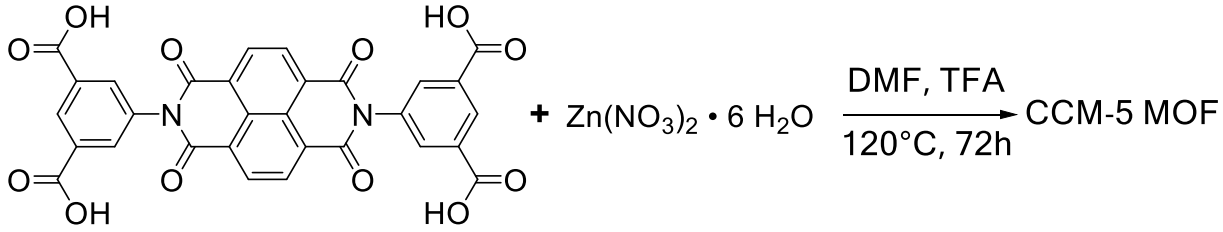

Scheme 3-2. General synthetic procedure for the preparation of the novel zinc-based MOF CCM-5.

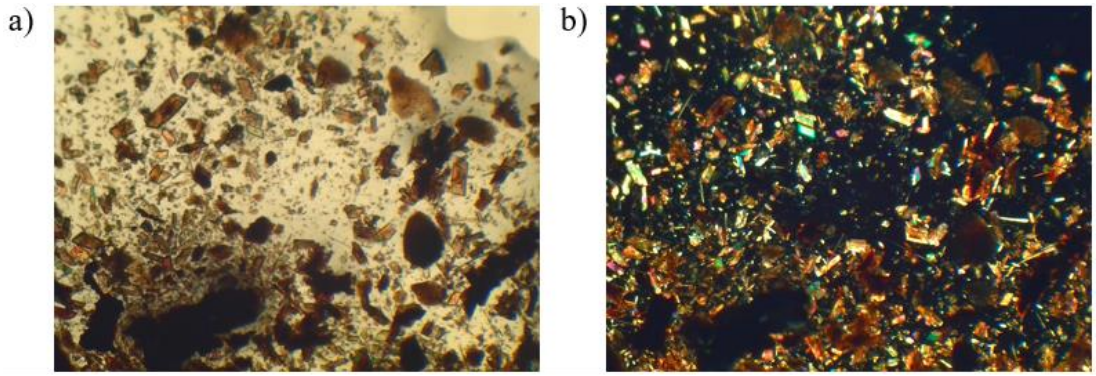

Figure 3-58. Optical microscopy images of single crystals of CCM-5 along with the dark amorphous product.

The FT-IR spectrum of the as-synthesised single crystals of CCM-5 is shown in **Figure 3-59a**. The appearance of bands centred at 2931 and 2862 cm^{-1} assigned to DMF C–H stretching indicates that, similarly to the CCM-series MOFs, DMF solvent molecules are either

encapsulated and/or coordinated inside the framework. Additionally, the bands centred at 1707 and 1667 cm^{-1} corresponding to the C=O stretching of the free acid (**Figure 3-59a**, black line) have shifted to 1715 and 1656 cm^{-1}, respectively, indicating that coordination bonds have formed between zinc(II) and **3.3**. On the other hand, the wide band attributed to the carboxylic acid O–H stretching has slightly diminished but still exists (**Figure 3-59a**, red line). Due to the large excess of metal ions in this reaction (4:1 M:L), it is unlikely that there is unreacted **3.3** present. Rather, this could indicate that while coordination bonds have formed between the carboxylic acid moieties and zinc(II), some organic linkers have not fully been deprotonated and exist in their protonated form as part of the framework structure. The TGA trace of CCM-5 is shown in **Figure 3-59b**, collected from room temperature up to 600°C under nitrogen atmosphere. A gradual weight loss of 22% up to 380°C is attributed to solvent loss from the pores of CCM-5. This is followed by the framework decomposition where a further 60% of weight is lost by 540°C.

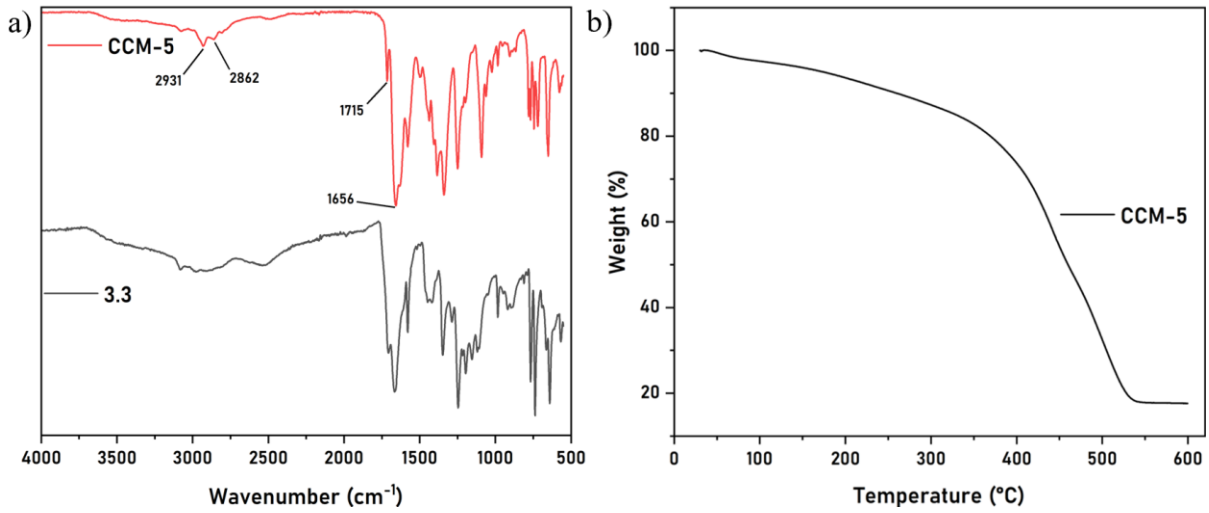

Figure 3-59. a) FT-IR spectra of MOF CCM-5 (red line) and organic linker **3.3** (black line) and b) TGA thermogram of CCM-5.

Figure 3-60 shows the experimental and simulated PXRD patterns of the as-synthesised single crystals. Good agreement is observed between the calculated and experimental patterns, especially for the low angle peaks indicating high bulk purity. A slight shift to a lower angle diffraction is observed in the experimentally obtained diffractogram. This is due to the data being collected at room temperature while the SC-XRD analysis was undertaken at 120K which results in a slight contraction of the unit cell and subsequently peaks at a slightly higher angle. The plank-shaped crystals exhibit preferred orientation similarly to the CCM-1–4 MOF single crystals. However, compared to the CCM-1–4 single crystals, this material appears to be slightly less crystalline as the peaks appear less sharp.

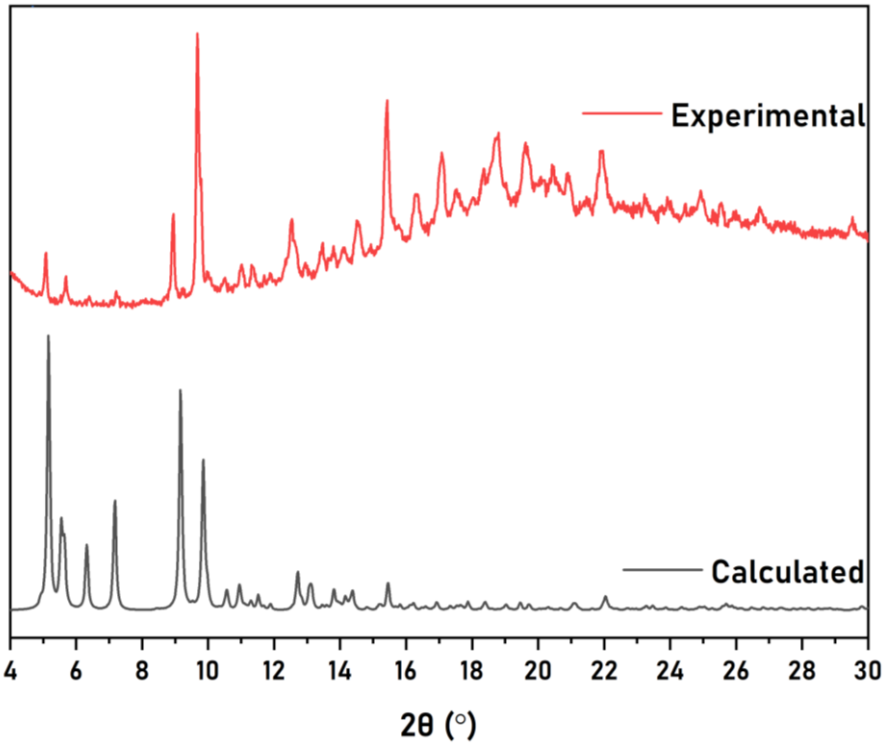

Figure 3-60. Powder X-Ray diffraction spectra of the as-synthesised single crystals (red pattern) and the calculated pattern obtained from single crystal X-ray diffraction analysis (black pattern).

Solution-state ^{1}H NMR spectroscopy was also employed to further characterise the as-synthesised single crystals (**Figure 3-61**). Similarly to the CCM-1–4 MOFs, full dissolution of CCM-5 crystals in d_6-DMSO was ensured by the addition of one drop of concentrated hydrochloric acid. The presence of signals attributed to the protons of **3.3** (8.32, 8.56 and 8.72 ppm) are observed in similar locations to the ones in the spectrum of the free linker (**Figure 3-56**) and closely match the values reported in the literature. An additional intense resonance at 5.45 ppm corresponds to that water from hydrochloric acid.

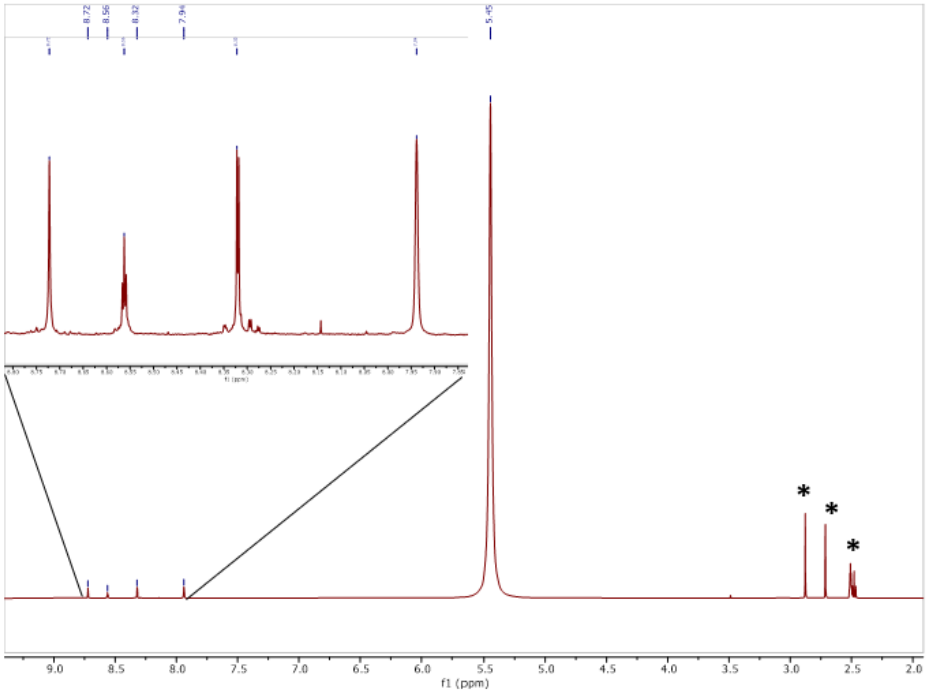

Figure 3-61. ^{1}H NMR spectrum of CCM-5 dissolved in d_6-DMSO including a zoom in of the region 7.94–8.72 ppm. Asterisks denote resonance peaks attributed to solvents.

The initial SC-XRD analysis of CCM-5 single crystals using a molybdenum Kα source provided sufficient data quality to resolve the structure of the framework. However, the data suffered from very low intensity of high angle ($2\theta > 40°$) reflections and any pore contents could not be modelled. With the aim of obtaining higher quality data, the single crystals were analysed using the synchrotron source on the I19 instrument at the Diamond Light Source (DLS). Unfortunately, the quality of data collected from DLS was of similar quality as that collected using the molybdenum Kα source. Encouragingly, however, the data collected from both sources yield identical structures. Thus, herein the discussion will be undertaken regarding the data collected from DLS. The crystal structure analysis reveals that the single crystals comprise a topologically complicated zinc MOF with an empirical formula $Zn_3(\mathbf{3.3}^{3-})_2$, **Figure 3-62**. The product crystallizes in the centrosymmetric *P*-1 space group and the asymmetric unit of CCM-5 contains three zinc metal centres and three anions of **3.3** (one full and two half molecules), resulting in a 1.5:1 ratio of metal:ligand (M:L). This is significantly lower than the ratio used for the synthesis (4:1 M:L). Attempts to replicate the synthesis at a 1.5:1 M:L ratio did not yield any single crystals. A detailed discussion on efforts to reproduce the synthesis of CCM-5 MOF single crystals is undertaken in Section 3.2.3.

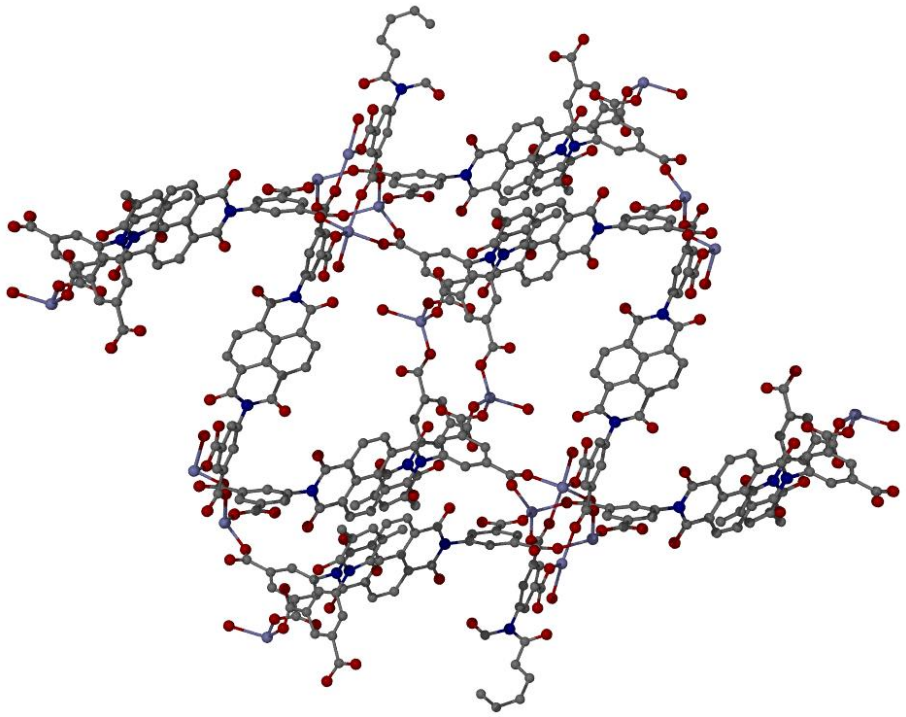

Figure 3-62. Single crystal structure of the unit cell of CCM-5 along the crystallographic *a* axis. Hydrogen atoms have been omitted for clarity. Grey: C. Red: O. Blue: N. Light purple: Zn. Hydrogen atoms omitted for clarity.

The Zn–$O_{3.3}$ coordination bond lengths vary over a range of 1.808(10) – 2.103(5) Å and the two Zn–O_{H2O} coordination bonds lengths are 2.071(6) and 2.144(11) Å. The metal centres in CCM-5 exhibit two different types of coordination modes where two of the three unique zinc(II) metal centres are 4-coordinate while the other is 5-coordinate. These two different coordination modes do not result in SBU clusters unlike some MOFs where metal centres exhibit different coordination modes.[14] Instead, CCM-5 exhibits mono- and binuclear SBUs as pictured in **Figure 3-63 a** and **b**. In the case of the binuclear SBU, the zinc(II) metal centres are 4- and 5-coordinated and adopt tetrahedral and distorted trigonal bipyramidal geometries, respectively. Both metal centres are coordinated to four different organic ligands and an additional water molecule is connected to one of the axial positions of the 5-coordinated zinc(II) centre. Overall, the two metal centres in the binuclear SBUs are connected by three organic linkers. In contrast, all mononuclear SBUs take on the tetrahedral geometry where one coordination bond is formed with the oxygen atom of a water molecule and the others come from the carboxylates of the organic linker (**Figure 3-63c**).

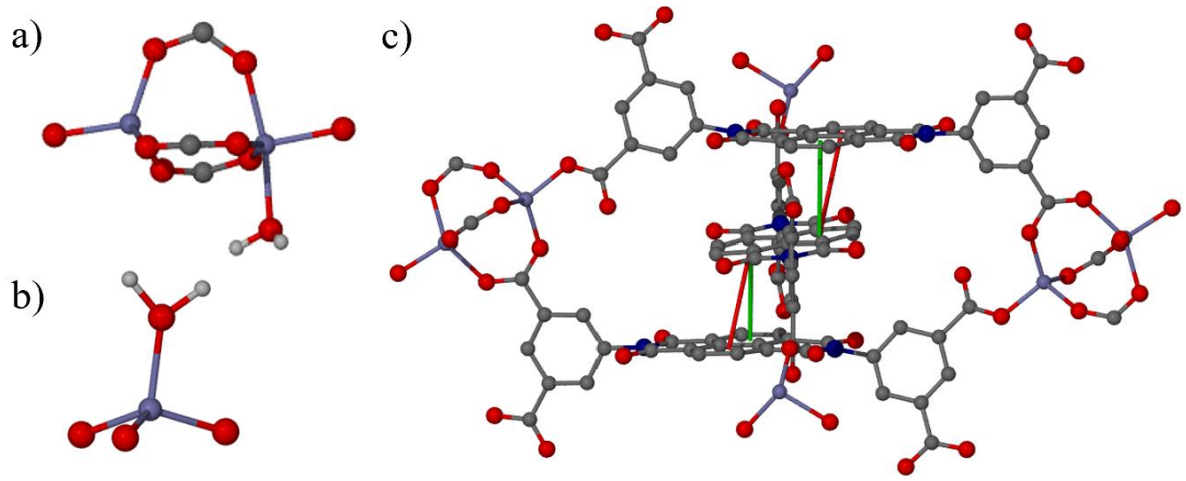

Figure 3-63. Secondary building units contained in the CCM-5 showing the a) dinuclear SBU and b) mononuclear SBU. c) Crystal structure of CCM-5 showing the interpenetration of **3.3**$^{2-}$ linkers and how they bridge the SBUs. Red and green solid lines indicate π–π interactions between the naphthalene moieties of **3.3**. Gray: C. Red: O. Blue: N. Purple: Zn. Hydrogen atoms omitted in c) for clarity.

Figure 3-63c shows the single crystal structure of CCM-5 as an interpenetrated MOF consisting of mono- and binuclear SBUs. This structure features two linkers of **3.3** interconnected *via* binuclear SBUs, with an additional ligand of **3.3** threading through them, facilitating π–π interactions between the linkers. Specifically, two distinct π–π interactions are observed between the naphthalene moiety of the threading linker and the linkers adjacent to it. These π–π interactions exhibit distances of 3.509(4) and 3.659(3) Å and are shown in solid red and green lines in **Figure 3-63c**. The orientation of the threading linker is slightly tilted, optimising the π–π interaction distances compared to a parallel alignment of the linker to its adjacent counterparts. These π–π interactions, outside of coordination bonds between metal centres and **3**, likely play an important role in stabilising the framework. The π–π interaction distances were measured by determining the interplanar distances between each of the fused benzene rings of the naphthalene moieties.

As the asymmetric unit contains three zinc(II) ions, the organic linker must balance this 6+ charge. Initially, the presence of fully deprotonated linkers of **3.3** with a 4- charge alongside two oxonium ions was considered to offset the 6+ charge from the zinc(II) ions. However, the absence of the asymmetric bending mode (υ_4) in the 1720–1740 cm^{-1} region, characteristic to oxonium ions, in the FT-IR spectrum of CCM-5 negates this scenario.[15] Another possibility is that there are no other ions present and the organic linkers exhibit either a 3– charge or a 4– and a 2– charge per asymmetric unit, *i.e.* the carboxylate groups are only partially deprotonated.

This possibility is supported by the FT-IR spectrum of CCM-5 which contains a smaller band attributed to the carboxylic acid stretching (3080–2529 cm^{-1}) as compared to the spectrum of the ligand **3.3**.

Measuring the C–O distances in CCM-5 could indicate which specific carboxylic acids could still be protonated. **Table 3-6** highlights the C–O and C=O bond lengths in **3.3** and CCM-5. The values that are next to each other are the bond lengths of a carboxylic acid group acid associated with the same carbon atom. For example, the values 1.292(14) and 1.223(12) Å belong to one particular carboxylic acid in the crystal structure of **3.3**, followed by three others. According to **Table 3-6**, the C–O bond lengths of free ligand **3.3** range from 1.292(14) to 1.344(13) Å while the C=O bond length ranges from 1.209(11) to 1.233 Å. As expected, the C=O bond lengths are significantly shorter as a result of the double bond between the carbon and the oxygen atoms. The longest C–O bond length in CCM-5 is 1.297(8) Å, which falls in the C–O bond length range measured in the crystal structure of **3.3**. This suggests that this particular carboxylic acid group could still be protonated. The second longest C–O bond length is that of 1.272(4) Å which falls outside of the range of protonated C–O bond length found in **3.3**. However, it does not necessarily rule out the presence of another protonated carboxylic acid group. Searching for zinc(II)-coordinated protonated carboxylic acids with the C–O bond length between 1.26 – 1.29 Å in the Cambridge Structural Database[16] (CSD, version 2023.3) yields 56 hits, a number of which four are MOFs.[17–20] Finally, **Table 3-6** shows that some C–O and C=O bond lengths are very similar to one another, making it very difficult to determine which oxygen atoms could still be protonated.

Table 3-6. Carboxylic acid C–O and C=O bond lengths measured in the crystal structures of the organic linker **3.3** and MOF CCM-5.

3.3		**CCM-5**	
C–OH (Å)	C=O (Å)	C–O (Å)	C=O (Å)
1.292(14)	1.233(12)	1.255(15)	1.218(14)
1.344(13)	1.218(11)	1.241(11)	1.117(12)
1.279(13)	1.219(11)	1.246(5)	1.244(5)
1.327(12)	1.209(11)	1.251(5)	1.240(5)
		1.260(6)	1.231(6)
		1.272(4)	1.254(5)
		1.267(5)	1.241(6)
		1.297(8)	1.194(7)

In order to gain more insight into the potential protonation state of the carboxylates in CCM-5, other zinc(II) and naphthalenediimide-based MOFs were compared. A search in the CSD identifies 11 MOF structures comprising ligand **3.3** and zinc(II), out of which two

MOFs,[21,22] form from **3.3** and zinc(II). Notably, one MOF, with the reference code FOMWOV[21], contains partially deprotonated linkers of **3.3** that are connected *via* zinc(II) SBUs. More specifically, FOMWOV contains two types of linkers – fully deprotonated (L^{4-}) and triply deprotonated (HL^{3-}). The authors report that the FT-IR results also support the partial deprotonation of the framework, with a small wide band representing the O–H stretching of the carboxylic acid being present in the spectrum of the MOF sample. This evidence strongly suggests that CCM-5 also contains partially deprotonated linkers of **3.3**, likely averaging a trianion ($\mathbf{3.3}^{3-}$) state as opposed to being fully deprotonated ($\mathbf{3.3}^{4-}$). This assertion is further supported by a broader CSD search revealing 187 crystal structures of zinc(II)-based MOFs with coordinated protonated carboxylic acid groups, revealing that such a coordination environment in not uncommon in MOFs. Overall, this data suggests that the organic ligands in CCM-5 are on average trianions and consequently will herein be referred to as $\mathbf{3.3}^{3-}$.

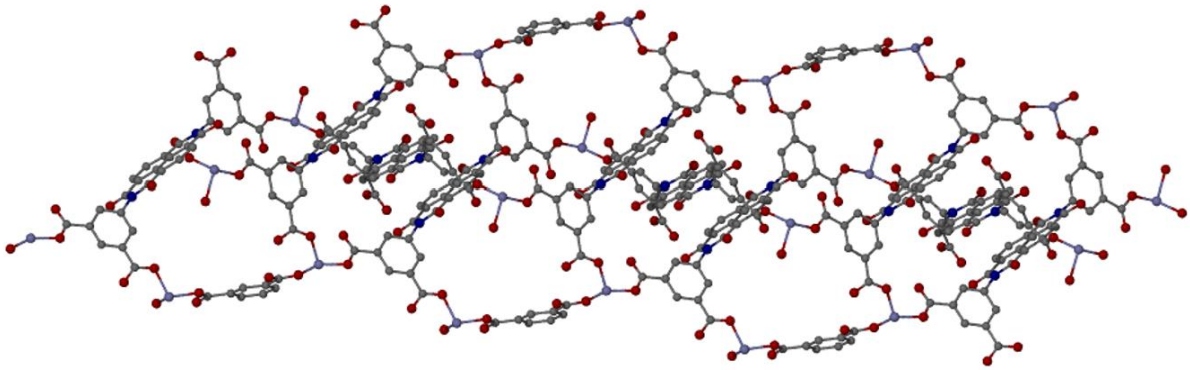

Figure 3-64. The packing arrangement of CCM-5 showing how the interpenetration is extended through the lattice. Grey: C. Red: O. White: H. Light purple: Zn. Hydrogen atoms omitted in c) and d) for clarity.

The packing arrangement of CCM-5 reveals that it is an interpenetrated network where $\mathbf{3.3}^{3-}$ linkers form sandwich-like π–π interactions (**Figure 3-64**). Two $\mathbf{3.3}^{3-}$ molecules coordinate to the dinuclear SBUs and form a macrocycle-like moiety. The third $\mathbf{3.3}^{3-}$ linker threads through this void and coordinates to the mononuclear tetrahedral SBUs. Thus, the mononuclear SBUs shown in **Figure 3-64** are bridged together by and guide the $\mathbf{3.3}^{3-}$ linkers that complete the sandwich-like π–π interactions between three independent organic linkers, as shown in **Figure 3-63c**. As a result, there is an interconnected web of channels that span through the framework and is manifested as channels of space. Due to there not being pores of discrete shapes, it is difficult to ascertain the exact size of these channels of space. However, the volume of space per unit cell is 3730 $Å^3$ (62.5% of unit cell) based on a probe radius of 1.2

Å, suggesting that CCM-5 is potentially capable of encapsulating larger molecular clusters than the CCM-series MOFs which contain 1608 $Å^3$ (51.1%) of void volume per unit cell.

To better understand the complex framework of CCM-5, the topology was analysed using the TOPOSPro software.[23] Instead of the standard representation method that was used to describe the CCM-series MOFs, the cluster representation method was employed for CCM-5. The simplification of frameworks using the cluster representation method can be undertaken either using the "single node" or "all node" deconstruction methods.[24] The main difference between these two methods is how the linkers and SBUs are simplified. For instance, in the "single node" method treats organic linkers and SBUs as one node. In the "all node" method, SBUs are also treated as one node but the branch points of the linkers are also treated as separate nodes. This means that the advantage of the "all node" method is that it provides a more accurate description of the topology for flexible ligands. **Figure 3-65** visualises how these simplifications are applied to the linker and SBUs that make up the structure of **3.3**. In the "single node" method shown with yellow spheres, the linker and SBUs are 4-connected (4-c node) while in the "all node" the linker and SBUs simplify to two 3-c nodes (green spheres). In the case of $\mathbf{3.3}^{3-}$ the "all node" method is expected to describe the topology more accurately as the shape of the linker is better simplified via two 3-c nodes. Still, both methods will be discussed herein for full clarity and understanding of the underlying topology of CCM-5.

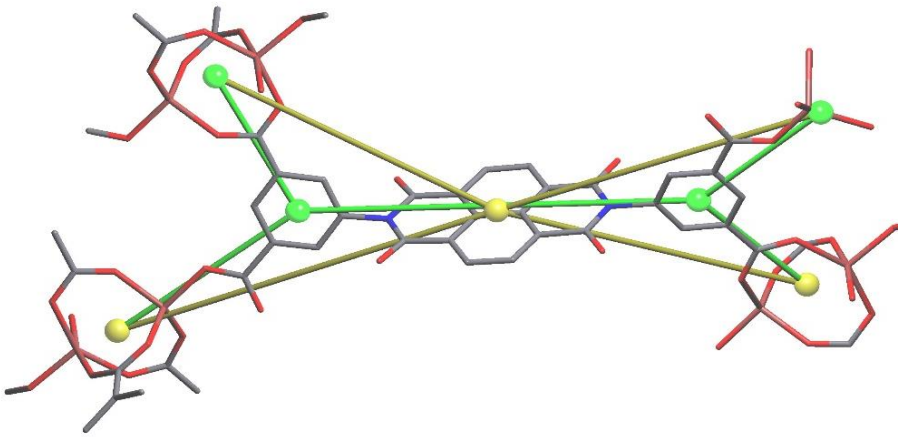

Figure 3-65. Visual representation of how the SBUs and the linker are simplified in the "single node" (yellow spheres) and "all node" (green spheres) methods. Image taken from TOPOS Pro software. Grey: C. Red: O. Blue: N. Brown: Zn.

First, the "single node" method was used to visualise the underlying net of CCM-5. **Figure 3-66a** shows how the simplified net looks like with respect to the real framework. The

"single node" approach yields a 5-nodal net with the point symbol $\{4.8^2\}_2\{4^2.6.8^3\}_2\{4^2.8^2.10^2\}\{4^2.8^4\}\{4^3.6.8^6\}_2$. While the connectivity of the underlying net relatively well represents the real packing arrangement, there are still empty spaces that are also mapped by the net which indicates it is not the most efficient way to simplify this net. **Figure 3-66b** shows the underlying net of CCM-5 along the [100] direction as determined by the "all node" method. The "all node" method yields a 6-nodal net with the point symbol $\{4.10^2\}_2\{4.12^2\}\{4.6.8\}\{4^2.6.8.10^6\}\{6.10^2\}$.

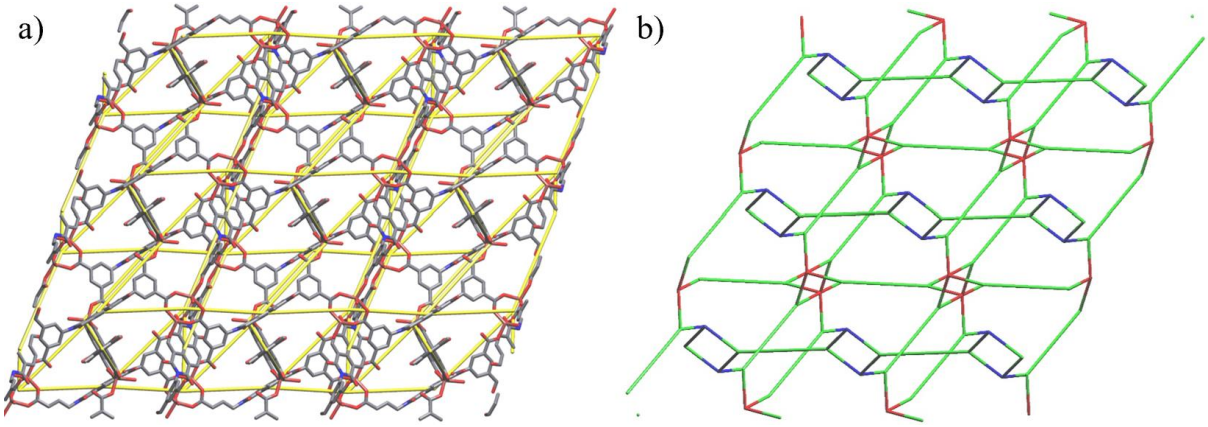

Figure 3-66. The underlying topology of CCM-5 as shown along the crystallographic *a* direction determined by using the a) single node method and b) all node method. In a) Grey: C. Red: O. Blue: N. Brown: Zn. Yellow: Underlying net. In b) Green: linker node. Red: dinuclear SBUs. Blue: mononuclear SBUs.

Due to the complicated nature of CCM- 5, it was subsequently studied how this MOF compares to other reported MOFs that utilise ligand **3.3**. The Cambridge Structural Database was searched for any MOFs that contain the organic linker and the search yielded 79 hits. The specific search and the details associated with it are outlined in Section 3.6.4. From these 79 hits, only 31 contain solely deprotonated **3.3** as the organic linker bridging SBUs while other MOFs contain mixed ligands. For example, the asymmetric unit of the CSD entry LARKOI[25] contains one unit of $\mathbf{3.3}^{4-}$ and two 3,5-diamino-1,2,4-triazole ligands bridging together zinc(II) secondary building units. From the 31 hits, one exhibits the same M:L ratio, in addition to only being made up of linkers of **3.3**, as that of CCM-5: RERVIW.[26] However, this framework contains manganese(II) metal centres instead of zinc(II) and as a result exhibits a different packing arrangement of the framework compared to that of CCM-5. RERVIW crystallises in monoclinic the $P2_1/c$ space group as opposed to the triclinic $P\bar{1}$ of CCM-5. Additionally, the topology of RERVIW exhibits Kagome lattice as a result of two anionic SBUs where manganese(II) metal centres adopt the square pyramidal coordination geometry.

Another structure from the 31 materials consisting only of ligand **3.3** is the abovementioned FOMWOV[21], which contains zinc(II) centres along with the sandwich-type π–π interactions of the organic linker resulting in an interpenetrated framework. In this case the M:L ratio is 4:3. The synthesis of FOMWOV was achieved *via* the solvothermal method where the reaction mixture (1:1 M:L ratio in DMF) was held at 110°C for 72 hours, then slowly cooled to room temperature over the course of 16 hours at the rate of 5°C h^{-1}, yielding brown block-shaped single crystals. These reaction conditions are very similar to those used to synthesise **3** with the main differences being that the latter was synthesised at 120°C and in the presence of TFA as a modulator. The structure of FOMWOV is described as a 1D+2D →3D self-interpenetrated array with dinuclear zinc(II) SBUs. In fact, FOMWOV is not a truly 1D+2D →3D net because it is simply a unique intercatenated framework. To truly be a 1D+2D →3D, the framework would have to be formed from 2-dimensional sheets that are penetrated through by a one-dimensional unit.[27] Additionally, FOMWOV also contains partially protonated carboxylic acid units of **3.3**. Two types of linkers are present: ones in which three of the four carboxylic acid groups belong to partially deprotonated (**3.3**$^{3-}$) and fully deprotonated linkers (**3.3**$^{4-}$). This stark similarity of fully and partially deprotonated organic linkers is likely due to the self-penetrated nature of both **3.3** and FOMWOV and likely arises from steric hindrance. The protonated carboxylic acid groups point towards the **3.3**$^{2-}$ linkers that are on the opposite side of the "sandwich" and thus there is no room for metal coordination. Alternatively, the carboxylic acid groups are facing this way in order to accommodate the mono- and dinuclear clusters that extend the framework structure, and any other conformation of these carboxylic acids would potentially result in a MOF of different size, shape and properties.

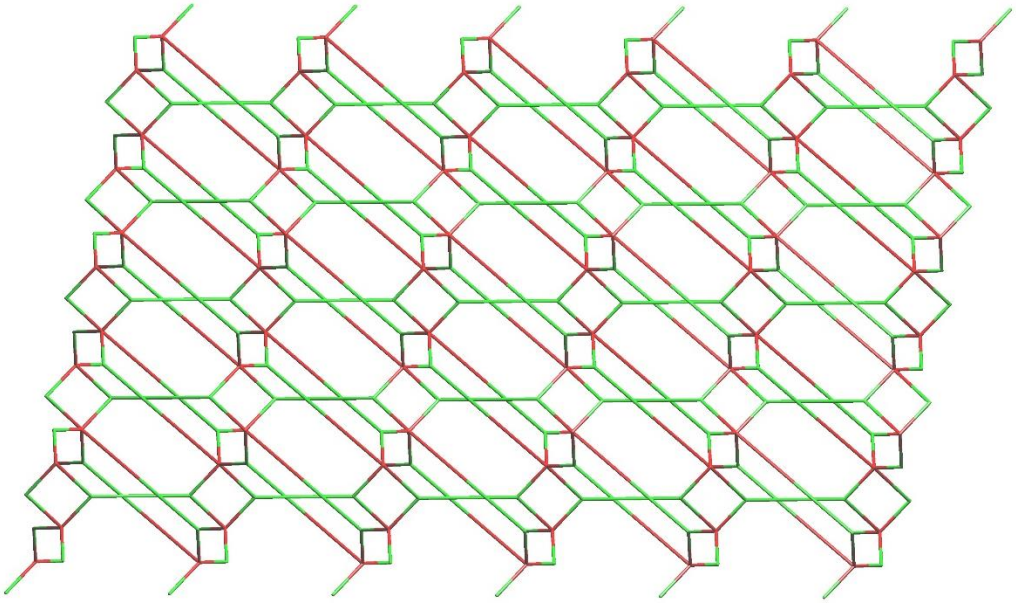

Figure 3-67. The underlying topology of FOMWOV as determined by the "all node" method shown along the [010] direction. Green: **3.3** node. Red: dinuclear SBU node.

To better compare these frameworks, the underlying topology of FOMWOV was also determined. In the reported article, the authors describe the framework as a (3,4,5)-connected net.[21] However, this underlying net is the result of using the "single node" method which simplifies the organic linker as a 4-c node. As previously discussed, this simplification does not yield the most accurate description of the underlying net. Thus, the "all node" method was employed to determine the underlying net of FOMWOV and is shown in **Figure 3-67**. Unlike CCM-5 which contains three separate nodes, the underlying net of FOMWOV consists of 2 nodes: the deprotonated organic linker (green) and the mononuclear zinc(II) SBU (red). This method yields a (3,3,5)-connected net as opposed to the (3,4,5)-connected net obtained by using the "single node" method. **Figure 3-67** shows that there are no "free" organic linkers, i.e. all organic linkers participate in the intercatenation. In contrast, there are layers of intercatenated and "free" organic linkers that bridge two adjacent mononuclear SBUs in the structure of CCM-5. The void volume in FOMWOV is 4661 $Å^3$, corresponding to 34.2% of the unit cell, a larger value than that of CCM-5. Consequently, both frameworks CCM-5 and FOMWOV are capable of encapsulating clusters of larger sizes than CCM-1–4 MOFs.

3.2.3 Efforts to Reproduce Single Crystals of CCM-5

As shown in **Figure 3-58**, the synthesis of CCM-5 single crystals also produces a dark-coloured byproduct, which from herein will be referred to as side product. The poor crystallinity of this side product inherently makes it impossible to realise for the aims of this study, *i.e.* using SC-

XRD to elucidate the molecular clusters confined in MOF materials. Nonetheless, establishing whether the side product corresponds to poorly crystalline CCM-5 MOF remains important. The powder pattern of this side product, shown in **Figure 3-68** (red trace), shows similarities to the CCM-5 single crystals (black trace) However, it appears that the peaks of this poorly crystalline material have shifted to slightly lower angles as compared to the single crystals of CCM-5. However, while there are two separate peaks at 9.0 and 9.7° for the crystals, the side product exhibits only one broader peak centred at 9.4°. Additionally, none of the synthesised materials exhibit peaks around 15.3° where there is a strong peak for the single crystals of CCM-5.

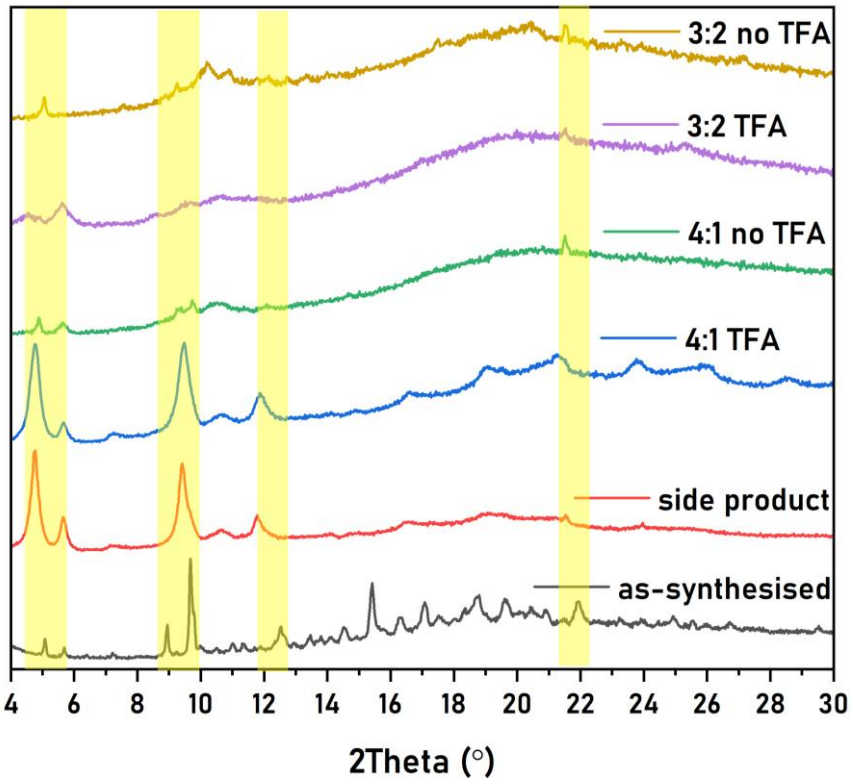

Figure 3-68. PXRD patterns of CCM-5 (black line) and the products from reactions containing the metal-to-ligand ratios of 4:1 with TFA (red line), 4:1 without TFA (blue line), 3:2 with TFA (green line) and 3:2 without TFA (purple line).

Reproducing the synthesis of CCM-5 in identical conditions (4:1 M:L ratio in the presence of trifluoroacetic acid) yielded the same side product as shown in **Figure 3-68** (green trace). Thus, the synthetic conditions were slightly altered in order to reproduce the synthesis of single crystals of CCM-5 consistently. First, while keeping all other conditions identical, the metal-to-ligand ratio was changed to 3:2 because this is the ratio of zinc(II):**3.3** in the single crystal structure of the CCM-5. Again, this results in the formation of poorly crystalline

material (**Figure 3-68**, purple trace). Other MOFs utilising the biphenyldicarboxylic acid ligand (CCM-2–4) were synthesised without the presence of trifluoroacetic acid as the modulator. Thus, 3:2 and 4:1 M:L ratio reactions were repeated without the presence of TFA and both reactions still yield a poorly crystalline MOF materials (**Figure 3-68**, green and beige traces, respectively). Due to time constraints further efforts towards the synthesis of single crystals of CCM-5 were not pursued and thus single crystals of CCM-5 were not successfully reproduced.

3.3 Synthesis and Characterisation of Lanthanum(III)-Based Naphthalenediimide MOFs

3.3.1 Crystallographic Characterisation

This work has shown that lanthanide-based metals, when combined with the H_2BPDC linker, produce MOFs with pore sizes large enough to encapsulate molecular clusters. This section explores the synthesis and characterisation of MOFs resulting from the integration of lanthanum(III) with **3.3**. A review by Howarth and co-workers discusses the use of 2-fluorobenzoic acid to facilitate the formation of cluster SBUs as opposed to metal chains, which could be beneficial towards synthesising mesoporous MOFs.[28] Thus, a solvothermal synthesis of **3.3** and lanthanum(III) nitrate hexahydrate in a 2:1 M:L ratio at 120°C for 72 hours in DMF was undertaken with 2-fluorobenzoic acid (2-FBA) as the modulator, yielding blue block-shaped single crystals (**Figure 3-69a**). SC-XRD analysis of these crystals reveals a MOF structure with an asymmetric unit comprising one half of linker **3.3** and one lanthanum(III) metal centre with one coordinated water molecule, yielding an empirical formula of La(**3**$^{4-}$)$_{0.5}$(2-FBA$^-$)(DMF)$_2$(H_2O) (CCM-6), **Figure 3-69b**. While single crystals of a MOF material were successfully synthesised, this MOF does not contain cluster-like SBUs and is microporous. Additionally, due to diffuse scattering of single crystals of CCM-6 observed during the data collection (**Figure 3-69c**), this model contains molecules with partial occupancy and high disorder. One coordination site is partially occupied by two DMF molecules, of which one is shown in **Figure 3-69b**. Another coordination site is partially occupied by one water and one DMF molecule, of which the water molecule is shown in **Figure 3-69b**. Finally, one coordination site is triply occupied by a two disordered units of 2-FBA and one DMF molecule, of which the 2-FBA is shown in **Figure 3-69b**. Finally, one non-coordinated DMF molecule is also present in the asymmetric unit. Any further solvent or modulator molecules could not be accurately modelled and were masked from the structure, accounting for 754 Å^3 and 234 electrons per unit cell.

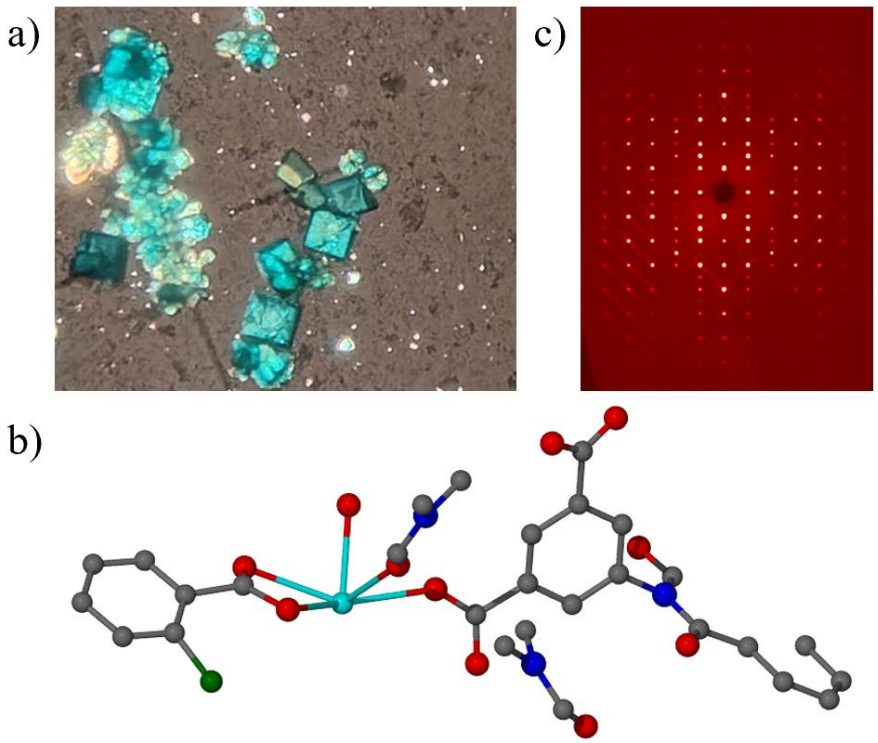

Figure 3-69. a) Microscope image of the block-shaped single crystals of CCM-6. b) Single crystal structure of the asymmetric unit of CCM-6. c) Diffuse scattering observed during the SC-XRD data collection of CCM-6 MOF. Gray: C. White: H. Red: O. Blue: N. Dark green: F. Light blue: La. Hydrogen atoms omitted for clarity.

CCM-6 crystallises in the monoclinic *C*2/*c* space group and contains dinuclear SBUs where two lanthanum(III) metal centres are connected to four linkers of **3.3**. Each lanthanum(III) metal centre adopts a 9-coordinate capped square antiprismatic coordination geometry. The La–O_3 coordination bond lengths range from 2.463(3) to 2.541(3) Å and the La–O_{H2O} coordination bond length is 2.525(4) Å. Unlike in CCM-5, all of the carboxylic acid groups in CCM-6 are fully deprotonated. The framework of CCM-6 is characterised by rectangular-shaped micropores with the size 13.4047(6) by 10.778(16) Å, indicated by solid blue and black lines in **Figure 3-70**, respectively. The framework contains a large void space of 4132 $Å^3$ (62.6% of unit cell volume). Consequently, compared to CCM-1 MOF (void space of 1608 $Å^3$, 51.1% of unit cell volume), both CCM-5 (3779 $Å^3$, 62.8% of unit cell volume) and CCM-6 contain larger voids and could encapsulate molecular clusters of larger sizes.

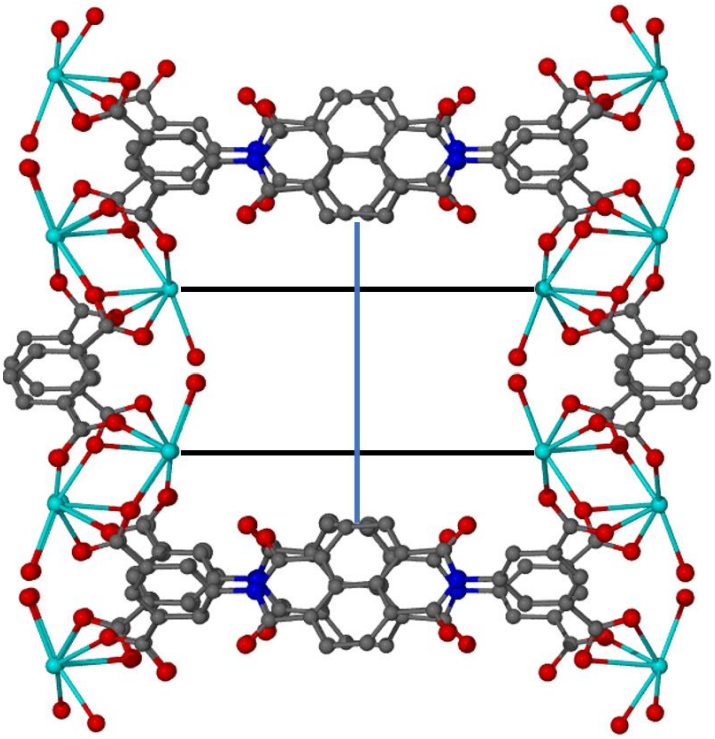

Figure 3-70. Single crystal structure of CCM-6 showing the rectangular pores observed in the framework. Gray: C. Red: O. Blue: N. Light blue: La. Black and blue lines indicate how the pore sizes were measured. Solvent molecules and hydrogen atoms have been omitted for clarity.

The PXRD pattern of CCM-6, along with its pattern simulated from SC-XRD data, is shown in **Figure 3-*71*** (black and red traces). The simulated and experimental patterns are in good agreement, indicating high bulk purity. Upon its synthesis, the yield of single crystals of CCM-6 was very low and only enough for SC-XRD and PXRD analyses. Consequently, the synthesis was repeated in identical conditions, again yielding blue single crystals. When the PXRD pattern of these crystals was obtained (**Figure 3-*71***, green trace), small differences in peak positions and shifts, as compared to the powder pattern of CCM-6, were observed. Notably, while most peak positions are nearly identical, the newly synthesised crystals exhibited additional peaks at higher angles. To study if there were any structural differences between CCM-6 and newly synthesised crystals, the latter were taken for SC-XRD analysis.

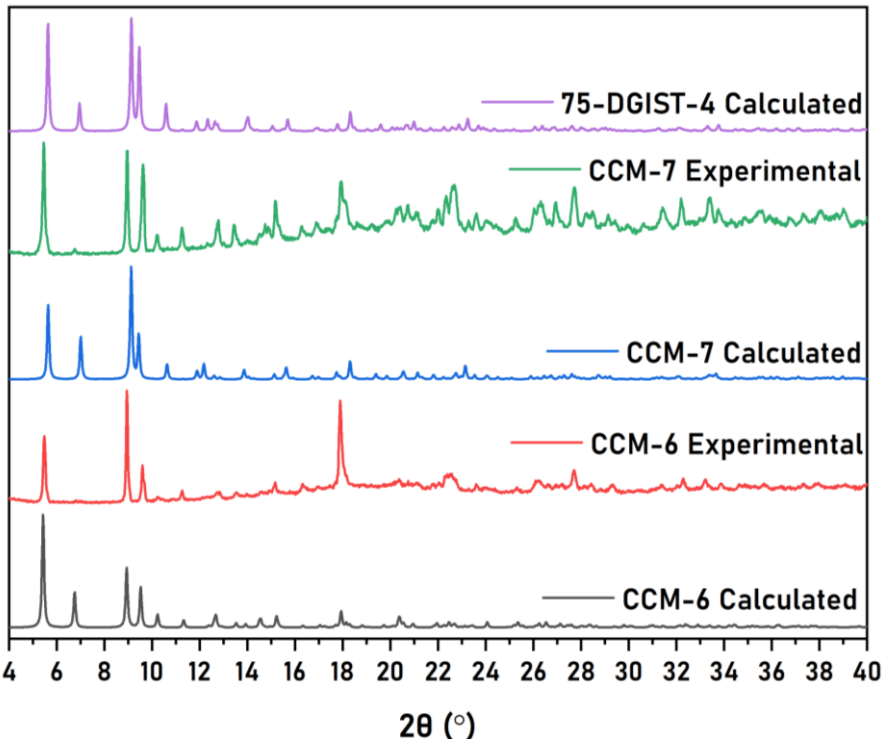

Figure 3-71. PXRD patterns of CCM-6 obtained experimentally (black trace) and simulated from SC-XRD data (red trace), CCM-7 obtained experimentally (blue trace) and simulated from SC-XRD data (green trace) and DGIST-4 simulated from the reported SC-XRD data.

The SC-XRD analysis reveals that the crystals comprise a lanthanum(III)-based framework with the empirical formula La(**3.3**$^{4-}$)$_{0.5}$(NO_3^-)$_{0.50}$(2-FBA$^-$)$_{0.50}$(DMF)$_2$ (CCM-7). The anionic 2-FBA and nitrate molecules bind to the same coordination site of lanthanum(III) resulting in their half occupancy. The coordination of nitrate groups is important in preventing steric hindrance effects occurring in the case of full occupancy by 2-FBA. The MOF, similarly to CCM-6, also crystallises in the monoclinic *C*2/*c* space group and contains dinuclear lanthanum(III) metal centres linked together by fully deprotonated linkers of **3.3** (**3.3**$^{4-}$). A search in the CSD shows that CCM-7 is isostructural to a previously reported MOF, with the reference code MAZFEC, referred to as 75-DGIST-4 by the authors.[29] However, the framework reported in the CSD contains neodymium(III) metal centres while its isostructural counterpart synthesised herein is made up from lanthanum(III). Additionally, the solvothermal synthesis of 75-DGIST-4 was undertaken with benzoic acid (BA) instead of 2-FBA resulting in a formula Nd(**3.3**$^{4-}$)$_{0.50}$(NO_3^-)$_{0.50}$(BA$^-$)$_{0.50}$(DMF)$_2$. Similarly to CCM-7, the asymmetric unit of 75-DGIST-4 contains two coordinated DMF molecules and one lanthanum(III) coordination centre is half occupied by NO_3^- and BA$^-$.

The expected powder pattern of 75-DGIST-4 is shown in **Figure 3-*7I*** (purple trace) which is identical to the calculated powder pattern of its lanthanum(III) MOF counterpart. In the 2022 report by Park and co-workers, the reported neodymium-based MOF is referred to as 75-DGIST-4 and thus will herein also be referred to as such. The unit cell sizes of DGIST-4, CCM-7 and CCM-6 and shown in **Table 3-7**. The unit cells of CCM-7 and 75-DGIST-4 materials are nearly identical, as expected for isostructural materials, while the unit cell of CCM-6 is slightly different along all axes. The analysis will henceforth focus on comparing the structural details of CCM-6 with the isostructural pair of CCM-7 and 75-DGIST-4. However, given that CCM-7 and 75-DGIST-4 are isostructural, only CCM-7 will be referred to when discussing differences between CCM-6 and the latter.

Table 3-7. Unit cell measurements of CCM-6, CCM-7 and 75-DGIST-4.

Axis	CCM-6	CCM-7	75-DGIST-4
a	32.9496(4)	31.4148(13)	31.471(6)
b	14.2814(3)	13.7596(6)	13.874(3)
c	14.2099(20)	14.5803(6)	14.395(3)

The similarities in the PXRD patterns of CCM-6 and crystals of CCM-7 (**Figure 3-*7I***, red and green traces, respectively) arise from nearly identical, yet not isostructural, framework structures. For reference, the simulated PXRD pattern of 75-DGIST-4 is also shown (purple trace). More specifically, CCM-7, similarly to CCM-6, crystallises in the *C*2/*c* space group and the asymmetric unit of the former comprises one lanthanum(III) metal centre along with one half of the linker of $\mathbf{3.3}^{4-}$. Additionally, CCM-7 exhibits identical 9-coordinate dinuclear SBUs to those observed in CCM-6. The underlying framework topologies of CCM-6 and CCM-7 along the *b* axis are shown in **Figure 3-72a** and **b**, respectively.

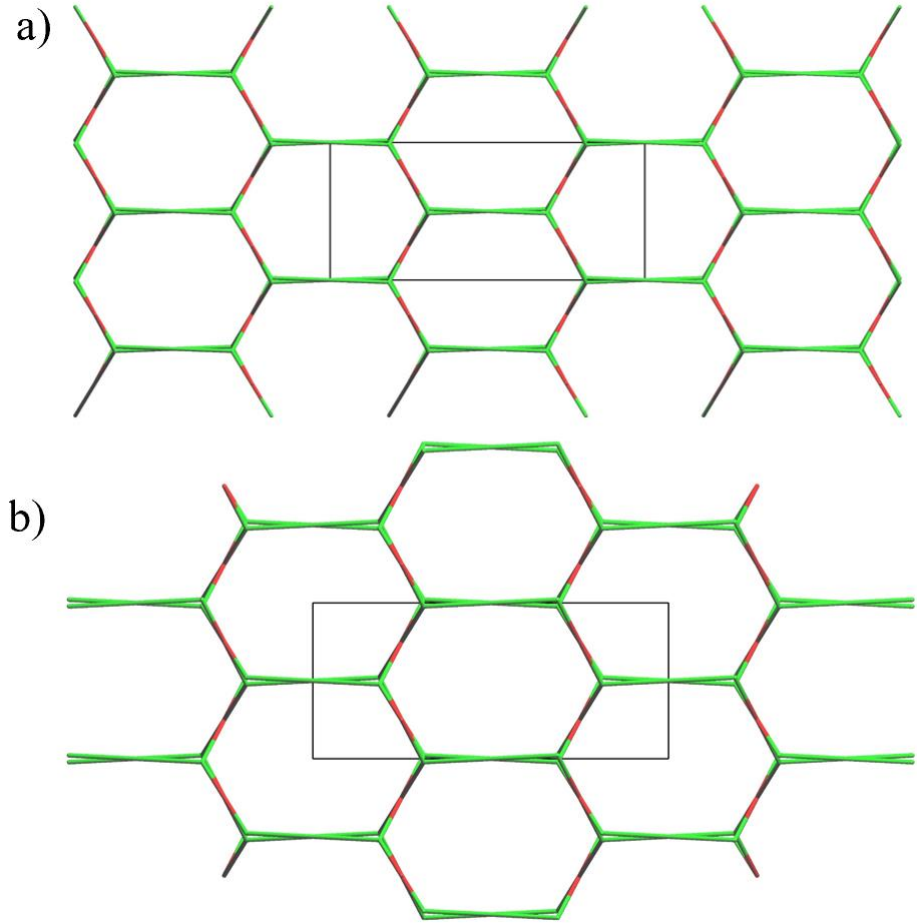

Figure 3-72. Underlying topologies of a) CCM-6 and b) CCM-7 (bottom) along the *c* axis. Green nodes represent the nodes of the linker **3.3** while the red nodes represent the dinuclear SBUs.

Similarly to the analysis of CCM-5, the all node approach was used to analyse CCM-6 and CCM-7 as it maps the organic linker more accurately than the single node method. **Figure 3-*72*a** shows the underlying topology of CCM-6, exhibiting honeycomb-like structure as depicted along the crystallographic *b* axis. The underlying nets of CCM-6 and CCM-7 are 2-nodal with the point symbols $\{6^2.8^2.10^2\}\{6^2.8\}_2$. The underlying topology of CCM-7 also exhibits a honeycomb-like pattern and appears to be identical to CCM-6. Honeycomb-like arrangement of frameworks are very common in MOFs and a plethora of reported MOF structures exhibit this framework pattern.[30–33] However, the crucial difference between CCM-6 and CCM-7 topologies lies in the orientation of the linker **3.3**. More specifically, the linkers in CCM-6 lie more parallel to one another than they do in CCM-7, and by extension 75-DGIST-4, consequently leading to the differences in unit cell measurements. These differences are a

consequence of the changes in the C–N–C angles in **3.3**. As shown in **Figure 3-*73*a** and **b**, these angles are 175.7(5) and 171.8(3)° in CCM-6 and CCM-7, respectively.

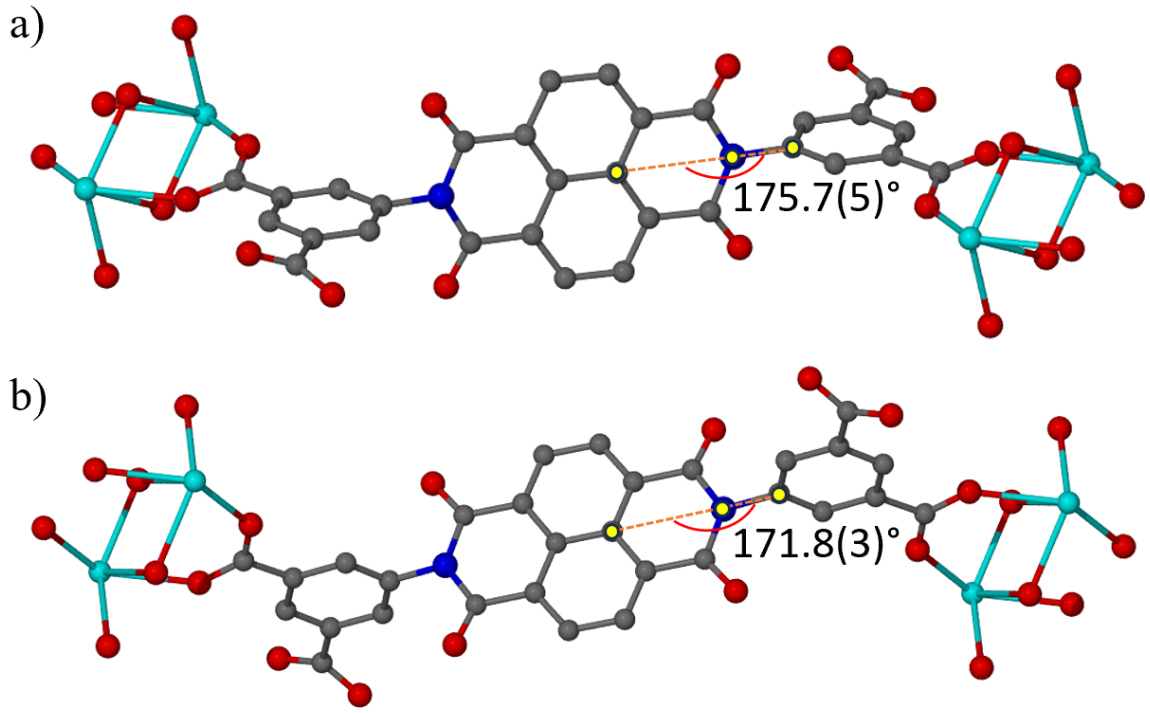

Figure 3-73. Single crystal structures of a) CCM-6 and b) CCM-7 showing the C–N–C angles measured in both frameworks. Gray: C. Red: O. Blue: N. Light blue: La. Hydrogen atoms omitted for clarity.

Due to time constraints and relatively poor yield of both CCM-6 and CCM-7, further characterisation or potential guest exchange data regarding CCM-6 and CCM-7 were not obtained. Future efforts should focus on the modifying the reaction conditions of CCM-6 MOF to obtain a higher yield, along with higher crystallinity. It is likely that the nature of the modulator plays an important role in this outcome, because 75-DGIST-4 single crystals were obtained by using imidazole as the modulator while the synthesis of the very similar framework CCM-6 was undertaken with 2-FBA as the modulator.[29]

The synthesis of lanthanum(III)-based MOFs with **3.3** was also attempted at a lower temperatures to study if higher quality single crystals could be obtained at these conditions. A DMF solution containing lanthanum(III) nitrate hexahydrate : **3.3** in a 2:1 ratio, respectively, was prepared, without the presence of a modulator. The solution was heated at 90°C for 72 hours, followed by 6 hours of cooling, which yielded transparent needle-shaped plate-like crystals (**Figure 3-74a**). Similarly to CCM-7, these crystals were analysed at the DLS. Single crystal analysis of these crystals yields a MOF which crystallises in the monoclinic *C*2/*c* space group with an asymmetric unit containing one lanthanum(III) metal centre, one unit of **3.3**, one

coordinated water and DMF molecule and seven non-coordinated DMF solvent molecules, La(**3.3**$^{3-}$)(DMF)$_8$(H_2O) (CCM-8), **Figure 3-74b**.[13] Due to their severe disorder, the non-coordinated DMF molecules could not be modelled accurately and were masked.

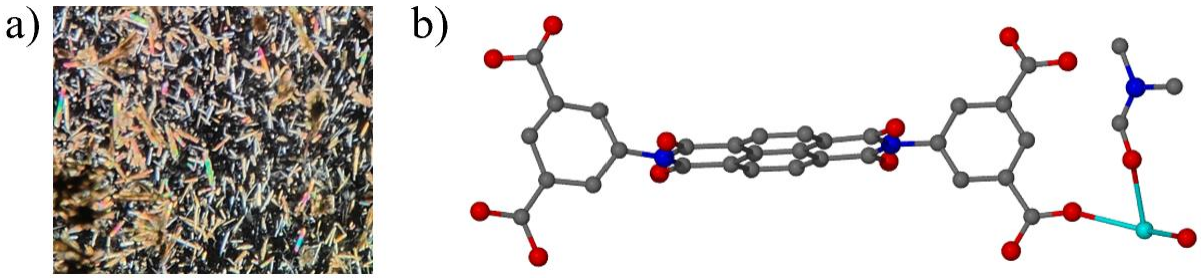

Figure 3-74. a) Picture of single crystals of CCM-8 under the polarising microscope. b) The crystal structure of the asymmetric unit of CCM-8. Gray: C. Red: O. Blue: N. Light blue: La. Hydrogen atoms have been omitted for clarity.

In CCM-8, the La-**O**$_{3.3}$ distances range from 2.427(3) to 2.626(8) Å. The lanthanum(III) metal centres take up the 8-coordinated (six oxygen atoms from five linkers of **3.3** and two dangling oxygen atoms from solvent molecules) square antiprismatic coordination geometry, and similarly to CCM-7, form dinuclear SBUs. However, unlike in CCM-7, one of the carboxylic acid groups of CCM-8 does not participate in any coordination bond formation with lanthanum(III). Thus, the linkers of **3.3** are trianions (**3.3**$^{3-}$) as opposed to any additional cations balancing out the fully deprotonated linker **3.3**$^{4-}$. In the 2022 report[29], the neodymium(III)-based isostructural MOF, 85-DGIST-5, was reported to contain the trianionic linker **3.3** without any additional presence of ions and a formula of Nd(**3.3**$^{3-}$)(DMF)(H_2O). Consequently, it is likely that the lanthanum(III)-based MOF counterpart exhibits the **3.3**$^{3-}$ linker.

The packing arrangement of CCM-8 along the *b* axis is shown in **Figure 3-75a**. The framework does not form honeycomb-like patterns as those observed in CCM-6 and CCM-7. This is also evident in the underlying topology of CCM-8, which is shown in **Figure 3-75b**, resulting in rhombic-shaped pores somewhat similar to those in CCM-1–4 MOFs. The void volume of CCM-8 is 7482 Å^3, considerably larger than those of any previous CCM-MOFs reported in this work, with the second largest void volume of 4132 Å^3 belonging to CCM-6 MOF. The size of the pores shown in **Figure 3-75a** is 20.8211(9) by 7.629(9) Å.

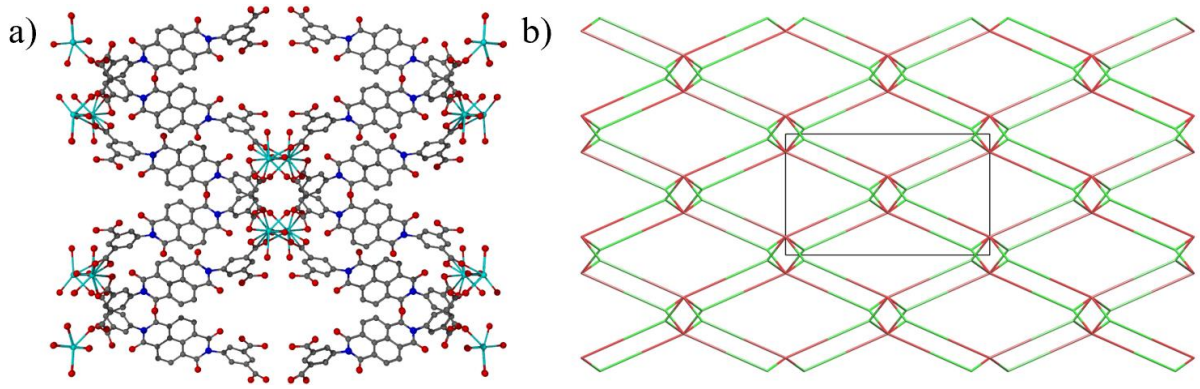

Figure 3-75. a) Single crystal packing arrangement of CCM-8 along the *c* axis. Gray: C. Red: O. Blue: N. Light blue: La. Hydrogen atoms omitted for clarity. C) The underlying topology of CCM-8 along the crystallographic *b* axis using the all node method. Red nodes: La dinuclear SBUs.

Overall, one novel (CCM-6) and two isostructural (CCM-7 and CCM-8, isostructural with MOFs previously reported in the literature[29]) lanthanum(III)-based MOFs with the tetratopic linker **3.3** have been reported herein. While these MOFs contain pores that are large enough for guest exchange, their diffraction quality is not as good as that of CCM-1–4 MOFs and the guest molecules could not be modelled inside the pores. Future efforts should focus on increasing the crystallinity of these frameworks by modifying the modulator used for their syntheses. Subsequent analyses of guest cluster formation could then be undertaken.

3.4 Conclusion

This chapter discussed the synthesis and characterisation of one novel intercatenated framework consisting of mono- and binuclear zinc SBUs bridged together by two types of deprotonated organic linkers. Two types of SBUs, mono- and dinuclear, are bridged together by the two types of $\mathbf{3.3}^{3-}$ organic linkers leading to a partially interpenetrated network with accessible pores. While certain similarities, such as the synthetic conditions, nature of the metal source and interpenetration, are observed between CCM-5 and another MOF, FOMWOV, it is the distinctive features of **3.3** that set it apart. While the framework of CCM-5 exhibits a complex underlying topology, its large pores and unique connectivity make it desirable for the purposes of this work. However, due to the poor yield accompanied with non-replicable synthesis of the single crystals, it was not studied to that end. Future efforts should, therefore, focus on optimising the reaction conditions to achieve a consistent synthesis CCM-5 in its crystalline form. This would enable the use of the framework as an effective confinement matrix for the capture and study of molecular clusters. Despite this promising attribute, challenges arising from the reproducibility of the synthesis of single crystals of CCM-5 have

precluded the ability to study the formation of clusters in this framework. Additionally, between the mono- and dinuclear SBUs of CCM-5, the water coordination sites can be targeted towards guest exchange. Additionally, in the context of the formation of small molecular clusters, when a guest molecule is introduced inside the pore it can act as a seed to attract more molecules into the framework.[34] In addition to the novel CCM-5 framework, the crystal structures of three lanthanum(III)-based MOFs (CCM-6–8) with the linker **3.3** were also reported. Similarly to CCM-5, the crystallinity of these frameworks was not good enough to accurately model any solvent molecules inside the pores. Consequently, future efforts should focus on increasing the crystallinity to yield frameworks that can be used to capture, and visualise *via* SC-XRD, molecular clusters.

3.5 Experimental Details

3.5.1 Synthesis of *N,N*'-bis(5-isophthalic acid)naphthalenediimide (3.3)

The synthesis of **3.3** was undertaken based on a procedure previously reported in the literature.[8] A one-pot synthesis of **3.3** was carried out in a 50 mL three-neck round-bottom flask, into which DMF (20 mL) was added. Subsequently, 5-aminosophthalic acid (0.76 g, 4.2 mmol) and naphthalene-1,4,5,8-tetracarboxylic acid (0.54 g, 2.0 mmol) were added to the solvent after which the mixture turned red. The mixture was refluxed at 110°C for 8 hours, by the end of which a light-beige-coloured precipitate had formed. Deionised water (10 mL) was added to ensure full precipitation and the precipitate was vacuum filtered and washed with ethanol (3 x 20 mL). The filtrate was placed in a vial and dried in an Abderhalden's drying pistol at 110 °C for 2 days. The product was obtained as a white powder. Yield = 1.08 g, 1.81 mmol, 91%.

^{1}H NMR (400 MHz, DMSO–d_6): δ = 13.51 (4H, s, COO**H**), 8.75 (4H, s, Ar**H**), 8.59 (2H, t, *J* = 1.6 Hz, Ar**H**), 8.35 (4H, d, *J* = 1.6 Hz, Ar**H**).

Elemental analysis calculated for $C_{30}H_{18}N_2O_4$. Expected C 57.15, H 2.88, N 4.44%. Found C 57.05, H 2.98, N 4.55%.

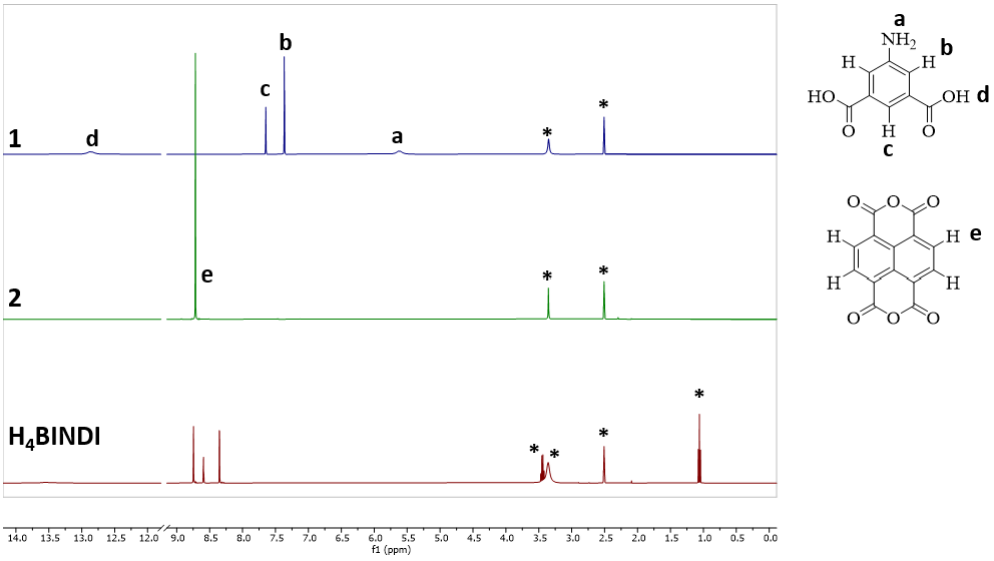

Figure 3-76. ^{1}H NMR spectra of 5-aminoisophthalic acid (**3.1**, blue trace), naphthalene-1,4,5,8-tetracarboxylic acid dianhydride (**3.2**, green trace) and **3.3** (red trace). All solvent peaks have been labelled with an asterisk. All spectra were acquired in d_6-DMSO. The ^{1}H NMR spectrum of **3.3** is only shown for comparison as it has been analysed in detail in **Figure 3-56**.

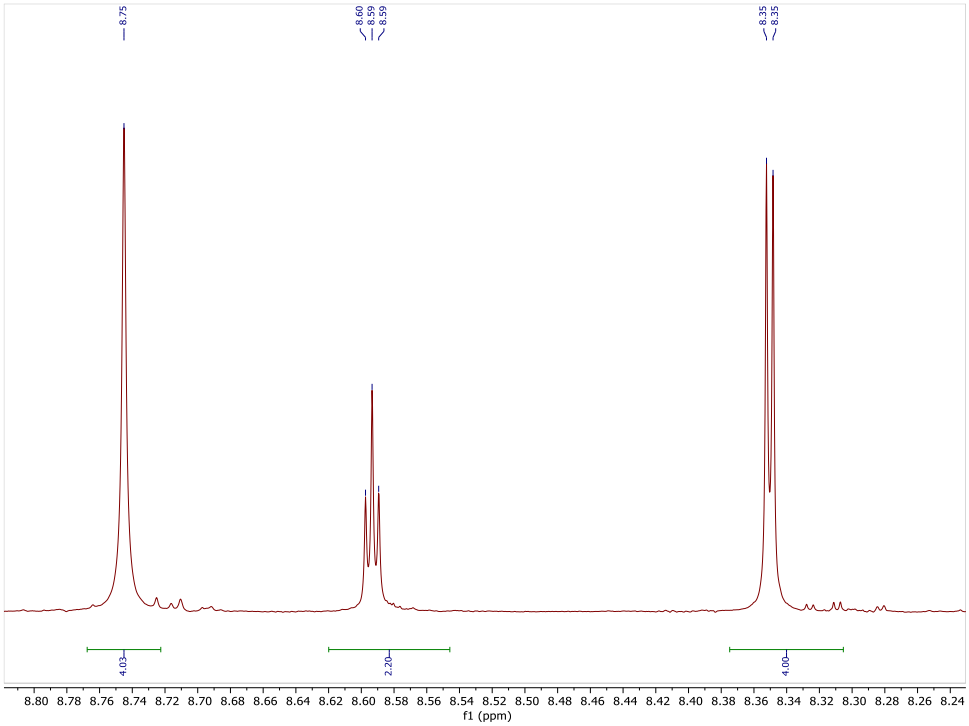

Figure 3-77. ^{1}H NMR spectrum of **3.3** zoomed in to the resonances attributed to the protons coming off the benzene and naphthalene moieties. Integration values and peak positions are also shown. Spectrum acquired in d_6-DMSO.

3.5.2 Synthesis of Metal-Organic Frameworks

CCM-5

In DMF (10 mL), *N,N*'-bis(5-isophthalic acid)naphthalenediimide (30 mg, 0.05 mmol) and zinc(II) nitrate hexahydrate (60 mg, 0.2 mmol) were mixed together. To this mixture, TFA (0.1 mL) was added and the mixture was sonicated for 5 minutes. The solution was transferred into an acid digestion vessel which was capped and placed into an isothermal oven. The vessel was heated at 120°C for 72 hours, followed by slow cooling to room temperature over 6 hours. The reaction yielded dark amorphous material with brown-coloured plate-like crystals.

CCM-6

N,N'-bis(5-isophthalic acid)naphthalenediimide (**3.3**) (30 mg, 0.05 mmol) and lanthanum(III) nitrate hexahydrate (43 mg, 0.1 mmol) were mixed together in DMF (12.04 mL). To this mixture, 2-fluorobenzoic acid (0.1 g) was added and the mixture was sonicated for 5 minutes. The solution was transferred into an acid digestion vessel which was capped and placed into a heated oven. The vessel was heated at 120°C for 72 hours, followed by slow cooling to room temperature over 6 hours. The reaction yielded light blue block-shaped single crystals. The reaction only yielded a few single crystals, which were used for SC-XRD and PXRD characterisation and the total yield was not established.

CCM-7

N,N'-bis(5-isophthalic acid)naphthalenediimide (**3.3**) (30 mg, 0.05 mmol) and lanthanum(III) nitrate hexahydrate (43 mg, 0.1 mmol) were mixed together in DMF (12.04 mL). To this mixture, 2-fluorobenzoic acid (0.2 g) was added and the mixture was sonicated for 5 minutes. The solution was transferred into an acid digestion vessel which was capped and placed into a heated oven. The vessel was heated at 120°C for 72 hours, followed by slow cooling to room temperature over 6 hours. The reaction yielded light blue block-shaped single crystals. The reaction only yielded a few single crystals, which were used for SC-XRD and PXRD characterisation and hence the total yield was not established.

CCM-8

N,N'-bis(5-isophthalic acid)naphthalenediimide (**3.3**) (30 mg, 0.05 mmol) and lanthanum(III) nitrate hexahydrate (43 mg, 0.1 mmol) were sonicated for 5 minutes in DMF (12.04 mL). The solution was transferred into an acid digestion vessel which was capped and placed into an heated oven. The vessel was heated at 90°C for 72 hours, followed by slow cooling to room temperature over 6 hours. The reaction yielded transparent plank-shaped single crystals which were characterised *via* SC-XRD analysis.

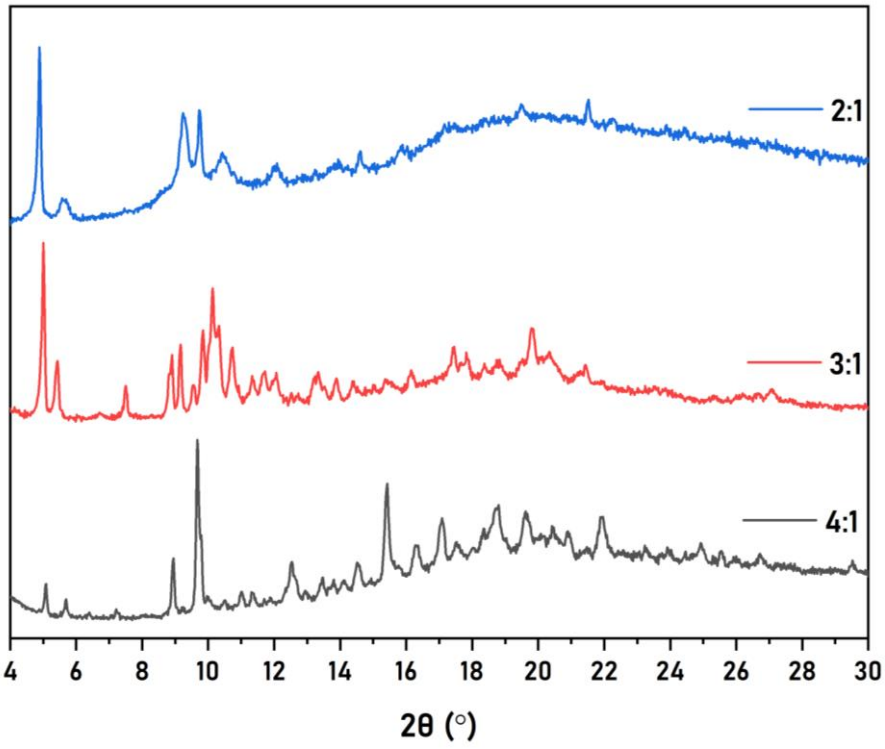

Figure 3-78. Powder X-Ray diffraction patterns of the initially tested CCM-5 MOF reactions using ratios of 2:1 (blue trace), 3:1 (red trace) and 4:1 (black trace) metal:ligand.

3.5.3 Crystallography Data

Table 3-8. Single crystal data for compound the DMSO solvate **3.3**.

Compound	**3.3**
Empirical formula	$C_{44}H_{44}N_2O_{18}S_6$
Formula weight	1081.19
Temperature/K	120.00
Crystal system	monoclinic
Space group	*P*2/*c*
a/Å	22.1615(15)
b/Å	4.9703(4)
c/Å	44.997(3)
α/°	90
β/°	104.161(2)
γ/°	90
Volume/Å^3	4805.7(6)
Z	4
ρ_{calc}g/cm^3	1.254
μ/mm^{-1}	0.262
F(000)	1888.0
Crystal size/mm^3	0.21 × 0.03 × 0.02
Radiation	Mo Kα (λ = 0.71073)
2Θ range for data collection/°	3.734 to 51
Index ranges	$-26 \leq h \leq 26$, $-6 \leq k \leq 5$, $-54 \leq l \leq 54$
Reflections collected	78105
Independent reflections	8892 [R_{int} = 0.1435, R_{sigma} = 0.0854]
Data/restraints/parameters	8892/211/646
Goodness-of-fit on F^2	1.030
Final R indexes [I>=2σ (I)]	R_1 = 0.0977, wR_2 = 0.2413
Final R indexes [all data]	R_1 = 0.1582, wR_2 = 0.2788

Table 3-9. Crystal data for CCM-5.

Compound	**CCM-5**
Empirical formula	$C_{108}H_{136}N_{20}O_{42}Zn_3$
Formula weight	2582.47
Temperature/K	100.00(2)
Crystal system	triclinic
Space group	P-1
a/Å	17.8760(2)
b/Å	19.7569(3)
c/Å	20.3741(5)
α/°	107.4749(17)
β/°	113.9318(14)
γ/°	97.1717(14)
Volume/Å^3	6017.16(18)
Z	2
ρ_{calc}g/cm^3	1.425
μ/mm^{-1}	0.635
F(000)	2700.0
Crystal size/mm^3	0.086 × 0.02 × 0.004
Radiation	Synchrotron (λ = 0.6889)
2Θ range for data collection/°	2.298 to 51.006
Index ranges	$-22 \leq h \leq 22$, $-24 \leq k \leq 24$, $-25 \leq l \leq 25$
Reflections collected	82313
Independent reflections	24439 [R_{int} = 0.1177, R_{sigma} = 0.1812]
Data/restraints/parameters	24439/740/829
Goodness-of-fit on F^2	0.940
Final R indexes [I>=2σ (I)]	R_1 = 0.0831, wR_2 = 0.2442
Final R indexes [all data]	R_1 = 0.1413, wR_2 = 0.2715

Table 3-10. Crystal data for CCM-6

Compound	**CCM-6**
Empirical formula	$C_{26}H_{26}FLaN_3O_{11.5}$
Formula weight	722.41
Temperature/K	120.00(10)
Crystal system	monoclinic
Space group	*C*2/*c*
a/Å	32.9496(4)
b/Å	14.2814(3)
c/Å	14.2099(2)
α/°	90
β/°	99.0780(10)
γ/°	90
Volume/Å^3	6602.95(19)
Z	8
ρ_{calc}g/cm^3	1.453
μ/mm^{-1}	1.357
F(000)	2888.0
Crystal size/mm^3	0.113 × 0.094 × 0.051
Radiation	Mo Kα (λ = 0.71073)
2Θ range for data collection/°	3.114 to 74.4
Index ranges	$-55 \leq h \leq 55$, $-23 \leq k \leq 23$, $-23 \leq l \leq 23$
Reflections collected	149784
Independent reflections	16129 [R_{int} = 0.0640, R_{sigma} = 0.0585]
Data/restraints/parameters	16129/0/218
Goodness-of-fit on F^2	1.046
Final R indexes [I>=2σ (I)]	R_1 = 0.0888, wR_2 = 0.2322
Final R indexes [all data]	R_1 = 0.1259, wR_2 = 0.2501
Largest diff. peak/hole / e Å^{-3}	2.20/-0.86

Table 3-11. Crystal data for CCM-7

Compound	**CCM-7**
Empirical formula	$C_{46}H_{35}FLa_2N_6O_{20}$
Formula weight	1288.62
Temperature/K	120.00
Crystal system	monoclinic
Space group	*C*2/*c*
a/Å	31.4148(13)
b/Å	13.7596(6)
c/Å	14.5803(6)
α/°	90
β/°	94.887(2)
γ/°	90
Volume/Å^3	6279.5(5)
Z	4
ρ_{calc}g/cm^3	1.363
μ/mm^{-1}	1.412
F(000)	2544.0
Crystal size/mm^3	0.282 × 0.252 × 0.2
Radiation	Mo Kα (λ = 0.71073)
2Θ range for data collection/°	4.9 to 72.294
Index ranges	$-51 \leq h \leq 52$, $-22 \leq k \leq 22$, $-23 \leq l \leq 24$
Reflections collected	120660
Independent reflections	14844 [R_{int} = 0.0368, R_{sigma} = 0.0255]
Data/restraints/parameters	14844/901/568
Goodness-of-fit on F^2	1.108
Final R indexes [I>=2σ (I)]	R_1 = 0.0537, wR_2 = 0.1574
Final R indexes [all data]	R_1 = 0.0743, wR_2 = 0.1773
Largest diff. peak/hole / e Å^{-3}	2.74/-0.98

Table 3-12. Crystal data for CCM-8.

Compound	**CCM-8**
Empirical formula	$C_{54}H_{70}LaN_{10}O_{21}$
Formula weight	1334.11
Temperature/K	100.00
Crystal system	monoclinic
Space group	C2/c
a/Å	36.4006(17)
b/Å	21.5471(14)
c/Å	16.7338(6)
α/°	90
β/°	92.942(4)
γ/°	90
Volume/Å^3	13107.5(12)
Z	8
ρ_{calc}g/cm^3	1.352
μ/mm^{-1}	0.676
F(000)	5512.0
Crystal size/mm^3	0.12 × 0.025 × 0.025
Radiation	Synchrotron (λ = 0.6889)
2Θ range for data collection/°	3.138 to 63.956
Index ranges	$-41 \leq h \leq 34$, $-31 \leq k \leq 19$, $-15 \leq l \leq 25$
Reflections collected	27015
Independent reflections	14928 [R_{int} = 0.0630, R_{sigma} = 0.1704]
Data/restraints/parameters	14928/1144/567
Goodness-of-fit on F^2	0.783
Final R indexes [I>=2σ (I)]	R_1 = 0.0549, wR_2 = 0.1400
Final R indexes [all data]	R_1 = 0.0895, wR_2 = 0.1462
Largest diff. peak/hole / e Å^{-3}	0.68/-0.96

3.5.4 Details of Topological Analysis

The topological analysis was undertaken with the software ToposPro.[23] The steps for the simplification of the framework topology was taken from the work of Öhrström and co-workers.[24] More specifically, the "all node" method was used to deconstruct the framework structure into the underlying nets due to its most accurate description of the underlying net. In short, the determination of the underlying topology consists of two steps. The first step involves removing hydrogen atoms and solvent molecules were removed from .cif file of the crystal structure of the corresponding MOF. Subsequently, the .cif file was loaded into ToposPro software and the underlying network was simplified using either the "single node" or "all node"

method. The difference in these methods is discussed in the results and discussion section. After the first step of the simplification, all 0-,1- and 2-connected nodes are removed to yield the underlying net. The topological analysis for FOMWOV was also undertaken using the "all node" method due to a more accurate description of the underlying net.

3.6 References

1 W. Lu, Z. Wei, Z. Y. Gu, T. F. Liu, J. Park, J. Park, J. Tian, M. Zhang, Q. Zhang, T. Gentle, M. Bosch and H. C. Zhou, *Chem. Soc. Rev.*, 2014, **43**, 5561–5593.

2 J. S. Qin, S. Yuan, Q. Wang, A. Alsalme and H. C. Zhou, *J. Mater. Chem. A*, 2017, **5**, 4280–4291.

3 S. Abednatanzi, P. Gohari Derakhshandeh, H. Depauw, F. X. Coudert, H. Vrielinck, P. Van Der Voort and K. Leus, *Chem. Soc. Rev.*, 2019, **48**, 2535–2565.

4 Z. Chen, K. O. Kirlikovali, P. Li and O. K. Farha, *Acc. Chem. Res.*, 2022, **55**, 579–591.

5 M. Eddaoudi, J. Kim, N. Rosi, D. Vodak, J. Wachter, M. O'Keeffe and O. M. Yaghi, *Science*, 2002, **295**, 469–472.

6 L. Tang, F. Fu, L. Gao, Q. Wei, Z. Zhang and Q. Liu, *Z. Anorg. Allg. Chem.*, 2013, **639**, 918–921.

7 W. Liang, P. M. Bhatt, A. Shkurenko, K. Adil, G. Mouchaham, H. Aggarwal, A. Mallick, A. Jamal, Y. Belmabkhout and M. Eddaoudi, *Chem*, 2019, **5**, 950–963.

8 D. Singh and J. B. Baruah, *Tetrahedron Lett.*, 2008, **49**, 4374–4377.

9 J. A. Perman, A. J. Cairns, Ł. Wojtas, M. Eddaoudi and M. J. Zaworotko, *CrystEngComm*, 2011, **13**, 3130–3133.

10 A. Mallick, B. Garai, M. A. Addicoat, P. S. Petkov, T. Heine and R. Banerjee, *Chem. Sci.*, 2015, **6**, 1420–1425.

11 R. Huo, C. Wang, M. Y. Wang, M. Y. Sun, S. Jiang, Y. H. Xing and F. Y. Bai, *Inorg. Chem.*, 2023, **62**, 6661–6673.

12 A. Mallick, B. Garai, M. A. Addicoat, P. S. Petkov, T. Heine and R. Banerjee, *Chem. Sci.*, 2015, **6**, 1420–1425.

13 A. L. Spek, *Acta Crystallogr.. Sect. C: Struct. Chem.*, 2015, **71**, 9–18.

14 X. Li, J. Liu, K. Zhou, S. Ullah, H. Wang, J. Zou, T. Thonhauser and J. Li, *J. Am. Chem. Soc.*, 2022, **144**, 21702–21709.

15 M. Okumura, L. I. Yeh, J. D. Myers and Y. T. Lee, *J. Phys. Chem.*, 1990, **94**, 3417–3427.

16 C. R. Groom, I. J. Bruno, M. P. Lightfoot and S. C. Ward, *Acta Crystallogr., Sect. B: Struct. Sci. Cryst. Eng. Mater.* , 2016, **72**, 171–179.

17 C. A. Anyama, H. Louis, B. E. Inah, T. E. Gber, J. O. Ogar and A. A. Ayi, *J. Mol. Struct.*, 2023, **1277**, 134825.

18 Z. H. Nie, L. Lu, M. Zheng, Z. Liao, G. Ye, A. Singh and A. Kumar, *J. Mol. Struct.*, 2021, **1245**, 131264.

19 G. Yuan, C. Zhang, K. Z. Shao, W. L. Zhou, X. Wei, F. C. Wang and Z. M. Su, *Inorg. Chem. Commun.*, 2019, **100**, 16–20.

20 Y. Ge, G. Li, D. Fu, L. Liu and B. Wu, *J. Coord. Chem.*, 2019, **72**, 1820–1832.

21 D. C. Zhong, L. Q. Liao, J. H. Deng, Q. Chen, P. Lian and X. Z. Luo, *Chem. Commun.*, 2014, **50**, 15807–15810.

22 H. L. Xu, X. S. Zeng, J. Li, Y. C. Xu, H. J. Qiu and D. R. Xiao, *CrystEngComm*, 2018, **20**, 2430–2439.

23 V. A. Blatov, A. P. Shevchenko and D. M. Proserpio, *Cryst. Growth Des.*, 2014, **14**, 3576–3586.

24 C. Bonneau, M. O'Keeffe, D. M. Proserpio, V. A. Blatov, S. R. Batten, S. A. Bourne, M. S. Lah, J. G. Eon, S. T. Hyde, S. B. Wiggin and L. Öhrström, *Cryst. Growth Des.*, 2018, **18**, 3411–3418.

25 R. Das, T. Ezhil and C. M. Nagaraja, *Cryst. Growth Des.*, 2022, **22**, 598–607.

26 Y. X. Tan, S. X. Lin, C. Liu, Y. Huang, M. Zhou, Q. Kang, D. Yuan and M. Hong, *Appl. Catal., B*, 2018, **227**, 425–432.

27 N. R. Brooks, A. J. Blake, N. R. Champness, J. W. Cunningham, P. Hubberstey, S. J. Teat, C. Wilson and M. Schröder, *J. Chem. Soc., Dalton Trans.*, 2001, 2530–2538.

28 F. Saraci, V. Quezada-Novoa, P. R. Donnarumma and A. J. Howarth, *Chem. Soc. Rev.*, 2020, **49**, 7949–7977.

29 S. Park, J. Lee, H. Jeong, S. Bae, J. Kang, D. Moon and J. Park, *Chem*, 2022, **8**, 1993–2010.

30 L. N. Ma, Z. H. Wang, L. Zhang, L. Hou, Y. Y. Wang and Z. Zhu, *ACS Appl. Mater. Interfaces*, 2022, **15**, 2971–2978.

31 A. Kumar, K. Banerjee, A. S. Foster and P. Liljeroth, *Nano Lett.*, 2018, **18**, 5596–5602.

32 J. M. Hu, V. A. Blatov, B. Yu, K. Van Hecke and G. H. Cui, *Dalton Trans.*, 2016, **45**, 2426–2429.

33 D. Sun, X. Zhao, J. Dou, D. Sen, P. Cui and Q. Wu, *Dalton Trans.*, 2012, **41**, 1928–1930.

34 N. Hanikel, X. Pei, S. Chheda, H. Lyu, W. Jeong, J. Sauer, L. Gagliardi and O. M. Yaghi, *Science*, 2021, **459**, 454–459.

Chapter 4 – Crystal Welding

4.1 Introduction

Molecular tectonics, a term first coined by Stephen Mann in 1993, describes the approach towards building high order structures on various length scales *via* molecular design and organised assembly.[1] This approach hinges on the design of supramolecular assemblies guided by molecular recognition, which is facilitated by tectons.[2] These building elements embody the requisite information for molecular recognition, for example intermolecular interactions, enabling the assembly of self-complementary or mutually complementary tectons within a system.[3,4] In 2000, Macdonald and co-workers first introduced a strategy to control molecular packing and crystal growth of composite materials by utilising a combination of hydrogen bonding interactions and coordination bonds between two tectons to epitaxially grow a new class of modular materials.[5] This concept was later built on by Hosseini and co-workers who defined this method of epitaxial growth of single crystals as crystal welding – a process where self-assembly is used to grow crystalline hierarchically organised architectures composed of either multiple or self-complementary tectons.[6] In their work, Hosseini and co-workers utilised a pair consisting of a dicationic organic tecton and an anionic metallatecton to produce isostructural molecular crystals by varying only the metal centre in the metallatecton. Needle-shaped crystals, exhibiting the colour reflecting the type of metal incorporated during their synthesis, were immersed in a solution containing the dicationic tecton, a metal source and a ligand, and left to evaporate. Within a day, a crystal incorporating the metal source in the solution had formed around the original "seed" crystal. Thus, the authors were able to weld crystals *via* the epitaxial growth of an isostructural phase onto the seed of the original crystal.

In previous chapters, this work focused on studying the assembly of confined molecular clusters with the aims of gaining more understanding, and potentially control, over nucleation processes. Such control is vital for predicting molecular assembly and structure, creation of crystal polymorphs, solvates and co-crystals.[7,8] Integrating crystal welding with controlled nucleation – to precisely predict the shape and size of formed by self-complementary or tectons or tecton pairs – could be a promising novel approach towards designing hierarchically organised architectures. Handa and co-workers reported in 2007 the epitaxial growth of two different metal complexes of 1,4,7-trimethyl-1,4,7'-triazacyclononane (**4.1**) and copper(II) chloride. The binuclear complex $[\{Cu(\mathbf{4.1})\}_2(\mu\text{-}Cl)_3]$ (**4.2**) forms yellow orthorhombic crystals while the mononuclear complex $[Cu(\mathbf{4.1})Cl_2]$ (**4.3**) forms green monoclinic crystals. As the solution containing copper(II) and **4.1** evaporates, green crystals of **6** start depositing on the

surface of the vial and as the solution becomes more concentrated, the equilibrium shifts to favouring the ionic yellow binuclear complex. The authors suggest this epitaxial growth proceeds on a molecular level with the ligand of the daughter phase integrating into the lattice of the parent phase. This mechanism suggests a method to control the epitaxial growth of complexes **4.2** and **4.3**, with potential expansion to isostructural complexes featuring different metal centres. Thus, the following work aims to provide insight into this phenomenon of concomitant epitaxial crystallisation of these coordination compounds in hopes of understanding and potentially gaining control of epitaxial growth in this system. Furthermore, by substituting the copper(II) centre with a alternative metals, this work will explore the crystal welding of isostructural **4.1**-based coordination compounds, extending the investigation to a structurally similar ligand 1,4,7-trithiacyclononane.

4.2 Triazacyclononane-Based Coordination Compounds

4.2.1 Copper-Triazacyclononane Coordination Compounds

The crystal structures of the coordination compounds **4.2** and **4.3**, along with the structure of ligand **4.1**, are shown in **Figure 4-79a–c**. The reported crystal structure of **4.2** is a tetrahydrate obtainable from polar solvents such as ethanol or THF while **4.3** is a hemisolvate of dichloromethane and can generally be obtained from non-coordinating solvents.[9] The binuclear complex of **4.2** contains two copper(II) metal centres coordinated to two ligands of **4.1** which are bridged by three chloride anions. As a result, **4.2** has an overall positive charge and is charge neutralised by a chloride counter anion. The copper(II) metal centres in **4.2** adopt a Jahn-Teller distorted octahedral geometry. On the other hand, **4.3** contains one square pyramidal copper(II) metal centre coordinated to one ligand and two chloride anions.

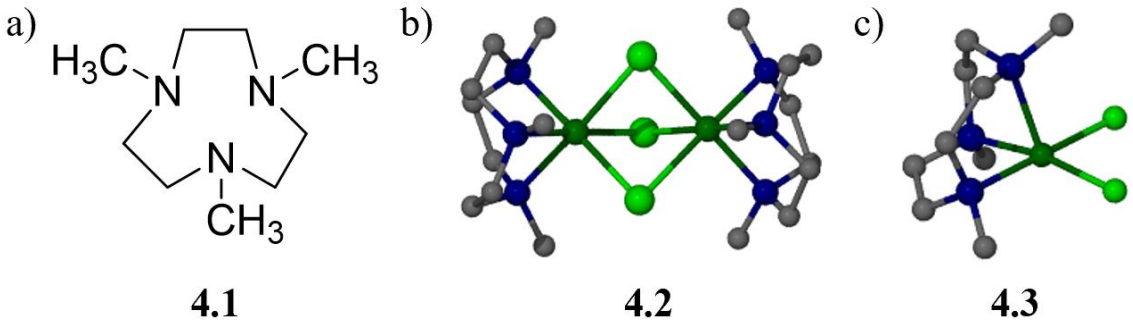

Figure 4-79. a) Structure of ligand **4.1**. b) Single crystal structure of the binuclear **4.2**. c) Single crystal structure of the mononuclear **4.3**. Gray: C. Blue: N. Light green: Cl. Dark green: Cu. Hydrogen atoms have been omitted for clarity.

According to the 2007 report by Handa and co-workers, the use of polar solvents results in the formation of olive-yellow crystals of the binuclear cation.[9] To reproduce this work, an ethanolic solution containing a 1:1 ratio of **4.1** and copper(II) chloride was left to slowly evaporate. Over the course of a day, green and yellow plate-like single crystals started appearing on the side of the vial, as shown in **Figure 4-80a** and **b**. The FT-IR spectra of the green and yellow crystals are shown in **Figure 4-81a**, along with the spectrum of the ligand **4.1**. The latter exhibits C–H stretching vibrations in the range of 2963 – 2758 cm^{-1}, C–H bending vibrations centred at 1450 cm^{-1} and C–N stretching at 1368 cm^{-1}, in good agreement with the values reported in literature.[10] The IR spectrum of the yellow crystals (**Figure 4-81a**, blue line) contains wide bands centred around 3500 and 1662 cm^{-1}, attributed to the O–H stretching and scissoring of coordinated water molecules. The bands ranging from 2983 to 2809 cm^{-1} are attributed to C–H stretching of **4.1**, which have considerably shifted, presumably also due to the coordination of the ligand to the copper(II) metal centre. Finally the C–N stretching band of **4.1** has shifted from 1368 to 1364 cm^{-1}. The IR spectrum of green crystals (**Figure 4-81**, red line) is very similar to that of the yellow crystals, also indicating to the formation of a coordination compound between **4.1** and copper(II).

SC-XRD analysis of the yellow crystals reveals a nearly identical crystal structure to that of the reported **4.2** with a formula $[\{Cu(\mathbf{4.1})\}_2(\mu\text{-}Cl)_3]Cl\bullet 4.5H_2O$ (**4.2a**), **Figure 4-80c**. The primary distinction between **4.2** and **4.2a** resides in the minor variance in the hydration level, with four and four and a half water molecules per unit of the coordination compound, respectively. These crystals proved difficult to handle; upon complete solvent evaporation, the crystal quality deteriorates within a few hours. Conversely, when crystals form on the side of the vial and the vial is capped with enough solvent in, the crystals re-dissolve. Thus, single crystals were subjected to SC-XRD analysis as soon as they had formed and were of sufficient size. Additionally, upon full evaporation of ethanol, green single crystals form at the bottom of the vial along with more olive-yellow-coloured crystals (**Figure 4-80b**), pointing to the concomitant crystallisation as reported by Handa and co-workers.[9] Unfortunately, the crystal quality of the green crystals was not good enough to determine their crystal structure via SC-XRD.

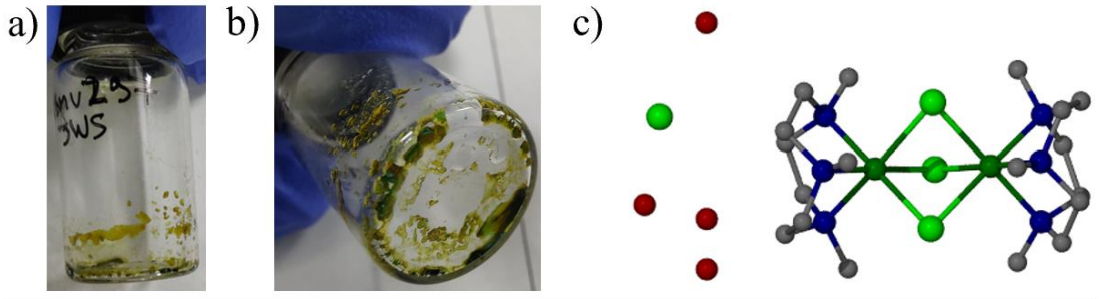

Figure 4-80. a) Olive-yellow-coloured single crystals of **4.2a** as observed on the side of the vial. b) Both olive yellow and green coloured single crystals seen at the bottom of the vial upon the evaporation of ethanol. c) Single crystal structure of **4.2a** with four water molecules and a chloride anion. Gray: C. Blue: N. Dark green: Cu. Light green: Cl. Hydrogen atoms omitted for clarity.

The PXRD patterns for yellow (Y) and green (G) crystals are shown in **Figure 4-81b** (black and red traces, respectively). The powder pattern of the yellow crystals matches very closely with that of the simulated pattern (**Figure 4-81b**, dark blue trace). The pattern obtained from the green crystals matches closely with both yellow and simulated patterns, with peaks at 12.5 and 14.7° not being observed. Additionally, the elemental analysis closely matches the composition expected for **4.2a** (Experimental Section 4.5.1). These findings suggest that both yellow and green crystals from this crystallisation process are associated with the binuclear coordination complex, contrary to the initial report by Handa and co-workers, which distinguished between yellow crystals as binuclear and green crystals as mononuclear complexes.[9]

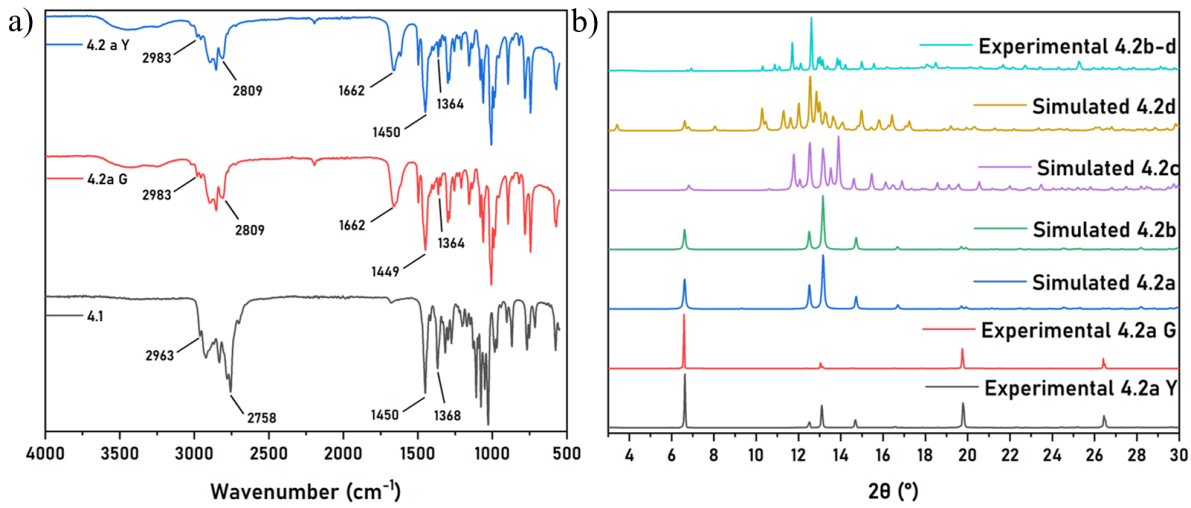

Figure 4-81. a) FT-IR spectra of **4.1**, **4.2a G** and **4.2a Y**. b) Experimentally obtained and simulated PXRD patterns coordination compounds **4.2a**–**d**. The powder pattern labelled experimental **4.2b–d** displays the PXRD pattern of all three crystalline products measured together, as opposed to three separate powder patterns of each compound (**4.2b**, **4.2c** and **4.2d**) superimposed.

Subsequent investigations focused on assessing the effect that changing the metal:ligand ratio has on the crystallization outcome. A solution with a 3:2 copper(II) chloride to **4.1** ratio was prepared in ethanol, which was again left to slowly evaporate. Under these conditions, three types of crystals formed in one vial – brown prisms, brown plates and green plates.[12] The green plate-like crystals have a formula of [{Cu(**4.1**)}$_2$(μ–Cl)$_3$]Cl•2CH$_3$OH (**4.2b**), **Figure 4-82b**. The crystal structure of **4.2b** is a methanol solvate containing a chloride anion. The solvate molecules were best modelled as methanol despite this solvent not being used to crystallise this compound. The presence of the solvent is likely due to atmospheric methanol being present when the open vial was left to slowly evaporate. The copper(II) metal centres take up a distorted octahedral geometry where Cu–Cl coordination bond lengths vary in the range of 2.3765(10)–2.5477(13) Å. The Cu–N coordination bond lengths in **4.2b** vary in the range of 2.099(3)–2.157(3) Å.

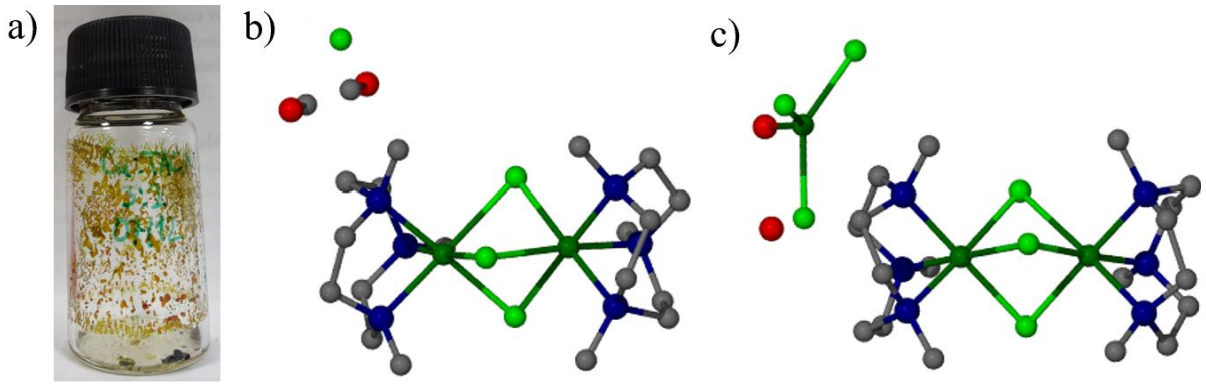

Figure 4-82. a) Picture of the vial showing the range of colours of the crystals determined to be **4.2b**–**d**. Single crystal structures of b) **4.2b** and c) **4.2c**. Gray: C. Red: O. Blue: N. Light green: Cl. Dark green: Cu. Hydrogen atoms omitted for clarity.

SC-XRD analysis of the brown prism-shaped crystals yields a formula of [{Cu(**4.1**)}$_2$(μ-Cl)$_3$][CuCl$_3$(H$_2$O)]•H$_2$O (**4.2c**), **Figure 4-82c**. The crystal structure contains one cationic binuclear coordination compound along with one water molecule and a counterion consisting of a 4-coordinated copper(II) with three chloride and one water molecule as ligands. In this structure, the octahedral copper(II) metal centres in the cationic complex form coordination bonds with the bridging chloride anions in the range of 2.3358(6)–2.7394(7) Å. The Cu–N coordination bond lengths vary in the range of 2.0777(12)–2.2109(12) Å. In **4.2c**, the copper(II) metal centre in the anion adopts the distorted square planar geometry with Cl–Cu–Cl and Cl–Cu–O angles (ligands coordinated opposite of one another that should have 180° coordination angle in an ideal octahedral geometry) of 143.2° and 139.4°, respectively. In the case of adjacent ligands, the two Cl–Cu–Cl angles are 98.1° and 100.5° while the two Cl – Cu

– O angles are closer to the ideal square planar geometry angles, standing at 95.1° and 91.2°. The $[CuCl_3(H_2O)]^-$ anion is rather rare, having been reported a mere 10 times in the CSD, also exhibiting the distorted square planar geometry.[11,12] Despite the coordination complex cation being identical to **4.2b**, the Cu–Cl coordination bonds formed in **4.2c** are significantly longer than those in **4.2b**.

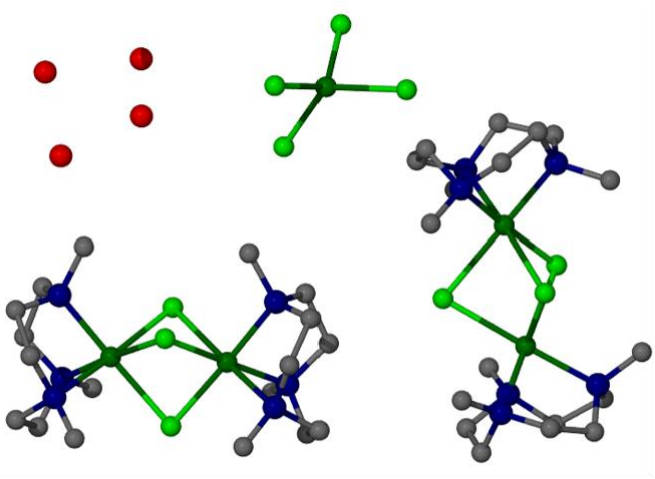

Figure 4-83. Single crystal structure of **4.2d**. Gray: C. Red: O. Blue: N. Light green: Cl. Dark green: Cu. Hydrogen atoms omitted for clarity.

The brown plate-like crystals have a formula of $[\{Cu(\mathbf{4.1})\}_2(\mu\text{-}Cl)_3]_2[CuCl_4]\bullet 4H_2O$ (**4.2d**), as depicted in **Figure 4-83**. This crystal structure contains two slightly different binuclear complexes which are overall charge balanced by a $[CuCl_4]^{2-}$ anion. Between the two copper(II) metal centres, the Cu–Cl coordination bond lengths do not vary as much as they do between complexes **4.2b** and **4.2c**. In **4.2d**, these coordination bond lengths are 2.3182(6)–2.8274(7) Å for one complex and 2.3074(7)–2.7118(9) Å for the other. The Cu–N coordination bond lengths in **4.2d** range from 2.067(2)–2.227(2) Å. The $[CuCl_4]^{2-}$ anion exhibits a distorted tetrahedral geometry with bond angles varying in the range 98.9–129.7°. This is a widely reported dianion, resulting in 625 hits in the CSD, exhibiting both square planar and tetrahedral geometries.[13,14]

Overall, these results show that crystallisation from ethanol favours the formation of the binuclear coordination compound where the coordination bond lengths, especially those of Cu–Cl, vary to a relatively large degree. However, the presence of green crystals, previously attributed to the mononuclear coordination compound, suggests that the colour change between yellow and green might not be necessarily due to the change in equilibrium favouring the mononuclear complex but is also associated with the nature of the counter anion of a given cationic binuclear coordination compound.

From a 3:1 (v:v) acetonitrile (ACN):DMSO solution containing a 1:1 ratio of **4.1** : copper(II) chloride, green plank-shaped single crystals formed (**Figure 4-84a**). SC-XRD analysis reveals that the crystals comprise a mononuclear coordination compound of formula [Cu(**4.1**)Cl_2] (**4.3a**), **Figure 4-84b**, identical to **4.3** The main difference between **4.3** and **4.3a** is that **4.3a** is a solventless equivalent of **4.3** while the crystal structure of the latter is a solvate containing DCM. The copper(II) metal centre is 5-coordinated and takes up a distorted square prismatic geometry with Cu–Cl coordination bond lengths of 2.2705(4) and 2.2781(4) Å and the equatorial bond angles varying in the range 83.20(5)–92.89(4)°. Both ACN and DMSO are polar, coordinating solvents and should thus favour the crystallisation of the binuclear **4.2**. Instead, the solvent evaporation method gives the solventless **4.3a**. Thus, not only does this reaction favour the formation of the mononuclear **4.3**, neither DMSO nor ACN are observed in the crystal structure despite DMSO being known to be a polar solvent that is difficult to remove from reaction products. The PXRD pattern of **4.3a** (**Figure 4-84d**, black trace) exhibits peaks that closely align with the pattern simulated from the SC-XRD data. The simulated powder pattern contains many peaks that are not observed in the experimental pattern. This is ascribed to preferred orientation crystals of **4.3a**, a common phenomenon in plank-shaped crystals and previously discussed in relation to CCM-series MOFs in Chapter 2 of this work.

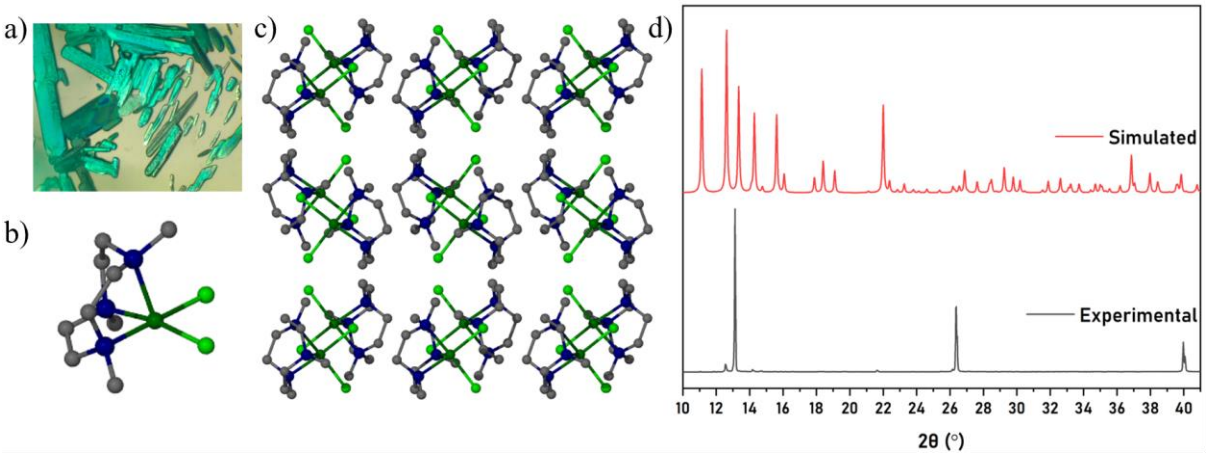

Figure 4-84. a) Microscope image of the green single crystals of **4.3a**. b) Single crystal structure of one unit of **4.3a**. c) Unit cell packing of **4.3a** as viewed along the *b* axis. D) PXRD pattern of the experimentally obtained **4.3a** crystals (black line) and the pattern simulated from the crystal structure (red line). Gray: C. Blue: N. Light green: Cl. Dark green: Cu. Hydrogen atoms omitted for clarity.

Copper(II) chloride is green while the colour of copper(II) bromide is black. The geometry of the coordination compounds between **4.1** and copper(II) chloride and **4.1** and copper(II) bromide should be nearly identical as the metal centre and the triazacyclononane

ligand do not change. Thus, epitaxial growth of coordination compounds between **4.1** and copper(II) bromide on top of **4.2** or **4.3** could be possible and would yield materials of different colours which can be visually distinguished. In order to test whether this type of epitaxial growth could be achieved, first it was studied whether it is possible to crystallise the coordination compound between **4.1** and copper(II) bromide. Indeed, single crystals of a coordination compound between **4.1** and copper(II) bromide were obtained from a 1:1 M:L solution in THF (**Figure 4-85a**). Gold-coloured small single crystals (**Figure 4-85b**) instantly precipitated from solution upon the addition of the ligand to the mixture of copper(II) bromide in THF.

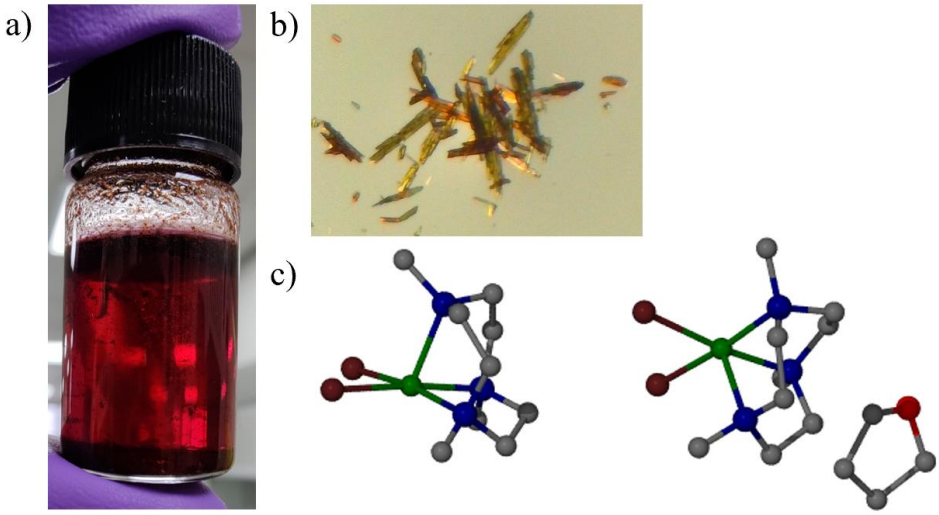

Figure 4-85.a) Image of the dark red THF solution with precipitated single crystals of **4.4**. b) single crystals of **4.4** under a microscope showing the shape and the colour. c) single crystal structure of the coordination compound of **4.4**. Gray: C. Bright red: O. Dark red: Br. Blure: N. Green: Cu. Hydrogen atoms omitted for clarity.

SC-XRD analysis reveals that the crystals comprise a mononuclear coordination compound with a 5-coordinated copper(II) metal centre which coordinates with two bromide ions and one ligand of **4.1**. **Figure 4-85c** shows the asymmetric unit of **4.4** contains two independent coordination compounds and one THF molecule with the formula [Cu(**4.1**)Br_2]·0.5THF. This structural arrangement mirrors that of compound **4.3a**, with the copper(II) metal centre maintaining the distorted square pyramidal geometry, thereby rendering crystals of **4.3a** and **4.3** isostructural. **Figure 4-86** shows the experimentally obtained and simulated powder patterns of **4.4**. Although the peaks indicated in yellow show reasonable alignment between the experimental and simulated patterns, the experimental pattern exhibits additional peaks absent in that of the simulated pattern. This observation may indicate that a

phase transition occurs when the crystals of **4.4** are removed from the mother liquor for an extended timeframe, such as during the PXRD pattern measurement. Nevertheless, given the strong correlation between elemental analysis and the crystal structure, this was not further investigated.

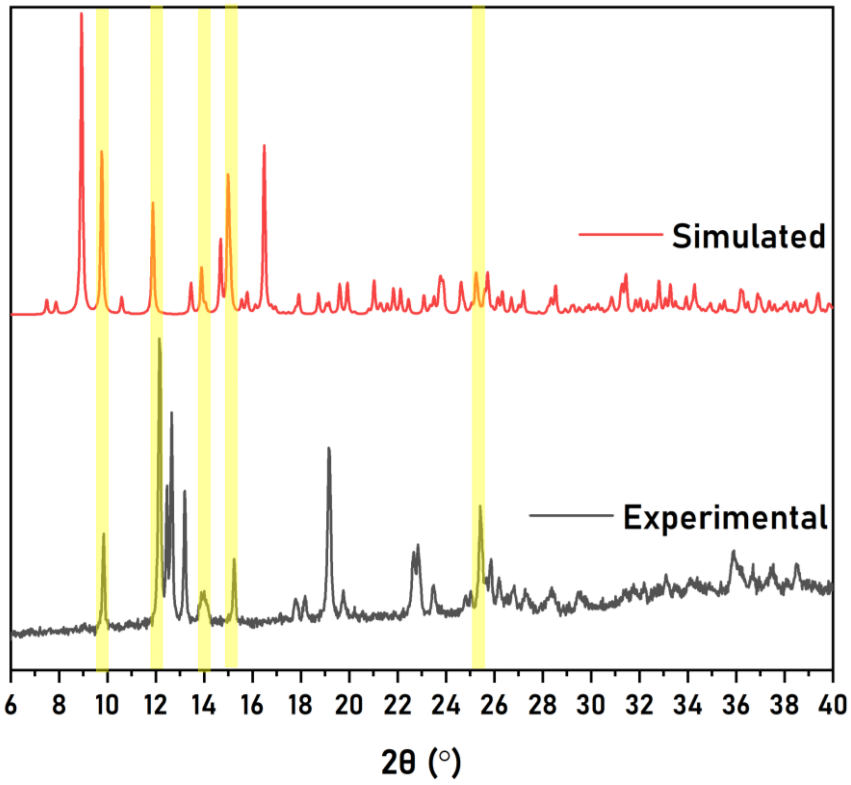

Figure 4-86. Powder X-Ray diffraction patterns of **4.4** obtained experimentally (black line) and simulated from the single crystal structure (red line).

Overall, copper(II) chloride has been shown to form different coordination compounds with the ligand **4.1**. While at first it was believed that polar coordinating solvents favour the formation of the cationic trichloro-bridged binuclear complex, it has been shown that the neutral mononuclear complex can also be prepared from such solvents. This shows how labile copper(II) is and that gaining control over the crystallisation outcomes is rather difficult. However, successful epitaxial growth of one phase of a copper-based coordination compound onto another could lead to gaining control over these crystallisation outcomes and is discussed in Section 4.2.4.

4.2.2 Nickel-Triazacyclononane Coordination Complexes

As single crystals of the mono- and binuclear copper complexes were successfully synthesised, the work focused on welding isostructural crystals of **4.2** with different metals. Nickel was selected for investigation due to its ability to form hexacoordinated metal complexes, akin to

those observed in **4.2a**–**d**, suggesting the potential for preparing an isostructural nickel-based coordination complex. The CSD contains one crystal structure of a binuclear coordination compound between nickel(II) and **4.1**.[15] However, this coordination compound is dichloro-bridged and not trichloro-bridged and thus is not isostructural to the binuclear copper(II) coordination complex with **4.1**. Preparation of nickel(II) coordination complexes with **4.1** was attempted initially in ethanol, but no single crystals were obtained. As the solvent mixture of ACN:DMSO yielded high quality single crystals of **4.3a**, this solvent system was also applied to prepare crystals of nickel(II) chloride with **4.1**. Thus, a mixed solvent solution of ACN:DMSO in a 3:1 ratio was used to dissolve nickel(II) chloride and **4.1** in a 1:1 ratio and the resulting solution was left to slowly evaporate at 70°C. Over the course of 1-2 weeks, blue needle-like crystals formed, as shown in **Figure 4-87a**.

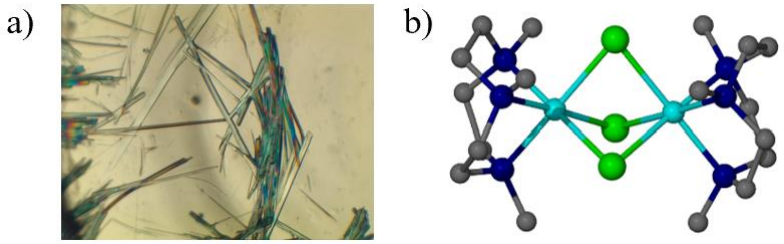

Figure 4-87. a) Microscope image of needle-shaped single crystals of **4.5**. b) Binuclear complex of **7**. Gray: C. Dark blue: N. Light green: Cl. Light blue: Ni. Hydrogen atoms have been omitted for clarity.

SC-XRD analysis reveals the structure of a binuclear metal complex with the formula $[Ni_2(\mathbf{4.1})_2(\mu\text{-}Cl_3)]Cl{\bullet}4H_2O$ (**4.5**), **Figure 4-87**. This material is similar to the copper(II) chloride analogue, namely a binuclear cationic complex with a trichloro bridge and two ligands of **4.1**. The 6-coordinated nickel(II) metal centre adopts an octahedral geometry with Ni–Cl distances ranging in 2.4357(6)–2.4433(7) Å. Crystals of the binuclear **4.5** were further characterised by PXRD and elemental analysis. The experimental X-ray powder diffraction pattern exhibits peaks that are shifted slightly to lower 2θ compared to pattern simulated from the low temperature SXRD data. The SXRD data is collected at 120 K and hence the simulated pattern corresponds to a contracted lattice at this lower temperature compared to room temperature. Additionally, the elemental analysis results match closely with the expected composition, further implying good bulk purity. The successful synthesis of this binuclear complex of **4.5** suggests that it could be possible to epitaxially grow the complex of **4.5** on to the template of **4.2a** and *vice versa*.

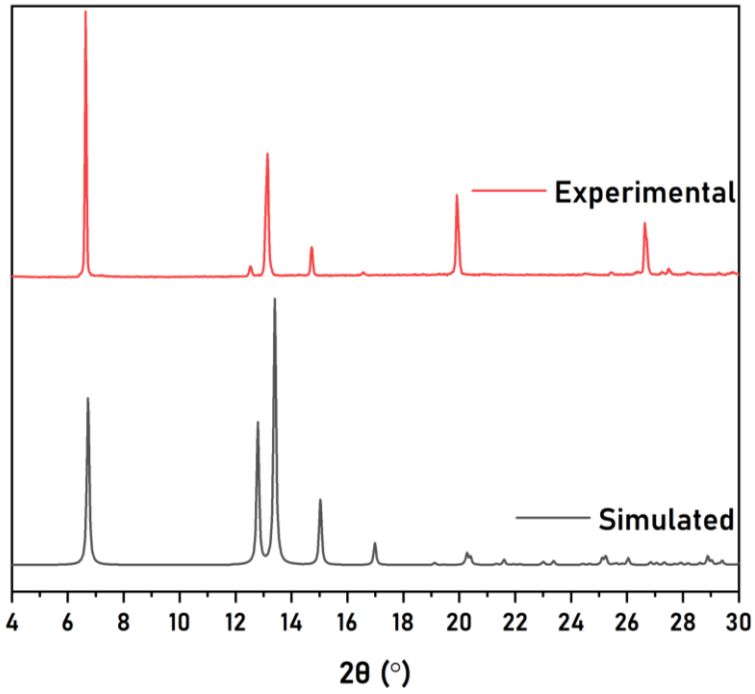

Figure 4-88. Simulated (black line) and experimentally obtained (red line) PXRD patterns of **4.5**.

4.2.3 Cadmium-Triazacyclononane Coordination Complexes

Following the work with nickel(II), cadmium(II) was selected as it also is capable of forming hexacoordinate complexes and could potentially be utilised toward the epitaxial growth of isostructural compounds. The reaction of **4.1** with cadmium chloride hemipentahydrate in a 1:1 ratio in ethanol gave irregularly shaped colourless crystals shown in **Figure 4-89a**. SC-XRD analysis reveals the formation of a trinuclear triazacyclononane-cadmium complex (**4.6**, **Figure 4-89a** and **b**) with a formula $[Cd_3(\mathbf{4.1})_2(\mu\text{-}Cl_6)(H_2O)_2]\bullet H_2O$. Despite the dissolution of a 1:1 mixture, the crystal structure contains a metal:ligand ratio of 3:2. Each cadmium(II) centre is hexacoordinated in a distorted octahedral coordination geometry. Two cadmium cations are coordinated to **4.1** and two bridging and one terminal chloride ligands while the central metal is coordinated to four chloride anions and two water molecules. The Cd–Cl coordination bond lengths vary in the range 2.5318(4)–2.6294(3) Å while the Cd–N coordination bonds vary in the range 2.3736(12)–2.4184(12) Å. The CSD contains only mononuclear coordination complexes between cadmium(II) and analogues of **4.1** and none that contain strictly **4.1** and cadmium(II), so **4.6** is a novel coordination complex.[16,17]

The crystals were further characterised *via* PXRD and elemental analysis. **Figure 4-90** shows the experimental powder pattern of **4.6** (black line) coupled with the powder pattern simulated from the single crystal structure (red line). There are close similarities between the two patterns suggesting that the obtained crystals are phase pure and no phase changes occur

when cooled to 120K to obtain the single crystal structure. The crystals were also analysed by elemental analysis. The expected carbon, hydrogen and nitrogen compositions closely match that of the obtained values, see experimental section. The close match between the expected and obtained results for all SXRD, PXRD and elemental analysis suggests that this material is phase pure and does not undergo spontaneous phase changes within weeks.

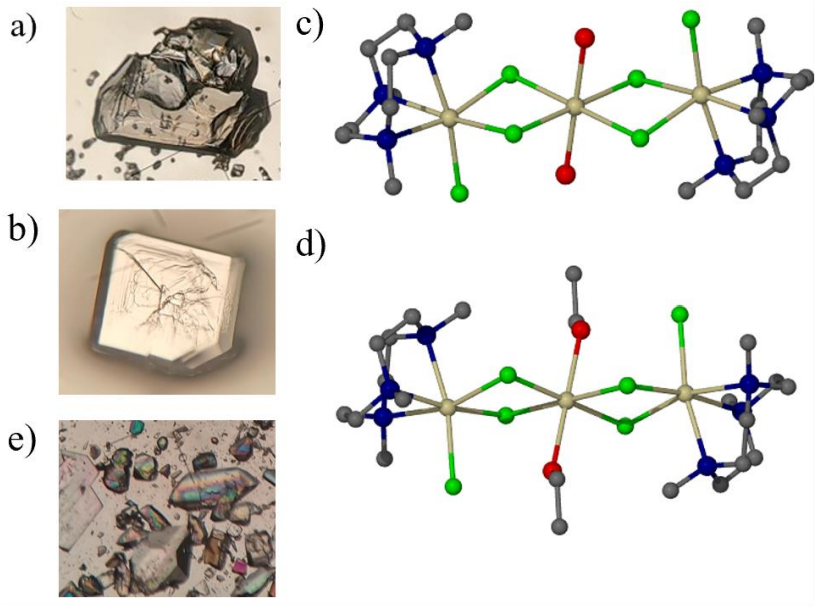

Figure 4-89. Microscope image of a single crystal of a) **4.6** and b) **4.7**. b) Single crystal structure of the trinuclear **9**. Gray: C. Dark blue: N. Red: O. Yellow: Cl. Light blue: Cd. H atoms have been omitted for clarity.

To replicate the crystallisation conditions that yielded the 3:2 M:L ratio of **4.6**, an ethanolic solution containing a 3:2 ratio of cadmium(II) : **4.1** was prepared and allowed to slowly evaporate. Overnight, plate-like single crystals formed **(Figure 4-89b)**. The SC-XRD analysis of these crystals reveals a trinuclear coordination complex identical to **4.6**, only with ethanol as the coordinating solvent instead of water, resulting on a formula $[Cd_3(\mathbf{4.1})_2(\mu\text{-}Cl_6)(CH_3OH)_2]$ (**4.7**), **Figure 4-89d**. The Cd–Cl coordination bonds are nearly identical to those in **4.6**, in the range 2.5506(3)–2.6266(3) Å and the same is for the Cd–N coordination bond lengths which range from 2.3711(9) to 2.4302(10) Å. The PXRD pattern of these crystals is shown in **Figure 4-90** (blue trace) which does not have a good agreement with the simulated powder pattern of **4.7** (**Figure 4-90**, green trace), potentially due to some phase transition when removed from the mother liquor.

Within 1–2 days following their formation, the plank-shaped crystals of **4.7** underwent a transformation into irregularly shaped single crystals resembling those of **4.6**, as shown in **Figure 4-89e**. The determination of the unit cell of these transformed crystals revealed a unit

cell identical to that of compound **4.6**. Consequently, a PXRD pattern of these irregularly shaped crystals was obtained to study whether **4.7** had transformed back into **4.6**. **Figure 4-90** (purple trace) shows the powder pattern of the transformed single crystals of **4.7**, which agree well with the experimentally obtained and simulated PXRD patterns of **4.6**. These results indicate that the single crystals of **4.7** indeed transformed into **4.6**. Following this transformation, single crystals of **4.6** were subsequently used for the epitaxial growth of nickel- and copper-based coordination complexes.

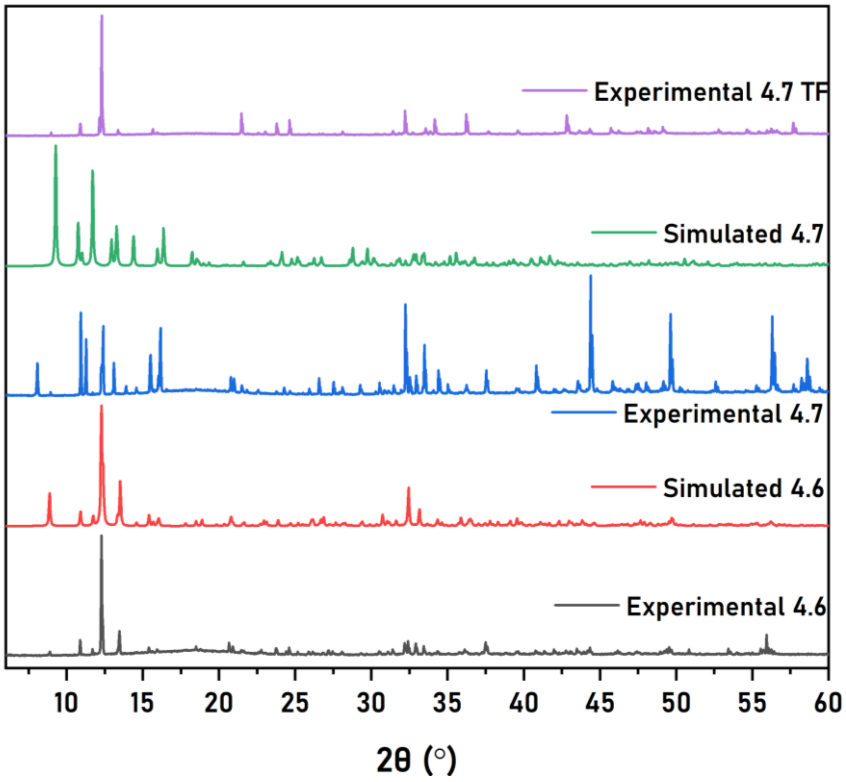

Figure 4-90. Experimental and simulated PXRD patterns of **4.6** (black and red traces), **4.7** (blue and green traces) and the crystals of transformed (TF) **4.7** (purple trace).

4.2.4 Epitaxial Growth of Single Crystals

In the pursuit of epitaxially growing one crystal phase onto another, compounds **4.2**–**4.6** were used to seed solutions of a metal salt and **4.1**. For instance, to seed the growth of **4.3a** copper(II) chloride and **4.1** in a 1:1 ratio was placed in a small vial. Subsequently, a single crystal of **4.2a** was placed inside the droplet and the vial was covered with a cap through which a needle was pierced in order to reduce the evaporation rate of ethanol. Unfortunately, the seed crystals always dissolved within the droplet. Additionally, the droplet evaporates within two hours after placing it in the vial. The combination of these two factors results in a mixture of crystals forming in the place of the solvent, as shown in **Figure 4-91a**. In this case, a seed crystal of **4.3a** was placed in a droplet taken from the ethanolic 1:1 M:L solution and left to evaporate

overnight. A mixture of green and light blue crystals formed, which were not further studied due to the dissolution of the seed crystal, which rendered epitaxial growth impossible. Due to additional time constraints, the green and blue crystals pictured in **Figure 4-91a** were not further characterised. Instead, different experimental conditions were subsequently pursued in order to ensure that the seed crystals to not dissolve.

Consequently, to overcome the dissolution of seed crystals and the fast evaporation of the droplet, a mixture of ACN:DMSO (3:1 v:v) was used, and this mixture was supersaturated with either copper(II) chloride, nickel(II) chloride or cadmium(II) chloride. The supersaturation was achieved by adding an excess amount of a given metal salt to the 1 mL of mixed solvent solution. A droplet of this mixture was placed in a vial along with a seed crystal, aiming to provide conditions where the seed would not dissolve and allowing more time for potential epitaxial growth to occur. A single crystal of **4.6** was placed in a droplet of ACN:DMSO solution containing copper(II) chloride and **4.1**. Over the course of 24 hours, the seed crystal remained while what appeared to be potentially epitaxially grown blue compound (**Figure 4-91b**). Unfortunately, when these crystals were moved, the blue areas turned out to be a dense liquid. Nonetheless, the experiment confirmed that the ACN:DMSO solvent mixture did not dissolve the seed crystal, a noteworthy observation despite the absence of epitaxial growth.

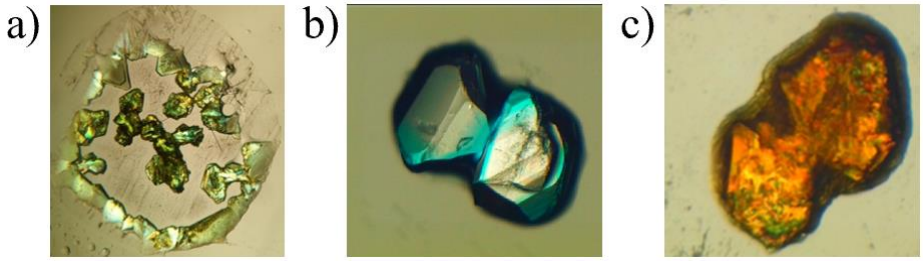

Figure 4-91. a) Microscope image of the resulting crystals when a seed of **4.3a** was placed in an ethanolic drop containing a 1:1 ratio of nickel(II) chloride and **4.1**. b) Blue dense liquid surrounding a seed crystal of **4.6**. c) Microscope image of the brown crystals of **4.2b** grown on top of the seed of **4.6**.

Table 4-13 shows the combinations of seed crystals and droplets tested and their crystallisation outcomes. The red box indicates that either no epitaxial growth was observed or crystals only formed from the droplet itself. In most cases, the droplet evaporated until a mixture of crystals was left and thus epitaxial growth was not observed. However, in the case where a seed crystal of **4.6** was used inside a droplet containing copper(II) chloride and **4.1**, brown crystalline solid (**Figure 4-91c**) formed on the surface of the seed crystal which was

indeed a crystalline material. SC-XRD analysis of this material yields a binuclear copper-based coordination compound containing a $[CuCl_3(H_2O)]^-$ anion, identical to that of **4.2b**.

Table 4-13: Combination of seed crystal and mixtures used to study epitaxial crystallisation. All droplets in this table have been taken from 3:1 ACN:DMSO solutions saturated with the indicated metal chloride salt. For more specific details, see experimental section 4.5.7.

Seed Crystal	Droplet	Outcome
4.2a	cadmium(II) : **4.1**	
4.2a	copper(II) : **4.1**	
4.2a	nickel(II) : **4.1**	
4.3a	cadmium(II) : **4.1**	
4.3a	copper(II) : **4.1**	
4.3a	nickel(II) : **4.1**	
4.4	cadmium(II) : **4.1**	
4.4	copper(II) : **4.1**	
4.4	nickel(II) : **4.1**	
4.5	cadmium(II) : **4.1**	
4.5	copper(II) : **4.1**	
4.5	nickel(II) : **4.1**	
4.6	cadmium(II) : **4.1**	
4.6	copper(II) : **4.1**	**4.2b**
4.6	nickel(II) : **4.1**	

While most of the sample appears brown, the material also contains green crystalline areas. These crystallites were too small for SC-XRD analysis and were thus not further studied. However, based on the previous study by Handa and co-workers, it is likely to be the mononuclear coordination complex **4.3a**. However, when both bi- and mononuclear species **4.2** and **4.3** form within crystals, it is generally the mononuclear **4.3** that forms first and templates the growth of the daughter binuclear phase. In the case of using **4.6** as a seed, it appears that the binuclear complex is the parent templating the occasional growth of the green daughter phase. Whether this is a result of using **4.6** as a seed or a solvent contribution is difficult to ascertain. Additionally, considering the drop where the seed crystal of **4.6** was placed was saturated with copper(II) chloride, it is possible that the presence of excess copper(II) chloride is the driving force behind the formation of **4.2b** which also crystallised from a solution with an excess of copper(II) chloride.

As copper(II) bromide successfully forms single crystals with **4.1** (**4.4**) isostructural to the mononuclear copper(II) chloride coordination compound (**4.3** and **4.3a**), the epitaxial growth of one on the other one was also attempted. To start with, a solution containing 1:1 ratio of copper(II) chloride and **4.1** in ACN:DMSO (3:1 v:v) was prepared and to a drop of it was added one small crystal of **4.4**. However, the single crystal of **4.4** dissolved and thus epitaxial

growth could not take place. Similarly, a drop of 1:1 copper(II) bromide : **4.1** from a 3:1 (v:v) ACN:DMSO solution was seeded with a green single crystal of **4.3**, which also dissolved. Thus, a 2:1:1 solution of **4.1** : copper(II) chloride : copper(II) bromide in 2 mL of ethanol was made up. Overnight, single crystals of green, brown and a mix of green and brown colour formed which were analysed *via* elemental analysis, PXRD and SC-XRD.

SC-XRD analysis reveals a binuclear coordination compound with a formula $[\{Cu(\mathbf{4.1})\}_2(\mu\text{-}Cl)_2][Cu_2Br_4(\mu\text{-}Br)_2]$ (**4.8**, **Figure 4-92a**). Interestingly, the binuclear coordination compound is only bridged by two chloride anions, unlike the trichloro-bridge observed in all of the other binuclear complexes. The complex is charge neutralised by a $[Cu_2Br_4(\mu\text{-}Br)_2]^{2-}$ anion. The SC-XRD structure refinement suggests that the bridging anions consist of both chloride and bromide in a 0.85:0.15 ratio, respectively. This could explain why crystals of different colours were observed in the vial. The experimentally obtained and simulated PXRD patterns of **4.8** are depicted in **Figure 4-92c**. There are many agreements in the peak positions between the two diffractograms (shaded yellow), but there are also a multitude of differences. This cannot be a temperature effect because in this case the peak positions would only slightly shift to lower angles in the simulated powder pattern.

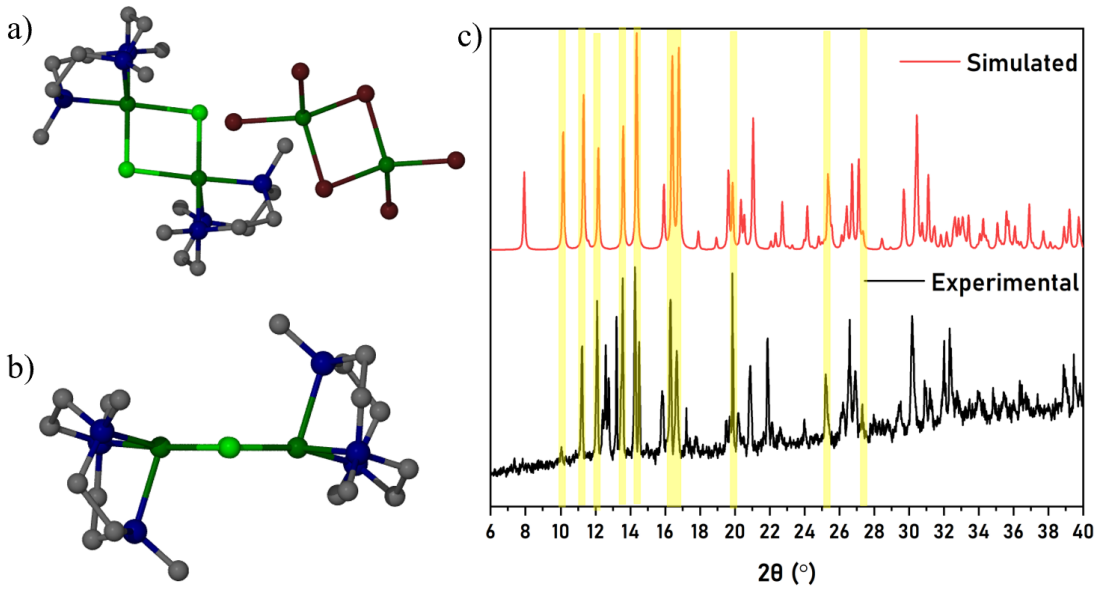

Figure 4-92. Single crystal structure of **4.8** a) along the *b* axis with the counterion and b) the side view showing the placement of the ligand. c) PXRD pattern of the experimentally obtained (black line) and simulated (red line) **4.8**. Gray: C. Blue: N. Light green: Cl. Dark red: Br. Dark green: Cu.

The structures of **4.2** and **4.3** are the most closely related to one another by their unit cell dimensions along the *a* direction (13.77 Å for **4.2** and 13.79 Å for **4.3**). However, the unit

cell values also account for the solvent molecules and do not represent the unit cell of the pure compound. Based on the reported unit cell dimensions, **4.2** and **4.3** are very similar along the *a* direction. Similarly, **4.4** and **4.5** exhibit unit cell dimensions somewhat similar to isostructural compounds, but the differences are still above 5%. Handa and co-workers propose that the epitaxial growth proceeds on a molecular basis along the direction of the ligand, as shown in **Figure 4-93**.[9] The arrangement of the ligand is nearly identical in each of the coordination compounds, regardless of the nature of the metal centre, the metal salt or the coordination geometry in each compound. This suggests that crystal growth could be occurring on a molecular level with the ligands arranging themselves along a specific direction within the crystal and crystal growth proceeding along said direction.

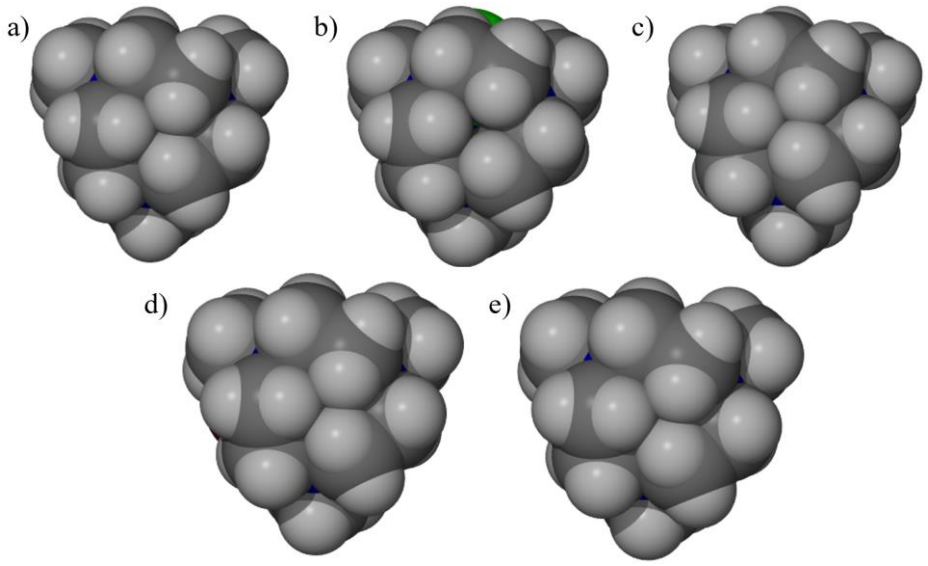

Figure 4-93. Spacefill mode view of a) reported **4.2** b) reported **4.3** c) **4.3a** d) **4.4** and e) **4.5** from the side of the ligand **4.1**.

4.3 Trithiacyclononane-Based Coordination Compounds

4.3.1 Nickel-Trithiacyclononane Coordination Compounds

Following the work with triazacyclononane-based coordination compounds, the focus was shifted towards the 1,4,7-trithiacyclononane ligand (**4.9**). This ligand is structurally similar to **4.1** while not possessing the methyl groups. The aim of this work was to study whether **4.9** would form similar mono- and binuclear compounds and if so, whether they could also be epitaxially grown onto one another. Using **4.9** is also advantageous in terms of studying isostructural coordination compounds, because if single crystals of isostructural compounds are successfully prepared, they will exhibit different colours. In this case, epitaxial growth of isostructural compounds with the same metal centres will result in crystals with two colours

and easily identifiable transition points. As **4.1** formed coordination compounds with copper(II), nickel(II) and cadmium(II), the efforts were focused on the crystallisation of these metals with **4.9**. Unfortunately, no coordination compounds between **4.9** and cadmium(II) were obtained.

Into a 3:1 ACN:DMSO solution, a 1:1 mixture of nickel(II) chloride : **4.9** was added and the vial was left to evaporate in an isothermal oven 70°C to increase to evaporation rate of DMSO which is involatile at room temperature. Over the course of 1–2 weeks, green prism-shaped single crystals formed on the side of the vial (**Figure 4-95a**). These crystals were characterised *via* FT-IR spectroscopy, PXRD, SC-XRD and elemental analysis.

The FT-IR spectrum of the green crystals is shown in **Figure 4-94a** (red line). The bands centred at 2981 and 1033 cm^{-1} are attributed to the C–H and S=O stretching of DMSO, respectively. The DMSO S=O stretching is centred at 1042 cm^{-1} and a shift in this wavenumber is indicative of formation of a coordination bond. Bands centred at 2926, 2904 cm^{-1} are attributed to the C–H stretching in **4.9** and finally the bands 1455 and 1402 cm^{-1} are attributed to C–H bending of **4.9**. Finally, the band at 670 cm^{-1} belongs to the C–S stretching of **4.9**. These values are in good agreement with those reported in literature for **4.9**.[18]

The SC-XRD analysis of these green crystals reveals a mononuclear coordination compound formed between nickel(II) and **4.9** with a formula $[(Ni(\mathbf{4.9})(Cl)_2]$•DMSO (**4.10**), as depicted in **Figure 4-94**. The nickel(II) metal centre is 6-coordinated to the tridentate ligand, two chloride anions and one DMSO molecule in a distorted octahedral geometry. The unit cell of **4.10** contains two nearly identical independent coordination compounds, as shown in **Figure 4-94c**. The Ni–S coordination bond length ranges from 2.3976(4) to 2.4179(4) Å and the Ni–Cl coordination range from 2.3629(4) to 2.3776(4) Å. The CSD does not contain any coordination compounds between **4.9** and nickel(II) in a 1:1 ratio, thus **4.10** is a novel coordination compound.

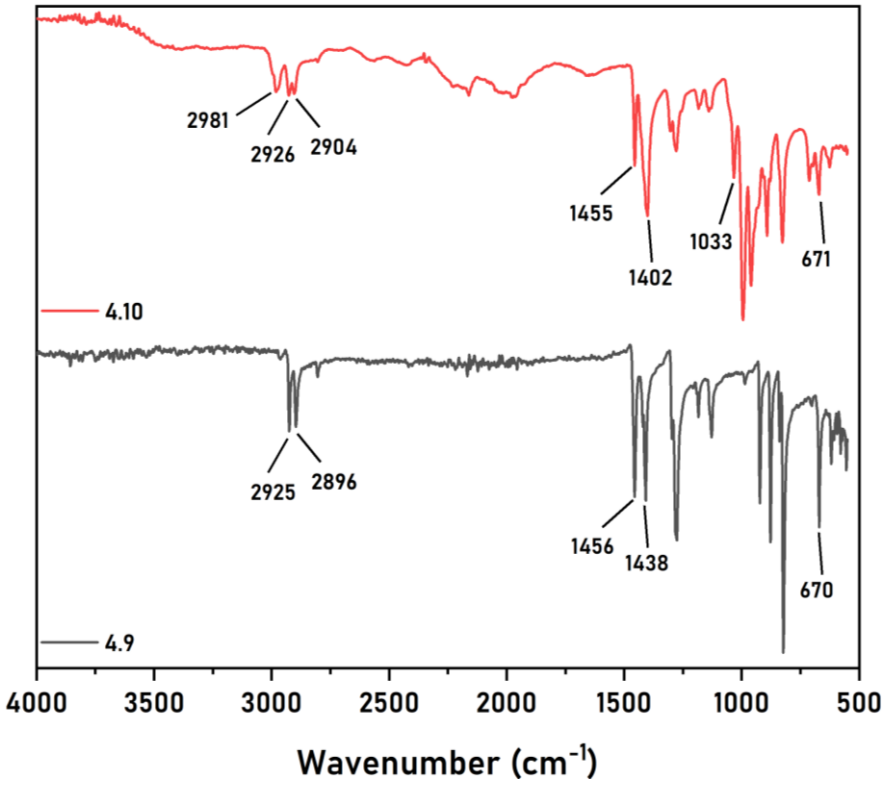

Figure 4-94. a) FT-IR spectrum of the ligand **4.9** and coordination complex **4.10**. Single crystal structures of b) the two independent molecules of **4.10** in the unit cell and c) the two independent molecules overlaid. Gray: C. Red: O. Light blue: Ni. Yellow: S. Green: Cl. Hydrogen atoms omitted for clarity.

However, after a few days after the initial green crystals had formed, the edges of the green crystals turned pink. Over the course of the following week, almost all crystals exhibited this pink colouration. The pink crystals were separated and analysed *via* SC-XRD, which revealed a different mononuclear nickel(II)-**4.9** cationic coordination compound with a M:L ratio of 1:2 and a formula of $[(Ni)_{0.5}$(**4.9**)]Cl•$2H_2O$ (**4.10**), **Figure 4-95e**. The Ni–S coordination bond lengths range from 2.3680(2) to 2.4074(2) Å. The Ni–S coordination bonds in this complex are shorter compared to those in **4.10** which suggests that this is thermodynamically more stable complex while that of **4.10** is the metastable coordination compound. The chloride anions form hydrogen bonded ribbons consisting of tetramers and hexamers with water molecules, as depicted in **Figure 4-95d**. In the coordination complex, nickel(II) still maintains a 6-coordinated environment and a distorted octahedral geometry.

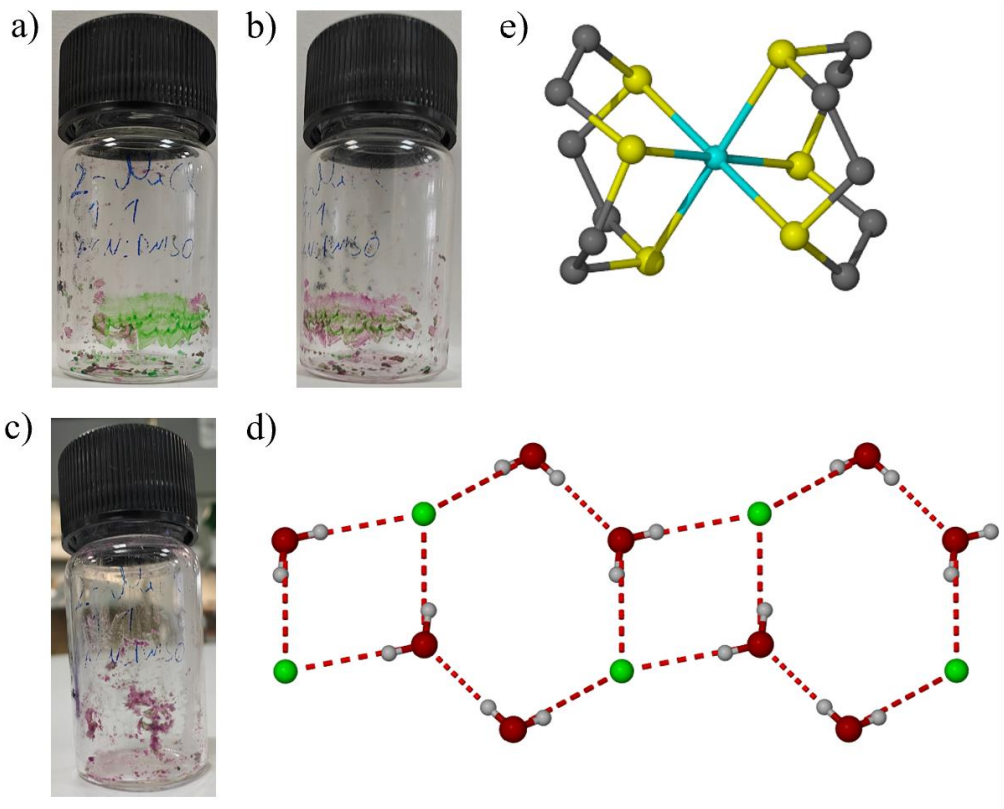

Figure 4-95. Pictures of a) the emergence of **4.11** at the corners of **4.10**, b) more pink crystals 3 days later and c) almost full exchange of green crystals into pink 6 days later. d) Single crystal structure of the hydrogen bonded ribbon between chlorine anions and water molecules. e) Single crystal structure of the binuclear complex **4.10**. Gray: C. White: H. Red: O. Yellow: S. Green: Cl. Light blue: Ni. Hydrogen atoms in e) omitted for clarity.

The crystals of **4.10** were further characterised *via* PXRD and elemental analysis. The experimentally obtained powder pattern of **4.10** (**Figure 4-96**, black line) exhibits high preferred orientation but good agreement between the two diffractograms at 12 and 26° indicates high bulk purity. Elemental analysis carried out on these crystals further supports the successful formation of this mononuclear **4.10** prior to its change to **4.11**. The newly formed crystals of **4.11** were also analysed *via* PXRD and were found to agree well with the pattern simulated from the crystal structure (**Figure 4-96**, blue and green traces). Additionally, elemental analysis results closely match with the expected composition of **4.11**.

The Cambridge Structural Database[19] contains 18 hits of coordination compounds between nickel(II) and **4.9**. Of these 18 hits, 10 are co-crystals thus leaving only 8 reported structures that are salts or solvates of nickel(II) and **4.9**. Only one of these eight structures is a binuclear compound consisting of a trichloro bridge and two nickel(II) and **4.9** units.[20] The seven that are left are all 1:2 nickel(II): **4.9** coordination compounds identical with **4.11**. Thus,

the 1:1 complex **4.10** has not been reported before and is a new structure. It is likely that this kinetic product has not been crystallised from other media before and the slow evaporation of DMSO allows for this complex to crystallise out.

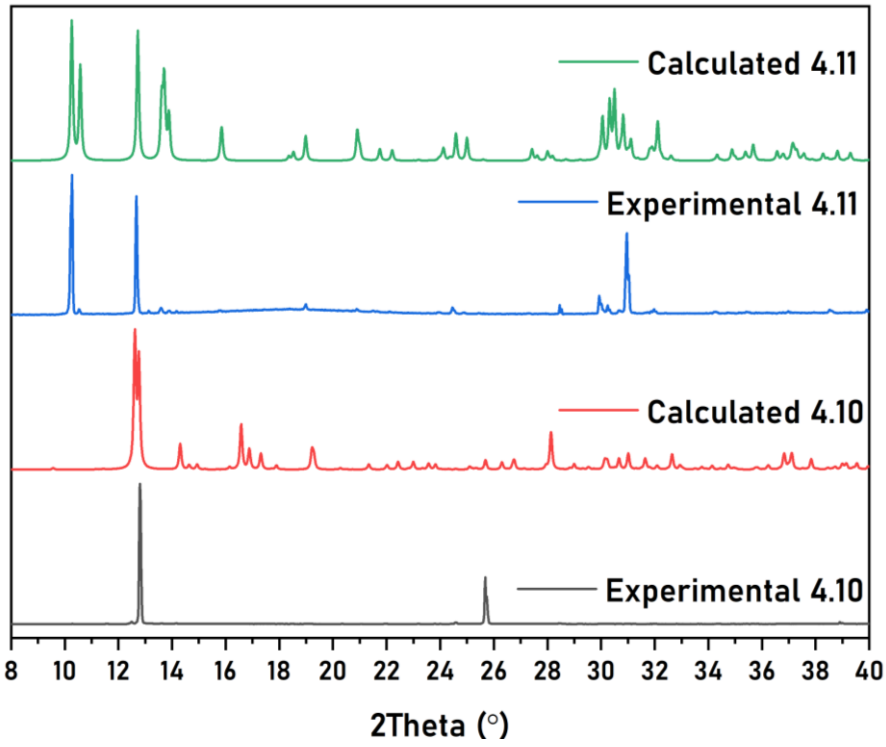

Figure 4-96. Experimentally obtained and simulated powder patterns of coordination compounds **4.10** and **4.11**.

Overall, coordination compounds consisting of nickel(II) and **4.9** exhibit a somewhat similar change in the crystal form as **4.2** and **4.3**. However, the mononuclear **4.10** does not become a binuclear complex. Rather, the coordinated chloride and solvent molecules become displaced by the **4.9** ligand resulting in the formation of a 1:2 nickel(II):**4.9** complex. In the case of the coordination complexes containing **4.1**, both the mono- and binuclear complexes consisted of a metal:ligand ratio of 1:1. Considering that nickel(II) also takes up the octahedral geometry as observed for complexes of **4.2a–d**, it should be possible to crystallise a binuclear trichloro-bridged complex consisting of nickel(II) and **4.9**. In fact, the CSD contains one entry of a binuclear and trichloro-bridged nickel-based coordination compound with **4.9**.[21] However, the authors only mention that this complex was obtained by reacting **4.9** with nickel(II) chloride and sodium borohydride in a mixed solvent consisting of acetonitrile and diethyl ether with no further instructions. Thus, future efforts can be focused on tailoring the crystallisation conditions towards controlling this multipolymorphic system and obtaining the trichloro-bridged complex.

4.3.2 Copper-Trithiacyclononane Coordination Compound

Along with nickel(II) and **4.9**, one crystal structure of copper(II) and **4.9** was also obtained. In a 3:1 (v:v) ACN:DMSO mixture, copper(II) chloride (0.1 mmol) was fully dissolved. Subsequently, **4.9** (0.1 mmol) was added to the resulting solution and instantly green crystals precipitated out (**Figure 4-97a**). **Figure 4-97b** shows the FT-IR spectra of the product (red line) along with pure **4.9** (black line). The peaks centred at 3382 and 1654 cm^{-1} are attributed to the O–H stretching of water molecules likely absorbed from the air. The peaks in pure **4.9** centred at 1438 and 1456 cm^{-1} are attributed to C–S stretching of the ligand molecule. These bands shift to 1438 and 1401 cm^{-1} in the spectrum of the product indicative of a formation bond forming with the sulfur atom. Finally, the more bands corresponding to the S=O (1014 cm^{-1}) and C–H stretching (2920 and 3008 cm^{-1}) in DMSO and C–H stretching (2896 and 2925 cm^{-1}) of **4.9** are also observed. This indicated that a coordination compound might have formed between **4.9** and copper(II) chloride. The green crystals were found to be too small for single crystal X-Ray diffraction analysis and consequentially were analysed by the I19 instrument at the Diamond synchrotron.

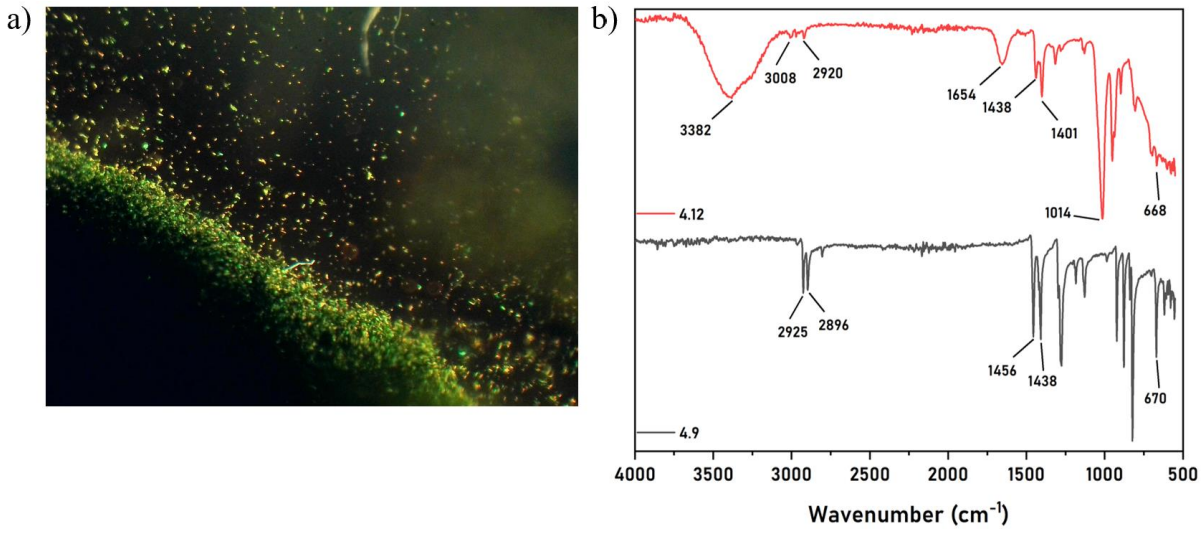

Figure 4-97. a) Microscope image of the small crystals of **4.12**. b) FT-IR spectra of pure ligand **4.9** (black line) and single crystals of **4.12** (red line). Relevant bands have been labelled and are discussed in the text.

The green single crystals comprise a copper(II): **4.9** coordination complex with a formula [Cu(**4.9**)Cl_2] (**4.12**), **Figure 4-98**. The complex crystallises in the orthorhombic crystal system and $P2_12_12_1$ space group. The copper(II) metal centre is 6-coordinated to one ligand of **4.9**, two chloride anions and one sulphur atom of an adjacent **4.9** molecule in a distorted octahedral geometry. Each molecule of **4.12** is oriented such as one sulfur atom points to the

copper(II) metal centre of the adjacent complex. As a result, adjacent molecules form coordination bonds with a Cu–S distance of 3.135(3) Å and a S–Cu–S angle of 155.36(6)°. While the coordination bond length is relatively long, the CSD contains 13 hits where the Cu–S distance is in the range 3.1–3.2 Å. Thus, it is not unreasonable to suggest that this coordination bond exists. The experimental PXRD pattern of the green crystals matches closely with that of the pattern calculated from the crystal structure data. The structure of **4.12** has been previously determined and exists in the CSD under the reference code YAKLOL).[22] The Cu–S coordination bond length between adjacent coordination compounds in YAKLOL is 3.205 Å, but the authors do not identify this as a coordination bond.

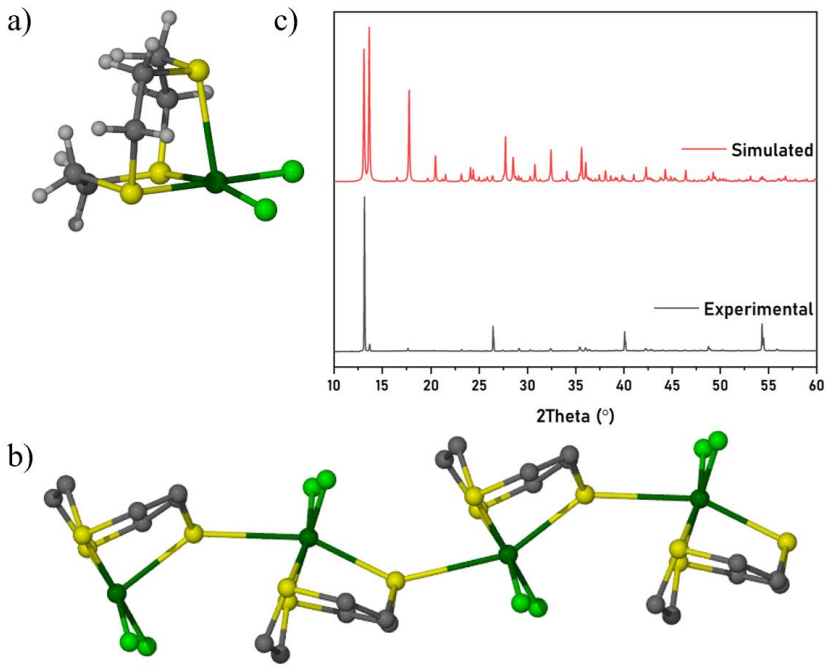

Figure 4-98. Single crystal structure of a) one unit of **4.12** and b) a chain of adjacent units of **4.12** showing the coordination between adjacent molecules of **4.12**. c) Experimental (black line) and simulated (red line) powder patterns of **4.12**. Gray: C. White: H. Yellow: S. Light green: Cl. Dark green: Cu. Hydrogen atoms in b) omitted for clarity.

4.4 Conclusions and Future Work

In conclusion, single crystals of various metals coordinated to the ligands **4.1** and **4.9** have been reported. It was shown that when the metal:ligand ratio is kept at 1:1, either the mono- or binuclear coordination compounds can be selectively crystallised, depending on the use of the solvent. However, when the ratio was changed to 2:1 M:L, the excess of metal results in the formation of crystals with brown and green colours. While green crystals were previously believed to belong to the mononuclear **4.3**, this work shows that also the binuclear compound exhibits this colour. However, any epitaxial growth of **4.2** onto **4.3** or *vice versa* was not achieved. A mononuclear complex of copper(II) bromide with **4.1** was obtained that is also isostructural to **4.3**, but attempts to epitaxially grow one phase on the other were unsuccessful. Instead, from a 1:1:1 mixture of the two copper salts and **4.1** crystallised a binuclear complex that contains both chloride and bromide bridging ligands in a 0.85:0.15 ratio, respectively. Crucially, this binuclear coordination complex contains only two bridging ligands as opposed to three that are present in every other binuclear complex. Overall, these results show that the lability of copper(II) metal makes it difficult to control the crystallisation of these compounds. Attempts to study the epitaxial growth using trithiacyclononane as a ligand were also unsuccessful, but yielded a novel kinetic crystal structure of nickel(II):**4.9** in a 1:1 ratio with two chloride and one DMSO ligand. This crystal transformed into the thermodynamic crystal consisting of two ligands of **4.9** coordinated to one nickel(II) metal centre.

Future efforts should expand on controlling the crystallisation of copper(II)-based coordination compounds with **4.1**. The lability of copper(II) makes it difficult to control the crystallisation of desired compounds. However, considering the high similarity between the obtained coordination compounds, expanding on the crystallisation conditions could be key towards potentially gaining control over the epitaxial growth of these compounds.

4.5 Experimental

4.5.1 Synthesis of [{Cu(4.1)}$_2$(μ-Cl)$_3$]Cl·4.5H$_2$O (4.2a)

Single crystals of **4.2a** were obtained by slowly evaporating a 2 mL ethanolic solution containing copper(II) chloride (0.013 g, 0.1 mmol) and **4.1** (19 μL, 0.1 mmol). The vial was covered with a parafilm and two holes were poked in to allow for a slow evaporation of ethanol. Over the course of 2 days, green single crystals formed. Yield: 49 mg, 71% based on crystallographic formula.

Elemental analysis calculated for [{Cu(**4.1**)}$_2$(μ-Cl)$_3$]Cl·2H$_2$O: Expected C 28.68 H 6.15, 11.15%. Found C 28.98, H 5.87, N: 11.51%.

Elemental analysis results reported herein differ slightly from the crystallographic formulae due to then handling of the samples after crystallisation. All samples were air dried for 24 hours prior to analysis, which likely resulted in the loss or change in the number of solvent molecules in the formulae corresponding to the elemental analysis results. In the case of **4.2a**, the formula determined by elemental analysis contains two water molecules as opposed to 4.5 in the crystallographic formula.

4.5.2 Synthesis of [{Cu(4.1)$_2$}(μ–Cl)$_3$]Cl·2CH$_3$OH, [{Cu(4.1)}$_2$(μ-Cl)$_3$][CuCl$_3$(H$_2$O)]·H$_2$O and [{Cu(4.1)}$_2$(μ-Cl)$_3$][CuCl$_4$]·4H$_2$O (4.2b–d, respectively)

Single crystals of **4.2b**–**d** were obtained by slowly evaporating a 2mL ethanolic solution containing copper(II) chloride (0.019g, 0.15 mmol) and **4.1** (19 μL, 0.1 mmol). The solution was sonicated for 5 minutes and subsequently covered with parafilm where two holes were poked to allow for a slow evaporation of ethanol. Over the course of 2 days, single crystals of **4.2b**–**d** formed within the vial. Due to the formation of three different crystal types which were grown on one another throughout the vial, it was impossible to determine the yield of these compounds separately.

4.5.3 Synthesis of [Cu(4.1)Cl$_2$] (4.3a)

Single crystals of **4.3a** were obtained from a 3:1 (v:v) ACN:DMSO mixed solvent solution to which copper(II) chloride (0.013 g, 0.1 mmol) and **4.1** (19 μL, 0.1 mmol) were added. The solution was sonicated for 5 minutes and subsequently left to evaporate at 70°C. Over the course of 1–2 weeks, green plank-shaped single crystals formed. Yield: 25 mg, 83% based on the crystallographic formula.

Elemental analysis calculated for [Cu(**4.1**)Cl$_2$]•2H$_2$O. Expected: C 31.63, H 7.37, N 12.30%. Found C 31.44 H 7.21 N 12.40%.

The formula determined by elemental analysis contains two water molecules as opposed to none in the crystallographic formula.

4.5.4 Synthesis of [Cu(4.1)Br_2]·0.5THF (4.4)

Single crystals of **4.4** were obtained *via* the solvent evaporation method. In 4 mL of THF, of copper(II)bromide (0.022 g, 0.1 mmol) was added and the mixture was sonicated for 5 minutes. To this solution, **4.1** (0.1 mmol, 0.19 mL) was added and the solution turned dark red. Instantly, gold-coloured single crystals of **4.4** precipitated out of the solution and were characterised *via* SC-XRD, PXRD and elemental analysis. Yield: 25 mg, 59% based on the crystallographic formula.

Elemental analysis calculated for [Cu(**4.1**)Br_2]. Expected: C 27.39, H 5.36, N 10.65%. Found: C 27.32, H 5.32, N 10.20%.

The formula determined from the elemental analysis results does not contain THF as opposed 0.5 THF molecules in the crystallographic formula.

4.5.5 Synthesis of [Ni_2(4.1)$_2$(μ-Cl_3)]Cl•4H_2O (4.5)

Single crystals of **4.5** were obtained *via* the solvent evaporation method. More specifically, to a 3:1 MeCN:DMSO solution, nickel(II)chloride hydrate (0.013 g, 0.1 mmol) was added and the resulting solution was sonicated for 3 minutes. To this, **4.1** (0.19 μL, 0.1 mmol) was added and the vial was left uncapped in a 70°C isothermal oven until blue needle-shaped crystals formed. The crystals were characterised *via* SC-XRD, PXRD and elemental analysis. Yield: 58 mg, 86% based on the crystallographic formula.

Elemental analysis calculated for [Ni_2(**4.1**)$_2$(μ-Cl_3)]Cl•3H_2O. Expected: C 31.28, H 7.00, N 12.16%. Found C 31.15, H 6.77, N 12.08%.

The formula determined from the elemental analysis results contains three water molecules as opposed to four in the crystallographic formula.

4.5.6 Synthesis of [Cd_3(4.1)$_2$(μ-Cl_6)(H_2O)$_2$]•H_2O (4.6)

Single crystals of **4.6** were obtained *via* the solvent evaporation method. More specifically, 19 μL (0.1 mmol) of **4.1** was added to a 5 mL ethanolic solution of cadmium chloride hemipentahydrate (0.023 g, 0.1 mmol). Upon the addition of **4.1**, the mixture instantly became cloudy and formed a precipitate. When ethanol was allowed to slowly evaporate for days, colourless prism-shaped single crystals of **4.6** formed. The crystals were characterised by SC-XRD, PXRD and elemental analysis. Yield: 89 mg, 92% based on the crystallographic formula.

Elemental analysis: calculated for $[Cd_3(\mathbf{4.1})_2(\mu\text{-}Cl_6)(H_2O)_2]\bullet H_2O$. Expected: C 22.4 H 5.23 N 8.71%. Obtained: C 22.22 H 5.15 N 8.66%.

4.5.7 Synthesis of $[Cd_3(4.1)_2(\mu\text{-}Cl_6)(CH_3OH)_2]$ (4.7)

Single crystals of **4.7** were obtained *via* the solvent evaporation method. More specifically, 19 µL (0.1 mmol) of **4.1** was added to a 5 mL ethanolic solution of cadmium chloride hemipentahydrate (0.034 g, 0.15 mmol). Overnight, plank-shaped single crystals of **4.7** formed and were characterised by SC-XRD and PXRD. Elemental analysis of **4.7** was not undertaken due to the transformation of crystals to **4.6**.

4.5.8 Synthesis of Epitaxially Grown 4.2b

Epitaxial growth of crystals of **4.7** onto a seed crystal of **4.6** was undertaken in a droplet containing a mixed solvent of ACN:DMSO in a 3:1 ratio. The solution was saturated with copper(II) chloride after which **4.1** was added (0.19 µL, 0.1 mmol). A seed crystal of **4.6** was placed in the centre of this droplet which was subsequently left to evaporate at room temperature. Within 72 hours, a brown precipitate formed on and around the seed crystal.

4.5.10 Synthesis of $[\{Cu(4.1)\}_2(\mu\text{-}Cl)_2][Cu_2Br_4(\mu\text{-}Br)_2]$ (4.8)

To a vial containing 2 mL of ethanol, a 2:1:1 mixture of copper(II) chloride (0.013 g, 0.1 mmol), copper(II) bromide (0.022 g, 0.1 mmol) and **4.1** (19 µL, 0.1 mmol) was prepared. The solution was sonicated for 5 minutes to ensure full dissolution. A thin layer of parafilm with two holes was placed over the vial and the solution was left to evaporate. Within 2 days, green and brown single crystals formed. The crystals were characterised *via* SC-XRD, PXRD and elemental analysis.

Elemental analysis calculated for $[\{Cu(\mathbf{4.1})\}_2(\mu\text{-}Cl)_2][Cu_2Br_4(\mu\text{-}Br)]\bullet DMSO$. Expected: C 20.97 H 4.22 N 7.34%. Found: C 20.68 H 4.59 N 7.54%.

The formula determined from the elemental analysis results contains one DMSO molecule as opposed to none in the crystallographic formula.

4.5.11 Synthesis of $[(Ni(4.9)(Cl)_2]\bullet$DMSO (4.10)

Single crystals of **410** were grown by slowly evaporating a DMSO:ACN (1:3 v:v) solution into which a 1:1 ratio of nickel(II)chloride hydrate (0.1 mmol, 0.13 g) and **4.9** (0.018 g, 0.1mmol) was added. The uncapped vial was placed into a 70°C isothermal oven and after 2 weeks green crystals of **4.10** formed on the side of the vial.

Elemental analysis calculated for $[(Ni(\mathbf{4.9})(Cl)_2]\bullet 2DMSO$. Expected: C 25.76, H 5.19 %. Found: C 26.09, H 5.03%.

The formula determined from the elemental analysis results contains two DMSO molecules as opposed to one in the crystallographic formula.

4.5.12 Single Crystals of $[(Ni)_{0.4}(\mathbf{4.9})]Cl{\bullet}2H_2O$ (4.11)

Single crystals of **4.11** grew concomitantly on the green crystals of **4.10**. Over the course of a week, green crystals of **4.10** almost completely turned into pink crystals of **4.11**.

Elemental analysis calculated for $[(Ni(\mathbf{4.9})_2]Cl_2{\bullet}6H_2O$. Expected: C 24.09, H 6.06%. Found: C 23.70, H 5.51%.

The formula determined from the elemental analysis results contains six water molecules as opposed to two in the crystallographic formula.

4.5.13 Single Crystals of $[Cu(\mathbf{4.9})Cl_2]$ (4.12)

Single crystals of **4.12** were obtained by adding copper(II) chloride (0.013 g, 0.1 mmol) to a 3:1 (v:v) mixture of ACN:DMSO. When copper(II) chloride was fully dissolved, **4.9** (0.018g, 0.1 mmol) was added. Instantly, small green crystals precipitated out of the solution. The single crystal data was collected using Synchrotron radiation due to the small size of the crystals. The crystals were additionally characterised *via* PXRD and elemental analysis. Yield: 30 mg, 96% based on the crystallographic formula.

Elemental analysis calculated for $[Cu(\mathbf{4.9})Cl_2]$. Expected C 22.89 H 3.84%. Found: C 23.07 H 3.99%.

4.6 Crystallographic Data

Table 4-14. Crystal data for **4.2a**–**c**.

Compound	**4.2a**	**4.2b**	**4.2c**
Empirical formula	$C_{18}H_{51}Cl_4Cu_2N_6O_{4.5}$	$C_{18}H_{47}Cl_6Cu_3N_6O_2$	$C_{20}H_{50}Cl_5Cu_2N_6O_2$
Formula weight	692.52	782.93	710.99
Temperature/K	120.0	120.00	120.00
Crystal system	monoclinic	triclinic	monoclinic
Space group	P2/c	P-1	P2/c
a/Å	13.6066(5)	8.4340(3)	13.6119(4)
b/Å	13.4640(5)	14.2721(5)	13.4629(4)
c/Å	8.4597(4)	14.4171(5)	8.4691(2)
α/°	90	115.4850(11)	90
β/°	101.047(2)	91.8145(12)	101.0921(11)
γ/°	90	96.9720(12)	90
Volume/Å^3	1521.09(11)	1548.13(10)	1523.02(7)
Z	2	2	2
ρ_{calc}g/cm^3	1.512	1.680	1.550
μ/mm^{-1}	1.785	2.587	1.864
F(000)	726.0	804.0	742.0
Crystal size/mm^3	0.18 × 0.17 × 0.06	0.23 × 0.19 × 0.14	0.17 × 0.09 × 0.01
Radiation	MoKα (λ = 0.71073)	Mo Kα (λ = 0.71073)	Mo Kα (λ = 0.71073)
2Θ range for data collection/°	6.812 to 59.992	4.888 to 59.986	4.296 to 59.998
Index ranges	-19 ≤ h ≤ 19, -18 ≤ k ≤ 18, -11 ≤ l ≤ 11	-11 ≤ h ≤ 11, -20 ≤ k ≤ 20, -20 ≤ l ≤ 20	-19 ≤ h ≤ 19, -18 ≤ k ≤ 18, -11 ≤ l ≤ 11
Reflections collected	26786	54820	45005
Independent reflections	4420 [R_{int} = 0.0345, R_{sigma} = 0.0260]	8949 [R_{int} = 0.0292, R_{sigma} = 0.0199]	4437 [R_{int} = 0.0371, R_{sigma} = 0.0195]
Data/restraints/parameters	4420/12/171	8949/4/362	4437/16/173
Goodness-of-fit on F^2	1.067	1.034	1.152
Final R indexes [I>=2σ (I)]	R_1 = 0.0531, wR_2 = 0.1320	R_1 = 0.0227, wR_2 = 0.0515	R_1 = 0.0552, wR_2 = 0.1736
Final R indexes [all data]	R_1 = 0.0595, wR_2 = 0.1362	R_1 = 0.0257, wR_2 = 0.0527	R_1 = 0.0621, wR_2 = 0.1787

Table 4-15. Crystal data for **4.2d**, **4.3a** and **4.4**.

Compound	**4.2d**	**4.3a**	**4.4**
Empirical formula	$C_{36}H_{92}Cl_{10}Cu_5N_{12}O_4$	$C_9H_{21}Cl_2CuN_3$	$C_{11}H_{25}Br_2CuN_3O_{0.5}$
Formula weight	1429.41	305.73	430.70
Temperature/K	120.00	120.0	120.0
Crystal system	triclinic	orthorhombic	monoclinic
Space group	P-1	Pbca	$P2_1/n$
a/Å	8.3553(2)	14.0148(7)	14.9065(4)
b/Å	14.0339(4)	13.2604(7)	11.8171(3)
c/Å	26.3449(7)	14.0282(7)	18.1225(5)
α/°	101.2511(10)	90	90
β/°	90.5135(10)	90	92.9230(10)
γ/°	103.7579(9)	90	90
Volume/Å^3	2937.87(14)	2607.0(2)	3188.15(15)
Z	2	8	8
ρ_{calc}g/cm^3	1.616	1.558	1.795
μ/mm^{-1}	2.282	2.059	6.373
F(000)	1478.0	1272.0	1720.0
Crystal size/mm^3	0.19 × 0.08 × 0.03	0.19 × 0.14 × 0.02	0.19 × 0.03 × 0.03
Radiation	Mo Kα (λ = 0.71073)	Mo Kα (λ = 0.71073)	MoKα (λ = 0.71073)
2Θ range for data collection/°	4.816 to 61.998	5.13 to 59.998	4.4 to 59.994
Index ranges	-12 ≤ h ≤ 12, -20 ≤ k ≤ 20, -38 ≤ l ≤ 38	-19 ≤ h ≤ 19, -18 ≤ k ≤ 18, -19 ≤ l ≤ 19	-20 ≤ h ≤ 20, -16 ≤ k ≤ 16, -25 ≤ l ≤ 25
Reflections collected	114370	44453	54141
Independent reflections	18678 [R_{int} = 0.0448, R_{sigma} = 0.0333]	3803 [R_{int} = 0.0444, R_{sigma} = 0.0215]	9288 [R_{int} = 0.0487, R_{sigma} = 0.0408]
Data/restraints/parameters	18678/6/616	3803/0/143	9288/13/327
Goodness-of-fit on F^2	1.051	1.063	1.021
Final R indexes [I>=2σ (I)]	R_1 = 0.0410, wR_2 = 0.0860	R_1 = 0.0262, wR_2 = 0.0583	R_1 = 0.0308, wR_2 = 0.0529
Final R indexes [all data]	R_1 = 0.0517, wR_2 = 0.0901	R_1 = 0.0333, wR_2 = 0.0609	R_1 = 0.0524, wR_2 = 0.0584

Table 4-16. Crystal data for **4.5**, **4.6**, and **4.7**.

Compound	**4.5**	**4.6**	**4.7**
Empirical formula	$C_{18}H_{50.5}Cl_4N_6Ni_2O_{4.25}$	$C_{18}H_{50}Cd_3Cl_6N_6O_4$	$C_{22}H_{54}Cd_3Cl_6N_6O_2$
Formula weight	678.36	964.54	984.61
Temperature/K	120.0	120.0	120.00
Crystal system	monoclinic	monoclinic	monoclinic
Space group	P2/c	$P2_1/n$	$P2_1/n$
a/Å	13.5795(3)	8.5685(2)	9.5715(2)
b/Å	13.4279(3)	15.0605(4)	16.0566(4)
c/Å	8.4271(2)	13.8558(3)	11.8314(3)
α/°	90	90	90
β/°	101.7606(8)	106.8280(10)	91.7650(10)
γ/°	90	90	90
Volume/Å^3	1504.38(6)	1711.47(7)	1817.45(7)
Z	2	2	2
ρ_{calc}g/cm^3	1.498	1.872	1.799
μ/mm^{-1}	1.641	2.348	2.209
F(000)	717.0	956.0	980.0
Crystal size/mm^3	0.18 × 0.15 × 0.09	0.18 × 0.14 × 0.13	0.26 × 0.18 × 0.06
Radiation	Mo Kα (λ = 0.71073)	Mo Kα (λ = 0.71073)	Mo Kα (λ = 0.71073)
2Θ range for data collection/°	4.312 to 59.996	6.554 to 60	6.134 to 59.996
Index ranges	-19 ≤ h ≤ 19, -18 ≤ k ≤ 18, -11 ≤ l ≤ 11	-12 ≤ h ≤ 12, -21 ≤ k ≤ 21, -19 ≤ l ≤ 19	-13 ≤ h ≤ 13, -22 ≤ k ≤ 22, -16 ≤ l ≤ 16
Reflections collected	25075	28417	53889
Independent reflections	4371 [R_{int} = 0.0258, R_{sigma} = 0.0182]	4949 [R_{int} = 0.0237, R_{sigma} = 0.0166]	5263 [R_{int} = 0.0293, R_{sigma} = 0.0142]
Data/restraints/parameters	4371/0/179	4949/6/188	5263/1/186
Goodness-of-fit on F^2	1.056	1.083	1.083
Final R indexes [I>=2σ (I)]	R_1 = 0.0410, wR_2 = 0.0860	R_1 = 0.0153, wR_2 = 0.0342	R_1 = 0.0130, wR_2 = 0.0283
Final R indexes [all data]	R_1 = 0.0517, wR_2 = 0.0901	R_1 = 0.0170, wR_2 = 0.0348	R_1 = 0.0144, wR_2 = 0.0287

Table 4-17. Crystal data for **4.8**, **4.10** and **4.11**.

Compound	**4.8**	**4.10**	**4.11**
Empirical formula	$C_{18}H_{52}Br_{1.58}Cl_{2.42}Cu_2N_6O_5$	$C_8H_{18}Cl_2NiOS_4$	$C_{12}H_{32}Cl_2NiO_4S_6$
Formula weight	771.78	388.07	562.34
Temperature/K	150.0	120.00	120.00
Crystal system	triclinic	monoclinic	triclinic
Space group	P-1	$P2_1/c$	P-1
a/Å	8.4451(4)	14.0933(4)	7.5869(2)
b/Å	13.7705(7)	12.3739(3)	8.8360(3)
c/Å	13.8418(7)	17.3098(4)	9.0090(3)
α/°	79.299(2)	90	93.5818(9)
β/°	82.867(2)	100.4292(9)	104.7352(9)
γ/°	79.706(2)	90	106.9979(9)
Volume/$Å^3$	1549.35(13)	2968.77(13)	552.42(3)
Z	2	8	1
$\rho_{calc}g/cm^3$	1.654	1.737	1.690
μ/mm^{-1}	3.656	2.207	1.703
F(000)	793.0	1600.0	294.0
Crystal size/mm^3	0.21 × 0.07 × 0.03	0.22 × 0.12 × 0.07	0.12 × 0.11 × 0.09
Radiation	MoKα (λ = 0.71073)	Mo Kα (λ = 0.71073)	Mo Kα (λ = 0.71073)
2Θ range for data collection/°	4.628 to 59.998	4.07 to 62	7.278 to 59.998
Index ranges	-11 ≤ h ≤ 11, -19 ≤ k ≤ 19, -19 ≤ l ≤ 19	-20 ≤ h ≤ 20, -17 ≤ k ≤ 17, -25 ≤ l ≤ 25	-10 ≤ h ≤ 10, -12 ≤ k ≤ 12, -12 ≤ l ≤ 12
Reflections collected	37233	112885	14112
Independent reflections	8970 [R_{int} = 0.0395, R_{sigma} = 0.0338]	9439 [R_{int} = 0.0402, R_{sigma} = 0.0181]	3201 [R_{int} = 0.0224, R_{sigma} = 0.0184]
Data/restraints/parameters	8970/15/362	9439/0/318	3201/0/131
Goodness-of-fit on F^2	1.055	1.107	1.023
Final R indexes [I>=2σ (I)]	R_1 = 0.0420, wR_2 = 0.0925	R_1 = 0.0234, wR_2 = 0.0490	R_1 = 0.0165, wR_2 = 0.0399
Final R indexes [all data]	R_1 = 0.0498, wR_2 = 0.0961	R_1 = 0.0271, wR_2 = 0.0502	R_1 = 0.0181, wR_2 = 0.0407

Table 4-18. Crystal data for **4.12**.

Compound	**4.12**
Empirical formula	$C_6H_{12}Cl_2CuS_3$
Formula weight	314.78
Temperature/K	100.00
Crystal system	orthorhombic
Space group	$P2_12_12_1$
a/Å	7.3864(6)
b/Å	10.7201(5)
c/Å	13.4906(10)
α/°	90
β/°	90
γ/°	90
Volume/Å^3	1068.23(13)
Z	4
ρ_{calc}g/cm^3	1.957
μ/mm^{-1}	2.830
F(000)	636.0
Crystal size/mm^3	0.1 × 0.025 × 0.01
Radiation	Synchrotron (λ = 0.68890)
2Θ range for data collection/°	4.704 to 51.006
Index ranges	-7 ≤ h ≤ 8, -13 ≤ k ≤ 13, -16 ≤ l ≤ 16
Reflections collected	6437
Independent reflections	1956 [R_{int} = 0.0952, R_{sigma} = 0.2093]
Data/restraints/parameters	1956/0/110
Goodness-of-fit on F^2	0.963
Final R indexes [I>=2σ (I)]	R_1 = 0.0737, wR_2 = 0.1702
Final R indexes [all data]	R_1 = 0.1020, wR_2 = 0.1758

4.7 References

1 S. Mann, *Nature*, 1993, **365**, 499–505.

2 M. Simard, D. Su and J. D. Wuest, *J. Am. Chem. Soc.*, 1991, **113**, 4696–4698.

3 Y. Jiao, Y. Qiu, L. Zhang, W. G. Liu, H. Mao, H. Chen, Y. Feng, K. Cai, D. Shen, B. Song, X. Y. Chen, X. Li, X. Zhao, R. M. Young, C. L. Stern, M. R. Wasielewski, R. D. Astumian, W. A. Goddard and J. F. Stoddart, *Nature*, 2022, **603**, 265–270.

4 M. Wais Hosseini, R. Ruppert, P. Schaeffer, D. Cian, N. Kyritsakas and J. Fischer, *J. Chem. Soc., Chem. Commun.*, 1994, 2135–2136.

5 J. C. MacDonald, P. C. Dorrestein, M. M. Pilley, M. M. Foote, J. L. Lundburg, R. W. Henning, A. J. Schultz and J. L. Manson, *J. Am. Chem. Soc.*, 2000, **122**, 11692–11702.

6 C. R. R. Adolf, S. Ferlay, N. Kyritsakas and M. W. Hosseini, *J. Am. Chem. Soc.*, 2015, **137**, 15390–15393.

7 W. I. Cross, N. Blagden, R. J. Davey, R. G. Pritchard, M. A. Neumann, R. J. Roberts and R. C. Rowe, *Cryst. Growth Des.*, 2003, **3**, 151–158.

8 A. E. S. Van Driessche, N. Van Gerven, P. H. H. Bomans, R. R. M. Joosten, H. Friedrich, D. Gil-Carton, N. A. J. M. Sommerdijk and M. Sleutel, *Nature*, 2018, **556**, 89–94.

9 J. W. Steed, A. E. Goeta, J. Lipkowski, D. Swierczynski, V. Panteleon and S. Handa, *Chem. Commun.*, 2007, 813–815.

10 S. Y. AlQaradawi, H. S. Bazzi, A. Mostafa and E. M. Nour, *Spectrochim. Acta, Part A*, 2008, **71**, 1594–1598.

11 T. Manfredini, G. C. Pellacani, A. Bonamartini-Corradi, L. Pietro Battaglia, G. G. T. Guarini, J. G. Giusti, G. Pon, R. D. Willett and D. X. West1, *Inorg. Chem.*, 1990, **29**, 2221–2228.

12 S. Nalla and M. R. Bond, *Acta Crystallogr., Sect. C: Cryst. Struct. Commun.*, 2011, **C67**, m185–m194.

13 H. Fu, C. Jiang, C. Luo, H. Lin and H. Peng, *Eur. J. Inorg. Chem.*, 2021, **2021**, 4984–4989.

14 Y. L. Xu, Y. Cai, J. Y. Yu, Y. Xu, Y. Yang, S. H. Fang, J. R. Zhou, Y. Z. Huang and C. L. Ni, *J. Mol. Struct.*, 2022, **1256**, 132543.

15 A. A. Korlyukov, M. Yu Antipin, S. P. Knyazev, E. G. Gordeev, M. V Pecherskii, A. S. Frenkel and P. A. Storozhenko, *Russ. J. Gen. Chem.*, 2005, **75**, 1870–1873.

16 Z. Zhang, Z. R. Geng, X. W. Kan, Q. Zhao, Y. Z. Li and Z. L. Wang, *Inorg. Chim. Acta*, 2010, **363**, 1805–1812.

17 Z. Zhang, L. Z. Wu, Z. R. Geng and Z. L. Wang, *Inorg. Chim. Acta*, 2014, **415**, 14–21.

18 Y. S. Park and H. F. Shurvell B', *J. Mol. Struct.*, 1995, **355**, 169–176.

19 C. R. Groom, I. J. Bruno, M. P. Lightfoot and S. C. Ward, *Acta Crystallogr., Sect. B: Struct. Sci. Cryst. Eng. Mater.* , 2016, **72**, 171–179.

20 A. J. Blake, M. A. Haicrow and M. Schroder, *Acta Crystallogr., Sect. C: Cryst. Struct. Commun.*, 1992, **48**, 1844–1844.

21 A. J. Blake, M. A. Halcrow and M. Schroder, *Acta Cryst.*, 1992, **C48**, 1844–1846.

22 J. Shen and J. Pickardt., *Z. Naturforsch., B: Chem. Sci.*, 1992, **47**, 1736–1736.

5. Closing Remarks

This work aims to gain understanding over molecular assembly under the conditions of confined spaces and epitaxial crystal growth. To understand molecular assembly in confined spaces, single crystals of metal-organic frameworks (MOFs) were synthesised and small organic molecular clusters inside the pores of the frameworks were studied *via* single crystal X-Ray diffraction (SC-XRD). Epitaxial growth of isostructural coordination compounds was employed with aims of gaining control over crystallisation outcomes.

Firstly, single crystals of mesoporous lanthanide-based MOFs with the linker 4,4'-biphenyldicarboxylic acid (H_2BPDC) were synthesised solvothermally in DMF. These MOFs, labelled CCM-1–4, firstly reported elsewhere[1,2], were used to encapsulate small organic molecular clusters *via* single-crystal-to-single-crystal transition (SCSCT). This was achieved by soaking single crystals of MOFs inside a small amount of the guest liquid in order to exchange the solvent DMF molecules for the guest molecules. The guest exchange and framework crystallinity were characterised using Fourier Transform infrared (FT-IR) spectroscopy and powder X-Ray diffraction (PXRD) prior to SC-XRD analysis. Both partially and fully exchanged guest molecular clusters were visualised inside MOFs CCM-1 and CCM-2 *via* SC-XRD. Notably, pyridazine and 1,2,3-triazole encapsulated in CCM-1 (PYZ@CCM-1 and TAZ@CCM-1, respectively), form distinct clusters inside the framework pores, markedly differing from their bulk equivalents. For instance, TAZ@CCM-1 assembles into unique octamers comprising both *1H*- and *2H*-1,2,3-triazole tautomers stabilised *via* hydrogen bonding and π–π interactions. This approach, potentially when combined with crystal structure prediction (CSP)[3,4] models, could offer insights into uncovering novel polymorphs and mechanisms underlying the formation of sub-critical nuclei.

Two novel frameworks CCM-5 and CCM-6, along with two MOFs (CCM-7 and CCM-8) isostructural to those previously reported[5], based on the linker *N,N*-bis(5-isophthalic acid-1,4,5,8-naphthalenediimide (**3**) are also reported in this work. These frameworks exhibit larger void spaces than the previously discussed CCM-1–4 MOFs, facilitating the capture of molecular clusters of greater size. CCM-5, a zinc(II)-based MOF, features a complex interpenetrated topology determined *via* the TOPOSPro[6] software. CCM-6 is a lanthanum(III)-based framework very similar to a previously reported neodymium(III)-based framework.[5] Despite the poorer crystallinity of CCM-5–8 compared to CCM-1–4 MOFs, leading to significant disorder and challenges in accurately modelling the molecules inside the pores, these frameworks still provide an opportunity to study molecular clusters of larger sizes and

different shapes. Future efforts focusing on enhancing the crystallinity of the framework could lead to important findings towards furthering the understanding of molecular assembly processes under confined spaces.

The exploration of epitaxial growth for metal coordination compounds using the ligand 1,4,7-trimethyl-1,4,7-triazacyclononane (**4.1**) was undertaken, focusing on copper(II), nickel(II) and cadmium(II) metal salts. Among other crystallised compounds, this study yielded two mononuclear and isostructural coordination compounds from copper(II) chloride and copper(II) bromide salts, designated as **4.3** and **4.4**, respectively. As the colour of these compounds only differ *via* the nature of the metal salt, epitaxial growth of one compound onto the other was attempted. Unfortunately, any attempts at seeding the epitaxial growth of **4.3** onto **4.4** and *vice versa* were not successful. However, when both metal salts were mixed into a solution containing **4.1**, a binuclear coordination compound consisting of copper(II) metal centres bridged together by both chloride and bromide anions in a 0.85:0.15 ratio, respectively, was obtained. These results suggest that modifying the crystallisation conditions could potentially lead to successful epitaxial growth of these compounds. Unfortunately, any attempts at seeding the epitaxial growth of other crystal phases were unsuccessful. This work was also extended to the ligand 1,4,7-trithiacyclononane (**4.9**), culminating in one novel mononuclear coordination compound between **4.9** and nickel(II) chloride. This work shows that much effort needs to be put towards modifying the reaction conditions for successful epitaxial growth and control over crystallisation outcomes.

If this work was extended for one more year, future efforts should focus on reproducing the synthesis of single crystals of CCM-5 along with isoreticular expansion of CCM-1–4 MOFs in order to study molecular aggregation in larger but similarly shaped pores. Given more time, the efforts should also shift to combining the experimental results with DFT and CSP calculations. First, DFT calculations would aid in better understanding the aggregation mechanisms of the clusters inside CCM-MOFs. Additionally, CSP calculations would provide a polymorphic landscape of target molecules which could be indicative of the formation of any potential novel polymorphs within the framework voids. Finally, the formation of novel polymorphs could be probed by synthesising thin layers of MOF frameworks and using the pores to template the growth of polymorphs. This can be achieved by placing a droplet of a target molecule on the surface of the thin layer of the framework. As the molecules become ordered clusters within the pores, these clusters could potentially seed the growth of crystals of novel polymorphs on the surface of the thin layer of the framework.

5.1 References

1 J. Lee, N. W. Waggoner, L. Polanco, G. R. You, V. M. Lynch, S. K. Kim, S. M. Humphrey and J. L. Sessler, *Chem. Commun.*, 2016, **52**, 8514–8517.

2 Y. F. Han, X. H. Zhou, Y. X. Zheng, Z. Shen, Y. Song and X. Z. You, *CrystEngComm*, 2008, **10**, 1237–1242.

3 A. R. Oganov, C. J. Pickard, Q. Zhu and R. J. Needs, *Nat. Rev. Mater.*, 2019, 4, 331–348.

4 J. E. Carpenter and M. Grünwald, *J. Am. Chem. Soc.*, 2021, **143**, 21580–21593.

5 S. Park, J. Lee, H. Jeong, S. Bae, J. Kang, D. Moon and J. Park, *Chem*, 2022, **8**, 1993–2010.

6 V. A. Blatov, A. P. Shevchenko and D. M. Proserpio, *Cryst. Growth Des.*, 2014, **14**, 3576–3586.

Chapter 6 – General Experimental

6.1 Materials

All starting materials and solvents were purchased from Merck Life Sciences or Tokyo Chemical Industries and used without further purification.

6.2 Instrumentation and Characterisation of Compounds

6.2.1 Nuclear Magnetic Resonance (NMR) Spectroscopy

^{1}H and $\{^{1}H\}^{13}C$ NMR spectra were obtained using the Bruker Avance III-HD-400 spectrometer with operating frequencies of 400.07 and 100.57 MHz, respectively. Samples were prepared in 0.7 mL with a concentration of 1–3% (w/v). MOFs were dissolved by using the acid digestion method by adding a drop of HCl to a mixture of the MOFs in DMSO–d_6. Solid-state ^{13}C spectra were acquired at 100.63 MHz using a Bruker Avance III HD spectrometer and a 4 mm (rotor o.d.) magic-angle spinning probe and cross-polaristaion with a 1s recycle delay, 10ms contact time, ambient temperature and spin-rate of 10 KHz. Spectral referencing was performed with respect to an external sample of neat TMS and the data was collected by Dr. David Apperley.

6.2.2 Infrared (IR) Spectroscopy

FT-IR spectra were obtained using the PerkinElmer Spectrum 100 series spectrometer, fitted with a diamond universal Attenuated Total Reflectance (ATR) accessory. The spectra were collected in the range of 4000 cm-1 to 550 cm^{-1} at a resolution of 0.5 cm^{-1}.

6.2.3 Powder X-Ray Diffraction (PXRD)

XRPD patterns were measured using the Bruker AXS D8 Advance in BraggBrentano geometry, equipped with a Lynxeye Soller PSD detector. Samples were measured on a Si low background sample holder and analysed using Cu-Kα radiation at a wavelength of 1.5406 Å. Samples were scanned over an angle range of 3-60° 2θ with a step size of 0.02° and a scan rate of 1s per step.

6.2.4 Thermal Analysis

Thermogravimetric analysis (TGA) spectra were obtained using the Perkin Elmer Pyris I thermogravimetric analyser and differential scanning calorimetry (DSC) was performed using the Q1000 DSC from TA Instruments. Samples were run from room temperature up to designated temperatures under nitrogen atmosphere. Data was collected by William D. Carswell.

6.2.5 Elemental Analysis

Elemental analysis was performed with the Exeter CE-440 Elemental Analyser. Data was collected by Dr. Emily Unsworth.

6.2.6 Single Crystal X-Ray Diffraction (SC-XRD)

Single Crystal X-ray diffraction was performed using the Bruker D8 Venture diffractometer (high intensity Mo/Cu dual IμS2 sources, CMOS area detector, 3 circle goniometer and focusing mirrors) at 120.0 K using Mo Kα radiation (λ = 0.71073 Å). The diffractometer is equipped with the Cryostream 700+ (Oxford Cryosystems) open flow nitrogen cryostat (temp. range 80 – 500 K) and HELIX (Oxford Cryosystems) open flow helium cryostat (temp. range 25 – 300 K). Data for poorly diffracting crystals was obtained at 100K using Rigaku Saturn 724+ diffractometer at station I19 of the Diamond Light Source synchrotron (undulator, λ = 0.6889 Å, ω-scan, 1.0°/frame). Data were processed using the Bruker APEX II software and solved and refined using the Olex2[1] and SHELXL[2] softwares.

6.2.7 UV-Vis Spectroscopy

UV-Vis spectra were acquired on the Lambda 35 UV/Vis spectrometer in the range of 200–700 nm at a resolution of 1 nm using a quartz cuvette.

6.2.8 Fluorescence and Emission Spectroscopy

Luminescence spectra were collected on the Ocean Optics HR2000+ linear CCD coupled to a QP600-025-UV-BX fibre optic cable. The spectrum was collected using custom wrote software in LabView that corrects for pixel spectral sensitivity across the whole wavelength range (400–800 nm). The spectrum was collected using an integration time of 10 ms with 1000 spectra collected and averaged.

6.2.9 Topological Analysis of Metal-Organic Frameworks

The topological analysis of MOFs was undertaken using the software ToposPro.[3] All discussed materials were analysed using the “single node” and “all node” deconstruction methods as discussed in the work by Öhström and co-workers.[4]

6.3 References

1 O. V. Dolomanov, L. J. Bourhis, R. J. Gildea, J. A. K. Howard and H. Puschmann, *J Appl Crystallogr*, 2009, **42**, 339–341.

2 G. M. Sheldrick, *Acta Crystallogr., Sect. C: Struct. Chem.*, 2015, **71**, 3–8.

3 V. A. Blatov, A. P. Shevchenko and D. M. Proserpio, *Cryst. Growth Des.*, 2014, **14**, 3576–3586.

4 C. Bonneau, M. O'Keeffe, D. M. Proserpio, V. A. Blatov, S. R. Batten, S. A. Bourne, M. S. Lah, J. G. Eon, S. T. Hyde, S. B. Wiggin and L. Öhrström, *Cryst. Growth Des.*, 2018, **18**, 3411–3418.